ISSN 1580-2949
UDK 669+666+678+53 MTAEC9, 47(2)143–258(2013)

MATER. TEHNOL.	LETNIK VOLUME 47	ŠTEV. NO. 2	STR. P. 143–258	LJUBLJANA SLOVENIJA	MAR.–APR. 2013

VSEBINA – CONTENTS

IZVIRNI ZNANSTVENI ČLANKI – ORIGINAL SCIENTIFIC ARTICLES

STROKOVNI ČLANKI – PROFESSIONAL ARTICLES

UDK 621.794.4:546.65
Original scientific article/Izvirni znanstveni članek

ISSN 1580-2949
MTAEC9, 47(2)145(2013)

KINETICS OF WEATHERED-CRUST ELUTION-DEPOSITED RARE-EARTH ORE IN A LEACHING PROCESS

KINETIKA POSTOPKA LUŽENJA ELUCIJSKO NANESENE PREPERELE SKORJE RUDE REDKIH ZEMELJ

Lili Zhang[1,2], Xiangyi Deng[1,2], Wen Li[2], Yigang Ding[1], Ru'an Chi[1], Xiaohua Zuo[2]

[1]Key Laboratory for Green Chemical Process of Hubei Province and the Ministry of Education, Wuhan Institute of Technology, 430073 Wuhan, China
[2]School of Chemical and Materials Engineering, Hubei Polytechnic University, 435003 Huangshi, China
deng29606@sina.com, wenl@ualberta.ca

Prejem rokopisa – received: 2012-07-23; sprejem za objavo – accepted for publication: 2012-09-13

The leaching reaction kinetics of weathered-crust, elution-deposited rare earth with mixed ammonium salts was studied. The influence of the concentration of the reagents and the particle size of the ore on the leaching rate was investigated. The results showed that the diffusion process and the leaching rate could be improved by increasing the reagent concentration and decreasing the leaching flowing rate and particle size. The leaching process could be explained using the shrinking-core model, which could be controlled with the diffusion rate of the reacting reagents in a porous solid layer. The leaching rate followed the equation $1–2/3\eta – (1 – \eta)^{2/3} = 7.126 \times 10^{-4} C^{0.3038} R^{0.1942} t$.

Keywords: leaching reaction, leaching rate, rare-earth ore, leaching process

Proučevana je kinetika reakcije luženja preperele skorje elucijsko nanesene rude redkih zemelj. Preiskovan je bil učinek koncentracije reagentov in velikosti zrn rude na hitrost luženja. Rezultati so pokazali, da je mogoče proces difuzije in hitrost luženja povečati s povečanjem koncentracije reagentov ter z zmanjšanjem hitrosti luženja in zmanjšanjem velikosti delcev. Postopek luženja se lahko razloži z modelom krčenja jedra, ki ga je mogoče kontrolirati s kontroliranjem hitrosti difuzije reagentov, ki reagirajo v poroznem trdnem sloju. Hitrost luženja je skladna z enačbo
$1 – 2/3\eta – (1 – \eta)^{2/3} = 7{,}126 \times 10^{-4} C^{0{,}3038} R^{0{,}1942} t$.

Ključne besede: reakcija luženja, hitrost luženja, ruda redke zemlje, postopek luženja

1 INTRODUCTION

Weathered-crust, elution-deposited, rare-earth ore is China's unique rare-earth mineral resource.[1–3] There are many advantages of the ore: a widespread distribution of rich reserves, a low radioactivity, it is rich in the middle and heavy rare earths, it is an easily extracted rare earth, it is simple to process by leaching giving high-quality products, etc. The development and utilization of the ore in the world have a significant influence. In China, special attention has been paid to rare-earth mineral resources in recent years. Therefore, high efficiency and the comprehensive exploitation of the weathered-crust, elution-deposited, rare-earth ore was intensively investigated over the past decade.

The leaching of the rare-earth ore is a liquid-solid multiphase reaction process, where the most common reaction is carried out in two ways: by using the integral-scaled model and the shrinking-core model. In the latter, a mixed ammonium salt solution is used as a leaching agent, causing the particle size of the ore to change only a little during the leaching reaction. For this reason, the leaching process of the rare-earth ore is usually based on the shrinking-core model. The leaching rate is connected with the concentration, the temperature, the surface area of the solid phase, etc. The leaching process can be controlled by the outer diffusion, the inner diffusion, or the chemical reaction.[4,5] The influences of the concentration of the reagents and the particle size of the ore on the leaching rate were investigated to achieve a high rare-earth concentration, a low consumption of the leaching reagent and a high leaching rate.

2 EXPERIMENTAL WORK

2.1 Analysis of the ore samples

Ore samples are mostly random and taken from non-cemented sands; they are of a pale flesh-red color, containing clay minerals, quartz sand, rock-forming feldspar etc., obtained from Dingnan County of Jiangxi Province. They contain about 40–70 % of clay minerals, such as halloysite, illite, kaolinite and a small quantity of montmorillonite. Some 90 % of rare-earth ions adsorp-

Table1: The main components of the ore
Tabela 1: Glavne sestavine rude

main components	REO	SiO_2	Al_2O_3	Fe_2O_3	CaO	others
content (%)	0.1146	61.80	14.28	3.190	0.470	20.15

tion is in a state of kaolinite and mica. The chemical composition of the ore is presented in **Table 1**.

2.2 Process and Method

Prior to the leaching experiments, the ore sample was sieved through a +20 mesh, 20–60 mesh, 60–100 mesh, 100–140 mesh, +140 mesh to obtain five natural grain grades. Then the synthetic ore samples, according to the proportion of the natural grain grades, were weighed into a glass flask. The leaching agent with a certain liquid-solid ratio and a flow velocity puts the rare-earth ore into consideration. Then there is continuous leaching and the collected leaching solution. The RE^{3+} concentration was determined using the EDTA titration method,[6] measuring the volume of the leaching reagent. The leaching process was evaluated by the RE leaching rate, which was calculated according to the following formula:

$$\eta = \varepsilon/\varepsilon_0 \quad (1)$$

where ε and ε_0 are the amount of leaching-out RE^{3+} and the total RE^{3+} content of the sample ore.

2.3 Leaching mechanism for rare earth

The leaching process of the weathered-crust, elution-deposited, rare-earth ore is a kind of ion-exchangeable process between the positive ions in the solution and the clay minerals.[7,8] The chemical reaction equation is as follows:

$$[Al_4(Si_4O_{10})(OH)_8]m\cdot RE^{3+}_{(S)} + 3nNH_4^+(aq) \rightarrow \rightarrow [Al_4(Si_4O_{10})(OH)_8]m\cdot(NH_4^+)_{3n(S)} + nRE^{3+}_{(aq)} \quad (2)$$

The weathered-crust, elution-deposited, rare-earth ore is composed of ore particles, while the leaching process of the ore is a typical liquid-solid heterogeneous reaction. The leaching process can be described by the shrinking-core model and subdivided into five steps, as follows:[9]

- Diffusion of the leaching reagent (NH_4^+) through the film surrounding the particle to the surface of the clay minerals (Outer diffusion);
- Penetration and diffusion of NH_4^+ to the surface of the un-reacted core (Inner diffusion);
- Reaction of RE^{3+} with NH_4^+ (Chemical reaction);
- Diffusion of the RE^{3+} exchanged though the remainder back to the exterior surface of the clay minerals (Inner diffusion);
- Diffusion of the RE^{3+} exchanged though the exterior surface back into the solution of the fluid (Outer diffusion).

The kinetic control model of the RE leaching process can be divided into four models.[10,11]

1. Chemical reaction control:
   $1 - (1 - \eta)^{1/3} = k_1 t$
2. Diffusion through the liquid film control:
   $1 - (1 - \eta)^{1/3} = k_1 t$
3. Diffusion through the porous ore matrix control:
   $1 - \frac{2}{3}a - (1 - a)^{2/3} = k_3 t$
4. Mixed control:
   $1 - (1 - a)^{1/3} = \frac{k_1 k_2}{k_1 + k_2}\frac{C_0 M}{r_0 p}$

where, k_1, k_2, k_3 are the constants for the different control steps, respectively. a, t, C_0, r_0, p and M represent the rare-earth leaching rate, the leaching time, the initial concentration of the leaching reagent, the initial radius of the ore particle, the mole density of the ore particle and the mass of the ore particle, respectively.

3 RESULTS AND DISCUSSION

According to the optimum process of mixed ammonium salts, the leaching rare-earth ore experiment showed that the leaching rate of the rare-earth ore can reach up to 94.05 % when 2.0 % NH_4NO_3 and $(NH_4)_2SO_4$ with a quality ratio of 7 : 3, solid-liquid ratio of 0.5 : 1, and flow rate of 0.5 mL/min. The rare-earth leaching dynamics was researched on the basis of this process to determine the influence of the factors of the leaching rate and the control steps.

3.1 Effect of the leaching-reagent concentration

The initial average particle size of 0.2414 mm for the rare-earth ore was leached by different concentrations of mixed ammonium salts under the conditions of NH_4NO_3 and $(NH_4)_2SO_4$ with a quality ratio of 7 : 3 , a solid-liquid ratio of 0.5 : 1, and a flow rate of 0.5 mL/min. The influence of the different concentrations of reagents on the leaching rate was investigated. According to the reaction system, the reaction rate is proportional to the concentration of the product, increasing the leaching-

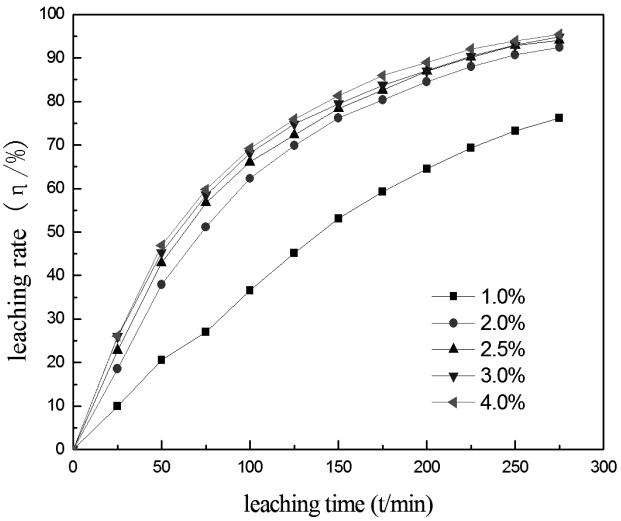

Figure 1: Effect of the concentration of reagents on rare-earth leaching rate
Slika 1: Vpliv koncentracije reagentov na hitrost luženja redke zemlje

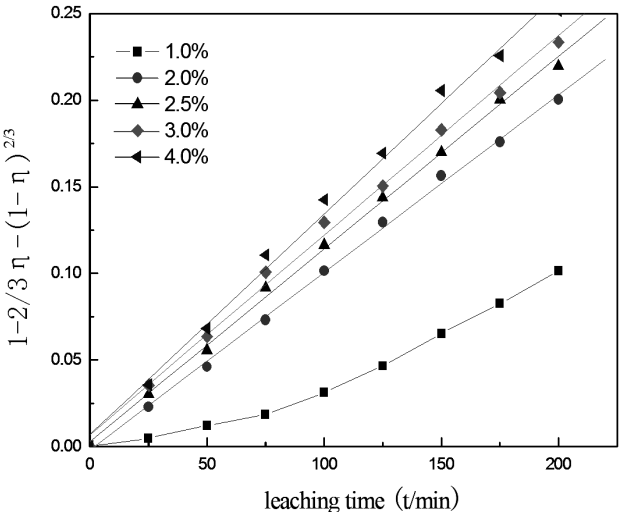

Figure 2: Leaching kinetic data for different concentrations of rare earth

Slika 2: Podatki za kinetiko luženja pri različnih koncentracijah redke zemlje

agent concentration is conducive to an improvement of the leaching reaction rate, thereby increasing the rare-earth leaching rate. **Figure 1** shows how the leaching rate of the rare earth increases as the initial concentration of ammonium salt increases, when the leaching agent concentration of 2.0 % in 275 min for the rare-earth leaching rate is 92.79 %, with the mass fraction of leaching agent increases, the unit volume of ammonium nitrate leaching agent rate increases, leading to the main leaching agent in a large number of Al^{3+} impurities, some of which will cover the surface of the rare-earth ore and hinder RE^{3+} leaching.

The date of the rare-earth leaching rate was substituted into the shrinking-core model in **Figure 2**. When the mass fraction of the leaching agent is greater than or equal to 2 %, it satisfies the equation $1 - 2/3\eta - (1 - \eta)^{2/3} = kt$. Indicating that the leaching process step of the rare-earth ore is inner-diffusion controlled, and it can be used in the model equation:

$$1 - 2/3\eta - (1 - \eta)^{2/3} = k'C^aR^bt \quad (3)$$

where η is the rare-earth leaching rate (%); C is the concentration of the leaching reagent (g/L); R is the initial radius of the ore particle (mm) and t is the leaching time (min). This equation reflects the influence of leaching concentration and the particle size of the rare earth on the leaching rate.

Figure 2 can be drawn for different concentrations of the NH_4NO_3 and $(NH_4)_2SO_4$ compounds of the rare-earth leaching agent and the apparent rate constant k value, assuming that the apparent rate constant is proportional to the power function of the concentration of the leaching agent, for which $\ln k = B + a \ln C$, and a least squares linear fit with the slope requirements.

Figure 3 shows a linear relationship between ln k and ln C, and the apparent reaction order is 0.3038, so that a = 0.3038.

3.2 Effect of the particle size of the ore

A rare-earth ore with a different particle size was leached by mixed ammonium salts under the condition of 2 % NH_4NO_3 and $(NH_4)_2SO_4$ with a quality ratio of 7 : 3, a solid-liquid ratio of 0.5 : 1, and a flow rate of 0.5 mL/min. The influence of the different particle size on the leaching rate was investigated.

Figure 4 presents the effect of particle size on the rare-earth leaching. It shows that the rare-earth leaching rate of ore particles with a smaller size is greater. It is known that the smaller the particle size, the more pores, and at the same time this shortens the length of the pore, thereby reducing the resistance of the inner diffusion and shortens the spread time with the effect of speeding up the rare-earth leaching. The leaching process could be

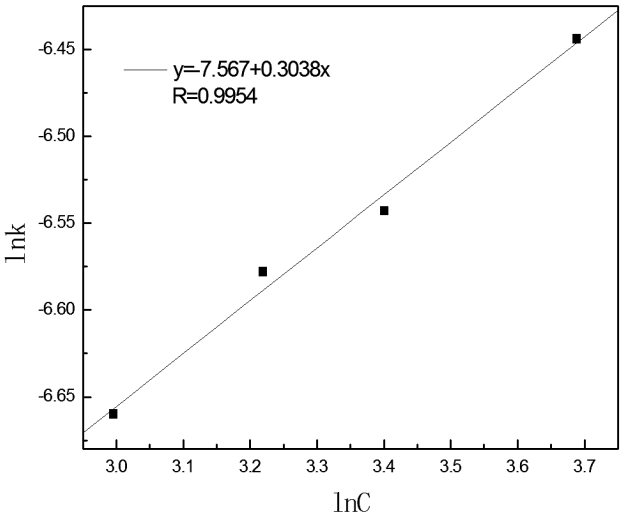

Figure 3: Relation between ln C and ln k

Slika 3: Odvisnost med ln C in ln k

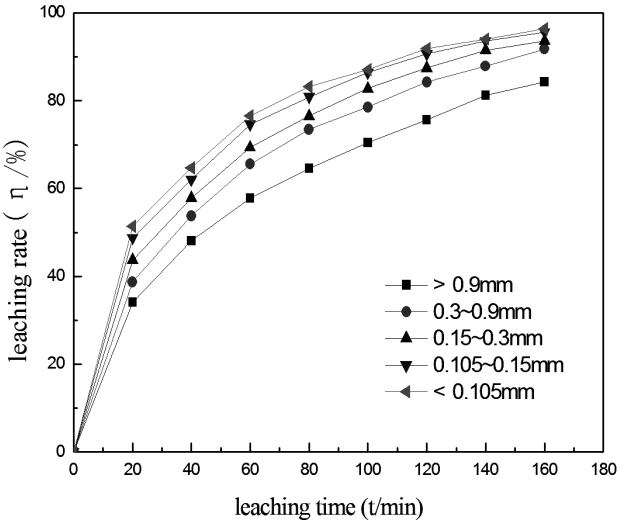

Figure 4: Effect of particle size on rare-earth leaching rate

Slika 4: Učinek velikosti zrn na hitrost luženja redke zemlje

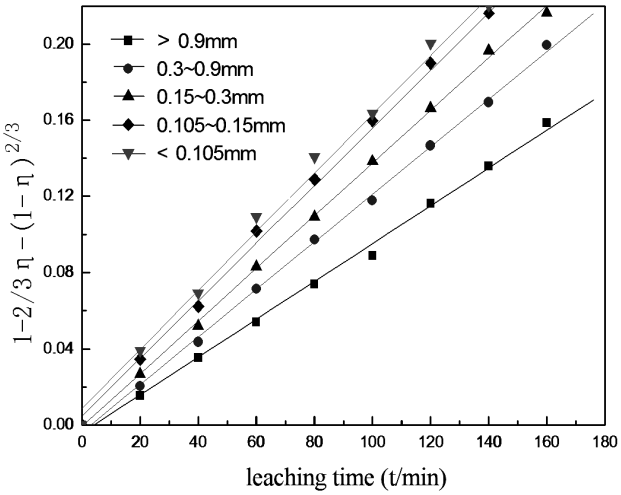

Figure 5: Leaching kinetic data for rare earths of different particle size

Slika 5: Podatki o kinetiki luženja redke zemlje pri različnih velikostih zrn

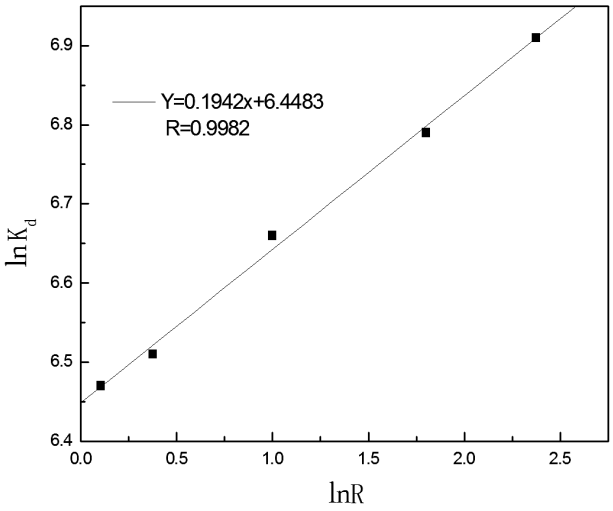

Figure 6: Relation between ln k_d and ln R

Slika 6: Odvisnost med ln k_d in ln R

explained with the shrinking-core model according to the ore particle-size experiment in **Figure 5**.

As shown in **Figure 6**, a good linearity exists between ln k_d and ln R, and the leaching process could be controlled by the diffusion rate of the reacting reagents in a porous solid layer. Furthermore, ln k_d = 6.4483 + 0.1942 ln R, so that b = 0.1942.

a and b were presented in the equation $1 - 2/3\eta - (1 - \eta)^{2/3} = k'C^aR^bt$, changing one factor, fixing others at the same time, so that k' is 7.126×10^{-4}. As a result, the equation of the mixed ammonium salts leaching the rare-earth ore is:

$$1 - 2/3\eta - (1 - \eta)^{2/3} = 7.126 \times 10^{-4}\ C^{0.3038}R^{0.1942}t \qquad (4)$$

4 CONCLUSIONS

The leaching kinetics of weathered-crust, elution-deposited, rare earth with mixed ammonium salts was investigated. The shrinking-core model with inner diffusion control was used to describe the leaching process of the rare earth. It was summarized as follows: the leaching rate increases with the increasing leaching reagent concentration and a decreasing of the particle size. The kinetics of the weathered-crust, elution-deposited, rare-earth leaching equation can be expressed as:

$$1 - 2/3\eta - (1 - \eta)^{2/3} = 7.126 \times 10^{-4}\ C^{0.3038}R^{0.1942}t.$$

Acknowledgement

This work was financially supported by National Natural Science Foundation of China (50974098) and Innovation team Fund of the Ministry of Education (IRT 0974).

5 REFERENCES

[1] R. Chi, J. Tian, Weathered crust elution-deposited rare earth ores [M], Nova Science Publishers, Inc., New York, 2008

[2] R. Chi, Z. Guocai, Rare earth partitioning of granitoid weathering crust in southern China [J], Transactions of Nonferrous Metal Society of China, 8 (**1998**) 4, 693–704

[3] R. Chi, J. Tian, Review of weathered crust rare earth ore [J], Journal of the Chinese rare earth society, 25 (**2007**), 641–650

[4] T. Xunzhong, L. Maonan, In-situ Leach Mining Of Ion-Absorbed Rare Earth Mineral [J], Mining research and development, 17 (**1997**) 2, 1–4

[5] M. Dingcheng, Metallurgical kinetic study [M], Central South University of Technology Publisher, 1987

[6] F. Zhaoheng, Leaching [M], Metallurgical Industry Publishers, 2007

[7] C. Ruan, D. Zuxu, O. Zhigao, W. Yuanxin, W. Cunwen, Correlation analysis on partition of rare earth in ion-exchangeable phase from weathered crust ores [J], Transactions of Nonferrous Metal Society of China, 16 (**2006**), 1421

[8] Y. Huiqin, O. Y. K. Xian, R. Guohua, A Study on Leaching Rare Earth from the Weathered Elution deposited Rare Earth Ore with Compound Leaching Reagent [J], Jiangxi Science, 23 (**2005**) 6, 721–726

[9] J. Tian, Y. Jingqun, Kinetic and mass transfer study on leaching a south china rare earth ore [J], Rare Metal, 22 (**1996**) 5, 330–342

[10] J. Tian, L. Shengliang, Y. Jingqun, Kinetic study on leaching a south china rare earth ore [J], Engineering Chemistry and Metallurgy, 16 (**1995**) 3, 354–357

[11] H. Y. Sohn, M. E. Wadsworth, Extraction metallurgy rate process [M], Metallurgical Industry Publishers, 1983

UDK 621.74.047:537.533.35
Original scientific article/Izvirni znanstveni članek

ISSN 1580-2949
MTAEC9, 47(2)149(2013)

MICROSTRUCTURAL AND PHASE ANALYSIS OF CuAlNi SHAPE-MEMORY ALLOY AFTER CONTINUOUS CASTING

MIKROSTRUKTURNA IN FAZNA ANALIZA SPOMINSKE ZLITINE CuAlNi PO KONTINUIRNEM LITJU

Mirko Gojić[1], Stjepan Kožuh[1], Ivan Anžel[2], Gorazd Lojen[2], Ivana Ivanić[1], Borut Kosec[3]

[1]University of Zagreb, Faculty of Metallurgy, Aleja narodnih heroja 3, 44103 Sisak, Croatia
[2]University of Maribor, Faculty of Mechanical Engineering, Smetanova 17, 2000 Maribor, Slovenia
[3]University of Ljubljana, Faculty of Natural Sciences and Engineering, Aškerčeva cesta 12, 1000 Ljubljana, Slovenia
gojic@simet.hr

Prejem rokopisa – received: 2012-07-24; sprejem za objavo – accepted for publication: 2012-09-14

The results of the characterization of a CuAlNi shape-memory alloy after continuous casting technology are shown. Using this procedure a bar with a diameter of 8 mm was manufactured. After solidification of the alloy the microstructure characterization was carried out using optic microscopy (OM), scanning electron microscopy (SEM), differential scanning calorimetry (DSC) and X-ray diffraction (XRD) methods. Our results showed that the as-cast alloy consisted of the parent β_1 and β_1' martensite phases. The martensite phase primary as the needle-like inside grains was observed. Martensite laths have different orientations inside particular grains. It was found that the average grains size is 98.78 μm. The grain diameter near to the external surface is higher than in the center. The average hardness of the alloy was 275 HV1.

Keywords: shape memory alloys, martensite, continuous casting, grain size

Prikazani so rezultati karakterizacije spominske zlitine CuAlNi po postopku kontinuirnega litja. Po navedeni proceduri so bile izdelane palice premera 8 mm. Po strjevanju zlitine je bila izvedena karakterizacija mikrostrukture z uporabo metod optične mikroskopije (OM), vrstične elektronske mikroskopije (SEM), diferencialne vrstične kalorimetrije (DSC) in rentgenske strukturne analize (XRD). Rezultati so pokazali, da lita zlitina sestoji iz izhodne faze β_1 in martenzitne faze β_1'. Opažena je bila martenzitna faza v obliki iglic v primarnih zrnih. Letve martenzita imajo različne orientacije v posameznih zrnih. Ugotovili smo, da je srednja velikost zrn 98,78 μm. Premer zrn v v bližini zunanje površine je večji kot v centru. Srednja trdota zlitine je bila 275 HV1.

Ključne besede: spominske zlitine, martenzit, kontinuirno litje, velikost zrna

1 INTRODUCTION

Shape-memory alloys (SMAs) demonstrate the ability to return to some previously defined shape or size when they are exposed to the appropriate thermal treatment. The condition necessary to enable the memory effect is the presence of a reversible phase transformation of austenite to martensite. Such phase transformations can be obtained by mechanical (loading) or thermal methods (cooling and heating). The main types of SMAs are Ni-Ti (nitinol), Cu-based and Fe-based alloys[1–8]. The main advantage of Cu-based SMAs is their low price compared to other SMAs. The properties of Cu-Al-Ni alloys are superior to those of Cu-Zn-Al alloys due to their wide range of useful transformation temperatures and small hysteresis. Cu-Al-Ni alloys can be applied at higher temperatures (close to 200 °C).

Generally, ternary Cu-based shape-memory alloys show a very large grain size. This problem can be solved by the addition of appropriate refining elements (Zr, Ti, B etc.) due to the formation of precipitates that limit the grain size and grain growth[9–11] and/or by applying the technology of rapid solidification. Generally, one of reasons for using the technique of rapid solidification is to obtain a small grain size for the SMAs[12,13]. The grain sizes obtained in the Cu-base are of the order of 10 μm in alloys produced by powder metallurgy and by rapid solidification[14]. Melt-spinning is the most commonly used technique for the production of ribbons[15,16]. In recent years the continuous casting technique is one of the technologies for production of SMAs due to the special competitive growth mechanism of the crystals and formation of a cast product with a favorable texture[17,18].

In the present paper the microstructure of Cu-Al-Ni SMAs obtained directly from the melt by continuous casting techniques are shown. The main aim of this paper was to obtain a homogenous martensite microstructure by solidification without any heat-treatment procedure.

2 EXPERIMENTAL

The Cu-Al-Ni shape-memory alloy (a bar of 8 mm diameter) was fabricated by means of the continuous casting technique using a device for vertical continuous casting that is connected with a vacuum induction furnace. The heating temperature was 1230 °C. The

process of casting including the initial melting and solidification was performed using a vacuum or protective atmosphere. The characterization of the alloy was carried out by optical microscopy (OM), scanning electron microscopy (SEM) equipped with energy-dispersive spectroscopy (EDS), differential scanning calorimetry (DSC) and X-ray diffraction (XRD) methods. For microstructural observations, the samples were grinded (120–800 grade paper) and polished (0.5 μm Al_2O_3). Later on, the samples are etched in a solution composed of 2.5 g $FeCl_3$ and 48 ml methanol in 10 ml HCl. The procedure for etching consisted of etching for 2 min, inter polishing for 2 min, and later etching for 1 min. The grain-size measurements were carried out by OM using the grain cutting line method. Hardness tests were carried out using the Vickers method (HV1). The differential scanning calorimetry (DSC) measurements were employed using a device under an argon atmosphere in the temperature range from room temperature to 300 °C. The rates of heating and cooling were 10 K/min. In order to determine the phase composition the X-ray diffraction (XRD) measurements were performed. CuKα radiation was used.

3 RESULTS AND DISCUSSION

The chemical composition analysis of the alloy was done using EDS analysis (**Figure 1**). The results showed that the chemical composition of the alloy was 82.73 % Cu, 13.16 % Al and 4.11 % Ni (mass fractions). The microstructures of the lateral and longitudinal cross-sections of the bar after continuous casting are characteristic of a continuously casted bar (**Figure 2**). Under the surface there was a layer of fine equiaxiad grains followed by a region of long fringe crystals oriented towards to the centre of the cross-section where again equiaxiad grains appeared (**Figures 2a** and **b**). The orientation of the crystals was changed. The fringe crystals were formed at an angle with an average value of around 60° with the longitudinal bar axis. In according to Lojen et al.[19] the maximum achieved velocity of

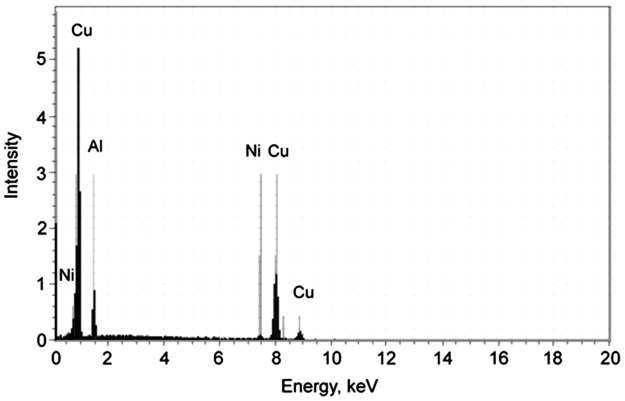

Figure 1: EDS spectrum of CuAlNi shape-memory alloy
Slika 1: EDS-spekter spominske zlitine CuAlNi

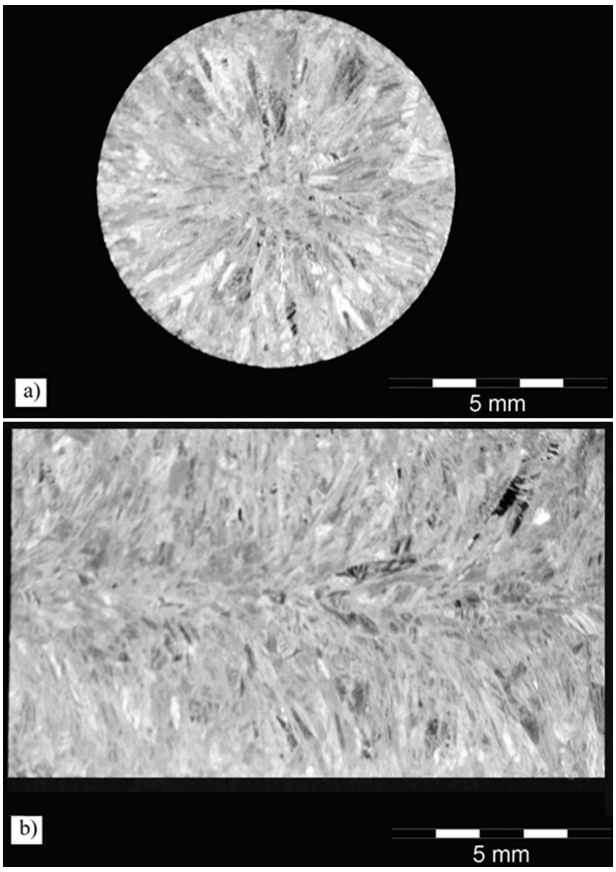

Figure 2: a) Lateral and b) longitudinal cross-section of bar after continuous casting
Slika 2: a) Prečni in b) vzdolžni prerez kontinuirno ulite palice

the solidification front was about 2.1 mm/s. It is possible that the crystallization front that simultaneously proceeds from the outer part of the bars to its centre causes a preferential orientation of the growing grains. The average hardness of the alloy was 275 HV1.

Figure 3 shows OM micrographs of the CuAlNi alloy after the continuous casting procedure. The grain boundaries are clearly visualized. As can be seen, the micrographs of the specimens show the typical martensite microstructure. Martensite laths have different orientations into particular grains. The grain size depends on the place from which the samples were taken. The grain diameter near to the external surface is higher than in the center.

An average grain size of 98.78 μm was observed for as-cast specimens. The number of grains per was 20.3 mm^{-2}. For an average grain size from 50 μm to 100 μm the fracture strain in the martensite phase is of the order of 10 %, which is sufficient for shape-memory applications. The grain size of the rapidly solidified alloys is determined by the amount of undercooling prior to the crystallization. Our results for bars after continuous casting showed that the sizes of grains vary from the surface towards the center of the bars. The increase in the grain diameter causes an increase of the M_s tem-

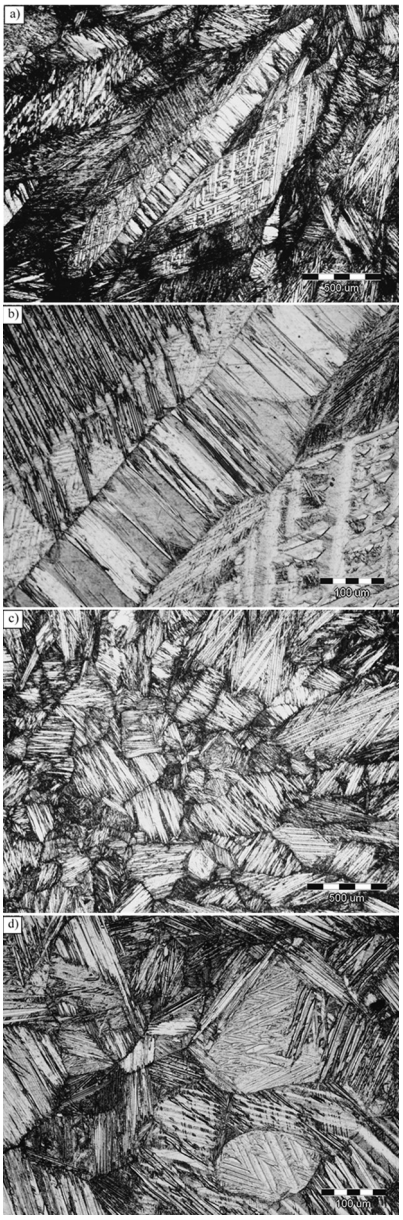

Figure 3: OM micrographs of the CuAlNi shape-memory alloy: a), b) near the external surface and c), d) in the center
Slika 3: OM mikrostrukture spominske zlitine CuAlNi: a), b) v bližini zunanje površine in c), d) v centru

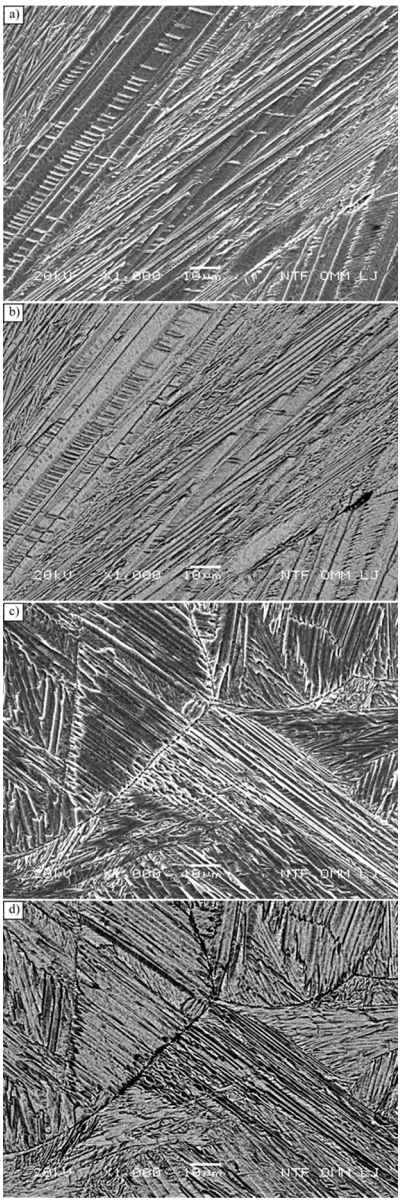

Figure 4: SEM micrographs of the CuAlNi shape-memory alloy: a), b) in longitudinal and c), d) lateral cross-section: a, c – SEI; b, d – BEI
Slika 4: SEM mikrostrukture spominske zlitine CuAlNi: a), b) v vzdolžnem in c), d) prečnem prerezu: a, c – SEI; b, d – BEI

perature. A similar behavior was already observed for the Cu-Al-Ni-Mn and Cu-Al-Ni-Mn-Ti shape-memory alloys[20] obtained using the melt-spinning technique. The temperature M_s depends on the grain size according to the relation $\Delta M_s \propto d^{1/2}$, where ΔM_s is the difference between the temperature M_s of the melt-spun ribbons (small grains) and the bulk alloy (large grains) and d is the mean grain diameter.

The martensitic microstructure was confirmed with the SEM micrographs (**Figure 4**). This microstructure is the result of the beta-phase of the Cu-Al-Ni alloys transforming into the martensite phase by cooling below the M_s temperature. The martensite is formed primarily as the needle-like shape. In some fields the V-shape

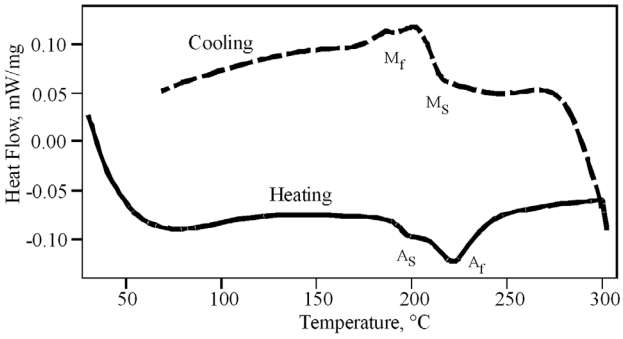

Figure 5: DSC curves of CuAlNi bar during cooling and heating
Slika 5: DSC-krivulje palic CuAlNi med ohlajanjem in ogrevanjem

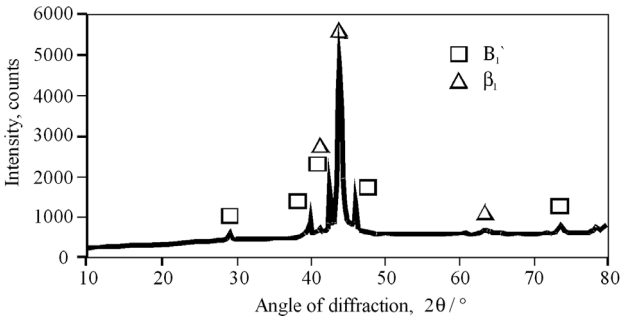

Figure 6: XRD spectrum of CuAlNi shape-memory alloy after continuous casting
Slika 6: XRD-spekter spominske zlitine CuAlNi po kontinuirnem litju

martensite was observed. This is a typical self-accommodating, zig-zag, martensite morphology, which is characteristic for the β_1' martensite in the CuAlNi alloy[21]. The parallel bands in the martensite can be considered as twin-like martensite.

Figure 5 shows DSC curves during heating and cooling. The temperature phase transformation are: M_s = 215 °C, M_f = 169 °C, A_s = 229 °C and A_f = 191 °C. It can be seen that the CuAlNi alloy is a possible candidate for high-temperature usage. **Figure 6** shows the X-ray profile of the as-casted alloy. Our XRD analysis showed that the alloy after continuous casting consisted of the parent β_1 and β_1' martensite phases.

4 CONCLUSIONS

The microstructure of a CuAlNi shape-memory alloy after continuous casting consisted of the parent β_1 and β_1' martensite phases. The martensite laths have different orientations into particular grains. The grain size depends on the place from which the samples are taken. The grain diameter near to the external surface is higher than in the center. It was found that the average grain size was 98.78 μm in particular grains. The temperature phase transformations determined by DSC measurements were: M_s = 215 °C, M_f = 169 °C, A_s = 229 °C and A_f = 191 °C. The average hardness of the alloy was 275 HV1.

Acknowledgements

This work was supported by EUREKA Project E! 3704 RSSMA "Rapidly Solidified Shape Memory Alloys" by the Ministry of Science, Education and Sports of the Republic of Croatia.

5 REFERENCES

[1] M. Gojić, Metalurgija, 31 (**1992**) 2/3, 77–82
[2] K. Otsuka, C. M. Wayman, Shape memory alloys, Cambridge University Press, Cambridge, 1998, 97–116
[3] D. Ćorić, M. Franz, Welding, 50 (**2007**) 5/6, 179–187
[4] N. M. Lohan, B. Pricop, J. G. Bujoreanu, N. Cimpoesu, Int. J. Mat. Res., 102 (**2011**) 11, 1345–1351
[5] H. Kubo, H. Otsuka, S. Farjami, T. Maruyama, Scripta Materialia, 55 (**2006**) 11, 1059–1062
[6] K. Otsuda, X. Ren, Progress in Materials Scienc, 50 (**2005**), 511–678
[7] T. Hu, L. Chen, S. L. Wu, C. L. Chu, L. M. Wang, K. W. K. Yeung, P. K. Chu, Scripta Materialia, 64 (**2011**), 1011–1014
[8] M. Gojić, S. Kožuh, B. Kosec, I. Anžel, Properties and Application of Shape Memory Alloys, Proceedings 9th Scientific Research Symposium with International Participation: Metallic and Nonmetallic Materials-production-properties and application, University of Zenica, Faculty of Metalurgy and Materials Science, Zenica, 2012, 13–26
[9] C. E. Sobrero, P. La Roca, A. Roatta, R. E. Bolmaro, J. Mlarría, Materials Science and Engineering A, 536 (**2012**), 207–215
[10] V. Sampath, Effect of Zr on Microstructure and Transformation Temperatures of Cu-Al-Ni Shape memory Alloys, Proc. Int. Conf. on Smart Materials, Bangalore, India, 2005, SC-148–156
[11] P. Zhang, A. Ma, S. Lu, G. Liu, P. Lin, J. Jiang, C. Chu, Materials and Design, 32 (**2011**), 348–352
[12] J. V. Wood, P. H. Shingu, Metallurgical Transactions, 15A (**1984**) 4, 471–480
[13] M. Izadinia, K. Dehghani, Trans. Nonferrous Met. Soc. China, 21 (**2011**), 2037–2043
[14] G. N. Sure, L. C. Brown, Metallurgical Transactions, 15A (**1984**) 8, 1984–1613
[15] A. C. Kneissl, E. Unterweger, G. Lojen, Advanced Engineering Materials, 8 (**2006**) 11, 1113–1118
[16] T. Goryczka, Archives of Metallurgy and Materials, 54 (**2009**) 3, 755–763
[17] M. Gojić, L. Vrsalović, S. Kožuh, A. Kneissl, I. Anžel, S. Gudić, B. Kosec, M. Kliškić, Journal of Alloys and Compounds, 509 (**2011**), 9782–9790
[18] Z. Wang, X. F. Liu, J. X. Xie, Materials Science and Enginnering A, 532 (**2012**), 536–542
[19] G. Lojen, A. C. Kneissl, M. Gojić, R. Rudolf, M. Čolić, I. Anžel, Livarski vestnik, 57 (**2010**) 4, 172–193
[20] J. Dutkiewicz, T. Czeppe, J. Morgiel, Materials Scinece and Engineering A, 573–275 (**1999**), 703–707
[21] U. Sari, I. Aksoy, Journal of Alloys and Compaunds, 417 (**2006**), 138–142

UDK 532.6:620.17
Original scientific article/Izvirni znanstveni članek

ISSN 1580-2949
MTAEC9, 47(2)153(2013)

CHARACTERIZATION AND DETERMINATION OF MECHANICAL PROPERTIES OF YBCO SUPERCONDUCTING THIN FILMS WITH MANGANESE USING THE TFA-MOD METHOD

KARAKTERIZACIJA IN DOLOČITEV MEHANSKIH LASTNOSTI SUPERPREVODNE TANKE PLASTI YBCO Z MANGANOM PO METODI TFA-MOD

Osman Culha[1], Isil Birlik[2], Mustafa Toparli[2], Erdal Celik[2], Sebastian Engel[3], Bernhard Holzapfel[3]

[1]Celal Bayar University, Department of Materials Engineering, Muradiye Campus, Manisa, Turkey
[2]Dokuz Eylul University, Department of Metallurgy and Materials Engineering, Tinaztepe Campus, Buca, Izmir, Turkey
[3]Leibniz-Institut für Festkörper- und Werkstoffforschung (IFW), Solid-State and Materials Research, Helmholtzstraße 20, 01069 Dresden, Germany
isil.kayatekin@deu.edu.tr

Prejem rokopisa – received: 2012-07-26; sprejem za objavo – accepted for publication: 2012-10-04

The aim of this study is to determine the microstructure, superconducting and mechanical properties of $YBa_2Cu_3O_{6.56}$ (YBCO) and YBCO thin films with a manganese (Mn) addition. All the YBCO superconducting films (undoped and Mn-doped) were dip-coated onto (001) $SrTiO_3$ (STO) single-crystal substrates with a metalorganic deposition using the trifluoroacetate (TFA-MOD) technique. The phase analysis, microstructure, surface morphologies and critical temperature (T_c) of the superconducting thin films were determined with an X-ray diffractometer (XRD), a scanning electron microscope (SEM), an atomic force microscope (AFM) and an inductive T_c measurement system. Since the main issue of this study is to determine the mechanical-property variations of the superconducting thin films with/without a Mn addition, the adhesion strength of these films on a STO substrate was tested with a Shimadzu scratch tester. Depending on the Mn addition, the critical forces of pure films increase from 56.23 mN, 58.63 mN and 60.11 mN for pure YBCO, YBCO with 0.05 g and 0.10 g of Mn. Furthermore, Young's modulus and the hardness of the undoped and Mn-doped YBCO thin films were measured with a CSM Berkovich nanoindenter using the load-unload sensing analysis under a 0.3 mN applied load.

Keywords: superconducting films, sol-gel synthesis, mechanical properties, nanoindentation

Namen te študije je določiti mikrostrukturo, superprevodne in mehanske lastnosti $YBa_2Cu_3O_{6.56}$ (YBCO) in tanke plasti YBCO z dodatkom mangana (Mn). Vse superprevodne plasti YBCO (nedopirane in dopirane z Mn) so bile nanesene na monokristalni substrat (001) $SrTiO_3$ (STO) s kovinoorganskim nanosom s trifluoracetatno tehniko (TFA-MOD). Fazna analiza, mikrostruktura, morfologija površine in kritična temperatura (T_c) superprevodne tanke plasti so bile določene z rentgenskim difraktometrom (XRD), vrstičnim elektronskim mikroskopom (SEM), mikroskopom na atomsko silo (AFM) in induktivnim merilnim sistemom za T_c. Ker je bila glavna naloga te študije določanje spreminjanja mehanskih lastnosti YBCO z dodatkom Mn in brez njega, je bila preizkušena adhezivnost te plasti na STO-podlago s Shimadzu preizkuševalnikom za razenje. Odvisno od dodatka Mn kritična sila v čisti plasti narašča od 56,23 mN, 58,63 mN in 60,11 mN za čisti YBCO, YBCO z 0,05 g in 0,10 g Mn. Poleg tega sta bila izmerjena tudi Youngov modul in trdota nedopirane in z Mn dopirane tanke plasti YBCO z nanomerilnikom trdote CSM Berkovich z analizo zaznavanja obremenjeno – neobremenjeno pri uporabljeni obremenitvi 0,3 mN.

Ključne besede: superprevodna plast, sol-gel sinteza, mehanske lastnosti, nanopreizkušanje trdote

1 INTRODUCTION

After the discovery of high-T_c superconductors (HTS), their various applications have been tested in various areas. These materials are supposed to increase the performance of devices such as magnetic resonance imaging (MRI) in medicine, energy-storage systems in a transformer, magnetic separators, levitation, nuclear magnetic resonance (NMR), generators, engines, cables, superconducting wires and tapes, accelerators, electromagnets, electronic transistors and bolometers.[1,2]

HTS thin films with a sharp resistive transition, high critical current density J_c and low flux noise offer the potential for such applications.[3] Extensive studies are currently being carried out worldwide on $YBa_2Cu_3O_{6.56}$ (YBCO) films grown on different single-crystal and metal-based substrates[4]. Many YBCO thin films have been developed using different deposition processes. Most of them use high vacuum techniques such as pulse laser deposition (PLD) and magnetron sputtering that can create high critical current densities on YBCO thin films. Nevertheless, they require significant start-up costs for long-length coated-conductor production[5]. On the other hand, thin films prepared with non-vacuum techniques like metal-organic decomposition using triflouroacetic acid (TFA-MOD) which is a sol-gel-related method, show similar superconducting properties and are relatively simple and inexpensive[6]. High-quality YBCO films with high J_c can be fabricated in a TFA-MOD process[7]. Finding the optimum process parameters for a coating solution can be challenging, but once the coating solution is found, it is very easy to obtain high J_c YBCO superconductors with supreme reproducibility. Although the TFA-MOD process using

metal acetates as the starting materials is more cost effective than vacuum processes, the highly purified metal acetates are expensive and thus it is desirable to find a more economic route. Recently, several attempts to use oxide powders, such as the commercially available YBCO powder, as the starting materials have been reported and they have shown high J_c for the YBCO films compared to the other methods.[8]

In this paper we present a new approach by combining the superior properties of a solvent, especially 2,4-pentanedionate, and a commercially available YBCO powder with TFA, acetone and propionic acid as the preliminary study. Therefore, YBCO superconducting films were produced with $BaMnO_3$ from the solutions prepared with the cheap and commercially available YBCO powders and Mn 2,4-pentanedionate, TFA propionic acid and acetone. In practical applications, the importance of the mechanical properties of YBCO-based films cannot be ignored. Superconducting films with poor mechanical properties are useless, even if they possess good transport and flux-pinning properties. Since an addition of particles as pinning centers results in important changes on the microstructure of thin films, their effect on micromechanical properties such as Young's modulus, hardness and adhesion strength also have to be investigated with respect to the particles type and quantity.

2 THEORETICAL BACKGROUND FOR MECHANICAL PROPERTIES

The scratch test is used to measure the interfacial adhesion for a range of different coatings.[9–19] During the test, a diamond indenter is drawn over the surface of a sample tested under a normal force, which is increased either stepwise or continuously until the critical normal force is reached, at which a well defined coating failure occurs.[9] Then, force is taken as a measurement of the adhesion between the coating and the substrate. The onset of a coating failure can be monitored with optical microscopy, acoustic emission (AE) and friction-force measurements[10]. It has been suggested that the coating adhesive failure is directly associated with a sudden increase in the friction force.[11,12] It is generally accepted that the scratch test is suitable for the coatings of a thickness ranging from 0.1 μm to 20 μm and this covers a large number of engineering applications.[13]

The adhesion strength (F) of the films was calculated by using equation (1) for the average value of three measurements. The scratch was examined with an optical microscope and the critical load, at which the coating was removed, was determined. The adhesion strength, F (in MPa), was calculated by using equation (1):[20]

$$F = \frac{H}{\left[(\pi R^2 H - W_c)/W_c\right]^{1/2}} \quad (1)$$

where H is the Brinell hardness value (kg mm^{-2}) of the $SrTiO_3$ (STO) substrate and R is the radius of the stylus (μm) and W_c is the critical force.

On the other hand, indentation tests are used to determine elasto-plastic properties such as Young's modulus, yield strength and the strain-hardening exponent[21] of thin films. Young's modulus may be inferred from the unloading indentation load-depth curve and the yield strength from the maximum indentation load. In addition, a method to extract the flow stress and the strain-hardening exponent using indentation data has been researched.[22–27] The indentation hardness of materials is measured in several ways by forcing an indenter having a specific geometry (ball, cone, and pyramid) into a specimen's surface.[28] The conventional microhardness value can be determined with an optical measurement of the residual impression left behind upon a load release. The development of depth-sensing indentation equipment has allowed an easy and reliable determination of two of the most commonly measured mechanical properties of materials: the hardness and Young's modulus.[26,29]

Two mechanical properties, namely, elastic modulus (E) and microhardness (H) can be obtained from the load and penetration-depth data. A typical load-penetration-depth curve can be investigated using a related reference.[30] During an indenter loading, the test material is subjected to both elastic and plastic deformations. One of the challenges in studying mechanical properties of thin films is that the traditional methods used to evaluate mechanical properties of bulk materials are not applicable for thin films and so far there is no standard test method for the evaluation of mechanical properties of thin films.[31] New methods, such as depth-sensing nanoindentation, microbridge test, uniaxial tensile test and ultrasonic method are being developed[32–35] for the measurement of mechanical properties of thin films. Among these methods, the depth-sensing nanoindentation technique provides a continuous record of the variation of indentation load with the penetration depth into a specimen and this technique has been an area of considerable attention in recent years due to its high resolution at a low load scale. Currently, the nanoindentation technique is being applied to determine hardness and Young's modulus, while limited studies are available to develop an effective method to obtain the plastic properties of thin films with a nanoindentation technique. For example, Nix[34] has utilized a nanoindentation technique to study the strength properties of thin films. Giannakopoulos and Suresh[32] have developed a step-by-step method to obtain the mechanical properties of materials from the nanoindentation experimental data. The indentation response of a thin film on a substrate is a complex function of the elastic and plastic properties of both the film and the substrate and it is essential to understand how the intrinsic mechanical properties of a film can be determined from the overall mechanical response of a film/substrate system. As the values of

elastic modulus and hardness, determined from indentations, should not depend on the value of *h* (indentation depth) and, therefore, on the value of the maximum load, the indentation depth should not exceed 10–20 % of the coating thickness, otherwise the results will be affected by the properties of the substrate.[21–30]

3 EXPERIMENTAL PROCEDURE

3.1 Preparation of the solutions

Y-Ba-Cu-O based solution was prepared from a commercial $YBa_2Cu_3O_{6.56}$ powder (yttrium-barium-copper oxide) with propionic acid, trifluoroacetic acid (TFA), acetone and 2,4-pentanedionate under atmospheric conditions at room temperature. The 8.3045 g YBCO powder was weighted out in order to prepare a 0.25 M and 50 ml solution. After 10 ml of propionic acid was added to the YBCO powder, the mixture was being dissolved in 25 ml of TFA at 45 °C for 60 min using an ultrasonic mixer (Sonorex digital 10P). The solvents were being removed at 100 °C for 60 min with a hot plate to yield a blue-sticky-glassy residue with a high viscosity. The solution of the film was made by dissolving the residue with up to 50 ml of TFA. The solvents were being evaporated from the solution again at 60 °C for 60 min until a highly viscous solution of a transparent-blue colour was obtained. After adding up to 50 ml of acetone into the solution, 15 ml of propionic acid and 5 ml of TFA were incorporated into the obtained viscous solution, and then a standard transparent solution was prepared. Finally, Mn alkoxide was separately added into 5 ml of the transparent solution with a low content of 2,4-pentanedionate as presented by the flow chart in **Figure 1**.

3.2 Coating process

Initially, (100) STO single-crystal substrates with the dimensions of 10 mm × 10 mm × 0.75 mm were rinsed in acetone using a standard ultrasonic cleaner. After that, the solutions were deposited on the substrates during a dip-coating process with a withdrawal speed of 0.3 cm/s in a vacuum atmosphere. The dip coating involves a formation of a film through a liquid-entrainment process that may be either batch or continuous in nature. The general steps include an immersion of the substrate into the dip-coating solution, a start-up, during which a withdrawal of the substrate from the solution begins, a film deposition, a solvent evaporation, and a continued drainage as the substrate is completely removed from the liquid bath. The film thickness formed in dip coating is mainly governed by the viscous drag, gravitational forces, and the surface tension.

The deposited gel films were converted to an epitaxial pure YBCO and a YBCO film with $BaMnO_3$ nanoparticles through a combination of the calcining and heat-treatment procedures. The gel film was dried from

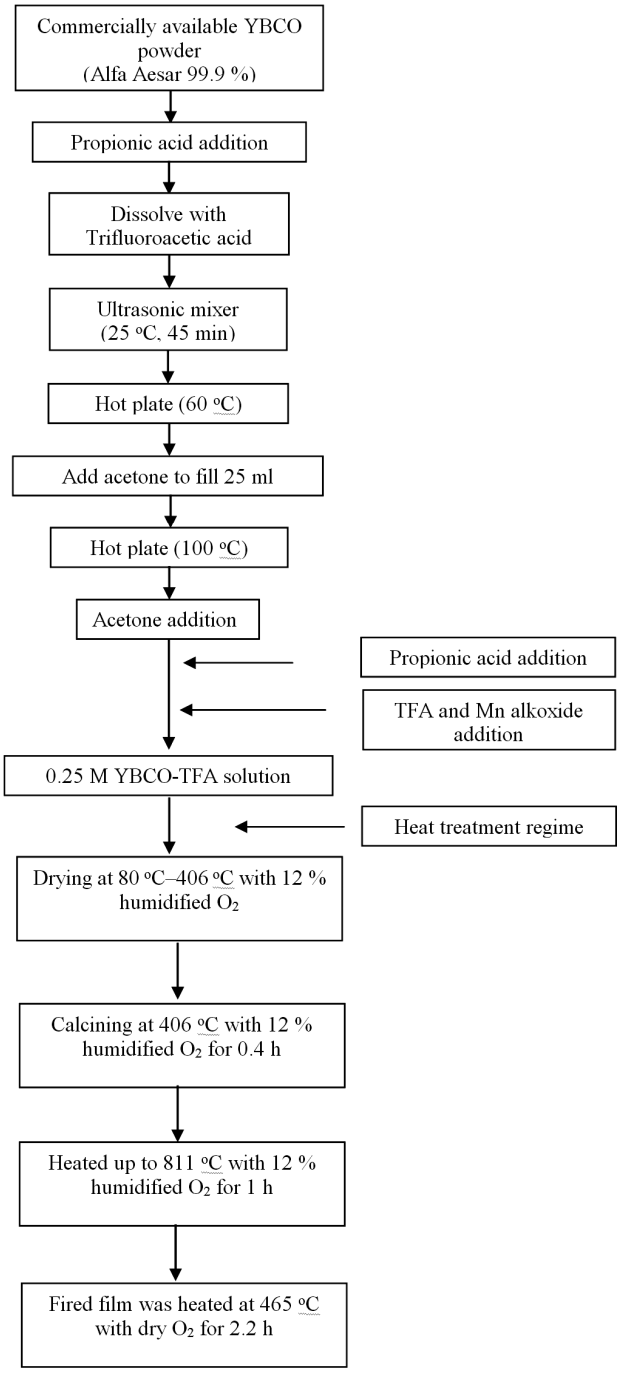

Figure 1: Flow chart of the TFA-MOD technique
Slika 1: Potek postopka TFA-MOD

80 °C to 406 °C in 12 % humidified oxygen. After the calcining was performed at 406 °C for 0.4 h in 12 % humidified nitrogen, the film was being heated up to 811 °C for 1 h in 12 % humidified nitrogen and the fired film was consequently heat treated at 465 °C for 2.2 h in a dry oxygen atmosphere. In order to obtain highly textured thin films on the STO substrate, the oxygen content was 500 ml O_2 during the heat-treatment process at 465 °C for 2.2 h as expressed in **Figure 1**.

3.3 Characterization process

The structural development of the produced thin films was investigated using X-ray diffraction (XRD-Rigaku D/MAX-2200/PC) patterns, recorded using the Co Kα irradiation (wavelength, λ = 0.178897 nm) and the scanning range was between 2θ = 10° and 90°. The surface topographies and additional particle effects on the microstructure of the films were examined with a high resolution SEM (JEOL JSM 6060). The surface morphologies of the films were measured with an atomic force microscope (AFM). The resistivity-temperature behaviors of the superconductive thin films were determined and the critical temperatures, T_c, were obtained depending on the additional particle content.

3.4 Mechanical properties of the films

The load on a Rockwell C diamond with a tip radius of the stylus (R) of 15 μm was linearly increased from 0 mN to 98 mN at the loading speed of 1 mN/s for the scratch test. In addition, the scratch speed of the diamond tip was 2 μm/s. The testing temperature and humidity percentage were 20.3 °C and 50 %, respectively. The scratch was examined with an optical microscope and the critical force (W_c) value, at which the coating removed from the substrate was determined three times for each sample. The hardness and Young's modulus of the produced thin films were measured under 0.3 mN of the applied peak load three times with the CSM Berkovich nanoindentation tester (the loading-unloading test mode) to determine additional particle effects on mechanical properties.

4 RESULTS AND DISCUSSION

4.1 Characterization of the films

Figure 2 (**a**–**c**) shows the XRD patterns of pure YBCO, YBCO with 0.05 g and 0.10 g Mn on the STO single-crystal substrate obtained with the TFA-MOD method. XRD patterns showed that the pure YBCO film has (001) major diffraction peaks corresponding to the

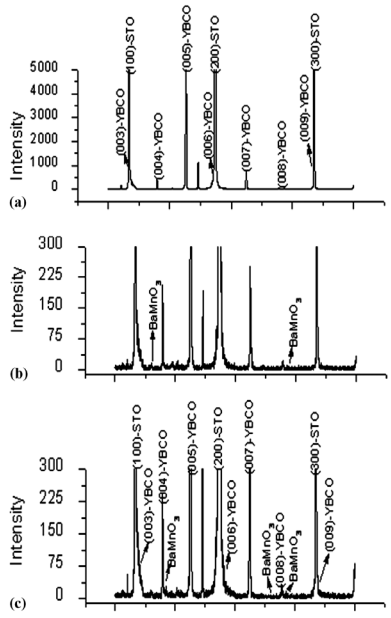

Figure 2: XRD patterns of: a) pure YBCO, b) YBCO with 0.05 g and c) 0.10 g $BaMnO_3$ nanoparticles

Slika 2: Rentgenski praškovni posnetki (XRD): a) čisti YBCO, b) YBCO z 0,05 g in c) 0,10 g $BaMnO_3$ nanodelci

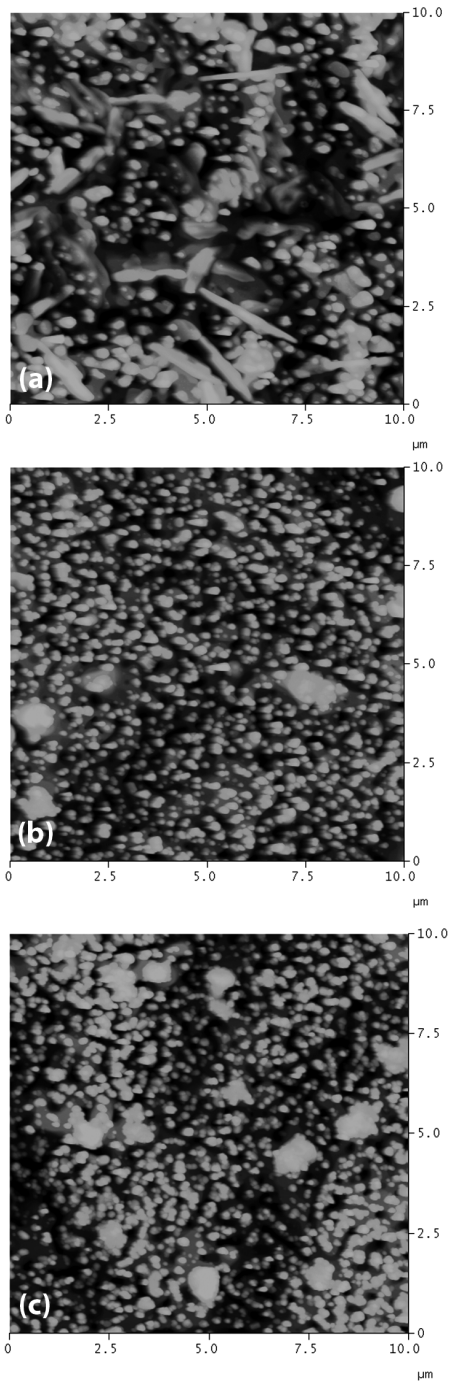

Figure 3: AFM study of YBCO thin films with: a) 0 g, b) 0.05 g and c) 0.10 g $BaMnO_3$ nanoparticles

Slika 3: AFM-študija YBCO tanke plasti z: a) 0 g, b) 0,05 g in c) 0,10 g $BaMnO_3$ nanodelci

(00l) parallel plane. It is worth mentioning that YBCO films with a high intensity were grown on the STO substrate using the TFA-MOD method. In addition, no second phases such as $Y_2Cu_2O_5$, BaF_2 and CuO were found in the case, where only a pure YBCO phase was formed. Apart from that, $BaMnO_3$ perovskite peaks with a low intensity were determined on account of the Mn-doping effect. However, XRD peaks from the $BaMnO_3$ perovskite second phase were hardly detected even for the film that was prepared using a precursor solution containing a 0.10 g Mn dopant.

The effects of $BaMnO_3$ nanoparticles on the microstructure of YBCO thin films were identified in **Figure 3**. According to the AFM results, all the films show typical CuO_x precipitatates with 100–200 nm diameters, which are regularly found on the surface of TFA-MOD samples. When the Mn content increased from 0 g to 0.10 g, the surface-roughness values of pure YBCO thin films and the YBCO thin films with $BaMnO_3$ nanoparticles changed from 21 nm to 33 nm depending on the Mn doping content. Nevertheless, a clear change in the YBCO surface was observed.

Figures 4, 5 and **6** show SEM micrographs of pure YBCO and the YBCO films with $BaMnO_3$ nanoparticles. Figure 4 shows surface topographies of the pure YBCO film with the a-axis which decrease the superconducting properties. These films were produced using the standard YBCO transparent solution. However, the decreasing superconducting properties with the a-axis were eliminated using the Mn doping in the standard YBCO precursor solution as clearly depicted in **Figures 5** and **6**. SEM micrographs indicate that structural defects can be reacted as nanodots or nanoparticles (due to the Mn addition) along the *c*-axis of the YBCO film. These properties result in an enhanced pinning over the pure YBCO film. Since Mn reacts with Ba and a $BaMnO_3$ perovskite structure forms in the YBCO film during the heat-treatment process, the microstructures of superconducting thin films were changed as expected.

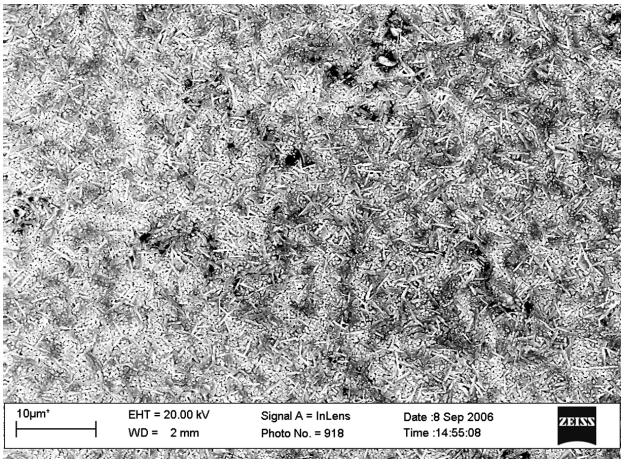

Figure 4: Surface morphology of a pure YBCO film with the a-axis produced using the standard YBCO transparent solution

Slika 4: Morfologija površine čiste plasti YBCO z a-osjo, izdelane s standardno prozorno raztopino YBCO

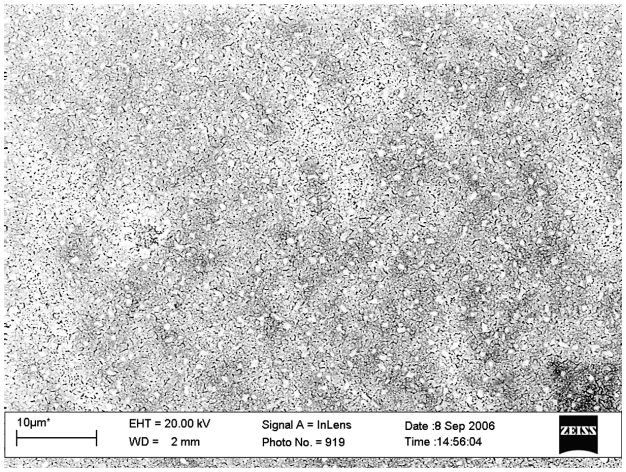

Figure 5: Surface morphology of an YBCO film with $BaMnO_3$ nanoparticles produced using the YBCO transparent solution with 0.05 g Mn doping

Slika 5: Morfologija površine YBCO tanke plasti z $BaMnO_3$ nanodelci, izdelane s prozorno raztopino YBCO, dopirano z 0,05 g Mn

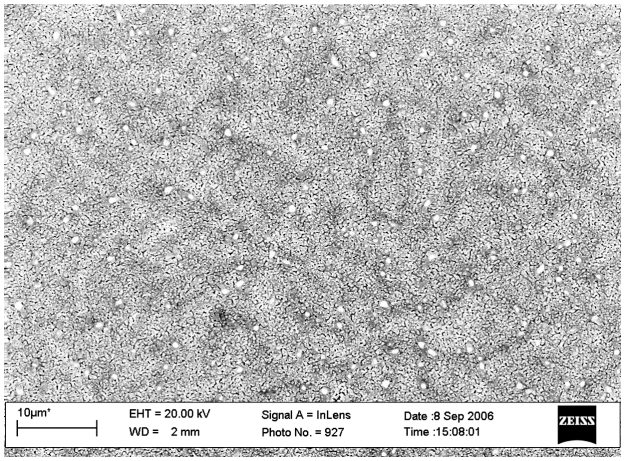

Figure 6: Surface morphology of an YBCO film with $BaMnO_3$ nanoparticles produced using the YBCO transparent solution with 0.10 g Mn doping

Slika 6: Morfologija površine YBCO tanke plasti z $BaMnO_3$ nanodelci, izdelane s prozorno raztopino YBCO, dopirano z 0,10 g Mn

The dependences of the inductively measured critical transition temperature (T_c) and transition width (ΔT_c) on the amount of $BaMnO_3$ in the structure are shown in **Figure 7**. It can be seen that there is sharp decrease in the resistivity near 90 K where the critical-temperature value of pure YBCO is 90.4 K. When the quantity of additional particles increases from 0.05 g to 0.10 g, the critical temperature changes from 90.2 K to 90 K. These additional particles do not affect the critical temperature and only behave as impurities or second phases for the flux-pinning properties.

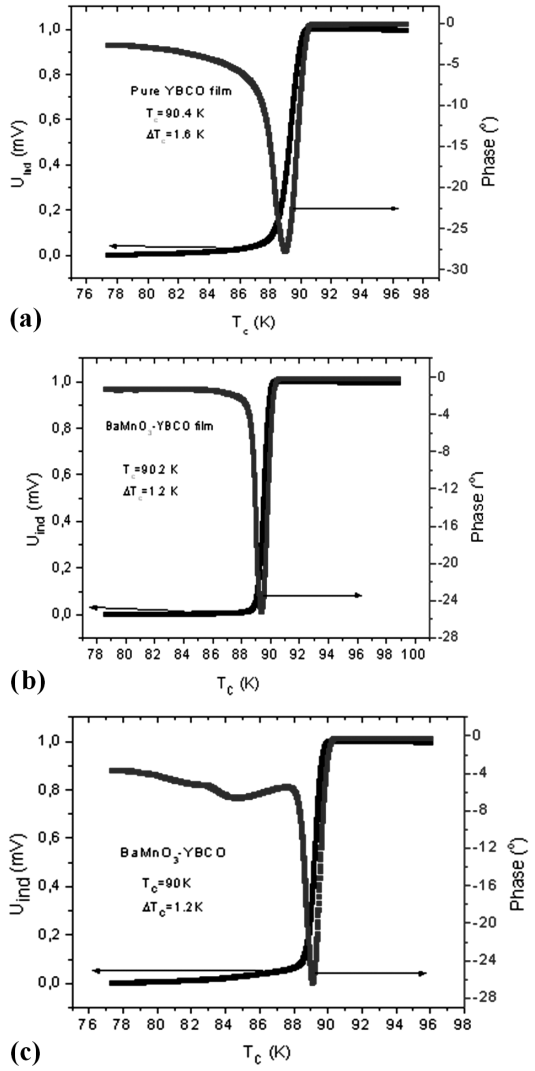

Figure 7: Critical-temperature values of YBCO thin films with: a) 0 g, b) 0.05 g and c) 0.10 g $BaMnO_3$ nanoparticles

Slika 7: Vrednosti kritične temperature YBCO tanke plasti z: a) 0 g, b) 0,05 g in c) 0,10 g $BaMnO_3$ nanodelci

4.2 Determination of mechanical properties

The analysis of the scratch test gives critical-force values of the produced thin films. These critical-force values correspond to the first peak in the cartridge output percentage – the test force graphical curve obtained from the scratch-test machine. The bond strengths, critical-force and Brinell-hardness values of pure YBCO and YBCO with $BaMnO_3$ nanoparticles are presented in **Table 1**. The hardness value of the substrate was converted to Brinell hardness (*H*) with the Standard Hardness Conversion Tables for Metal and the adhesion strength (F) of the coatings was calculated as a MPa unit using equation (1).[20] It is clearly seen from **Table 1** that pure YBCO, the YBCO thin films with 0.05 g and 0.1 g of $BaMnO_3$ nanoparticles have the critical forces of 56.23 mN, 58.63 mN and 60.11 mN, respectively. Therefore, the calculated adhesion strength of the films increases from 160 MPa to 173 MPa depending on the $BaMnO_3$ formation in the microstructure.

As expected, the mechanical strength against the internal forces caused by the flux pinning rather than the magnitude of the critical current density, may become the factor limiting the performance of HTS thin films for high-current density applications. For the bulk pure YBCO material, this problem has been already discussed in [36]. In this study, an increasing J_c and an improvement in the flux-pinning properties of the YBCO films with the $BaMeO_3$ perovskite nanoparticles (Me : Mn), as the pinning centers, on $SrTiO_3$ (STO) are aimed at with the trifluoroacetic acid-metal organic deposition (TFA-MOD). Since the general purpose is to determine the mechanical properties such as Young's modulus and the hardness of a pure YBCO thin film and the YBCO thin films with a Mn addition (Mn reacts as $BaMnO_3$), an instrumented nanoindentation test was applied to both samples. This time, the importance of the applied load and the indentation size is apparent. As presented in **Table 2**, the ratios of the indentation depths and the film thicknesses are applicable for an instrumented indentation with an applied load of 300 μN. A smoothing procedure was applied to all of the instrumented indentation results of the samples. Another parameter, which can affect the indentation test, is the surface roughness. It has a very active role in an indentation experiment at the nanoscale. If the surface roughness is larger than the maximum indentation depth, the curve has very scattered data characteristic for the loading and unloading parts.

Table 1: Brinell hardness, critical force and bond strengths of YBCO and YBCO with Mn

Tabela1: Trdota po Brinellu, kritična sila in trdnost vezave YBCO in YBCO z Mn

Sub-strate	Brinell hardness substrate (HB)	Indenter radius (μm)	Material	Average critical force (mN)	Adhesion strength (MPa)
STO	143	15	Pure YBCO	56 ± 1.2	160 ± 1.1
			YBCO with 0.05 g Mn	59 ± 1.8	168 ± 1.7
			YBCO with 0.1 g Mn	60 ± 1.6	173 ± 1.5

Table 2: Maximum depth, residual depth and film thickness of pure YBCO and YBCO with additional particles

Tabela 2: Maksimalna globina, preostala globina in debelina plasti čistega YBCO in YBCO z dodatnimi delci

Material	Force (μN)	Maximum depth (nm)	Residual depth (nm)	Film thickness (nm)
YBCO	300	40.24 ± 6.4	30.12 ± 7.8	292 ± 9
YBCO with 0.05 g Mn	300	42.32 ± 9.4	32.11 ± 8.7	297 ± 5
YBCO with 0.10 g Mn	300	42.45 ± 5.9	33.53 ± 4.4	294 ± 6

The YBCO-based thin film has suitable properties for ceramic materials, such as hardness and stiffness, together with the tendency to fracture. However, the references about the mechanical properties of this material, particularly the yield strength and the stress-strain curve, are scarce. The mechanical properties (hardness, Young's modulus and fracture toughness) of the YBCO samples have been examined with the techniques such as ultrasound[37], X-ray diffraction[38] and nanoindentation[39]. The reported values of Young's modulus for Y-123 are within the range of E = 40–200 GPa. This large scatter may be due to the residual porosity and a poor contact between the grains[40]. Other authors,[41] also using nanoindentation and applying the loads between 30 mN and 100 mN, reported the values of E = 171–181 GPa for the YBCO samples textured with the Bridgman technique, which is in agreement with Johansen. The nanohardness values in the range of 7.8–8.0 GPa at the maximum loads of 30 mN were recently reported in several researches for the bulk, single-crystal YBCO.[38–41] Roa et al. (2007) found a hardness value of (8.9 ± 0.1) GPa obtained with a nanoindentation on the YBCO samples textured with the Bridgman technique.

After obtaining the loading-unloading (load-displacement) curves, force-time and depth-time graphs for pure YBCO and the YBCO films with 0.05 g and 0.1 g Mn (reacting as $BaMnO_3$) under a applied peak load of 300 μN, some characteristic indentation parameters were listed in **Tables 2** and **3**. According to the indentation results in **Table 2**, the maximum and residual depths of the YBCO-based thin films under the same indentation loads were increased from (40.24 ± 6.4) nm to (42.45 ± 5.9) nm and from (30.12 ± 7.8) nm to (33.53 ± 4.4) nm, respectively. Furthermore, as represented in **Table 3**, the elastic modulus and indentation hardness of the YBCO-based thin films were decreased from (88.54 ± 3.1) GPa to (79.11 ± 1.9) GPa and from (12.51 ± 5.1) GPa to (5.75 ± 1.1) GPa under a load of 300 μN. Although the indentation load was fixed at 300 μN, the indentation hardness was decreased as if the indentation size affected the mechanical properties. Since the hardness is accepted as an inherent material property, it should not vary with the indentation load and size but may change with different phase formations. The indentation hardness was decreased with the formation of the $BaMnO_3$ content in the YBCO thin-film structure. According to this explanation, it can be concluded that the pure YBCO thin film is harder and more brittle than the $BaMnO_3$ additional ones. As listed in **Table 3**, the indentation hardness of the YBCO-based thin films decreased with an increased Mn content in the structure. The elastic-modulus variation of the YBCO-based thin films is also shown in **Table 3**. Although the hardness was very sensitive to the maximum indentation depth and the thickness/indentation-depth ratio of the samples and it changed from 12.51 GPa to 5.75 GPa, the elastic modulus of the YBCO-based thin films did not show a sharp decrease. However, as listed in **Table 3**, the elastic modulus of pure YBCO, YBCO with 0.05 g Mn, and YBCO with 0.10 g Mn was calculated to be 88.54 GPa, 83.41 GPa, and 79.11 GPa, respectively. After considering the hardness and elastic modulus of the YBCO-based thin films with AFM, SEM and the critical temperature value, T_c, it was found that the second phase of $BaMnO_3$ did not continuously improve the mechanical and superconducting properties. When the Mn content increased from 0 g to 0.15 g, the $BaMnO_3$ phases occurred and made the structure more ductile than the pure one. According to the T_c measurement, a sharp decrease in T_c could be considered and the ΔT_c values of the YBCO-based films were very small up to the addition of 0.15 g Mn. In this case ΔT_c was 4.2 K for the YBCO thin film with a 0.15 g Mn addition ($BaMnO_3$) and a sharp decrease in the resistivity could not be seen easily as presented **Figure 7**.

Table 3: Indentation-experiment results for pure YBCO and YBCO with additional particles
Tabela 3: Preizkus trdote čistega YBCO in YBCO z dodanimi delci

Material	Force (μN)	Hardness (HV)	Indentation hardness (GPa)	Young's modulus (GPa)
YBCO	300	695 ± 28	12.51 ± 4.8	88.54 ± 3.1
YBCO with 0.05 g Mn	300	525 ± 16	8.21 ± 1.2	83.41 ± 1.8
YBCO with 0.10 g Mn	300	495 ± 21	5.75 ± 1.1	79.11 ± 1.9

5 CONCLUSION

In this study, YBCO films with/without the Mn solutions were prepared by dissolving commercially available YBCO powders in propionic acid, trifluoroacetic acid (TFA) and acetone. The prepared solutions were dip coated on the STO single-crystal substrates. The following microstructural and mechanical results were obtained:

- XRD patterns show that the produced YBCO films have (001) and parallel plane reflections for pure YBCO and the YBCO with the $BaMnO_3$ thin film.
- According to the AFM study, topographic properties and the roughness of thin films were increased with an increase in the amount of nanoparticles (acting as a pinning center) in the film structure.
- SEM micrographs indicate that the structural defects consisted of the nanodots or nanoparticles of $BaMnO_3$ along the c-axis of the YBCO film. These properties resulted in an enhanced pinning over the pure YBCO film.
- It can be seen from the T_c analysis that there is a sharp decrease in the resistivity near 90 K.
- Critical force values of pure YBCO and of the YBCO-based thin films with 0.05 g and 0.1 g $BaMnO_3$ were found to be (56.23, 58.63 and 60.11)

mN, respectively. The calculated adhesion strength of the films increased from 160 MPa to 173 MPa depending on the $BaMnO_3$ addition.

- The calculated Young's modulus of YBCO thin films decreased with the $BaMnO_3$ formation. The same effects can be seen in the hardness variation of pure YBCO and the YBCO thin films with the $BaMnO_3$ nanoparticles.

6 REFERENCES

[1] N. Hari Babu, K. Iida, D. A. Cardwell, Enhanced magnetic flux pinning in nanocomposite Y-Ba-Cu-O superconductors, Physica C, 445–448 (**2006**), 353–356

[2] Y. Yoshida, K. Matsumoto, M. Miura, Y. Ichino, Y. Takai, A. Ichinose, M. Mukaida, S. Horii, Controlled nanoparticulate flux pinning structures in $RE_{1+x}Ba_{2-x}Cu_3O_y$ films, Physica C, 445–448 (**2006**), 637–642

[3] B. Lakew, J. C. Brasunas, S. Aslam, D. E. Pugel, High T_c, transition-edge superconducting (TES) bolometer on a monolithic sapphire membrane-construction and performance, Sensor. Actuat. A-Phys., 114 (**2004**), 36–40

[4] B. Dwir, L. Pavesi, J. H. James, B. Keilelt, D. Pavuna, F. K. Reinhart, A simple high temperature superconducting thin film optical bolometer, Supercond. Sci. Technol., 2 (**1989**), 314–316

[5] Y. A. Jee, M. Li, B. Ma, V. A. Maroni, B. L. Fisher, U. Balachandran, Comparison of texture development and superconducting properties of YBCO thin films prepared by TFA and PLD processes, Physica C, 356 (**2001**), 297–303

[6] Y. Yamada, S. Kim, T. Araki, Y. Takahashi, T. Yuasa, H. Kurosaki, Critical current density and related microstructures of TFA-MOD YBCO coated conductors, Physica C, 357 (**2001**), 1007–1010

[7] X. M. Cui, B. W. Tao, J. Xiong, X. Z. Liu, J. Zhu, Y. R. Li, Effect of annealing time on the structure and properties of YBCO films by the TFA–MOD method, Physica C, 432 (**2005**), 147–152

[8] S. Y. Lee, S. A. Song, B. J. Kim, J. A. Park, H. J. Kim, G. W. Hong, Effect of precursor composition on J_c enhancement of YBCO film prepared by TFA-MOD method, Physica C, 445–448 (**2006**), 578–581

[9] J. Lia, W. Beres, Three-dimensional finite element modelling of the scratch test for a TiN coated titanium alloy substrate, Wear, 260 (**2006**), 1232–1242

[10] P. Hedenqvist, S. Hogmark, Experiences from scratch testing of tribological PVD coatings, Tribol. Int., 30 (**1997**), 507–516

[11] J. Valli, U. Mäkelä, Applications of the scratch test method for coating adhesion assessment, Wear, 115 (**1987**), 215–221

[12] J. Sekler, P. A. Steinmann, H. E. Hintermann, The scratch test: different critical load determination techniques, Surf. Coat. Technol., 36 (**1988**), 519–529

[13] K. Holmbert, A. Matthewst, H. Ronkainen, Coatings tribology-contact mechanisms and surface design, Tribol. Int., 31 (**1998**), 107–120

[14] K. Holmbert, The basic material parameters that control friction and wear of coated surfaces under sliding, Tribologia-Fin. J. Tribol., 19 (**2000**), 3–18

[15] P. A. Steinmann, Y. Tardy, H. E. Hintermann, Adhesion testing by the scratch test method: the influence of intrinsic and extrinsic parameters on the critical load, Thin Solid Films, 154 (**1987**), 333–349

[16] P. J. Burnett, D. S. Rickerby, The relationship between hardness and scratch adhesion, Thin Solid Films, 154 (**1987**), 403–416

[17] S. J. Bull, Failure modes in scratch adhesion testing, Surf. Coat. Technol., 50 (**1991**), 25–32

[18] S. J. Bull, Spallation failure maps from scratch testing, Mater. High Temp., 13 (**1995**), 169–174

[19] S. J. Bull, Failure mode maps in the thin film scratch adhesion test, Tribol. Int., 30 (**1997**), 491–498

[20] S. T. Gonczy, N. Randall, An ASTM standard for quantitative scratch adhesion testing of thin, hard ceramic coatings, Int. J. Appl. Ceram. Tech., 2 (**2005**), 422–428

[21] W. C. Oliver, G. M. Pharr, An improved technique for determining hardness and elastic-modulus using load and displacement sensing indentation experiments, J. Mater. Res., 7 (**1992**), 1564–1583

[22] A. E. Giannakopoulos, S. Suresh, Determination of elastoplastic properties by instrumented sharp indentation, Scripta Mater., 40 (**1999**), 1191–1198

[23] A. E. Giannakopoulos, P. L. Larsson, R. Vestergaard, Analysis of vickers indentation, Int. J. Solids Struct., 31 (**1994**), 2679–2708

[24] Y. F. Gao, H. T. Xu, W. C. Oliver, G. M. Pharr, Effective elastic modulus of film-on-substrate systems under normal and tangential contact, J. Mech. Phys. Solids, 56 (**2008**), 402–416

[25] S. Shim, H. Bei, E. P. George, G. M. Pharr, A different type of indentation size effect, Scripta Materialia, 59 (**2008**), 1095–1098

[26] Y. Huang, F. Zhang, K. C. Hwang, W. D. Nix, G. M. Pharr, G. Feng, A model of size effects in nano-indentation, J. Mech. Phys. Solids, 54 (**2006**), 1668–1686

[27] G. M. Pharr, Measurement of mechanical properties by ultra-low load indentation, Mat. Sci. Eng. A- Struct., 253 (**1998**), 151–159

[28] Y. Gogotsi, T. Miletich, M. Gardner, M. Rosenborg, Microindentation device for in situ study of pressure-induced phase transformations, Rev. Sci. Instrum., 70 (**1999**), 4612–4617

[29] W. Zhu, P. J. M. Bartos, Application of depth-sensing microindentation testing to study of interfacial transition zone in reinforced concrete, Cement Concrete Res., 30 (**2000**), 1299–1304

[30] O. Uzun, U. Kolemen, S. Celebi, N. Guclu, Modulus and hardness evaluation of polycrystalline superconductors by dynamic microindentation technique, J. Eur. Ceram. Soc., 25 (**2005**), 969–977

[31] Z. Shan, S. K. Sitaraman, Elastic–plastic characterization of thin films using nanoindentation technique, Thin Solid films, 437 (**2003**), 176–181

[32] A. E. Giannakopoulos, S. Suresh, Scr. Mater., 40 (**1999**), 1191

[33] R. P. Vinci, J. J. Vlassak, Annu. Rev. Mater. Sci., 26 (**1996**), 431

[34] W. D. Nix, Mater. Sci. Eng. A, 237 (**1997**), 37

[35] L. De Fazio, S. Syngellakis, R. J. K. Wood, F. M. Fugiule, G. Sciume, Nanoindentation of CVD diamond: comparison of an FE model with analytical and experimental data, Diam. Relat. Mater., 10 (**2001**), 765–769

[36] J. Lia, W. Beres, Three-dimensional finite element modelling of the scratch test for a TiN coated titanium alloy substrate, Wear, 260 (**2006**), 1232–1242

[37] F. Sandiumenge, T. Puig, J. Rabier, J. Plain, X. Obradors, Optimization of flux pinning in bulk melt textured 1–2–3 superconductors; Bringing dislocations under control, Adv. Mater., 12 (**2000**), 375

[38] S. Block, G. J. Piermarini, R. G. Munro, W. Wong-Ng, The bulk modulus and Young's modulus of the superconductor $Ba_2Cu_3YO_7$, Adv. Ceram. Mater., 2 (**1987**), 601

[39] H. T. Johansen, Flux-pinning-induced stress and magnetostriction in bulk superconductors, Superconducting Science and Technology, 13 (**2000**), 121–137

[40] H. M. Ledbetter, M. W. Austin, S. A. Kim, M. Lei, Elastic constants and Debye temperature of polycrystalline yttrium barium copper oxide ($YBa_2Cu_3O_{7-x}$), J. Mater. Res., 2 (**1987**), 786

[41] J. J. Roa, X. G. Capdevila, M. Martinez, F. Espiell, M. Segarra, Nanohardness and Young's modulus of YBCO samples textured by the Bridgman technique, Nanotechnology, 18 (**2007**), 385

UDK 519.61/.64:669.58:669.14.018.291
Original scientific article/Izvirni znanstveni članek

ISSN 1580-2949
MTAEC9, 47(2)161(2013)

DISTORTION OF THE SUBSTRUCTURE OF A 20-ft SHIPPING CONTAINER EXPOSED TO ZINC HOT-DIP GALVANIZING

SPREMINJANJE MER PODSTRUKTURE PRI 20 ft TRANSPORTNEM KONTEJNERJU PRI VROČEM POTOPNEM CINKANJU

Ivana Ivanović[1], Aleksandar Sedmak[2], Rebeka Rudolf[3], Leo Gusel[3], Biljana Grujić[1]

[1]Innovation Center, Faculty of Mechanical Engineering, University of Belgrade, Kraljice Marije 16, 11000 Belgrade, Republic of Serbia
[2]Faculty of Mechanical Engineering, University of Belgrade, Kraljice Marije 16, 11000 Belgrade, Republic of Serbia
[3]University of Maribor, Faculty of Mechanical Engineering, Smetanova ulica 17, 2000 Maribor, Slovenia
iivanovic@mas.bg.ac.rs

Prejem rokopisa – received: 2012-08-21; sprejem za objavo – accepted for publication: 2012-10-03

The main goal of this study was to build a model for a numerical simulation of hot-dip galvanizing of a 20-ft ISO shipping container. For that purpose, the basic transient thermo-mechanical problem of a steel structure under the influence of the temperature characteristic for a zinc hot-dip galvanizing bath was analyzed. Numerical calculations were performed for a simple part and for the complex substructure of the container. Calculations were carried out on the Salome-Meca platform using a Netgen mesh generator and a Code_Aster finite-element solver.

Keywords: shipping container, structural steel, zinc hot-dip galvanizing, transient heat transfer, distortion

Glavni namen te študije je bila izdelava modela za numerično simulacijo vročega potopnega cinkanja 20 ft ISO transportnega kontejnerja. Zato smo analizirali osnovni termomehanski problem jeklene konstrukcije zaradi vpliva toplote med vročim potopnim cinkanjem. Numerični izračuni so bili izvršeni za enostavni del in za kompleksno podstrukturo kontejnerja. Izračuni so bili izvršeni na platformi Salome-Meca z uporabo generatorja mreže Netgen in programske opreme Code_Aster na osnovi metode končnih elementov.

Ključne besede: transportni kontejner, konstrukcijsko jeklo, vroče potopno cinkanje, prenos toplote, deformacija konstrukcije

1 INTRODUCTION

This study is a part of a wider research launched in order to develop an innovative 20-ft ISO shipping container with a longer lifetime. Since shipping containers have to face hard handling and hard weather conditions, zinc hot-dip galvanizing, if possible, in the form of an integrated welded structure, may represent the best way to achieve this goal.

The dimensions of the 20-ft ISO shipping container are 6.058 m × 2.348 m × 2.591 m with a net weight of approximately 2 400 kg. The skeleton of the container is composed of various steel profiles made of 235–420 graded structural steel. Profiles are welded to the cubical corner fittings thus forming an orthogonal skeleton. The wall and roof panels are composed of welded corrugated steel sheets. The panels are welded continually to the rest of the structure. The material thickness varies depending upon the type of the element.

The entire skeleton will be taken into consideration as a numerical model, despite the fact that the 20-ft shipping container is larger than any existing galvanizing bath, which means that in actual conditions it cannot be galvanized as a whole.[1] On the other hand, it seems that it would be much more efficient to complete most of the construction before galvanizing. Welding of galvanized steel is possible, but it requires a special approach that differs greatly from the standard steel welding techniques.[2]

The temperature of the zinc bath is slightly above 450 °C. If other requirements for the preparation of an object for galvanizing are fulfilled, this temperature should not have a great influence on the mechanical properties of the structural steel in the mentioned structural steel grades.[1,3] Problems were expected to arise due to an extremely complex structure. For example, one of the most important requirements for galvanizing is that the thickness of the material of different parts that are going to be galvanized together must be as uniform as possible. Large differences in the thicknesses will result in different heating and cooling of the material, and will increase the risk of undesirable large distortions. In the case of the shipping container, the thickness ranges from 28 mm in some regions of the corner fittings, 4.5 mm to 12 mm for the profiles in the skeleton and, finally, to 2 mm for the wall panel.

Problems will also arise in several areas of the structure where the hollow sections are completely sealed by the other parts of the structure. These sections must be replaced with open sections or vent/drain holes must be provided. An even greater problem is the

numerous corners of the element connections that also need to be supplied with vent/drain holes.

When it comes to numerical simulation, there is very little information on previous studies dealing with zinc hot-dip galvanizing, especially those dealing with the fluid dynamics of zinc at the temperature of the galvanizing bath, and the fluid dynamics of the galvanizing bath. Some insight into the field could be gained from a thermal analysis carried out, during the solidification, on the moving surface in a finite bath given in [4]. Concerning a transient three-dimensional thermo-mechanical numerical analysis, there is a great number of papers dealing with this subject within the welding researches.[5–8] The basic thermo-mechanical analysis, at some level similar to this one, is performed and described in [9,10].

This is a highly idealized analysis of a real-time problem, and numerous real-time conditions are ignored deliberately.

2 GENERAL-MODELING DESCRIPTION

2.1 Geometry of the model

The skeleton used as a model for numerical simulations of the zinc hot-dip galvanizing of a 20-ft ISO shipping container is presented in **Figure 1**. The skeleton model is composed of two front-corner posts, two outer rear-corner posts, two bottom side rails, two top side rails, a door sill, the lower part of the door header, a front sill, a front-top end rail, three types of floor cross-members, two forklift-pocket top plates and, finally, four top- and four bottom-corner fittings.

It was already mentioned that some elements in the construction should be omitted or replaced in order to avoid closed hollow sections. Such sections are undesirable in galvanizing, but also need special treatment during a numerical simulation. The initial examples, the most sensitive to changes, are the corner posts. The

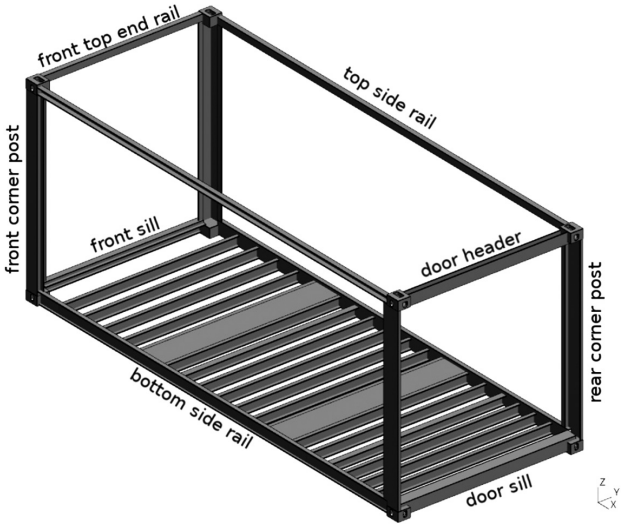

Figure 1: Skeleton of the 20-ft ISO shipping container
Slika 1: Ogrodje 20 ft ISO ladijskega kontejnerja

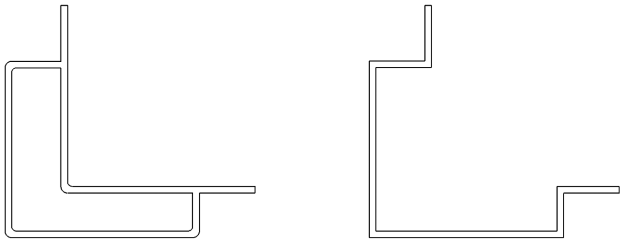

Figure 2: Cross sections of the front-corner-post profiles
Slika 2: Prereza profilov kotnih drogov v sprednjem delu

front-corner post is planned to be a 6 mm thick, S235JR-steel closed profile as illustrated in **Figure 2** (left). When welded to the corner fittings, this profile will form a closed hollow section. Therefore, in simulations, the closed profile is replaced by a standard-shaped open profile of the same thickness as illustrated in **Figure 2** (right). To simplify an already complex geometry, the edge filleting is omitted here, as well as for all the other elements.

The rear-corner-post profile consists of an inner and outer part. A standard 6 mm thick outer profile, planned to be made of the S420NL steel, is kept in the numerical model. The inner part could not be omitted from the real skeleton, but it is assumed that it can be added afterwards. The notches for door-hinge-pin lugs, which are usually made on the outer part of the rear-corner post, are omitted to simplify the geometry.

Bottom side rails (4.5 mm S420NL steel) are introduced without the two forklift-pocket openings. Only the standard U-shaped lower part of the door header (4 mm S355NL steel) is included. For the two top side rails and for the front-top end rail (4 mm S355NL steel), the standard square tubes are replaced with the channel-shaped steel sections.

The elements of the skeleton are connected to the construction with corner fittings. The dimensions of the corner fittings are much smaller than the dimensions of the other elements, 178 mm × 162 mm × 118 mm, but the thickness of the walls is much higher, and it ranges from 10 mm to 28 mm. They have a specific geometry since they are designed for lifting, stacking and securing the container. The real form of the top-corner fitting is illustrated in **Figure 3** (left). A simplified form, attached

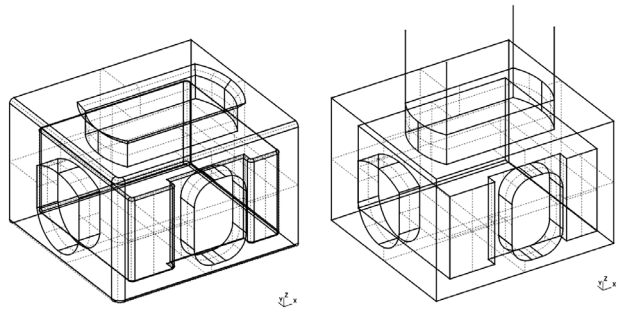

Figure 3: Top-corner-fitting geometry
Slika 3: Geometrija gornjega vogala

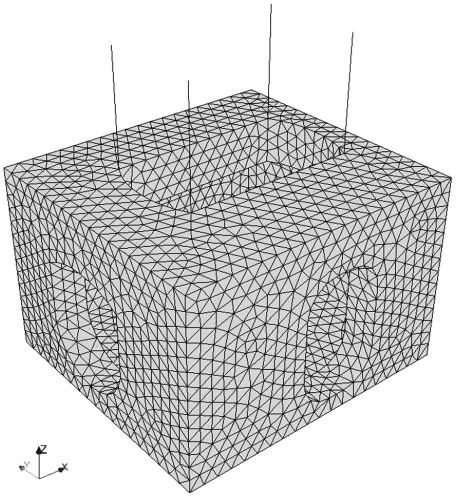

Figure 4: Example of a Netgen three-dimensional tetrahedral mesh
Slika 4: Primer tridimenzionalne tetraedrične mreže Netgen

to the cables in a way that will be used for numerical simulations, is presented in **Figure 3** (right).

2.2 Numerical procedures

All pre-processing and post-processing work is performed using an open-source Salome-Meca platform. From the mesh module in Salome-Meca, an open-source Netgen mesh generator is applied to generate an automatic three-dimensional tetrahedral mesh. An example of the mesh generated on the top-corner fitting, with the maximum edge size of 9 mm, resulting in 14 358 tetrahedral elements, is illustrated in **Figure 4**.

The molten zinc bath is kept at a constant temperature of 450 °C during all numerical simulations. The top-corner fitting and the whole skeleton are chosen separately for the simulations. The bottom side of each model is placed in an xy plane. The plane is placed so as to be parallel to the surface of the zinc bath. The models are suspended with four steel cables (**Figure 3** (left) and **Figure 4**). In this manner, for the purpose of the numerical model of the skeleton, the mechanism for vertical lifting of the container from the top corner fittings is simplified and replaced only by cables. Cable thickness is selected so that its elongation is reduced to a minimum.

A transient thermomechanical analysis is performed with the open-source finite-element solver Code_Aster. The thermomechanical properties of the steel are kept constant during the simulations. In the linear thermal analysis, convection boundary conditions are imposed on all the surfaces. An immersion is simulated at a constant velocity of 0.004 m/s and with two different constant heat-transfer coefficients, one at the immersed surfaces and the other at the surfaces outside the zinc bath. The initial temperature of the object and the temperature of the surroundings are the same, 25 °C. The thermal loads and the weight of the model are introduced in a non-linear static analysis. The cables are fixed at one end and connected to the selected points of the object (the corner fitting or skeleton) at the other end.

3 RESULTS AND DISCUSSIONS

Simulations were performed on a desktop PC with an Intel Core i5-2300 CPU running at 2.8 GHz and with 4 GB RAM. Because of the limited computer resources, a simple top-corner fitting model was chosen for general model verifications and validations.

3.1 Top-corner fitting

Corner fittings are the smallest parts of a container construction with very different wall thicknesses. Points 8, 9, 10 and 11, which were used for the presentations of the results obtained for different mesh densities, are illustrated in **Figure 5**. The thickness of the walls around the bottom point 9 is 20 mm on the sides and 10 mm at the bottom. The thickness around the bottom point 8 is 20 mm and 10 mm on the sides. The thickness of the top wall, where points 11 and 10 are situated, is approximately 28 mm. In the case of a velocity of 0.004 m/s, the corner fitting is fully immersed after approximately 30 s.

The temperature results for the selected points are illustrated in **Figure 6a**. The results are presented from the beginning of the simulation until 630 s. It can be seen that the temperatures of four points differ throughout the entire simulation. The maximum value of the temperature difference between the two bottom points is approximately 33 °C, and is reached at 240 s. The temperature of the zinc bath was not reached at the end of the simulation, despite the fact that the corner fitting was immersed fully for 10 min. The maximum temperature was reached at point 8 and has the value of 408 °C.

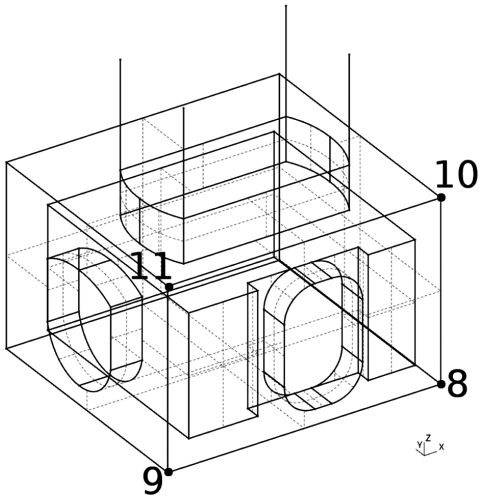

Figure 5: Positions of points 8, 9, 10 and 11
Slika 5: Pozicije točk 8, 9, 10 in 11

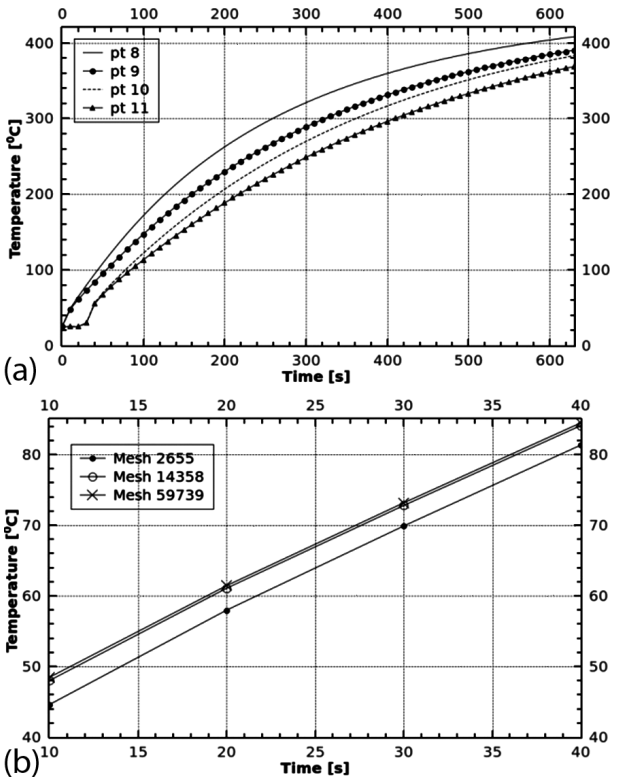

Figure 6: a) Temperature at points 8, 9, 10 and 11 from the beginning of the simulation until 630 s for the mesh of 14 358 elements and b) the temperature at point 9 for three different mesh densities from 10 s to 40 s

Slika 6: a) Temperature v točkah 8, 9, 10 in 11 od začetka simulacije do 630. sekunde za mrežo s 14 358 elementi in b) temperature v točki 9 za tri gostote mreže od 10. sekunde do 40. sekunde

The results obtained using three different mesh densities are presented in **Figure 6b**. The values for the coarse mesh of 2 655 elements (the maximum edge size is 20 mm) are significantly different from the other two sets of values (for the mesh of 14 358 elements the maximum edge size is 9 mm, and for the mesh of 59 739 elements the maximum edge size is 5 mm). The difference was around 3.5 °C at the beginning of the simulation, and around 1 °C at the end of the simulation.

At the beginning of the simulation the temperature at some points of the mesh fell below the assigned initial temperature of the model, which is equal to the temperature of the surroundings. This error decreased with an increase in the mesh density.

The previous discussions are confirmed with **Figure 7**, where the temperature distribution, at 30 s (**a**) and at 630 s (**b**), is presented for the mesh of 14 358 elements. At 30 s, when the phase of immersion is just finished, some parts of the corner fitting are still at the initial temperature of 25 °C. This is an obvious consequence of the already mentioned numerical error caused by the finesse of discretization.

Compared to the temperature of the other previously selected points (**Figure 5**), the highest temperature is in the vicinity of point 8, and is around 80 °C. The tempe-

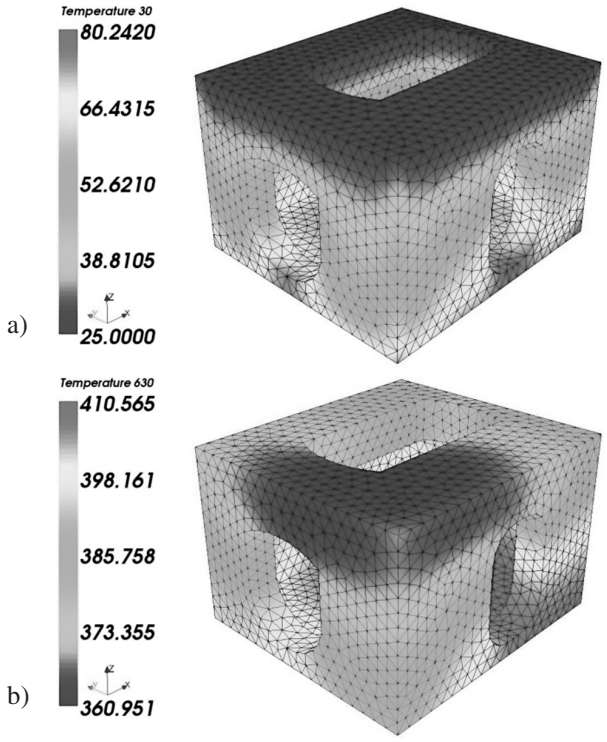

Figure 7: Temperature distribution at the top-corner fitting at: a) 30 s and b) at 630 s for the mesh of 14 358 elements

Slika 7: Razporeditev temperature v vrhnjem kotnem spoju pri: a) 30 s in b) pri 630 s za mrežo s 14 358 elementi

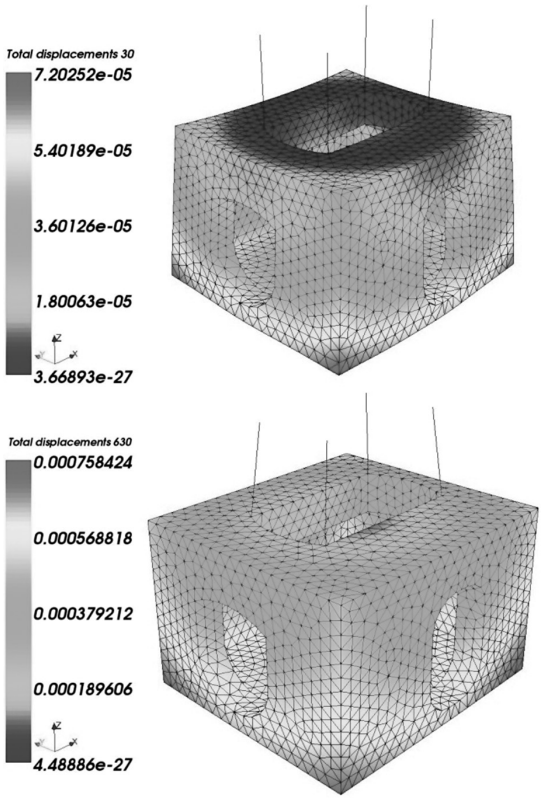

Figure 8: Total displacements at the top-corner fitting at 30 s (scale 200) and at 630 s (scale 40) for the mesh of 14 358 elements

Slika 8: Skupni raztezki v vrhnjem kotnem spoju pri 30 s (skala 200) in pri 630 s (skala 40) za mrežo s 14 358 elementi

rature difference between these points is even more evident at the end of the simulation as illustrated in **Figure 7b**. At 630 s, the maximum temperature is approximately 410 °C, and it is 40 °C lower than the temperature of the zinc bath. The corresponding total displacements are illustrated in **Figure 8**.

3.2 Skeleton

In the case of the skeleton, two mesh densities were used for numerical simulations. The maximum edge size of the finer mesh was equal to the critical edge size of the corner fitting (20 mm). The immersion phase takes approximately 648 s. Because of the limited computer resources, a coarser mesh of 241 623 elements (the maximum edge size of 60 mm) was used to reach the end of the immersion phase. The total displacements and temperature distributions at (50, 350, and 650) s are illustrated in **Figure 9**.

As expected, for this mesh density the minimum temperature at any time was lower than the initial temperature of 25 °C. The temperature of the zinc bath was almost reached at the lower parts of the skeleton by the end of the simulation. The maximum temperature at 650 s, illustrated in **Figure 9** (bottom right), was approximately 449 °C.

It is not hard to notice large differences in the temperature at different positions of the skeleton. Especially at the beginning of the immersion, these temperature differences can produce large distortions. For example, from the temperature distribution at 50 s illustrated in **Figure 9** (top right), it can be seen that the temperature is much higher at the bottom than at the top of the bottom side rails. The temperature of the bottom-corner fittings is even lower. The largest distortions are found in the central area of the floor construction, at the central cross members, and at the two forklift-pocket top plates (**Figure 9** (top left)). There is an obvious distortion of the bottom side rails. This distortion affects the very end of the front corner posts, near the corner fittings. The influence of the distortion of the floor construction on the outer part of the rear corner posts is even more pronounced, but it is also better distributed along the posts than in the case of the front corner posts. At 350 s, the top side rails started to deform as a result of the distortion of the lower half of the skeleton (**Figure 9** (center right)).

The maximum value of the total displacements reached in the first 50 s is around 12.5 mm, in the next 300 s it is increased by only 5 mm, and in the next 300 s it is increased by an even smaller value of only 3 mm.

The influence of the mesh density, for the mesh of 241 623 elements with the maximum edge size of 60 mm, and the mesh of 490 420 elements with the maximum edge size of 20 mm, from 80 s to 120 s, at the point 621 with the coordinates (0, 0, 0), is illustrated in **Figure 10**. A simulation for the finer mesh was executed for the period of up to 200 s. The temperature difference was between 3.5 °C at the beginning of the simulation and 2.5 °C at 200 s. The values of the total displacements, from 80 s to 120 s, were higher for the coarser mesh.

The temperature at different points on the bottom-corner fitting and in its vicinity is presented in **Figure 11**. During the simulation, the temperature was the highest at point 4 067, which is at the bottom of the front sill, and at point 31 870, which is at the bottom of the bottom side rail. The thickness of the material of these profiles is 4.5 mm.

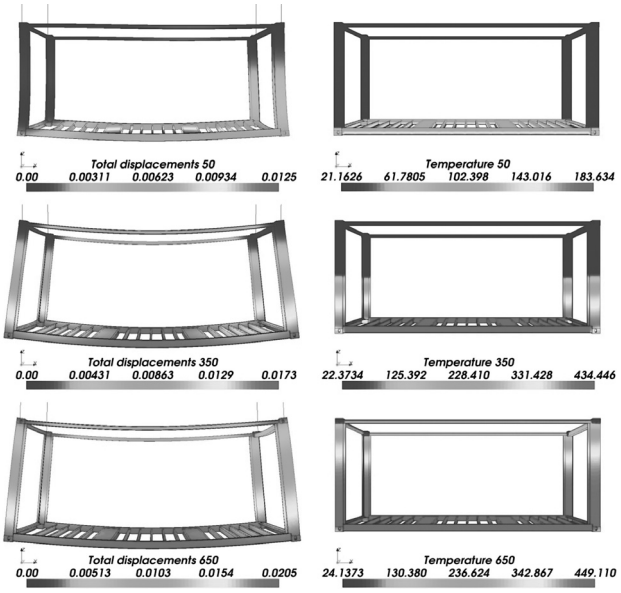

Figure 9: Total displacements (the scale factor of 20) and temperature distributions at (50, 350, and 650) s for the skeleton in the case of a mesh of 241 623 elements (the maximum edge size of 60 mm)

Slika 9: Celotni raztezek (faktor skale 20) in razporeditev temperature pri (50, 350 in 650) s za ogrodje v primeru mreže z 241 623 elementi (maksimalna velikost roba 60 mm)

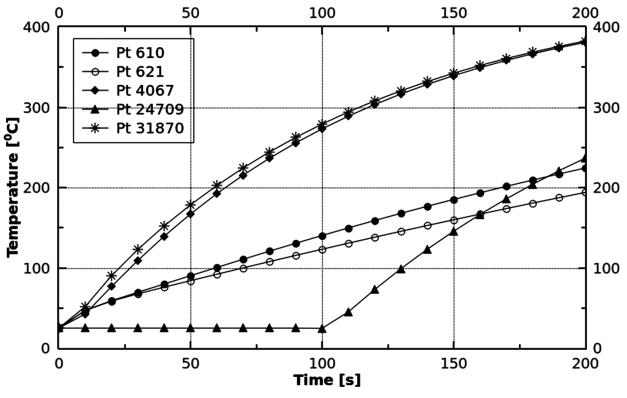

Figure 10: Temperature and total displacements at point (0, 0, 0) for the two different mesh densities, a mesh of 241 623 elements with the maximum edge size of 60 mm, and a mesh of 490 420 elements with the maximum edge size of 20 mm, from 80 s to 120 s

Slika 10: Temperatura in celotni raztezek v točki (0, 0, 0) za dve različni gostoti mreže: mreže z 241 623 elementi, maksimalna velikost roba 60 mm, in mrežo s 490 420 elementi, maksimalna velikost roba 20 mm, od 80 s do 120 s

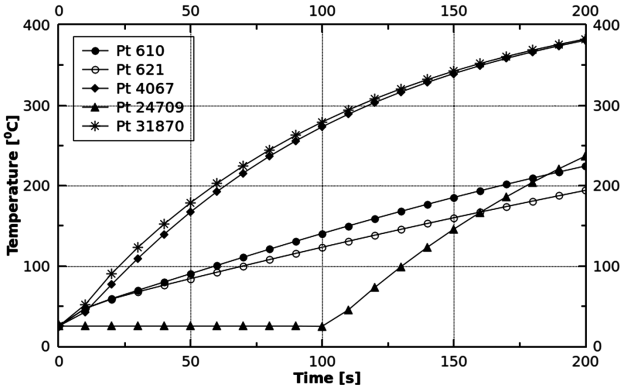

Figure 11: Temperature at different points of the skeleton, on and around the bottom-corner fitting, from the beginning of the simulation to 200 s, for the mesh of 490 420 elements
Slika 11: Temperature v različnih točkah ogrodja na spodnjem vogalnem spoju in okrog njega od začetka simulacije do 200 s v primeru mreže s 490 420 elementi

Points 621 and 610 are on the bottom-corner fitting and their positions are equivalent to those of points 11 and 10, illustrated in **Figure 5**. As expected, the temperature of point 610 was higher than the temperature of point 621, as presented in the case of the corner fittings. Both temperatures were lower than the temperatures of the points on the bottom profiles.

The last presented point is at the front-corner post, just above the bottom-corner fitting. The thickness of the material of the front-corner post is 6 mm. This point starts to heat up 100 s after the above-presented points, but in the following 100 s it exceeds the temperature of the two points on the bottom-corner fitting.

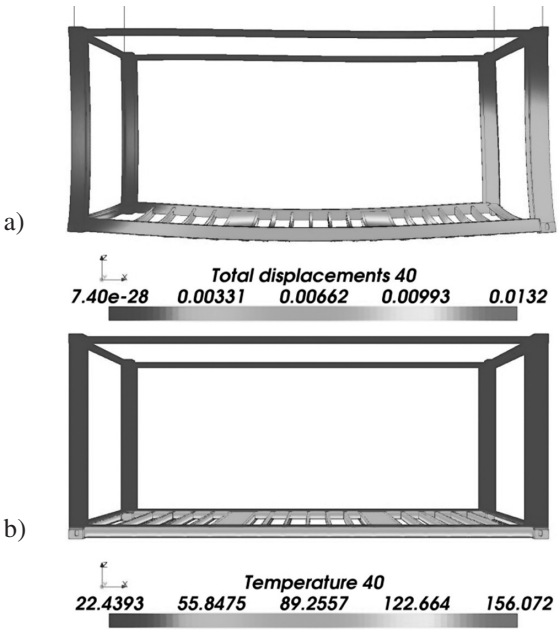

Figure 12: a) Total displacements (scale 20) and b) the temperature distribution at 40 s for the mesh of 490 420 elements
Slika 12: a) Skupni raztezek (skala 20) in b) razporeditev temperature pri 40 s za mrežo s 490 420 elementi

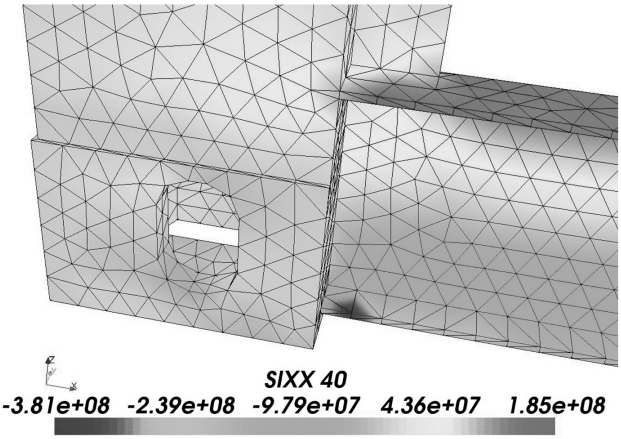

Figure 13: Maximum stress at the bottom side rail near the front-bottom-corner fitting at t = 40 s
Slika 13: Maksimalna napetost v spodnjem stranskem profilu blizu spodnjega sprednjega vogalnega spoja pri t = 40 s

The distributions for the finer mesh at 40 s are presented in **Figure 12**. While the minimum temperature for the coarse mesh at 50 s, presented in **Figure 9** (top right), was approximately 21 °C, for the finer mesh this value was around 22 °C at 40 s (**Figure 12b**). Also, the maximum value for the total displacements was almost 1 mm higher at 40 s for the finer mesh than at 50 s for the coarser mesh (**Figure 9** (top left)).

The maximal stresses at 40 s, illustrated in **Figure 13**, were located at the bottom of the bottom side rails near the front bottom-corner fittings. The bottom rail is planned to be made of 4.5 mm thick S420NL steel, and its maximum stress value is 381 MPa.

4 CONCLUSIONS

Three-dimensional linear thermal and nonlinear static analyses, of the top-corner fitting as a part of the container structure and of the entire skeleton as the container substructure, were performed to initiate the analysis of the distortion of a 20-ft ISO shipping container exposed to the temperature of a zinc hot-dip galvanizing bath. Numerical simulations were carried out using open-source CAE software: Salome-Meca, Netgen, and Code_Aster. The temperature was the only transient boundary condition. The temperature of the galvanizing bath, the velocity of immersion, and the thermomechanical properties of steel were kept constant during all the simulations. Tests were carried out within the limits of the very poor computer resources. However, satisfactory initial results were obtained and sufficient information was gathered to make a general image of the container-substructure behavior under the influence of the zinc hot-dip galvanizing-bath temperature.

Acknowledgements

The authors would like to acknowledge the financial support given under the EUREKA E! 5009 Galvacont project.

5 REFERENCES

[1] IGAG, INGAL Specifiers Manuel, Available: www.ingal.com.au/igsm.htm

[2] G. Livelli, T. Langill, Guidelines for Welding Galvanized Steel, PCI Journal, (**1998**), 40–48

[3] L. Mraz, J. Lesay, Problems with reliability and safety of hot dip galvanized steel structures, Soldagem and inspecao, 14 (**2009**) 2, 184–190

[4] H. Zhang, K. M. Moallemi, S. Kumar, Thermal Analysis of the Hot Dip-Coating Process, Journal of Heat Transfer, 115 (**1993**), 453–460

[5] M. Berković, S. Maksimović, A. Sedmak, Analysis of Welded Joints by Applying the Finite Element Method, Structural Integrity and Life, 4 (**2004**) 2, 75–83

[6] D. Veljić, M. Perović, A. Sedmak, M. Rakin, N. Bajić, B. Medjo, H. Dascau, Numerical Simulation of the Plunge Stage in Friction Stir Welding, Structural Integrity and Life, 11 (**2011**) 2, 131–134

[7] D. Veljić, M. Perović, A. Sedmak, M. Rakin, M. Trifunović, N. Bajić, D. Bajić, A Coupled Thermo-Mechanical Model of Friction Stir Welding, Thermal Science, 16 (**2012**) 2, 527–534

[8] M. Perović, D. Veljić, M. Rakin, N. Radović, A. Sedmak, N. Bajić, Friction-Stir Welding of High-Strength Aluminium Alloys and a Numerical Simulation of the Plunge Stage, Mater. Tehnol., 46 (**2012**) 3, 105–111

[9] W. J. Rudd, S. W. Wen, P. Langenberg, B. Donnay, A. Voelling, T. Pinger, M. Feldmann, J. Carpio, J. A. Casado, J. A. Alvarez, F. Gutierrez-Solana, Failure mechanisms during galvanising, Office for Official Publications of the European Communities, Luxembourg, 2008

[10] M. Feldmann, T. Pinger, D. Schäfer, R. Pope, G. Sedlacek, Hot-dip-zinc-coating of prefabricated structural steel components, Office for Official Publications of the European Communities, Luxembourg, 2010

UDK 621.762:621.95:519.233.4
Original scientific article/Izvirni znanstveni članek

ISSN 1580-2949
MTAEC9, 47(2)169(2013)

OPTIMIZATION OF THE DRILLING PARAMETERS FOR THE CUTTING FORCES IN B_4C-REINFORCED Al-7XXX-SERIES ALLOYS BASED ON THE TAGUCHI METHOD

OPTIMIRANJE PARAMETROV VRTANJA ZA SILE VRTANJA PRI ZLITINAH Al-7XXX, OJAČANIH Z B_4C S TAGUCHIJEVO METODO

Ahmet Taşkesen[1], Kenan Kütükde[2]

[1]Gazi University, Department of Manufacturing Engineering, 06500 Teknikokullar, Ankara, Turkey
[2]Gazi University, Institute of Science and Technology, 06500 Teknikokullar, Ankara, Turkey
taskesen@gazi.edu.tr

Prejem rokopisa – received: 2012-08-23; sprejem za objavo – accepted for publication: 2012-09-28

In this study, drilling tests of aluminum-based composites produced with the powder-metallurgy (PM) technique and reinforced with boron-carbide (B_4C) particles were carried out with three different types of drills under dry cutting conditions. In order to determine the mechanical properties of the produced composites, hardness and tensile tests were performed. Moreover, the effects of the machining parameters such as cutting speed, feed rate, particle fraction and cutting-tool material, and of their interactions on the thrust force and cutting torque were determined with the Taguchi experimental design. Drilling parameters were optimized in terms of cutting forces (thrust force and torque). Furthermore, an analysis of variance (ANOVA) was conducted to obtain the degree of the effect of the parameters. The most influential control factors for the cutting forces were found to be the particle fraction and feed rate. According to the experimental results, the thrust force and cutting torque increased significantly as the feed rate or the particle content increased. On the other hand, the influence of the drill-bit material and the interactions of the factors for the cutting forces were quite low.

Keywords: B_4C, powder metallurgy, drilling, cutting force, torque, Taguchi method

V tej študiji so bili narejeni preizkusi vrtanja kompozita na osnovi aluminija, ojačanega z borovim karbidom (B_4C) in izdelanega po postopku prašne metalurgije (PM), s tremi različnimi svedri in pri suhem vrtanju. Za določitev mehanskih lastnosti izdelanega kompozita je bila izmerjena trdota in opravljeni so bili natezni preizkusi. Poleg tega so bili določeni s Taguchijevo eksperimentalno tehniko parametri obdelave, kot so hitrost rezanja, hitrost podajanja, delež delcev, material za orodje za rezanje in njihov vpliv na potisno silo ter navor pri rezanju. Parametri rezanja so bili optimirani glede na sile rezanja (potisna sila in navor). Poleg tega je bila narejena analiza variance (ANOVA), da bi dobili stopnjo vpliva parametrov. Ugotovljeno je bilo, da sta najbolj vplivna kontrolna faktorja na sile rezanja delež delcev in hitrost podajanja. Skladno z rezultati preizkusov potisna sila in navor močno narasteta, če se poveča hitrost podajanja ali poveča vsebnost delcev. Po drugi strani so razmeroma majhni vplivi materiala svedra in medsebojni vpliv faktorjev na sile rezanja.

Ključne besede: B_4C, prašna metalurgija, vrtanje, sila rezanja, navor, Taguchijeva metoda

1 INTRODUCTION

The composition of many composite materials used in engineering applications consists of additives providing a better hardness and resistance and of the matrix material that holds these substances together as well as allowing ductility and toughness.[1] Due to their high specific strength, superior wear resistance, low thermal expansion and lightweight, metal-matrix composites (MMCs), widely used, especially in aerospace and automotive industry, have attracted the attention of the researchers.[2–4] However, in spite of these advantages, the machinability of these composites is difficult.[5–12]

A drilling process is one of the last production stages that have to be done before the assembly step. The past studies relating to the drilling of MMCs have revealed that Al_2O_3 and SiC are mostly used as a reinforcement material in an aluminum composite material.[3,5–8,12–14] However, there are no adequate studies on the drilling of the B_4C-reinforced aluminum composites. An inclusion of the B_4C particles as a reinforcement material has the advantage of having a higher hardness (≈4200 HV) than the other ceramics such as SiC (≈3500 HV) and Al_2O_3 (≈2300 HV).[2,15]

In the previous studies regarding the drilling machinability of MMCs, it is stated that an increase in the cutting speed does not significantly affect the thrust force, and that the most important factor increasing the thrust force is the feed rate.[3,10,16] Moreover, the particle content in the composite material as well as the drilling tool are of importance for the drilling of aluminum-matrix composites; and the lowest drilling forces are obtained with polycrystalline diamond (PCD) drills.[3] In addition, the coated carbide tools produce more thrust forces than the uncoated carbide drills.[16] Heat-treatment conditions also have a significant effect on the cutting forces and the highest tool forces were observed (nearly twice) when drilling aged the composites.[6,8] On the other

hand, while an addition of graphite to a composite material positively affects both the cutting forces and the machinability, it adversely affects the strength of the composite material.[2,5,12] With respect to the cutting-tool material, lower thrust forces are obtained when through-tool cooling is performed.[7] However, the cutting torques produced with conventional cooling (the cooling method, in which the cooling fluid is sprayed from the outside to the cutting zone) are lower than those produced with the through-tool cooling and dry drilling. Thrust forces also increase depending on the drilled hole number.[7] From the point of view of the cutting forces, the results of drilling fiber-reinforced composites are similar to the results of drilling MMCs.[9,11]

The Taguchi design method is a useful tool for determining the effect of machining parameters and their significance levels. A plan of experiments can be conducted with the Taguchi method with the purpose of analyzing the data and obtaining the information about the property of a certain process. This method uses orthogonal arrays for defining the experiment plan.[4,13,14,16] Its important advantage is the fact that it saves experimental effort and time, reducing the cost. Furthermore, the results other than the conducted experiments can be predicted with a great accuracy by using this method. In recent times, a variety of applications of the Taguchi method have been performed in many areas.

The aim of this study was to introduce the Taguchi method in determining the optimum drilling conditions for the thrust force and drilling torque when drilling an Al7XXX alloy reinforced with three different mass fractions of B_4C particles. For this purpose, the effect of the control factors such as spindle speed, feed rate, particle fraction and cutting tool on the cutting forces were investigated. Significance levels of individual factors were determined with ANOVA. The values predicted with the Taguchi method were compared with the experimental results.

2 EXPERIMENTAL PROCESS

2.1 Production of Composite Materials

In this work, 7xxx-series aluminum alloy (including mass fractions: 5 % zinc, 3.5 % copper and 2.5 % of magnesium) was used as the matrix element. B_4C ceramic powders under 325 meshes were used as the reinforcement element. To investigate the effects of different reinforcement fractions on the machinability, three different weight fractions of B_4C particles were selected as 10 %, 15 % and 25 %. The mixture was cold pressed in the mold under the pressure of 25 MPa in an electrical furnace. Then the internal temperature of the furnace was fixed at 540 °C and the composite materials were produced by applying the liquid-phase sintering method for half an hour. Later the produced samples were subjected to the hardness, tensile and drilling tests. For the hardness test, three hardness measurements were performed on each sample by using OKO SEIKI hardness-measurement equipment and the mean of the hardness values was used. Tensile tests were also carried out by placing each specimen into a 60-ton Tinius Olsen tensile-test device. Tensile-test specimens were prepared according to the EN 10002-1 standard by turning the sintered blocks as shown in **Figure 1**.

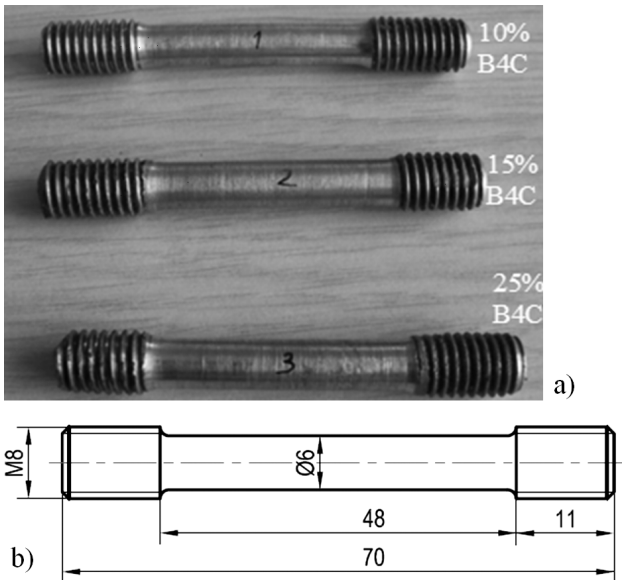

Figure 1: Tensile-test specimens: a) prepared test specimens, b) technical drawing of a test specimen
Slika 1: Preizkušanci za natezni preizkus: a) pripravljeni preizkušanci, b) tehnična risba preizkušanca

2.2 Test Setup and the Drilling Process

For the drilling tests of the produced MMCs, a computer numerically controlled (CNC) vertical machining center (VMC-550 Johnford Fanuc Series O-M) having the capacity of 15 kW and 3 500 r/min was used. The machining conditions and geometrical properties of the drills are given in **Table 1**. The cutting forces were measured for all the drilling experiments with three previously unused, different, 8-mm drills. Each test was repeated twice and the mean values were used. A total of 100 holes were drilled in addition to 27 Taguchi experiments for confirmation purpose. The length of the drilled composites was 12 mm. A KISTLER 9272 dynamometer was used to measure the thrust force and torque during the drilling process. **Figure 2** shows the schematic image of the drilling setup[17]. A picture of the produced composite, attached to a specially developed and manufactured fixture, after being drilled with the CNC vertical machining center, is depicted in **Figure 3**. After measuring the thrust forces and drilling torques, the results were recorded into a computer environment using the KISTLER DynoWare software. The average value of the measured cutting forces was taken into account so that the conical section of the tool tip was completely inside the workpiece. A sample output of the

Table 1: Machining conditions
Tabela 1: Pogoji obdelave

Machine tool	Johnford VMC-550 Fanuc Serial O-M CNC controlled vertical machining center	
Drills	HSS:	Φ 8 mm, 135° tool tip angle, spiral, 30° helical angle
	Uncoated carbide:	Φ 8 mm, 140° tool tip angle, spiral, 30° helical angle
	TiAlN-coated carbide:	Φ 8 mm, 140° tool tip angle, spiral, 30° helical angle
Workpiece materials	Mass fractions: 10 % B_4C/Al, 15 % B_4C/Al and 25 % B_4C/Al composite	
Cutting parameters	Spindle speeds (n): 1000 r/min, 1500 r/min, 2000 r/min, 2500 r/min Feed rates (f) : 0.1 mm/r, 0.2 mm/r, 0.3 mm/r	

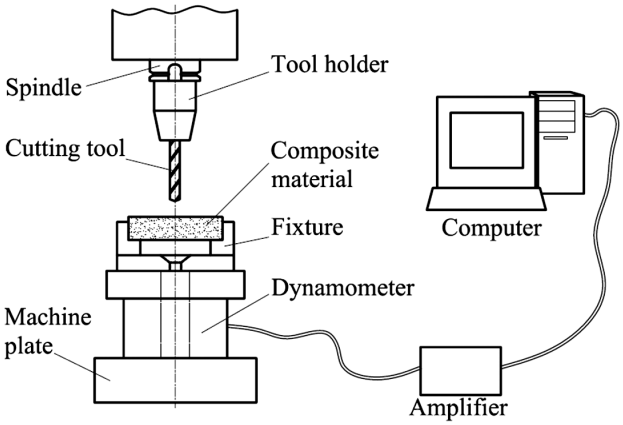

Figure 2: Schematic presentation of the measuring setup
Slika 2: Shematski prikaz sestava za merjenje

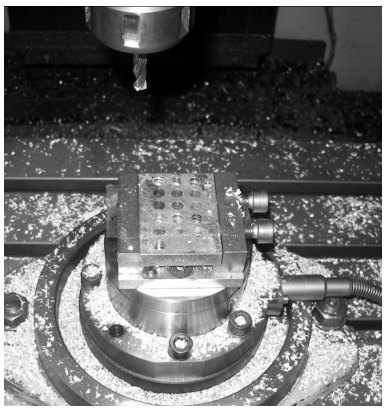

Figure 3: Drilling setup
Slika 3: Preizkus vrtanja

dynamometer showing the variation of the cutting force and torque is given in **Figure 4**.

3 RESULTS AND DISCUSSION

3.1 Microstructure and Mechanical Properties

The microstructure of the produced composites is shown in **Figure 5**. A homogeneous distribution of the ceramic particles over the composite alloy can be seen from this figure. According to the hardness test results, the average hardnesses of the specimens with mass fractions 10 % B_4C, 15 % B_4C and 25 % B_4C were meas-

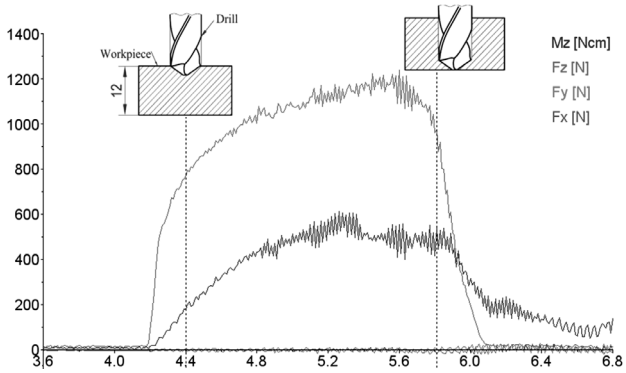

Figure 4: Typical cutting forces observed when spindle speed = 1500 r/min, feed = 0.3 mm/r, the work piece contains the mass fraction 10 % B_4C and the drill used is made of HSS
Slika 4: Značilna sila rezanja pri hitrosti vrtenja vretena = 1500 r/min, podajanje 0,3 mm/r, obdelovanec je vseboval masni delež 10 % B_4C, sveder je bil iz HSS-jekla

ured as 61 HRB, 79 HRB and 87 HRB, respectively. These hardnesses were significantly higher than that for the Al7075 alloy (43 HRB) but close to the Al7075–T6 alloy (87 HRB).[18] The hardness of the composites increased as the particle fraction increased due to the hard nature of the ceramic particles.

The results of the strength and elongation (%) for each sample are given in **Table 2**. The highest yield and

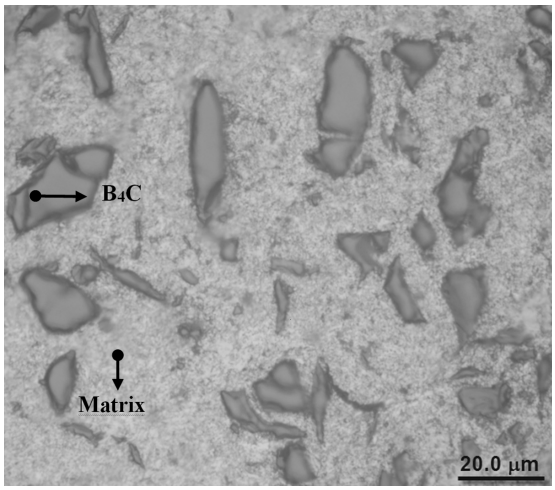

Figure 5: Microstructure of the composite having the mass fraction 15 % B_4C
Slika 5: Mikrostruktura kompozita z masnim deležem 15 % B_4C

tensile strength values were obtained when the B_4C particle fraction was 15 %. Generally, an increase in the particle fraction increases the strength of the composite material but, at the same time, reduces ductility due to an increased dislocation density.[19] In this study, it was observed that the ceramic reinforcements added to the aluminum matrix reduced the ductility of the composite material and made it more brittle (**Table 2**). The fact that the strength of the composite having 25 % particle fraction was lower than the strength of the composites having mass fractions 10 % B_4C and 15 % B_4C can be attributed to the increase in the interfacial decompositions between the particles and the matrix.[20]

Table 2: Strength results of the B_4C-reinforced MMC
Tabela 2: Trdnost MMC, ojačanega z B_4C

B_4C particle mass fraction *w*/%	Yield strength MPa	Tensile strength MPa	Elongation %
10	491	527	22.2
15	532	599	6.9
25	328	408	4.8

3.2 Cutting Forces and Torques

According to the experimental results, the effects of the cutting parameters such as particle fraction, cutting speed, feed rate and cutting-tool material on the thrust force and torque were given in **Figures 4** and **5**. The cutting forces increased with the particle weight fraction, and the rate of this increment for HSS tools was higher than that for the carbide tools with greater particle fractions. An increase in the weight fraction of the B_4C particles within the aluminum matrix increased the hardness of the composite causing a rapid tool wear due to a more intense contact with the cutting edge. Therefore, increasing both the weight fraction and the area of hard particles being in contact with the cutting tool resulted in an increase in the friction and flow strength of the cutting tool-chip as well as the cutting tool-workpiece interface. On the other hand, it could be observed from **Figures 6** and **7** that the thrust force and cutting torque increased with the feed rate, but they decreased with the cutting speed. Previous researchers stated that the most important factor affecting the cutting forces was the feed rate[3,8–12,16] and this was confirmed by our study. Since the chip volume removed per revolution of the cutting tool increased with an increase in the feed rate, the thrust force and cutting torque increased as well.[21]

When experimental results were analyzed in terms of the cutting-tool material, higher thrust forces, ranging from 150 N to 250 N, were produced with HSS tools than with carbide tools while drilling the 25 % B_4C reinforced MMCs. This situation could be attributed to the hardness of the cutting tool and to the wear mecha-

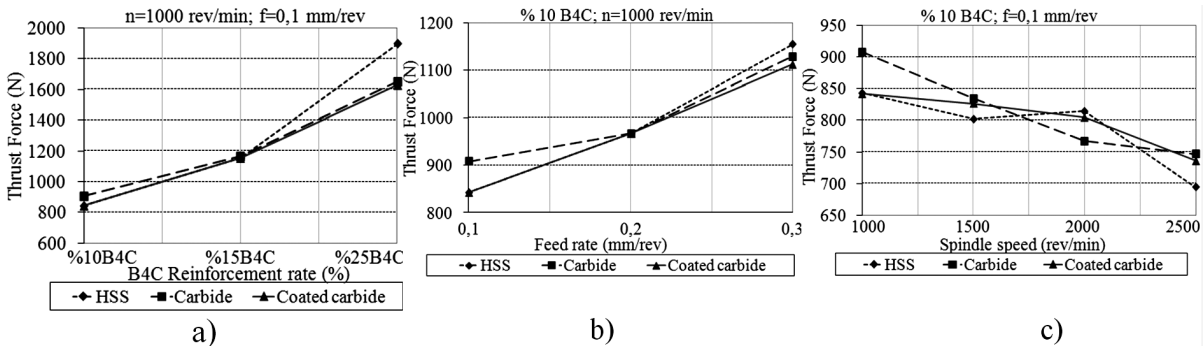

Figure 6: Effect of machining parameters on the thrust force: a) particle mass fraction, *w*/%, b) feed rate, mm/r, c) spindle speed, r/min
Slika 6: Vpliv parametrov obdelave na potisno silo: a) vsebnost delcev v masnih deležih, *w*/%, b) hitrost podajanja, mm/r, c) hitrost vrtenja vretena, r/min

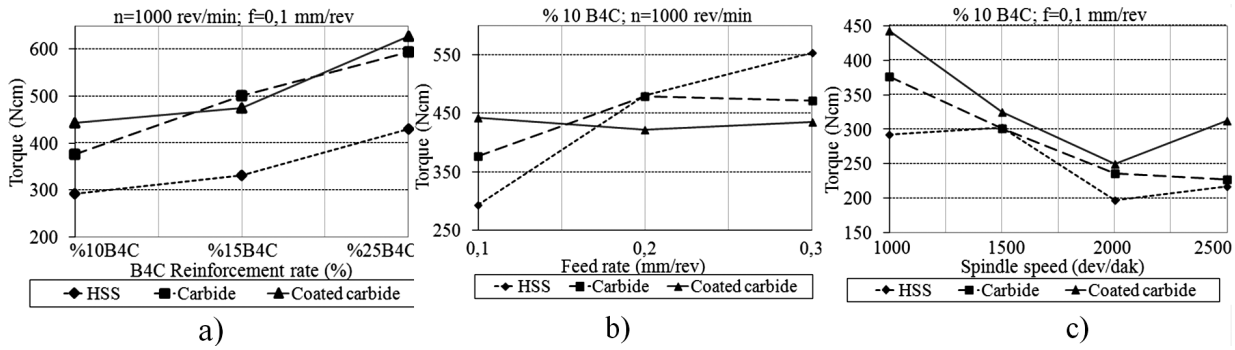

Figure 7: Effect of machining parameters on the drilling torque: a) particle mass fraction, *w*/%, b) feed rate, mm/r, c) spindle speed, r/min
Slika 7: Vpliv parametrov obdelave na navor pri vrtanju: a) vsebnost delcev v masnih deležih, *w*/%, b) hitrost podajanja, mm/r, c) hitrost vrtenja vretena, r/min

nisms of the drilling tool. Since HSS tools had a lower hardness than carbide tools, higher thrust forces were produced with HSS drills, especially with a higher particle fraction due to the tool flank wear. When the particle fraction was less than 25 %, the difference between the thrust forces produced by HSS and carbide tools was relatively lower (20 N–40 N). However, the test results indicated that HSS drills generally produced less cutting torques than carbide drills as shown in **Figure 7**. This condition might be attributed to the point angle of the drill because the thrust force and cutting torque increased with an increased point angle.[22] Therefore, it was concluded that HSS drills produced less cutting torques than carbide drills due to having a point angle smaller by 5° than carbide drills. Consequentially, although lower cutting forces were produced by PCD diamond tools according to the existing literature[3], carbide tools could be preferred for machining MMCs taking into account the production-cost balance.

3.3 Optimization with the Taguchi Method

In this section, optimization of drilling parameters was carried out in terms of drilling forces with the Taguchi analysis. The importance order of the effects of each control factor on drilling forces was identified. For this purpose, the factors selected in the Taguchi experimental design and the levels of these factors are shown in **Table 3**. A four-factor, 27-line and three-level L_{27} (3^{13}) orthogonal array was chosen since it has the ability to control the interactions among the factors.[23–25]

In the Taguchi method, there are three categories such as "the smallest is better", "he biggest is better" and "the nominal is better" for the calculation of the signal/noise (S/N) ratio. In this study, since "the lowest" thrust-force and cutting-torque values were desired for the optimization, "the smallest is better" calculation method was chosen. In the i_{th} experiment, the S/N ratio η_i can be calculated using the following equation[14,26,27]:

$$\eta_i = -10 \log_{10}\left(\frac{1}{n}\sum_{i=1}^{n} Y_i^2\right) \quad (1)$$

where n is the number of replications and Y_i is the measured characteristic value (i.e, the thrust force or cutting torque). The calculated S/N ratios (η) of the thrust forces and cutting torques are given in **Table 4**.

Table 3: Factors and levels used in the experiments
Tabela 3: Faktorji in stopnje, uporabljene pri eksperimentu

Process parameters	Units	Levels		
		Level 1	Level 2	Level 3
Particle fraction (A)	%	10	15	25
Feed rate (B)	mm/r	0.1	0.2	0.3
Spindle speed (C)	r/min	1000	1500	2000
Drill material (D)		HSS	Carbide	TiAlN-coated carbide

Table 4: Experimental design with the L_{27} orthogonal array and the S/N ratios
Tabela 4: Oblikovanje preizkusov z ortogonalno razporeditvijo L_{27} in razmerje S/N

Test No	A	B	C	D	Thrust force (N)	S/N ratio for thrust force	Torque (N cm)	S/N ratio for torque
1	1	1	1	1	843.2	–58.52	293	–49.34
2	1	1	2	2	834.3	–58.43	300.9	–49.57
3	1	1	3	3	804.3	–58.11	249.3	–47.93
4	1	2	1	2	966.8	–59.71	478.4	–53.60
5	1	2	2	3	924.1	–59.31	344	–50.73
6	1	2	3	1	880.7	–58.90	294	–49.37
7	1	3	1	3	1113.3	–60.93	434.7	–52.76
8	1	3	2	1	1048	–60.41	446.6	–53.00
9	1	3	3	2	1096	–60.80	291.3	–49.29
10	2	1	1	2	1168	–61.35	500.3	–53.99
11	2	1	2	3	1062	–60.53	398.5	–52.01
12	2	1	3	1	973.3	–59.77	309.1	–49.80
13	2	2	1	3	1244	–61.90	496.7	–53.92
14	2	2	2	1	1132	–61.07	370.6	–51.38
15	2	2	3	2	1089	–60.74	340	–50.63
16	2	3	1	1	1313	–62.37	578.3	–55.24
17	2	3	2	2	1310	–62.35	328	–50.32
18	2	3	3	3	1218	–61.71	388.5	–51.79
19	3	1	1	3	1631	–64.25	627.1	–55.95
20	3	1	2	1	1655	–64.37	434.1	–52.75
21	3	1	3	2	1374	–62.76	415.4	–52.37
22	3	2	1	1	1826	–65.23	496.2	–53.91
23	3	2	2	2	1477	–63.39	492.8	–53.85
24	3	2	3	3	1379	–62.79	547.8	–54.77
25	3	3	1	2	1835	–65.27	674.1	–56.57
26	3	3	2	3	1629	–64.24	641	–56.14
27	3	3	3	1	1441	–63.17	492.2	–53.84

The arithmetic average of S/N ratios for the levels of each control factor was calculated with respect to the thrust force and the cutting torque (**Table 5**). In addition, after arranging the difference between the maximum and minimum S/N ratios for each factor in a descending order, the degree of influence of each factor on the thrust force or cutting torque was found. Accordingly, the effective control factors for the thrust force were particle fraction, feed rate, spindle speed and drill-bit material (**Table 5**). The optimum machining parameters for the thrust force and drilling torque are found at the level where each factor has the largest S/N ratio.[14] Therefore, the optimal machining conditions for the thrust force were found to be the particle fraction of 10 %, feed rate of 0.1 mm/r, spindle speed of 2000 r/min and drill material of TiAlN-coated carbide. Similarly, the optimal machining conditions for the drilling torque were found to be the particle fraction of 10 %, feed rate of 0.1 mm/r, spindle speed of 2000 r/min and a HSS drill.

The effect graph of each control factor for the thrust force and drilling torque, according to the mean responses, was given in **Figures 8a** and **8b**, respectively. Both **Figures 8a** and **8b** showed that the thrust force and

drilling torque increased with an increase in the particle fraction and the feed rate, while the thrust force and cutting torque decreased with an increase in the spindle speed. However, the effect of the drill-bit material on the thrust force was very low.

Table 5: Average S/N ratios for each factor and level with regard to thrust force and cutting torque
Tabela 5: Povprečje razmerja S/N za vsak faktor in stopnjo glede na potisno silo in navor pri rezanju

	Level	A	B	C	D
For thrust force	1	–59.4564*	–60.8976*	–62.1689	–61.5337
	2	–61.3091	–61.4479	–61.5665	–61.6429
	3	–63.941	–62.361	–60.9711*	–61.53*
	Difference	4.4846	1.4634	1.1978	0.1092
	rank	1	2	3	4
For torque					
	1	–50.6201*	–51.5226*	–53.9199	–52.0704*
	2	–52.1194	–52.4621	–52.194	–52.2421
	3	–54.462	–53.2168	–51.0877*	–52.8891
	Difference	3.8419	1.6942	2.8322	0.8187
	rank	1	3	2	4

* = Optimal level

3.4 Analysis of Variance (ANOVA)

The purpose of the analysis of variance was to determine which parameter significantly affects the cutting forces.[28] ANOVA was performed to find whether individual factors and their interactions that affect the cutting forces were meaningful. According to the ANOVA results presented in **Table 6**, the most influential factor for the thrust force was found to be the particle fraction of 80.23 %. The other important factors were feed rate (6.72 %) and spindle speed (6.73 %). Similarly, the most influential factor for the drilling torque was found to be the particle fraction of 45.99 %, followed by spindle speed (25.25 %) and feed rate (8.75 %) as seen in **Table 7**. In addition, the effect of the drill-bit material on the cutting forces was found to be small. F_{test} values for the cutting forces, with regard to the factor interactions, were not meaningful since they were smaller than F_{table} values.[27] Hence, the statistical significance of interactions was minimum and it could be neglected.

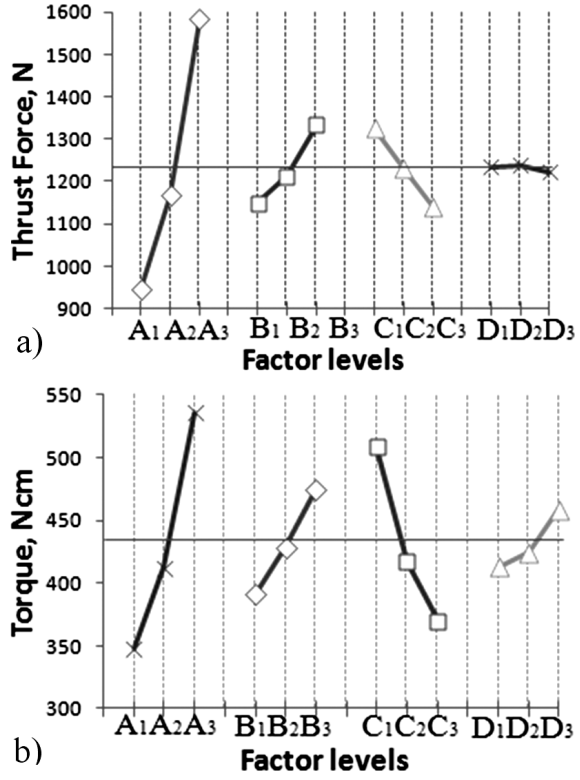

Figure 8: Mean effect graphs of responses: a) thrust force, b) drilling torque
Slika 8: Graf učinka povprečnih rezultatov: a) potisna sila, b) navor pri vrtanju

Table 6: ANOVA results for the thrust force
Tabela 6: Rezultati ANOVA za potisno silo

Factor	*DF*	*SS*	*V*	F_{test}	*PD*
Particle fraction (A)	2	1882587	941294	210.5	80.23
Feed rate (B)	2	157716	78858	17.63	6.721
Spindle speed (C)	2	157829	78915	17.65	6.726
Drill material (D)	2	1250	624.9	0.1397	0.053 3
AxB	4	25505	6376	1.426	1.087
AxC	4	79868	19967	4.465	3.404
BxC	4	15006	3751	0.8388	0.639 5
Error	6	26835	4472		1.144
Total	26	2346595			100

DF: Degree of Freedom, *SS*: Sum of Squares, *V*: Variance, *PD*: Percentage Distribution. $F_{table(0.05;2;6)} = 5.14$, $F_{table(0.05;4;6)} = 4.53$

Table 7: ANOVA results for the drilling torque
Tabela 7: Rezultati ANOVA za navor pri vrtanju

Factor	*DF*	*SS*	*V*	F_{test}	*PD*
Particle fraction (A)	2	163615	81808	15.92	45.99
Feed rate (B)	2	31123	15562	3.029	8.749
Spindle speed (C)	2	89834	44917	8.742	25.25
Drill material (D)	2	10230	5115	0.995	2.876
AxB	4	11959	2990	0.582	3.362
AxC	4	12466	3116	0.607	3.504
BxC	4	5689	1422	0.277	1.599
Error	6	30829	5138		8.666
Total	26	355745			100

DF: Degree of Freedom, *SS*: Sum of Squares, *V*: Variance, *PD*: Percentage Distribution. $F_{table(0.05;2;6)} = 5.14$, $F_{table(0.05;4;6)} = 4.53$

3.5 Confirmation Experiments

The final step of the Taguchi experimental design process includes confirmation experiments.[14,27] For this aim, the results of the experiments were compared with the predicted values with the Taguchi method and the error rates were obtained. S/N ratios $\eta_{predict}$ were predicted using the following model:[14,26]

$$\eta_{predict} = \eta_m + \sum_{i=1}^{k} (\eta_i - \eta_m) \quad (2)$$

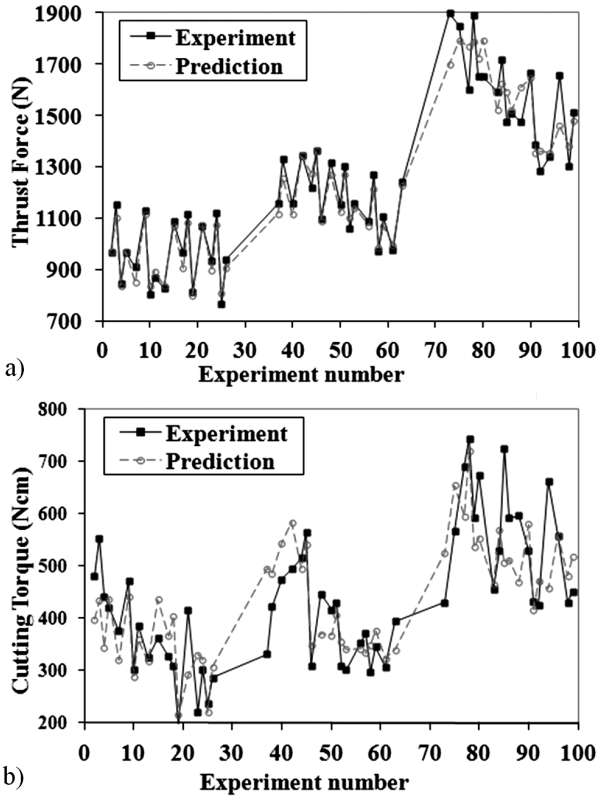

Figure 9: Comparison of the predicted and experimental results: a) thrust force (R^2 = 0.946), b) drilling torque (R^2 = 0.644)

Slika 9: Primerjava napovedanih in eksperimentalno določenih rezultatov: a) potisna sila (R^2 = 0,946), b) navor pri vrtanju (R^2 = 0,644)

where η_m is the total mean of the S/N ratios, η_i is the mean S/N ratio at the optimum level and k is the number of the main design parameters that significantly affect the performance characteristics.

After predicting the S/N ratios other than 27 experiments (with Eq.2), the thrust forces and drilling torques were calculated using the following equation:[26]

$$Y_{predict} = 10^{(\frac{-S/N}{20})} \quad (3)$$

where $Y_{predict}$ is the thrust force or drilling torque with regard to the S/N ratio. **Figure 9** represents the comparison between the predicted and experimental results according to the experiment numbers. These results show that the Taguchi method can be applied successfully in predicting the thrust forces with the coefficient of determination R^2 = 0.946 (**Figure 7a**). The value of R^2 for the prediction of the cutting torques was 0.644, but the R^2 value for 54 of 100 experiments was 0.85.

4 CONCLUSIONS

In this study, aluminum MMCs containing three different weight fractions of B_4C particles were produced with the PM technique, and drilling experiments were carried out to study the effects of the machining parameters on the thrust force and cutting torque. Moreover, the optimum drilling parameters were obtained for the performance characteristics (thrust force and torque) using the Taguchi analysis. The obtained results can be summarized as follows:

- An increase in the proportion of the B_4C particle caused a decreased ductility of the material but an increased hardness of the composite. The highest tensile strength was obtained with the 15 % B_4C particle fraction.
- According to the experimental results, the cutting forces significantly increased with an increase in the B_4C fraction and the feed rate but decreased with an increase in the spindle speed.
- HSS tools produced more thrust forces than the two carbide tools especially when drilling the composites with higher particle fractions. On the other hand, the coated and the solid carbide tools produced similar thrust forces. However, the coated tools produced somewhat higher drilling torques than the uncoated ones.
- With the Taguchi and ANOVA analysis, the effective factors for the thrust force and drilling torque were found to be the particle-weight fraction and feed rate, respectively. Furthermore, the effects of the cutting tool material and the interactions of the factors on the thrust force and cutting torque were found to be very low.

Acknowledgments

This research was supported by the Gazi University under the Project Number 07/2008-8.

The authors wish to thank the TOBB Economy and Technology University for providing laboratory opportunities during the course of the research work. The authors express their gratitude to MİTAŞ CİVATA and Mr. Serdar Iskender for enabling the tensile and impact tests for the fabricated composite materials.

5 REFERENCES

[1] R. G. Budynas, R. Budynas, K. Nisbett, Shigley's Mechanical Engineering Design, McGraw-Hill, 2010

[2] V. Songmene, M. Balazinski, Machinability of graphitic metal matrix composites as a function of reinforcing particles, CIRP Annals - Manufacturing Technology, 48 (**1999**) 1, 77–80

[3] M. Ramulu, P. N. Rao, H. Kao, Drilling of (Al2O3)p/6061 metal matrix composites, Journal of Materials Processing Technology, 124 (**2002**) 1–2, 244–254

[4] S. Basavarajappa, G. Chandramohan, J. P. Davim, Some studies on drilling of hybrid metal matrix composites based on Taguchi techniques, Journal of Materials Processing Technology, 196 (**2008**) 1–3, 332–338

[5] C. A. Brown, M. K. Surappa, The machinability of a cast aluminium alloy-graphite particle composite, Materials Science and Engineering, 102 (**1988**) 1, 31–37

[6] S. Barnes, I. R. Pashby, A. B. Hashim, Effect of heat treatment on the drilling performance of aluminum/SiC MMC, Applied Composite Materials, 6 (**1999**) 2, 121–138

[7] S. Barnes, I. R. Pashby, Through-tool coolant drilling of aluminum/SiC metal matrix composite, Journal of Engineering Materials and Technology, Transactions of the ASME, 122 (**2000**) 4, 384–388

[8] J. P. Davim, A. Monteiro Baptista, Cutting force, tool wear and surface finish in drilling metal matrix composites, Proceedings of the Institution of Mechanical Engineers, Part E: Journal of Process Mechanical Engineering, 215 (**2001**) 2, 177–183

[9] A. M. Abrão, J. C. C. Rubio, P. E. Faria, J. P. Davim, The effect of cutting tool geometry on thrust force and delamination when drilling glass fibre reinforced plastic composite, Materials and Design, 29 (**2008**) 2, 508–513

[10] M. T. Hayajneh, A. M. Hassan, A. T. Mayyas, Artificial neural network modeling of the drilling process of self-lubricated aluminum/alumina/graphite hybrid composites synthesized by powder metallurgy technique, Journal of Alloys and Compounds, 478 (**2009**) 1–2, 559–565

[11] D. Iliescu, D. Gehin, M. E. Gutierrez, F. Girot, Modeling and tool wear in drilling of CFRP, International Journal of Machine Tools and Manufacture, 50 (**2010**) 2, 204–213

[12] Y. Altunpak, M. Ay, S. Aslan, Drilling of a hybrid Al/SiC/Gr metal matrix composites, International Journal of Advanced Manufacturing Technology, 60 (**2012**) 5–8, 513–517

[13] A. N. Haq, P. Marimuthu, R. Jeyapaul, Multi response optimization of machining parameters of drilling Al/SiC metal matrix composite using grey relational analysis in the Taguchi method, International Journal of Advanced Manufacturing Technology, 37 (**2008**) 3–4, 250–255

[14] G. Tosun, Statistical analysis of process parameters in drilling of AL/SIC P metal matrix composite, International Journal of Advanced Manufacturing Technology, 55 (**2011**) 5–8, 477–485

[15] A. R. Ahamed, P. Asokan, S. Aravindan, M. K. Prakash, Drilling of hybrid Al-5%SiCp-5%B4Cp metal matrix composites, International Journal of Advanced Manufacturing Technology, 49 (**2010**) 9–12, 871–877

[16] S. Basavarajappa, G. Chandramohan, J. P. Davim, M. Prabu, K. Mukund, M. Ashwin, M. Prasannakumar, Drilling of hybrid aluminium matrix composites, International Journal of Advanced Manufacturing Technology, 35 (**2008**) 11–12, 1244–1250

[17] C. C. Tsao, H. Hocheng, Effect of tool wear on delamination in drilling composite materials, International Journal of Mechanical Sciences, 49 (**2007**) 8, 983–988

[18] Y. Kazancoglu, U. Esme, M. Bayramoglu, O. Guven, S. Ozgun, Multi-objective optimization of the cutting forces in turning operations using the Grey-based Taguchi method, Mater. Tehnol., 45 (**2011**) 2, 105–110

[19] H. Zhang, M. W. Chen, K. T. Ramesh, J. Ye, J. M. Schoenung, E. S. C. Chin, Tensile behavior and dynamic failure of aluminum 6092/B4C composites, Materials Science and Engineering A, 433 (**2006**) 1–2, 70–82

[20] E. Mohammad Sharifi, F. Karimzadeh, M. H. Enayati, Fabrication and evaluation of mechanical and tribological properties of boron carbide reinforced aluminum matrix nanocomposites, Materials and Design, 32 (**2011**) 6, 3263–3271

[21] J. S. Strenkowski, C. C. Hsieh, A. J. Shih, An analytical finite element technique for predicting thrust force and torque in drilling, International Journal of Machine Tools and Manufacture, 44 (**2004**) 12–13, 1413–1421

[22] S. Jayabal, U. Natarajan, Influence of cutting parameters on thrust force and torque in drilling of E-glass/polyester composites, Indian Journal of Engineering and Materials Sciences, 17 (**2010**) 6, 463–470

[23] J. P. Davim, Study of drilling metal-matrix composites based on the Taguchi techniques, Journal of Materials Processing Technology, 132 (**2003**) 1–3, 250–254

[24] C. C. Tsao, Taguchi analysis of drilling quality associated with core drill in drilling of composite material, International Journal of Advanced Manufacturing Technology, 32 (**2007**) 9–10, 877–884

[25] C. C. Tsao, H. Hocheng, Evaluation of thrust force and surface roughness in drilling composite material using Taguchi analysis and neural network, Journal of Materials Processing Technology, 203 (**2008**) 1–3, 342–348

[26] R. K. Roy, A primer on the Taguchi method / Ranjit K. Roy, Van Nostrand Reinhold, New York, 1990

[27] K. Palanikumar, Experimental investigation and optimization in drilling of GFRP composites, Measurement, Journal of the International Measurement Confederation, 44 (**2011**) 10, 2138–2148

[28] U. Esme, Use of grey based Taguchi method in ball burnishing process for the optimization of surface roughness and microhardness of AA 7075 aluminum alloy, Mater. Tehnol., 44 (**2010**) 3, 129–135

UDK 669.14:533.9:539.92
Original scientific article/Izvirni znanstveni članek

ISSN 1580-2949
MTAEC9, 47(2)177(2013)

WEAR PROPERTIES OF AISI 4140 STEEL MODIFIED WITH ELECTROLYTIC-PLASMA TECHNOLOGY

OBRABNE LASTNOSTI JEKLA AISI 4140, MODIFICIRANEGA S TEHNOLOGIJO ELEKTROLITSKE PLAZME

Aysun Ayday, Mehmet Durman

Sakarya University, Faculty of Engineering, Department of Metallurgical and Materials Engineering, 54187 Sakarya, Turkey
aayday@sakarya.edu.tr

Prejem rokopisa – received: 2012-08-29; sprejem za objavo – accepted for publication: 2012-10-09

An electrolytic-plasma treatment (EPT) was applied to the surface of AISI 4140 steel and the wear behavior under dry sliding conditions was studied for different treatment parameters. The modified samples were characterized before and after the wear testing using metallographic, SEM-microscope and microhardness techniques. The test results indicate that the wear resistance of the AISI 4140 steel can be improved by means of electrolytic-plasma technology (EPT). The wear resistance increases with an increased modified-layer hardness due to a transformation to the martensitic structure.

Keywords: plasma, microhardness, wear

Preučevane so bile obrabne lastnosti pri suhem drsenju in različnih parametrih z elektrolitsko plazmo obdelane površine jekla AISI 4140. Modificirani vzorci so bili karakterizirani pred preizkusom obrabe in po njem z uporabo metalografije, z vrstičnim elektronskim mikroskopom (SEM) in meritvijo trdote. Rezultati so pokazali, da se obrabna odpornost jekla AISI 4140 lahko poveča s tehnologijo elektrolitske plazme (EPT). Obrabna odpornost se povečuje s povišanjem trdote modificirane plasti zaradi pretvorbe v martenzitno mikrostrukturo.

Ključne besede: plazma, mikrotrdota, obraba

1 INTRODUCTION

As an advanced surface-processing technique, electrolytic-plasma treatment (EPT) has been successfully used to improve the hardness, the wear resistance and the corrosion resistance of materials[1]. When hardening is not necessary for a whole surface or bulk of material, EPT is a suitable method for treating a specific location on a surface[2]. Electrolytic-plasma (heating-quenching) hardening is a standard hardening mechanism involving two main steps: "austenitizing", during which the material is heated above the critical temperature for the austenite formation (but below the melting point) and "quenching" or cooling down, where austenite is transformed into martensite. The heating or quenching of medium and high-carbon steels can change the steel microstructures, which causes variations in the mechanical and physical properties and affects the behavior of the steels under service conditions and operations[3,4].

EPT is characterized by several process parameters: voltage, current, electrolyte, duration, and heating-quenching rate. All these parameters are strongly correlated to each other and affect the final hardening results; for this reason process modeling seems to be a good approach to the process optimization. In this study, the wear resistance of the electrolytic-plasma-modified AISI 4140 steel was evaluated under dry sliding conditions and compared with the AISI 4140 steel samples. The modified samples were characterized before and after the wear tests with metallographic, SEM microscope and microhardness techniques.

2 EXPERIMENTAL DETAILS

The test material was the commercial AISI 4140 low-alloy steel with the composition (in mass fractions, %) of 0.4 C, 0.22 Si, 0.77 Mn, 0.04 S, 0.035 P, 0.8 Cr and 0.25 Si. The diameter of cylindrical samples was 20 mm and the height was 10 mm. All the samples were modified with EPT. The EPT voltage, heating and cooling times were 310–260 V, 3 s and 3 s, respectively, depending upon the thermal cycle and the process temperature. The sample codes and the EPT parameters are listed in **Table 1**.

The morphology of the modification layer was investigated with a scanning electron microscope (SEM Joel, JSM 6060-LU). The hardness measurements were conducted on the cross-sections of the samples with a Vickers microhardness tester. The test load was 100 g for the hardness measurements at the cross-sections. The temperature distribution of the samples from the plasma-treated side to the internal side was investigated via thermocouples during the process. The surface temperature data were collected from the system with the aid of a computer data-acquisition system.

The wear tests were performed both on the original AISI 4140 and on the EPT-modified specimens to determine the optimum process parameters. All the wear

Table 1: EPT parameters
Tabela 1: EPT-parametri

Parameter code	Electrolytic solution	Heating (V)	Cooling (V)	Total time (s)	Thermal cycle
EPT–0	Original AISI 4140				
EPT–4	Na_2CO_3; 12 %	310	260	(3 and 3) s × 4 = 24 s	4
EPT–5	Na_2CO_3; 12 %	310	260	(3 and 3) s × 5 = 30 s	5
EPT–6	Na_2CO_3; 12 %	310	260	(3 and 3) s × 6 = 36 s	6

Table 2: Maximum surface-hardness, surface-temperature and wear-rate values
Tabela 2: Maksimalna trdota površine, temperatura površine, vrednosti obrabe

	Original AISI 4140 (EPT-0)	EPT-4	EPT-5	EPT-6
Max. surface hardness ($HV_{0.1}$)	200	800	900	930
Surface temperature (°C)	ø	600	780	835
Wear rate ($mm^3/(N\ m)$)	9.06 E-05	5.05 E-05	4.87 E-05	4.66 E-05

tests were carried out under dry sliding conditions at room temperature using a ball-on-disc (CSM tribometer), friction- and wear-test machine. The counterpart was an Al_2O_3 ball (Φ = 6 mm) according to DIN 50 324 and ASTM G 99-95a. The tests were performed with a nominal load of 3 N and a sliding speed of 0.10 m/s for the total sliding distance of 200 m.

3 RESULTS AND DISCUSSION

The cross-sectional SEM images of the EPT-6 sample showed that it typically consisted of a modified diffusion zone (**Figure 1**). This figure shows the microstructure of the cross-section of the EPT-modified steel. The following zones are visible in the diffusion layer: the hardened zone (HZ), the heat-affected zone (HAZ) and the base material (BM). During EPT, austenite transforms completely or partially to martensite and thus the micro-

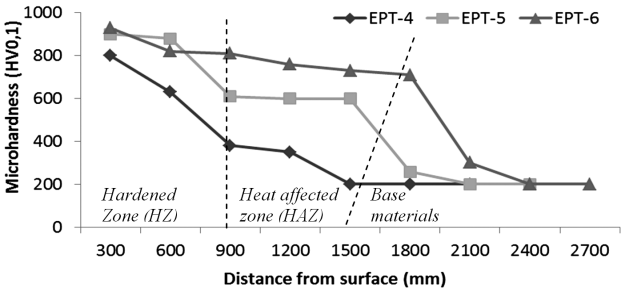

Figure 2: Microhardness profiles of the EPT-modified samples
Slika 2: Profili mikrotrdote vzorcev, modificiranih z EPT

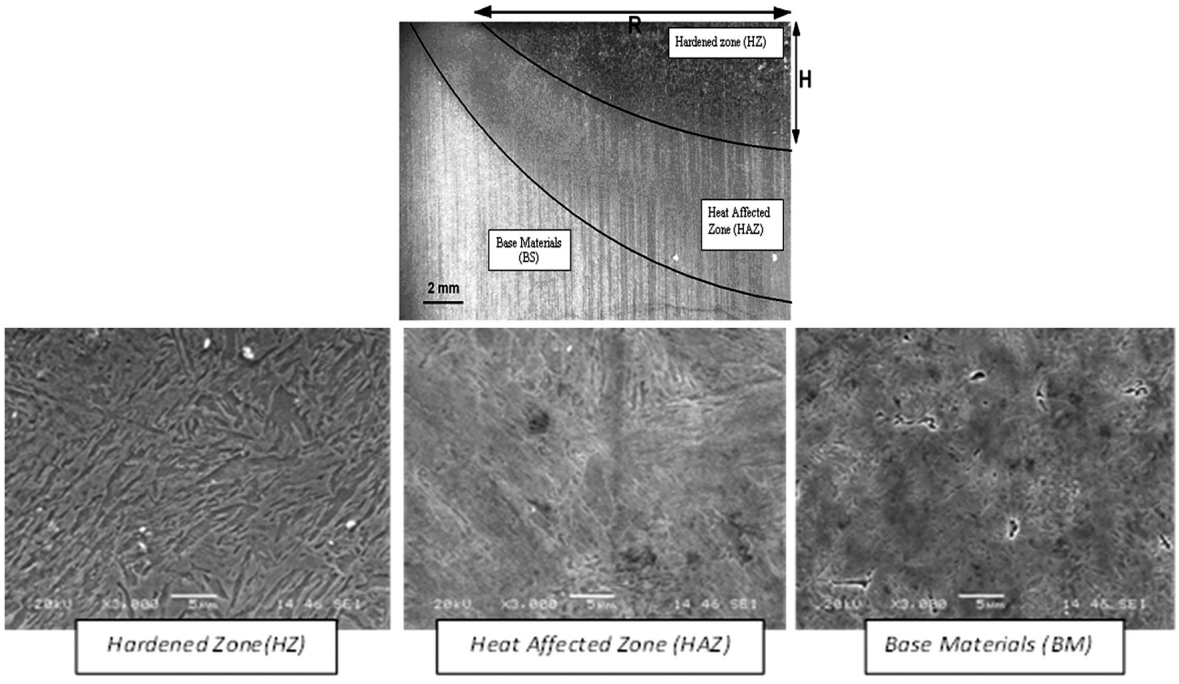

Figure 1: Cross-sectional appearance of the EPT-modified EPT-6 (*R* – radius of the modification area, *H* – HZ depth)
Slika 1: Prečni prerez vzorca EPT-6, modificiranega z EPT (*R* – polmer modificiranega področja, *H* – globina HZ)

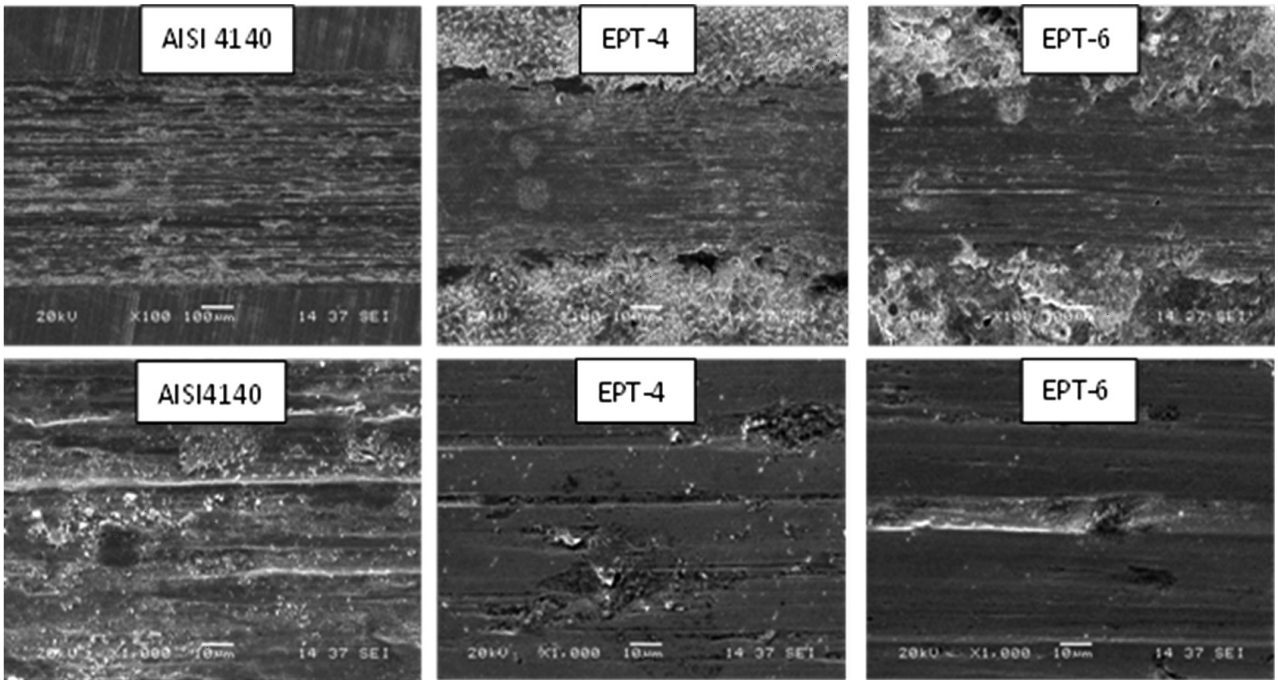

Figure 3: SEM micrographs of the original surface (EPT-0) and worn surfaces of AISI 4140, EPT-4 and EPT-6
Slika 3: SEM-posnetki originalne površine (EPT-0) in obrabljene površine AISI 4140, EPT-4 in EPT-6

structure of the HZ consists of martensite. An amount of the retained austenite may be present in this region[5]. In the neighborhood of the HZ with the base material, a narrow heat-affected zone was observed, consisting of martensite, bainite and some traces of the initial pearlitic structure. These are the most probable structures according to Refs. [5,6]. The microstructure of the base material is composed of ferrite and pearlite. The maximum microhardness of this hardened zone was 930 $HV_{0.1}$. The maximum microhardness of the second zone (HAZ) was 800 $HV_{0.1}$. From the plasma surface to the base metal, the hardness values decreased and the phase structure changed into a ferritic-pearlitic matrix; in this zone the hardness was measured as 200 $HV_{0.1}$, which is shown in **Figure 2**.

The values obtained for the maximum surface hardness, surface temperature and wear rate of different specimen groups are listed in **Table 2**. It is evident that EPT markedly improves the wear performance of the steel and that the degree of improvement depends on the EPT parameters. This means that the wear resistance increases with an increase in the thermal cycle. The thermal cycle was effective at rising the surface temperature. A high surface temperature affects the modification depth and the surface hardness. The wear rate obtained for the EPT-6 sample was lower than the rates obtained for the original AISI 4140 (EPT-0) or for the EPT-4 and EPT-5 samples. This is due to the microstructure of the EPT-6 sample, which had a martensitic structure. The microstructure of the EPT-6 surface, after the EPT treatment, was finer and more homogenous in comparison with the surfaces of EPT-4 and EPT-5.

Figure 3 shows the wear surfaces of the original AISI 4140 (EPT-0), the EPT-4 and EPT-6 samples, tested at a load of 3 N. EPT-6 shows quite a smooth surface with shallow, abrasive wear scars due to the high hardness of the sample. The original AISI 4140 (EPT-0) steel was tested under a similar wear-test condition. The plastic deformation was obvious in this case and was caused by a low surface hardness as shown in **Figure 3**. The worn-surface analysis revealed a severe abrasive wear of the original AISI 4140 (EPT-0) accompanied with a high degree of plastic deformation (**Figure 3** –AISI 4140).

4 CONCLUSIONS

It is evident that the wear rate of steel is increased significantly by EPT. The degree of improvement depends on the EPT-process conditions. The modified layer thickness and the surface hardness increase with the increasing surface temperature and thermal cycle. The specimens with the maximum hardness showed the maximum resistance to wear. Thus, the hardness of the surface is a very important factor with respect to the wear rate. The hardness results arise from the microstructures of the modified samples that had martensitic structures. An increase in the thermal cycle increases the wear resistance of EPT-6 due to a finer and more homogenous hardened zone. It was observed that the longer the heating and the cooling times, the greater was the hardened-layer thickness. The initial microstructure was fully martensitic, especially in the HAZ zone after the EPT-6 sample processing. When processing the other

samples, like EPT-4 and EPT-5, the microstructure transforms to a martensitic and also bainitic matrix. Therefore, the maximum microhardness values decrease from 930 HV to 200 HV during the experiments.

5 REFERENCES

[1] Y. N. Tyurin, A. D. Pogrebnyak, Electric Heating Using a Liquid Electrode, Surface and Coatings Technology, 142–144 (**2001**), 293–299

[2] C. Ye, S. Suslov, B. J. Kim, E. A. Stach, G. J. Cheng, Fatigue performance improvement in AISI 4140 steel by dynamic strain aging and dynamic precipitation during warm laser shock peening, Acta Materialia, 59 (**2011**), 1014–1025

[3] S. A. Jenabali Jahromi, A. Khajeh, B. Mahmoudi, Effect of different pre-heat treatment processes on the hardness of AISI 410 martensitic stainless steels surface-treated using pulsed neodymium-doped yttrium aluminum garnet laser, Materials and Design, 34 (**2012**), 857–862

[4] N. S. Bailey, W. Tan, Y. C. Shin, Predictive modeling and experimental results for residual stresses in laser hardening of AISI 4140 steel by a high power diode laser, Surface & Coatings Technology, 203 (**2009**), 2003–2012

[5] C. Soriano, J. Leunda, J. Lambarri, V. García Navas, C. Sanz, Effect of laser surface hardening on the microstructure, hardness and residual stresses of austempered ductile iron grades, Applied Surface Science, 257 (**2011**), 7101–7106

[6] C. T. Kwok, K. I. Leong, F. T. Cheng, H. C. Man, Microstructural and corrosion characteristics of laser surface-melted plastics mold steels, Materials Science and Engineering A, 357 (**2003**), 94–103

UDK 621.793:533.9:539.92
Original scientific article/Izvirni znanstveni članek

ISSN 1580-2949
MTAEC9, 47(2)181(2013)

TRIBOLOGICAL BEHAVIOR OF A PLASMA-SPRAYED Al_2O_3-TiO_2-Cr_2O_3 COATING

TRIBOLOŠKO PONAŠANJE S PLAZMO NAPRŠENEGA Al_2O_3-TiO_2-Cr_2O_3 NANOSA

Yeşim Sert, Nil Toplan

Sakarya University, Department of Metallurgical and Materials Engineering, Esentepe Campus, 54187 Sakarya, Turkey
toplan@sakarya.edu.tr

Prejem rokopisa – received: 2012-08-31; sprejem za objavo – accepted for publication: 2012-10-08

Alumina-titania, titania, chromia and chromia-titania coatings, deposited on aluminium substrates with atmospheric, plasma-spray, coating techniques (APSCTs), were tested on a low-frequency reciprocating-sliding tribometer. The surface wear of the coatings was investigated with SEM and optical microscopy. The denser Cr_2O_3 coatings showed a higher wear resistance than the more porous Al_2O_3-TiO_2 and TiO_2 coatings. An increase in the titania content diminishes the coating hardness and the wear resistance.

Keywords: Cr_2O_3-TiO_2, Al_2O_3-TiO_2 coatings, textile parts, plasma-spray coating, wear

Nanosi Al_2O_3-TiO_2, TiO_2, Cr_2O_3, Cr_2O_3-TiO_2 z atmosferskim plazemskim nanašanjem z brizganjem (APSCT) na podlago iz aluminija so bili preizkušeni na nizkofrekvenčnem protismernem drsnem tribometru. Obrabljena površina nanosa je bila preiskovana s SEM in svetlobno mikroskopijo. Gostejši nanos Cr_2O_3 je pokazal večjo odpornost proti obrabi kot bolj porozna nanosa Al_2O_3-TiO_2 in TiO_2. Povečanje vsebnosti TiO_2 zmanjšuje trdoto nanosa in zmanjša odpornost proti obrabi.

Ključne besede: nanosi Cr_2O_3-TiO_2, Al_2O_3-TiO_2, kosi tkanine, plazemski nanos z brizganjem, obraba

1 INTRODUCTION

It is well known that aluminum (Al) alloys have been considered to be some of the most useful and versatile materials because of their metallurgical characteristics, such as high strength-to-weight ratio, and high thermal conductivity. They are also easy to shape and relatively inexpensive. However, the low hardness results in poor tribological characteristics and prevents their wide use, especially in the situations where a hard surface is needed. To improve the wear resistance, many techniques, such as metal-matrix composites, plasma spraying, thermal spraying and hard anodizing have been explored[1].

The APSCT is an economical and effective method applied to various machine parts to improve the component performance in wear, corrosion, thermal barrier, and electric insulation. Plasma-sprayed Al_2O_3-TiO_2 has been widely used as a wear-resistant coating in textile, machinery and printing industries[2–5]. Cr_2O_3 has a wide range of applications such as green pigments, coating materials for thermal protection and wear resistance as well as refractory applications due to the high melting temperature (about 2435 °C)[3,6]. The present paper deals with the wear resistance of the plasma-sprayed alumina-titania, titania, chromia and chromia-titania coatings that increased the service life of the shutters (Al-based) used in the textile industry.

2 EXPERIMENTAL PROCEDURE

The commercial feedstock powders in the mass fractions 13 % TiO_2-Al_2O_3 (Metco 130), 40 % TiO_2-Al_2O_3 (Metco 131VF), 100 % TiO_2 (Metco 102) and 100 % Cr_2O_3 (Metco 106) were supplied by SULZER METCO Powder Technology. Al_2O_3, TiO_2 and Cr_2O_3 powders were premixed to form five different compositions (**Table 1**) and these were prepared on an aluminium alloy (AA1050). The mixtures were ball-milled for 2 h by using ZrO_2 balls and distilled water as the milling media to provide homogenous mixtures. After drying the powders were screened and sieved to

Table 1: Coating powders (*w*/%)
Tabela 1: Prahovi za nanašanje (*w*/%)

Composition	Al_2O_3	TiO_2	Cr_2O_3
1	87	13	–
2	60	40	–
3	–	100	–
4	–	50	50
5	–	–	100

Table 2: Plasma-spray parameters
Tabela 2: Parametri nabrizgavanja s plazmo

Coating parameters (for the 1–5 coded compositions)	
Primary-gas flow rate (Ar, L/min)	80
Secondary-gas flow rate (H_2, L/min)	15
Carrier-gas flow rate (Ar, L/min)	40
Spray distance (mm)	100
Current (A)	500
Voltage (V)	60–70

achieve the correct particle-size distribution needed for plasma spraying. Prior to the deposition process, aluminium substrates were grit blasted with Al_2O_3 particles and this was followed by ultrasonic cleaning in acetone for 15 min. A 40 kW plasma-spraying system (METCO 3MB) was utilized to produce the coatings using the parameters summarized in **Table 2**.

The surface roughness was measured with a surface-roughness tester (Perthometer M4P) and the average roughness Ra, defined as the arithmetic mean of the departures of the profile from the mean line, was used to quantify the coating-surface roughness. A scanning electron microscope (SEM) (JEOL JSM-6060LV) equipped with an energy dispersive X-ray spectrometer (EDS) was used to examine the microstructures and chemical compositions of the coatings. An X-ray diffraction analysis (XRD) was carried out on RIGAKU DMAX 2200 to determine the phases of the coating(s). The microhardness values of the specimens were taken from the cross-sections of the polished samples at the load of 200 g and after a loading time of 15 s using LEICA VMHT MOT microhardness equipment. The wear tests were performed using a low-frequency reciprocating-sliding tribometer, connected to a computer monitoring the dynamic coefficient of friction (in both sliding directions), relative humidity and temperature. The tests were performed by applying a load of 5 N to a single-crystal Al_2O_3 (sapphire) ball with a diameter of 6 mm. The wear specimens had the dimensions of 3 cm × 3 cm × 3 mm, the shear rate was 0.15 m/s and the sliding distance was 150 m. The values of the coefficient of friction were calculated from the normal load and the friction force was obtained from a digital oscilloscope. After the wear tests, the morphology of each wear scar was observed with SEM.

3 RESULTS AND DISCUSSION

Table 3 summarizes five different compositions of the coating-test results. While the TiO_2 coatings had the highest surface-roughness values, the values for the Cr_2O_3 coatings were found to be the lowest. Having a lower as-sprayed surface roughness is very important for technological applications because it reduces the number of post-deposition mechanical treatments necessary[7,8]. As a function of the substrate-surface roughness, the values of porosity and coating roughness increased, while the increase in the substrate-surface roughness grow up. The hardness values were also relatively reduced. The highest hardness, the lowest porosity and the lowest coating roughness were obtained at the value of the substrate roughness of 2.346 μm. The hardness values decrease with the increasing amounts of TiO_2 in the Al_2O_3-TiO_2 coatings. In the Cr_2O_3-TiO_2-based coatings, the hardness values increase with the amount of Cr_2O_3. An increase in the porosity amount will result in a decrease in the hardness of the coating. The lowest coefficient of friction (μ) was achieved in the 100 % Cr_2O_3 coatings. Hardness has a strong influence on wear resistance. The higher the hardness, the better is the wear resistance. It is well known that an addition of TiO_2 to an Al_2O_3 coating is to reduce the melting temperature of the oxide, thereby producing less porous and better performance coatings than the pure Al_2O_3 coatings. The melting temperature decreases due to the fact that TiO_2 has a lower melting temperature (1854 °C) than Al_2O_3 (2040 °C) and due to its ability to form a liquid solution with Al_2O_3. It is also noted that the trend displayed by the coating densities is consistent with that exhibited by the degree of melting, i.e., a high degree of melting (e.g., Cr_2O_3, 2435 °C) results in high density. Increasing the microhardness leads to the improvements in the wear resistance of the coatings. The grain size also has an effect on the wear resistance. The nanocoating has a higher wear resistance than the commercial coating although its hardness is lower than that of the commercial coating. A related study on the abrasive wear has revealed that nanocoatings could have a two-to-four-fold increase in the wear resistance in comparison with the commercial coatings[2,7].

Table 3: Surface roughness, hardness, density and friction coefficient of the coatings

Tabela 3: Hrapavost površine, trdota, gostota in koeficient trenja nanosa

Composition	1	2	3	4	5
R_a/μm	3.553	3.437	4.443	3.011	2.346
Hardness (HV)	1028	899	812	1010	1724
Relative density (%)	87.70	88.45	86.00	90.12	92.51
Average friction coefficient	0.142	0.190	0.223	0.144	0.074

The XRD analysis of the starting powders showed that the chromia powder consisted of an eskolaite phase (Cr_2O_3) and the alumina-titania powder of α-Al_2O_3 and anatase. It was also clear from XRD that the chromia coating consists of eskolaite, the chromia-titania coating consists of eskolaite and $Ti_2Cr_2O_7$ and the alumina-titania coating consists mainly of γ-Al_2O_3 with some α-Al_2O_3, Al_2TiO_5, a glassy phase and a small amount of rutile. A very low amount of crystalline TiO_2 indicates that it mostly dissolves in the molten Al_2O_3 [2,8].

The main wear mechanisms of plasma-sprayed ceramic coatings were reported to be a plastic deformation, crack formation and spalling due to fatigue, brittle fracture and material transfer. In the reciprocated dry sliding, wear debris was considerably involved in the wear process in the steady state. The worn surfaces of the Cr_2O_3 and TiO_2 coatings were observed with SEM at different magnitudes (**Figure 1**). In the SEM images the wear scar of the TiO_2 coating was much larger than that of the Cr_2O_3 coating. The Cr_2O_3 coating is the hardest and the most anisotropic among the plasma-sprayed ceramics due to its low interlamellar cohesion; the Al_2O_3-TiO_2 and TiO_2 coatings are the most isotropic but

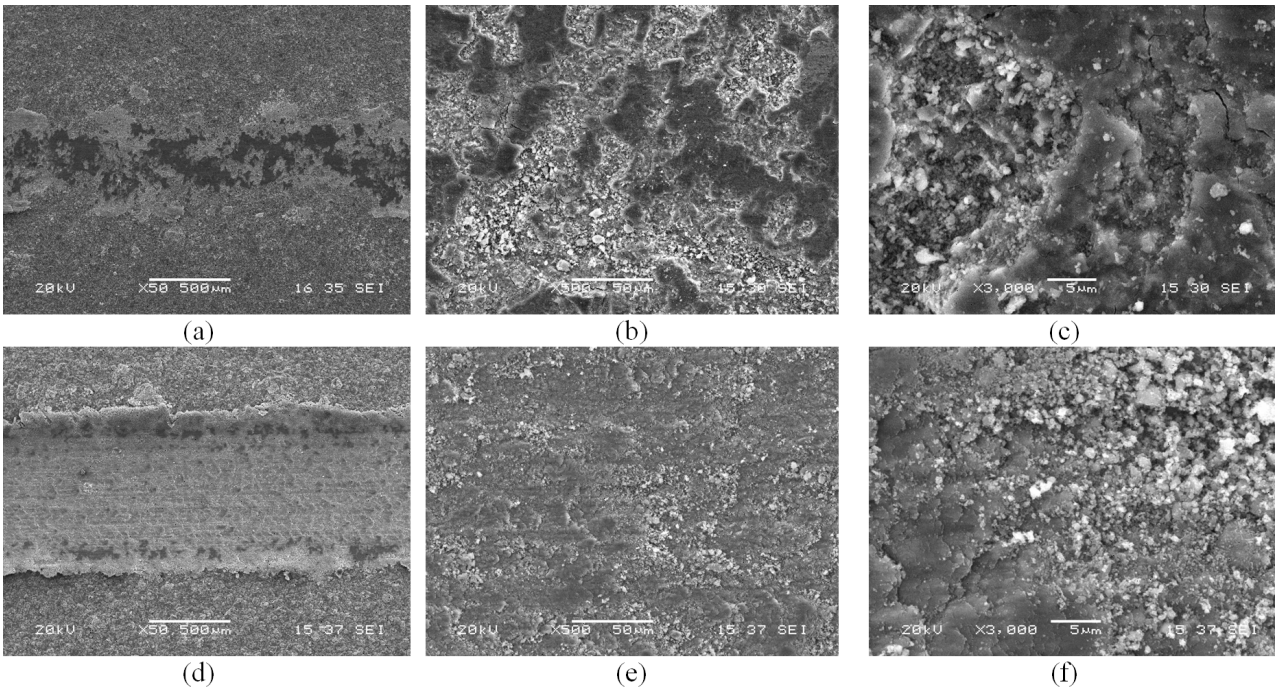

Figure 1: a), b), c) Worn surface morphologies of the Cr_2O_3 and d), e), f) TiO_2 coatings
Slika 1: a), b), c) Morfologija obrabljene površine nanosa Cr_2O_3 in d), e), f) TiO_2

also less hard and less tough due to the formation of an alumina-titania glassy phase which favors intersplat adhesion but turns out to be quite brittle[8]. The smooth film, formed due to a large plastic deformation of the adhered wear debris, strongly influenced the friction and wear behavior. For the plasma-sprayed Cr_2O_3 coatings, similar wear mechanisms were reported under dry sliding conditions and the role of the wear-protective film formed by a plastic deformation of the adhered and compacted debris particles was discussed[9]. The abrasive wear mechanism of the coatings does not only depend on the coating hardness and density, but also on the particle size, the type of the powder used, the coating microstructure, as well as on the microstructural change during a wear testing. The average coarser powder particle size causes an appearance of a significant number of unsmelted particles.

4 CONCLUSIONS

Alumina-titania, titania, chromia and chromia-titania coatings were deposited with APSCT to increase the wear behavior of the aluminium-based shutters. While the friction coefficient and the coating-surface roughness increased with an increase in the titania content, the coating density, hardness and wear resistance decreased.

5 REFERENCES

[1] K. Huang, X. Lin, C. Xie, T. M. Yue, J. Mater. Sci. Technol., 23 (**2007**) 2, 201–206
[2] M. Wang, L. L. Shaw, Surface and Coatings Technology, 202 (**2007**) 1, 34–44
[3] V. P. Singh, A. Sil, R. Jayaganthan, Wear, 272 (**2011**), 149–158
[4] S. Tao, Z. Yin, X. Zhou, C. Ding, Tribology International, 43 (**2010**), 69–75
[5] S. T. Aruna, N. Balaji, J. Shedthi, V. K. W. Grips, Surface & Coatings Technology, 208 (**2012**), 92–100
[6] A. Cellard, V. Garnier, G. Fantozzi, G. Baret, P. Fort, Ceramics International, 35 (**2009**), 913–916
[7] L. L. Shaw, D. Goberman, R. Ren, M. Gell, S. Jiang, Y. Wang, T. D. Xiao, P. R. Strutt, Surface and Coatings Technology, 130 (**2000**) 1, 1–8
[8] G. Bolelli, V. Cannillo, L. Lusvarghi, T. Manfredini, Wear, 261 (**2006**), 1298–1315
[9] H. S. Ahn, O. K. Kwon, Wear, 225–229 (**1999**), 814–824

UDK 536.7:536.65
Original scientific article/Izvirni znanstveni članek

ISSN 1580-2949
MTAEC9, 47(2)185(2013)

CHARACTERIZATION OF SELECTED PHASE-CHANGE MATERIALS FOR A PROPOSED USE IN BUILDING APPLICATIONS

KARAKTERIZACIJA IZBRANIH MATERIALOV S FAZNO PREMENO ZA PREDLAGANO UPORABO V GRADBENIŠTVU

Milan Ostrý[1], Radek Přikryl[2], Pavel Charvát[3]

[1]Brno University of Technology, Faculty of Civil Engineering, Institute of Building Structures, Veveří 95, 602 00 Brno, Czech Republic
[2]Brno University of Technology, Faculty of Chemistry, Purkyňova 464/188, 612 00 Brno, Czech Republic
[3]Brno University of Technology, Faculty of Mechanical Engineering, Technická 2, 616 69 Brno, Czech Republic
ostry.m@fce.vutbr.cz

Prejem rokopisa – received: 2012-09-02; sprejem za objavo – accepted for publication: 2012-09-28

The generally positive trend of ever-stricter requirements for the thermal insulation properties of building envelopes, leading to a significant reduction in the heat losses of modern buildings, has also brought about some negative aspects. Modern light-weight buildings with high-thermal-resistance envelopes are prone to overheating in the summer due to both solar and internal heat gains. This problem is often solved by installing mechanical cooling (air-conditioning) that leads to an increase in the energy consumption and, since electricity is mostly used to power the air-conditioning systems, the increase in the energy consumption for cooling can offset the heating-energy savings in terms of primary energy. A lot of attention has therefore been paid to the other means of temperature control in buildings, such as night-time ventilation and/or the building-integrated thermal storage. The phase-change materials that can store a rather large amount of heat in a narrow temperature interval around their melting point seem to be particularly suitable for this purpose. There are many ways of integrating PCMs into the building structures as well as the techniques that employ that extra thermal-storage capacity to provide thermal comfort for the occupants. This paper deals with the results of the laboratory testing of selected organic and inorganic phase-change materials for integration into building structures. Differential scanning calorimetry was used to obtain the melting ranges and enthalpies of fusion of the selected materials and thermogravimetry was used to explore the thermal stability (decomposition) of the materials at higher temperatures.

Keywords: thermal-energy storage (TES), heat-storage medium, phase-change materials (PCMs), organic materials, inorganic materials, sensible heat storage, latent-heat storage

Splošne pozitivne usmeritve v vedno ostrejše zahteve pri toplotni izolaciji poslopij vodijo k občutnemu zmanjšanju toplotnih izgub modernih zgradb in so prinesle tudi nekaj negativnih vidikov. Moderne, lahke zgradbe, z dobrim izolativnim ovojem so nagnjene k pregrevanju v poletju zaradi sončne in notranje toplote. Ta problem se pogosto rešuje s postavitvijo mehanskega ohlajevanja (air-conditioning), ki povzroči povečanje porabe energije, saj je elektrika najbolj pogosto uporabljena za pogon sistema ohlajanja, vendar pa se s stališča primarne energije povečuje poraba energije za ohlajanje, ki lahko celo preseže prihranke pri energiji za ogrevanje. Mnogo pozornosti je treba zato posvetiti drugim sredstvom za kontrolo temperature v zgradbah, kot so nočna ventilacija in/ali shranjevanje toplote integrirano v zgradbi. Materiali s fazno premeno lahko shranjujejo relativno velike količine toplote v temperaturnem intervalu okrog njihovega tališča in so zato videti posebno primerni za ta namen. Mnogo načinov je za vključitev PCM-materialov v strukturo zgradbe kot tudi tehnike, ki vključujejo shranjevanje ekstra toplotne kapacitete za zagotavljanje udobja stanovalcev. Članek obravnava rezultate laboratorijskih preizkusov izbranih organskih in anorganskih materialov s fazno premeno za njihovo vključitev v strukturo zgradbe. Diferenčna dinamična kalorimetrija je bila uporabljena za določanje področja taljenja in entalpije taljenja izbranih materialov, termogravimetrija pa za raziskovanje toplotne stabilnosti (dekompozicije) materialov pri povišanih temperaturah.

Ključne besede: shranjevanje toplotne energije (TES), sredstvo za shranjevanje toplote, materiali s fazno premeno (PCM), organski materiali, anorganski materiali, smiselno shranjevanje toplote, shranjevanje latentne toplote

1 INTRODUCTION

Thermal-energy storage systems have a wide variety of applications[1]. Heat (cold) can be stored by heating (cooling), melting (solidifying), vaporizing (liquefying) a medium or by reversible thermochemical reactions. Heat-storage media that undergo a phase change during the process of storage and release of energy are called phase-change materials (PCMs)[2]. The thermal-storage capacity of PCMs depends on the specific heat in each state and the latent heat of each phase transformation[3]. A large heat of fusion and the transition temperature in a required range are the two main characteristics determining the suitability of PCMs for a specific application. The determination of the selected properties of PCMs is the most important condition for a correct design of a new application of PCMs in buildings and for a prediction of the influence of the latent-heat storage on an indoor environment and energy savings. In practice there is a lack of reliable information about PCM properties and, therefore, only the results of validated laboratory experiments involving selected PCMs can help the investigators in designing and developing latent-heat storage systems. However, there are some limitations in the use of PCMs[4]:

- PCMs may interact with the building structure and change the properties of the building materials;

- there is a risk of a leakage of PCMs from the building structure;
- PCMs have a rather poor thermal conductivity in the solid state.

These problems are commonly solved with a proper PCM encapsulation.

Salt hydrates, paraffin waxes, fatty acids and eutectics of organic and non-organic compounds are the main categories of PCMs that have been considered for building use during the recent decades.

2 MATERIAL AND METHODS

Only the solid-liquid phase change of a material can be used when a material is integrated in a building structure. In some cases differential scanning calorimetry (DSC) is a standard method for a thermal analysis of PCMs. The most widely used scanning mode includes heating and cooling at a constant rate[5]. This dynamic method is used for the investigation of the melting and solidification enthalpies. **Figure 1** shows the solidification process of PCMs. The evolution of the released heat flux is the function of the external temperature T_{ext}, when this temperature is following a ramp[6]. The shape of the curve depends on the temperature rates. The latent heat of the phase change is calculated from the area under the curve and the external temperature rate that is constant in our case (e.g., 0.1 K min^{-1}, 1 K min^{-1}, 10 K min^{-1}):

$$l_f = \int_{t_1}^{t_2} Q(t)dt = \int_{T_e}^{T_0} Q(T_{ext}) \frac{\partial t}{\partial T_{ext}} = \frac{1}{v_{Text}} A_f \qquad (1)$$

where l_f is the latent heat of the phase transformation (J), Q is the heat flux (W), t is the time (s), T_o is the onset temperature (K), T_e is the end temperature (K), T_{ext} is the external temperature (K), v_{Text} is the external-temperature rate (K s^{-1}) and A_f is the area under the curve and the external-temperature rate (W K^{-1}).

There are inflections of the plotted curve on each side of the heat-flow peak temperature T_p. The onset temperature T_o and the end temperature T_e are the temperatures corresponding with the intersections between the tangents at the inflection points and the base line. The onset temperature and the peak temperature are often used for the characterization of PCMs.

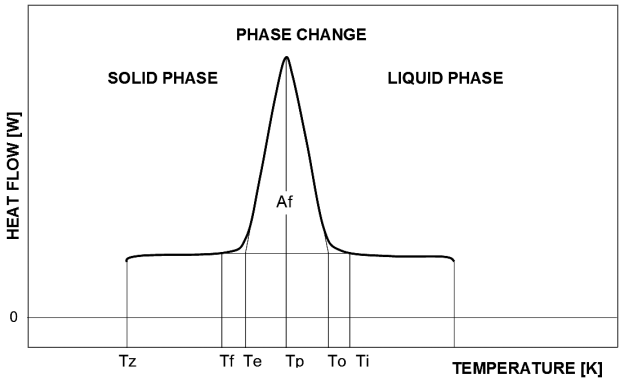

Figure 1: Characteristic temperatures for the solidification process
Slika 1: Značilne temperature pri procesu strjevanja

We have used selected non-commercial and commercial organic- and inorganic-based PCMs in our experiments. The list of selected PCMs is in **Table 1**. Perkin Elmer PYRIS1 DSC, equipped with a cooling device Perkin Elmer Intracooler 2P, was used for determining the thermal properties (the heat of fusion and the melting range). All DSC experiments were carried out at the temperature rate of 0.1 K min^{-1}.

A thermogravimetric apparatus (TGA) Q500 made by TA Instruments was used for the evaluation of the thermal stability of PCMs. The airflow rate was set to be 60 ml min^{-1} and the heating rate was 5 K min^{-1} from the room temperature to 600 °C. An open platinum pan was used as a sample holder. The weight of the samples was approximately 10 mg. The results of TGA determine the suitability of these materials in latent-heat-storage applications because the operating temperature must be below the thermal-decomposition temperatures of PCMs. The proposed operating-temperature range for building application was estimated to be between 18 °C and 30 °C.[7]

Table 1: PCMs tested in laboratory experiments
Tabela 1: PCM, preizkušeni v laboratorijskih preizkusih

Sample	Organic / inorganic	Source
$CaCl_2 \cdot 6H_2O$	inorganic	noncommercial
Parafol 16-97	organic	Sasol
Parafol 18-97	organic	Sasol
SP 22 A17	inorganic	Rubitherm
SP 25 A8	inorganic	Rubitherm
RT 21	organic	Rubitherm
RT 27	organic	Rubitherm
ThermusolHD26	inorganic	Salca

3 RESULTS AND DISCUSSION

Characteristics of all the samples were tested twice. The results in **Tables 2** and **3** represent the average values from both measurements. As already mentioned, all the experiments were carried out at the temperature rate of 0.1 K min^{-1}. Though the experiments carried out

Table 2: Peak temperatures of selected PCMs
Tabela 2: Vrhovi temperature izbranih PCM

Sample	Peak temperature in °C	
	Melting	Solidification
$CaCl_2 \cdot 6H_2O$	29.9	–
Parafol 16-97	18.8	16.1
Parafol 18-97	28.9	27.3
SP 22 A17	22.5	22.4
SP 25 A8	26.6	18.5
RT 21	22.8	22.6
RT 27	27.8	27.6
ThermusolHD26	27.0	21.5

at the temperature rate of 0.1 K min^{-1} take roughly 10 times more time than the experiments at the rate of 1 K min^{-1}, the slower rate was chosen because it is much closer to the real daily swing of indoor air temperature in summer in the rooms with natural ventilation without air-conditioning. PCM-based heat storage integrated in building structures is a way of controlling the indoor air temperature by storing and releasing the thermal energy from the solar radiation or internal heat gains.

Calcium chloride hexahydrate is a non-commercial salt-hydrate PCM. Parafol 16-97 is based on hexadecane, Parafol 18-97 is based on octadecane. Samples SP 22A17 and SP 25 A8 consist of a composition of salt hydrates and organic compounds. Samples RT 21 and RT 27 are based on n-paraffins and waxes. Thermusol HD26 represents a commercial group of salt-hydrate-based PCMs.

Table 3: Heat of fusion of tested PCMs
Tabela 3: Talilna toplota preizkušenih PCM

Sample	Heat of fusion in J g^{-1}	
	Melting	Solidification
$CaCl_2$–$6H_2O$	129.0	–
Parafol 16-97	223.6	–227.4
Parafol 18-97	221.3	–215.5
SP 22 A17	12.3	–11.9
SP 25 A8	71.4	–78.0
RT 21	116.7	–106.7
RT 27	139.7	–139.3
ThermusolHD26	132.4	–132.0

The possibility of a regeneration of PCMs (a rejection of stored heat) at night is very important for the building applications. The PCMs integrated with building structures absorb heat gains during the day and release the absorbed heat at night. If the heat absorbed during one day is not released at night the ability of PCMs to absorb heat the next day is reduced leading to a limited contribution to the room-temperature control. Two systems for the rejection of stored heat were studied at the Brno University of Technology in the past:

- a natural or mechanical ventilation of the indoor space;
- a circuit of cooled air or water integrated with the structure containing a PCM.

Only the PCMs with suitable melting- and solidification-temperature ranges can be used with each of the systems. As can be seen in **Table 2** calcium chloride hexahydrate is suitable only for the naturally ventilated spaces. The indoor temperature in the residential buildings and in the offices must be maintained between 20 °C and 26 °C. But a serious disadvantage of this material is its tendency to supercool during the solidification process. This kind of PCM cannot be used without a modification that reduces the supercooling effect. There are no results from the solidification process just because of the supercooling. On the other hand, Parafol 18-97, RT 27 and Thermusol HD26 could be used for the systems with ventilation of the interior. PCMs absorb cooling loads and release energy in the temperature range between 21 °C and 28 °C. This fact allows for cooling down the indoor environment only to 20 °C to reject the absorbed heat (the regeneration of PCMs). But these systems cannot commonly guarantee thermal comfort in the rooms during very hot summer days.

On the other hand, the temperature of cooled water or air in a separate circuit integrated with the building structures containing PCMs can be kept bellow 20 °C without a negative impact on the thermal comfort of the occupants. This fact allows for the use of the PCMs with a lower solidification range (e.g., SP 22A5 from the tested group).

As can be seen in **Figure 2** the samples of Parafol 16-97 and 18-97 have a very narrow range of melting and solidification temperatures, about 0.3 °C and 0.4 °C. This is an advantage for the short-term storage systems that represent building structures.

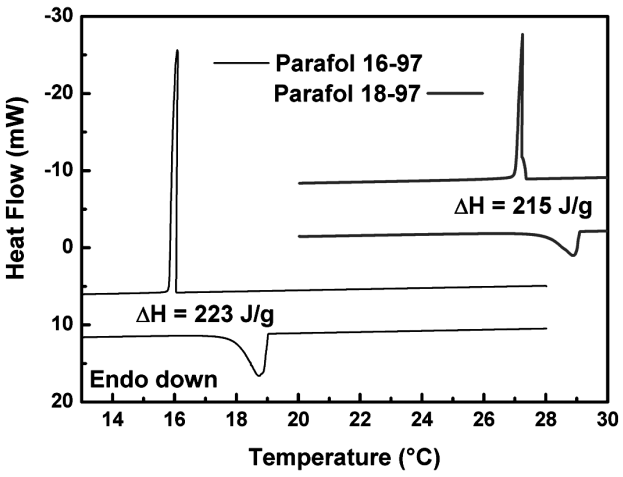

Figure 2: Results of DSC for Parafol 16-97 and Parafol 18-97
Slika 2: Rezultati DSC za Parafol 16-97 in Parafol 18-97

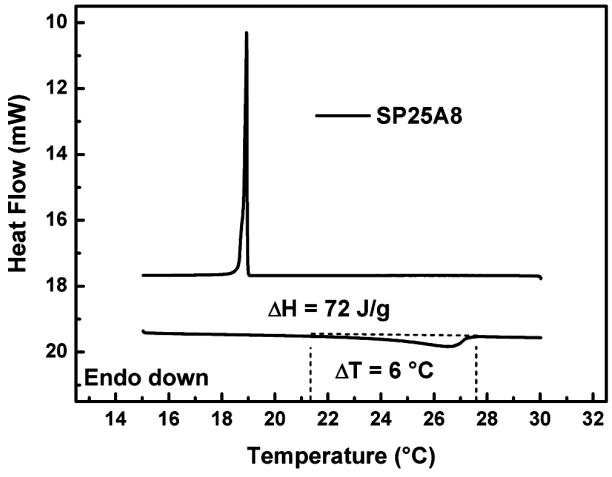

Figure 3: Results of DSC for SP 25A8
Slika 3: Rezultati DSC za SP 25A8

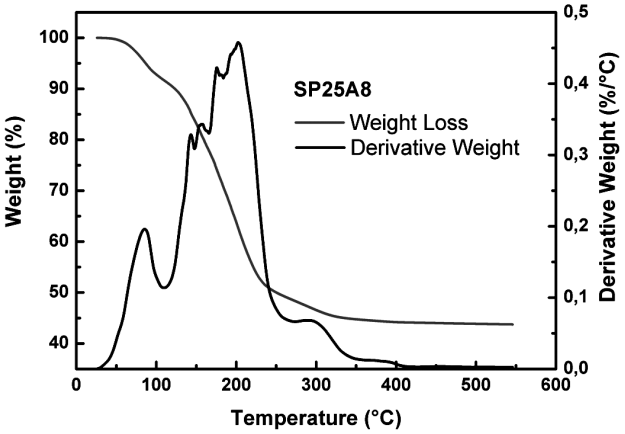

Figure 4: Example of results of a TGA analysis
Slika 4: Primer rezultatov TGA-analize

Compared to the paraffin-based PCMs, the PCMs that are a mixture of salt hydrates and organic compounds, tested in our experiment (**Figure 3**), have a wide range of melting temperatures and a rather narrow temperature range of solidification. This could be an advantage for the systems with a cooled-water loop, because the thermal energy can be slowly stored in a PCM during the day and quickly discharged at night by the cooled-water circuit.

All the materials tested in our experiments are suitable for building application from the point of view of thermal decomposition. The thermal decomposition of all the tested PCMs begins above the expected operation temperatures. The result for the sample composition of salt hydrates and organic compounds is shown in **Figure 4**.

The difficulties may occur with the use of salt-hydrate-based PCMs because of the changes in the water content. This effect was observed during the TGA at low temperatures. Therefore, salt-hydrate-based PCMs must be very tightly sealed in the containers.

4 CONCLUSION

A series of laboratory experiments was carried out to assess the suitability of the selected phase-change materials for the use in built environments. The purpose of a PCM-based building-integrated thermal storage is to contribute to the thermal stability or temperature control in buildings. All the tested materials were found suitable for this purpose from the point of view of thermal decomposition. That was due to rather low operating temperatures (mostly lower than 30 °C in buildings). All the tested materials exhibited the melting ranges that are suitable for building applications. However, the suitability of PCMs for integration with building structures from the point view of melting ranges and enthalpies of fusion depends, particularly, on the type of integrating and the type of rejecting stored heat.

Acknowledgement

This work was supported by the Czech Grant Agency under the project No. P104/12/1838 "Utilization of latent heat storage in phase change materials to reduce primary energy consumption in buildings".

5 REFERENCES

[1] A. Sharma, V. V. Tyagi, C. R. Chen, D. Buddhi, Review on thermal energy storage with phase change materials and applications, Renewable and Sustainable Energy Reviews, 13 (**2009**) 2, 318–345

[2] I. Dinçer, M. A. Rosen, Thermal Energy Storage: Systems and Applications, Chichester: John Wiley & Sons, Ltd., 2002, 579

[3] E. Günther, S. Hiebler, H. Mehling, R. Redlich, International Journal of Thermophysics, 30 (**2009**) 4, 1572–9547

[4] C. Y. Zhao, G. H. Zhang, Review on microencapsulated phase change materials (MEPCMS): Fabrication, characterization and applications, Renewable and Sustainable Energy Reviews, 15 (**2011**) 8, 3813–3832

[5] C. Castellón, E. Günther, H. Mehling, S. Hiebler, L. F. Cabeza, Determination of the enthalpy of PCM as a function of temperature using a heat-flux DSC – A study of different measurement procedures and their accuracy, International Journal of Energy Research, 32 (**2008**) 13, 1258–1265

[6] F. Kuznik, D. David, K. Johannes, J. J. Roux, A review on phase change materials integrated in building walls, Renewable and Sustainable Energy Reviews, 15 (**2011**) 1, 379–391

[7] J. Skramlik, M. Novotny, K. Suhajda, Modeling of diffusion in porous medium, International Conference on Numerical Analysis and Applied Mathematics ICNAAM 2011, Halkidiki, American Institute of Physics, 2011

UDK 519.61/.64:66.017
Original scientific article/Izvirni znanstveni članek

ISSN 1580-2949
MTAEC9, 47(2)189(2013)

IMPROVEMENT OF THE DAMPING PROPERTIES OF CARBON-FIBRE-REINFORCED LAMINATED PLASTICS USING DAMPING LAYERS

IZBOLJŠANJE DUŠENJA Z OGLJIKOVIMI VLAKNI OJAČANE LAMINIRANE PLASTIKE Z UPORABO PLASTI ZA DUŠENJE

Radek Kottner[1], Josef Vacík[2], Robert Zemčík[3]

[1]University of West Bohemia, European Centre of Excellence, New Technologies for Information Society, Univerzitní 22, 30614 Plzeň, Czech Republic
[2]University of West Bohemia, Department of Machine Design, Univerzitní 22, 30614 Plzeň, Czech Republic
[3]University of West Bohemia, Department of Mechanics, Univerzitní 22, 30614 Plzeň, Czech Republic
kottner@kme.zcu.cz

Prejem rokopisa – received: 2012-09-03; sprejem za objavo – accepted for publication: 2012-10-08

A suitable hybrid composite consisting of carbon-fibre-reinforced plastic and damping layers was investigated in terms of damping and natural frequencies using experiments and numerical simulations. The frequency response and the transient response of cantilever beams were analysed. The damping layers made from rubber or from a cork-rubber composite material were used in the investigated hybrid structure. A laser-measurement device and an accelerometer were used for the measurement of the responses. Pareto optimization was performed using three-dimensional numerical simulations with the aim to maximize the fundamental natural frequency and the damping ratio.

Keywords: hybrid, composite, carbon-fibre-reinforced plastic, rubber, damping

Sestavljeni kompozit iz plastike, ojačane z ogljikovimi vlakni in s plastmi za dušenje naravnih frekvenc, je bil preiskovan eksperimentalno in z numerično simulacijo. Analiziran je bil frekvenčni odgovor in prehodni odziv konzolnega nosilca. V preiskovani hibridni strukturi je bila plast za dušenje izdelana iz gume ali sestavljena iz gume in plute. Za meritve odgovora je bil uporabljen laserski merilnik in merilnik pospeška. Z uporabo tridimenzionalne numerične simulacije je bila izvršena Paretova optimizacija za maksimiranje osnovne naravne frekvence in količnika dušenja.

Ključne besede: hibrid, kompozit, z ogljikovimi vlakni ojačana plastika, guma, dušenje

1 INTRODUCTION

Recently, the conventional metallic structures have been replaced with composite structures thanks to their superior dynamic characteristics. For example, a higher specific stiffness of carbon-fibre-reinforced plastics (CFRPs) allows higher natural frequencies of the structures. Furthermore, the damping characteristics of CFRPs have higher values and, moreover, can be improved using an integration of the damping layers[1].

The aim of this work was to develop a suitable hybrid structure in terms of damping and natural frequencies. The investigated samples were the cantilever beams, whose damping layers were made from rubber or from the ACM87 cork-rubber composite material. The damping ratio for their fundamental natural frequency was analyzed.

2 THEORY

The equation of the motion of a damped system is[2]:

$$\boldsymbol{M}\ddot{\boldsymbol{q}} + \boldsymbol{C}\dot{\boldsymbol{q}} + \boldsymbol{K}\boldsymbol{q} = \boldsymbol{f}(t) \tag{1}$$

where $\boldsymbol{q}$[m], $\dot{\boldsymbol{q}}$[m s^{-1}], $\ddot{\boldsymbol{q}}$[m s^{-2}] are the vectors of the generalized coordinates and their 1st and 2nd differentiations with respect to time t; $\boldsymbol{f}$(t)[N] is the vector of the generalized time-dependent applied force; $\boldsymbol{M}$[kg] is the mass matrix of the system; $\boldsymbol{C}$[N s m^{-1}] is the damping matrix and $\boldsymbol{K}$[N m^{-1}] is the stiffness matrix. The motion of the discrete linear systems with a single degree of freedom can be described as:

$$\boldsymbol{m}\ddot{\boldsymbol{q}} + \boldsymbol{c}\dot{\boldsymbol{q}} + \boldsymbol{k}\boldsymbol{q} = \boldsymbol{F}(t) \tag{2}$$

In the case of free oscillations, Equation (2) can be consequently rewritten as:

$$\ddot{q} + 2\zeta\omega_0\dot{q} + \omega_0^2 q = 0 \tag{3}$$

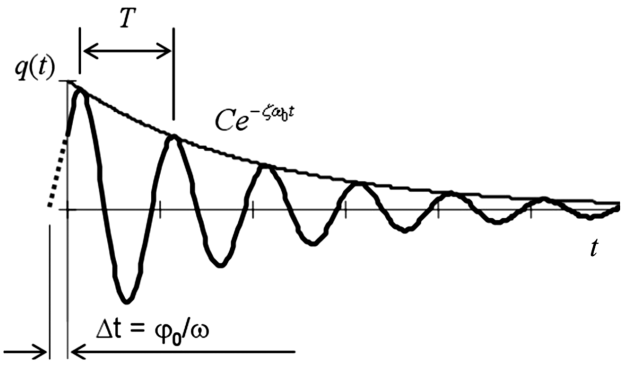

Figure 1: Response of an underdamped harmonic oscillator
Slika 1: Odgovor harmoničnega nedušenja

where the damping ratio ζ and the undamped natural frequency ω_0 are defined as:

$$\zeta = \frac{c}{2\sqrt{mk}} \tag{4}$$

$$\omega_0 = \sqrt{\frac{k}{m}} \tag{5}$$

In the case of an underdamped system ($0 < \zeta < 1$) the solution of Equation (3) representing the displacement of the system can be found in the following form:

$$q(t) = Ce^{-\zeta\omega_0 t}\sin(\omega t + \varphi_0) \tag{6}$$

where C[m] is the amplitude, ω[rad s^{-1}] is the damped natural frequency of the system and φ_0[rad] is the phase shift.

The damped natural frequency can be expressed as:

$$\omega = \omega_0\sqrt{1-\zeta^2} = \frac{2\pi}{T}\,2\pi f \tag{7}$$

where T[s] is the period of the waveform (**Figure 1**) and f is the damped natural frequency in Hertz.

Based on Equation (6), the exponential attenuation rate is then defined as:

$$b = \zeta\omega_0 \tag{8}$$

The damping ratio can be determined using the logarithmic decrement δ, which is defined as the natural logarithm of any two peaks:

$$\delta = \frac{1}{n}\ln\frac{q_0}{q_n} = \ln e^{-\zeta\omega_0 T} = \zeta\omega_0 T = bT = \frac{2\pi\zeta}{\sqrt{1-\zeta^2}} \tag{9}$$

where q_0 is the greater of the two amplitudes and q_n is the amplitude of a peak n periods away. The damping ratio is then found from the logarithmic decrement:

$$\zeta = \frac{\delta}{\sqrt{4\pi^2 - \delta^2}} \tag{10}$$

According to Rayleigh damping, the damping matrix $\boldsymbol{C}$ is given by:

$$\boldsymbol{C} = \alpha\boldsymbol{M} + \beta\boldsymbol{K} \tag{11}$$

where α and β are the Rayleigh constants. Assuming $\alpha = 0$ and the damping ratio ζ of both the CFRP and the damping materials is constant, the Rayleigh constant can be expressed as:

$$\beta = \frac{2\zeta}{\omega} \tag{12}$$

When the difference between the undamped natural frequency ω_0 and the damped natural frequency ω is negligible, the Rayleigh constants of the hybrid composite components can be determined as:

$$\beta_i = \frac{2\zeta_i}{\omega_{0,h}} \tag{13}$$

where ζ_i is the damping ratio of the hybrid composite component (CFRP or the damping material) and $\omega_{0,h}$ is the undamped natural frequency of the hybrid composite determined from the modal analysis.

3 EXPERIMENTS

Two types of CFRP and two types of damping layers were used in the experiments. A linear behaviour of all the materials was assumed. The mechanical properties of the materials are listed in **Tables 1** to **4**.[3] A modal analysis was used for an identification of the elastic-material properties[4].

Two cantilever flat bars consisting of unidirectional 913C-HTS CFRP and rubber were investigated. Sample A had a thickness of 7.8 mm (**Figure 2a**), sample B had a thickness of 12.9 mm (**Figure 2b**). The thickness of 913C-HTS CFRP was 2.7 mm and the thickness of rubber was 2.4 mm. The width of the bars was 19.8 mm, the length was 450 mm and the length of the clamping was 38 mm. The harmonic response after the initial deflection was investigated using an optoNCDT

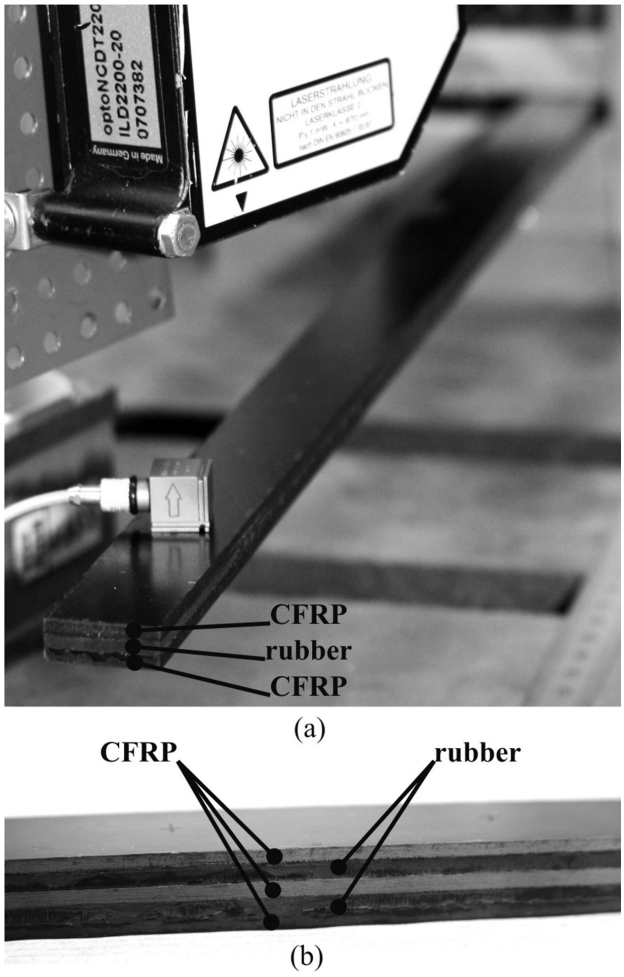

Figure 2: Cantilever flat bar consisting of 913C-HTS CFRP and rubber: a) sample A, b) sample B

Slika 2: Konzolna ploščata palica iz 913C-HTS CFRP in gume: a) vzorec A, b) vzorec B

Figure 3: Cantilever square tube consisting of K63712 CFRP and the ACM87 cork-rubber composite material: sample C
Slika 3: Konzolna kvadratna cev iz K63712 CFRP in ACM87 kompozitnega materiala pluta-guma; vzorec C

laser-measurement device or a Brüel & Kjaer 4507 accelerometer.

Table 1: Mechanical properties of 913C-HTS CFRP
Tabela 1: Mehanske lastnosti 913C-HTS CFRP

Longitudinal modulus	E_1	GPa	104
Transverse modulus	E_2	GPa	5.5
Shear modulus	G_{12}	GPa	2.4
Poisson's ratio	ν_{12}	–	0.34
Density	ρ	kg/m^3	1.500
Damping ratio	ζ	–	0.002

Table 2: Mechanical properties of K63712 CFRP
Tabela 2: Mehanske lastnosti K63712 CFRP

Longitudinal modulus	E_1	GPa	280
Transverse modulus	E_2	GPa	3.5
Shear modulus	G_{12}	GPa	1.7
Poisson's ratio	ν_{12}	–	0.38
Density	ρ	kg/m^3	1.470
Damping ratio	ζ	–	0.003

Table 3: Mechanical properties of rubber
Tabela 3: Mehanske lastnosti gume

Young's modulus	E	MPa	10
Poisson's ratio	ν	–	0.49
Density	ρ	kg/m^3	1 170
Damping ratio	ζ	–	0.072

Table 4: Mechanical properties of the ACM87 composite
Tabela 4: Mehanske lastnosti kompozita ACM87

Young's modulus	E	MPa	2.5
Poisson's ratio	ν	–	0.3
Density	ρ	kg/m^3	740
Damping ratio	ζ	–	0.112

Table 5: Results of the experiments and models
Tabela 5: Rezultati eksperimentov in modelov

	Damped natural frequency f /Hz		Damping ratio ζ	
	Exp.	Model	Exp.	Model
Sample A	35.5	37.8	0.034	0.031
Sample B	44.3	43.8	0.043	0.041
Sample C – clamped	44.0	43.7	0.039	0.004
Sample C – free	548	549	0.005	0.004

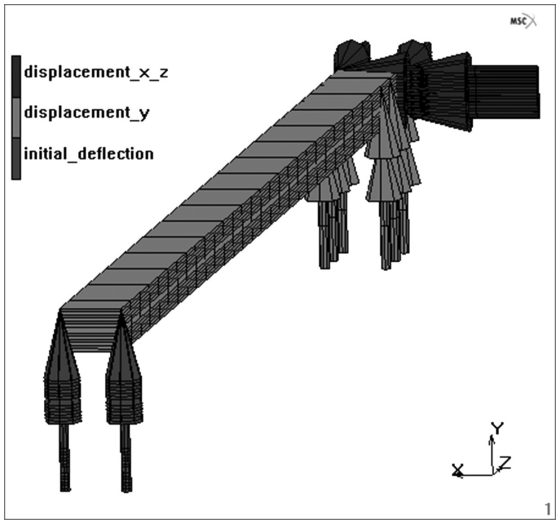

Figure 4: Boundary conditions of a model of a cantilever flat bar
Slika 4: Robni pogoji modela konzolne ploščate palice

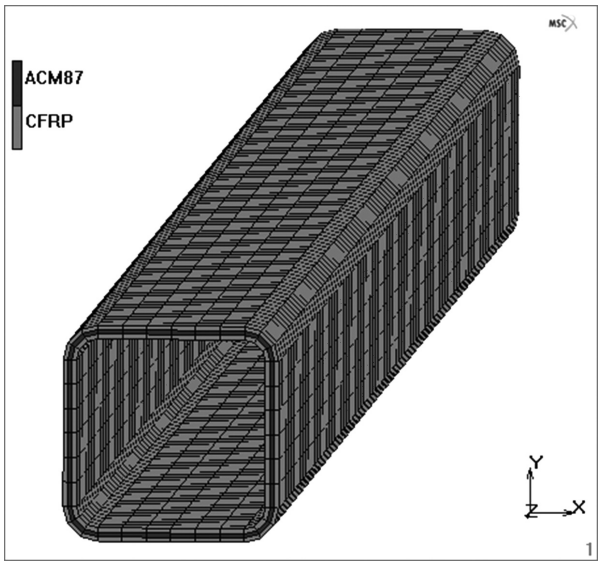

Figure 5: Model of a hybrid square tube
Slika 5: Model hibridne kvadratne cevi

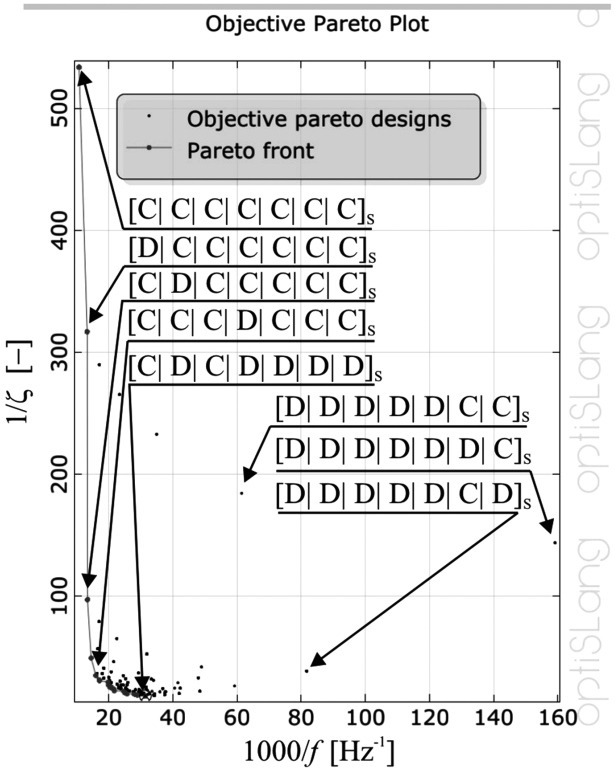

Figure 6: Pareto optimization results, "C" means CFRP, "D" means the damping layer
Slika 6: Rezultati Paretove optimizacije: "C" pomeni CFRP, "D" pomeni plast za dušenje

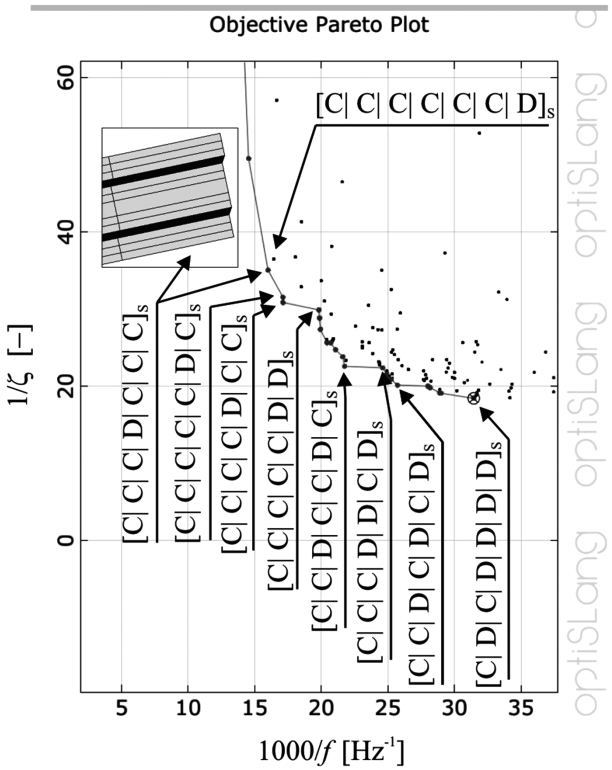

Figure 7: Detail of the Pareto front
Slika 7: Detajl Paretove linije

Further, the response of the cantilever square tube consisting of the wound K63712 CFRP and the ACM87 composite with a thickness of 6.5 mm (**Figure 3**) was investigated (Sample C). The thickness of K63712 CFRP was 2.4 resp. 2.1 mm and the thickness of the ACM87 composite was 2 mm. The width of the square tube was 103 mm, the tube length was 1 490 mm and the length of the clamping was 135 mm. However, the clamping was not sufficiently rigid. Therefore, the damping ratio was investigated also in the case of a free square tube (a tube hung on a rope).

The results are listed in **Table 5**.

4 NUMERICAL SIMULATIONS

Three-dimensional finite-element models were created in MSC.Marc using eight-node brick elements (with an assumed strain option) as shown in **Figures 4** and **5**. The CFRP materials were considered orthotropic and homogenous. The damping materials were considered isotropic and homogenous. The boundary conditions of the models of the cantilever beams are obvious from **Figure 4**. The undamped natural frequencies were obtained with a modal analysis. After an evaluation of the Rayleigh constant using Equation (12), the damped natural frequencies and the damping ratio were obtained with a transient analysis. The Newmark time integration scheme was used.

The created models were validated by comparing the experimental and numerical results listed in **Table 5**. The difference between the results for samples A and B was less than 9 %. In the case of the clamped sample C, the clamping was not sufficiently rigid as already mentioned above. Due to this fact, the damping ratio had a significantly higher value, which was confirmed with the experiment with the free sample C. The difference between the results involving the free sample C was less than 20 %.

A Pareto optimization was performed for the cantilever flat bar with the aim to maximize the fundamental natural frequency and the damping ratio. The analyzed bar was a symmetrical hybrid laminate with 14 layers consisting of 913C-HTS CFRP and rubber. The thickness of the layers was 1 mm and the fibre orientation of the CFRP layers was identical to the beam axis. The width of the bar was 20 mm, the length 450 mm and the length of the clamping was 30 mm. The Pareto front is shown in **Figure 6**, a detail of the front in **Figure 7**. It is obvious from both figures that the situation is very complex; therefore, the problem should be more precisely constrained.

5 CONCLUSION

The performed experiments and numerical simulations showed that the investigated natural frequencies and damping ratios of the hybrid composite structures

strongly depend on the placement of the damping layers in the hybrid cross-sections. The accurate place of the damping layers must be investigated for each application in dependence on the material of the layers, the geometry and the requested ratio between the fundamental natural frequency and the damping ratio.

Acknowledgement

This work was supported by the European Regional Development Fund (ERDF), within the project "NTIS – New Technologies for Information Society", European Centre of Excellence, CZ.1.05/1.1.00/02.0090, and by the research project no. P101/11/0288.

6 REFERENCES

[1] H. Y. Hwang, H. G. Lee, D. G. Lee, Clamping Effects on the Dynamic Characteristics of Composite Machine Tool Structures, Composite Structures, 66 (**2004**), 399–409

[2] V. Zeman, Z. Hlaváč, Kmitání mechanických soustav, ZČU Plzeň, 2004

[3] J. Vacík, V. Lašová, R. Kottner, J. Káňa, Experimental Determination of Damping Characteristics of Hybrid Composite Structure, In: Experimental Stress Analysis, Velké Losiny, Czech Republic, 2010

[4] R. Zemčík, R. Kottner, V. Laš, T. Plundrich, Identification of Material Properties of Quasi-unidirectional Carbon-epoxy Composite Using Modal Analysis, Mater. Tehnol., 43 (**2009**) 5, 257–260

UDK 621.792.3:669.715
Original scientific article/Izvirni znanstveni članek

ISSN 1580-2949
MTAEC9, 47(2)195(2013)

AA413.0 AND AA1050 JOINED WITH FRICTION-STIR WELDING

SPAJANJE ZLITINE AA413.0 IN AA1050 Z GNETENJEM

Sebastjan Kastelic[1,3], Janez Tušek[2], Damjan Klobčar[2], Jožef Medved[3], Primož Mrvar[3]

[1]Institut for Foundry and Heat Treatment, Litostrojska cesta 60, 1000 Ljubljana, Slovenia
[2]University of Ljubljana, Faculty of Mechanical Engineering, Aškerčeva 6, 1000 Ljubljana, Slovenia
[3]University of Ljubljana, Faculty of Natural Sciences and Engineering, Aškerčeva 12, 1000 Ljubljana, Slovenia
kastelic.sebastjan@gmail.com

Prejem rokopisa – received: 2012-09-03; sprejem za objavo – accepted for publication: 2012-10-09

Friction-stir-welding (FSW) technology has been growing since it was patented in 1991 at TWI. Since then the majority of research and industrial applications for joining aluminium alloys were made on wrought aluminium alloys. Lately several investigations have been done in FSW of dissimilar alloys. FSW also has a big potential in the casting industry – especially in high-pressure die casting (HPDC). In this article an investigation of a FSW dissimilar joint made from a casting aluminium alloy (AA413.0) and technically pure aluminium (AA1050) was done. This kind of joint can be used to make an assembled casting, joined with FSW with the aim to have a casting with different material properties or to join HPDC with FSW to assemble a casting with inner cavities.
In this article the temperature distribution of the FSW joint of a cast aluminum alloy and technically pure aluminum is investigated. In the experimental work several FSW parameters were tested: the tool speed, the tool rotation and the position of the tool regarding the joint center. During joining the temperature was measured with a thermocouple and the temperature distribution in steady state was calculated with the FEM program Sysweld. The microstructure and mechanical properties of the joint were investigated.

Keywords: friction-stir welding, AA413.0, AA1050, finite-element method

Spajanje z gnetenjem je tehnologija, ki se intenzivno razvija od patentiranja leta 1991 na Britanskem inštitutu za varjenje. V industrijski praksi je najbolj razširjena uporaba FSW-tehnologije za spajanje gnetnih aluminijevih zlitin. V zadnjem času se raziskave osredinjajo tudi na spajanje dveh različnih zlitin. Spajanje z gnetenjem ima velik potencial tudi v livarski industriji, še posebej pri tlačnem litju. Ta članek opisuje izvedeno eksperimentalno spajanje dveh različnih zlitin. Spojeni sta bili gnetna zlitina AA1050 in livarska zlitina AA413.0. Taki spoji imajo svojo uporabno vrednost pri sestavljenih ulitkih, kjer lahko s spajanjem različnih zlitin z različnimi fizikalnimi lastnostmi dosežemo nehomogene lastnosti sklopa, kjer je to potrebno. S spajanjem tlačnih ulitih delov lahko izdelamo sklope z notranjimi votlimi deli. Lastnosti tako izdelanih sklopov so primerljive z lastnostmi tlačnih ulitkov.
V članku so navedene temperature, izmerjene med spajanjem dveh različnih zlitin. Za določitev optimalnih parametrov spajanja je bilo le-to izvedeno pri različnih vrtljajih orodja in pri različnih hitrostih spajanja. Spoji so bili mehansko analizirani. Stacionarno temperaturno polje med spajanjem dveh različnih zlitin je bilo izračunano s programom Sysweld z metodo končnih elementov.

Ključne besede: spajanje z gnetenjem, AA413.0, AA1050, metoda končnih elementov

1 INTODUCTION

Aluminum die casting alloys are made with a rapid injection of a molten metal into metal molds under high pressure. Such an alloy has a dense and fine grain surface, resulting in excellent wear and fatigue properties. Approximately 85 % of aluminum die casting alloys are based on Al-Si-Cu. These alloys provide a good combination of the cost, strength, and corrosion resistance, together with high fluidities that are required for easy casting. In recent years, aluminum die casting alloys have been widely used in the automotive, electronics, machine and building industries because they are light and recyclable. However, these castings have their limitations arising from the casting-process limitations. This problem can be solved by joining several cast parts into one complex product. The welding of aluminum and its alloys has always represented a great challenge for designers and technologists. Fusion welding of aluminum die casting alloys is difficult due to the formation of welding defects, such as blowholes, and the welding deformation as a result of a high coefficient of thermal expansion of aluminum alloys. As welding defects result in decreased mechanical properties, this problem must be solved for the use in practical applications.[1,2]

From this point of view, friction-stir welding (FSW) was developed as a new joining process by The Welding Institute (TWI) in 1991.[3] The basic concept of FSW is remarkably simple. A non-consumable rotating tool with a specially designed pin and shoulder is inserted into the matching edges of the sheets or plates to be joined and traversed along the line of the joint (**Figure 1**). The tool serves two primary functions, the heating of a workpiece, and the movement of a material to produce the joint. The heating is accomplished by the friction between the tool and the workpiece, creating a plastic deformation of the workpiece. The localized heating softens the material around the pin and a combination of the tool rotation and translation leads to a movement of the material from the

Table 1: Chemical composition of AA1050 and AA413.0 in mass fractions, *w*/%[9]
Tabela 1: Kemijska sestava zlitine AA1050 in AA413.0 v masnih deležih, *w*/%[9]

	Al	Si	Fe	Cu	Mn	Mg	Zn	V
AA1050	99.5	max 0.25	max 0.4	max 0.05	max 0.05	max 0.05	max 0.05	max 0.05
AA413.0	rest	11–13	1.3	1.0	0.35	0.1	0.5	

Table 2: AA1050 and AA413.0 properties[9]
Tabela 2: Fizikalne lastnosti zlitine AA1050 in AA413.0[9]

	Liquidus temp.	Density	Tensile strength	Yield strength	Specific heat	Thermal conductivity	Electrical resistivity
	°C	g/cm^3	MPa	MPa	J/(kg K)	W/(m K)	nΩ m
AA1050	657	2.705	76	28	900	234	27.9
AA413.0	575–585	2.657	290	130	963	121	55.6

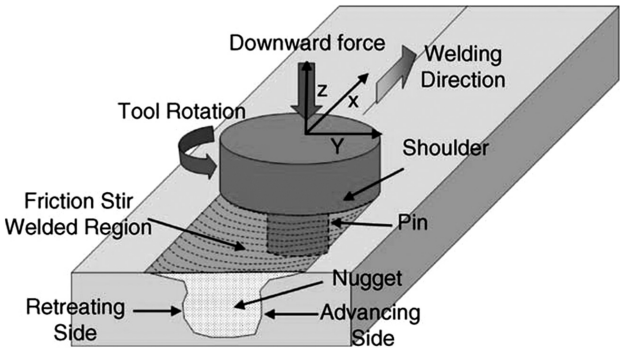

Figure 1: Schematic drawing of friction-stir welding[4]
Slika 1: Shematski prikaz spajanja z gnetenjem[4]

front of the pin to the back of the pin. As a result of this process a joint is produced in solid state. Because of the various geometrical features of the tool, the material movement around the pin can be quite complex. During a FSW process, the material undergoes an intense plastic deformation at an elevated temperature, resulting in a generation of fine and equiaxed recrystallized grains. The fine microstructure of the friction-stir welds produces good mechanical properties.[4,5]

FSW is effective in joining a number of different materials. Until now it has been aluminum alloys that FSW has been most successfully applied to. The reason for this is a combination of the process simplicity and a wide use of aluminum alloys in the mayor industries. FSW can be used for joining aluminum alloys that are difficult to fusion weld. FSW dominates in the fabrication of aluminum components and panels. Now even friction-stir spot welding (FSSW) is being intensively studied.[6,7]

Only a limited number of FSW-joint studies have been done on cast aluminum alloys, although they have been intensively studied.[4,8]

2 EXPERIMENTAL WORK

In this work an investigation of the temperature field of a FSW joint made from two different aluminum alloys has been done. The first alloy is a common cast alloy AA413.0 (AlSi12Cu), the other is made from pure aluminum AA1050 (Al 99.5 %). Such a joint is very interesting because it is made of alloys with different properties. The chemical compositions of AA1050 and AA413.0 are presented in **Tables 1**[9] and **2**[9].

In the experimental work two plates were joined. The joint was made on a milling machine Prvomajska ALG 2008. For this experiment the optimal feeding speed was 235 mm/min and the rotational speed of the tool was 475 min^{-1}. The tool was inclined at an angle of 3° as presented in **Figure 2**. The tool presented in **Figure 3** was made of hot-work tool steel H13. The dimensions of the used tool can be seen in **Figure 4**. The AA1050 alloy was on the retreating side and the AA413.0 alloy was on the advancing side. These parameters were selected on the basis of several tests involving the selected tool, plate thickness and milling-machine gear ratio.

The dimensions of the plates were 380 mm × 60 mm × 6 mm. To each plate a K-type thermocouple was mounted. Thermocouples were connected with the National Instrument CompactDAQ NI 9213 analog digital converter which was connected to the Labview software. The sampling rate was 10 Hz.

During FSW the model temperature distribution was numerically calculated with the Sysweld finite-element modeling software. The FSW module in Sysweld

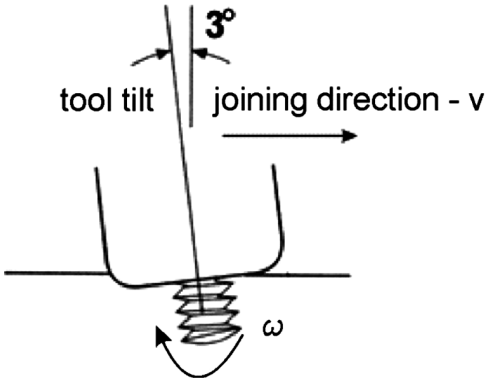

Figure 2: Tool tilt
Slika 2: Nagib orodja

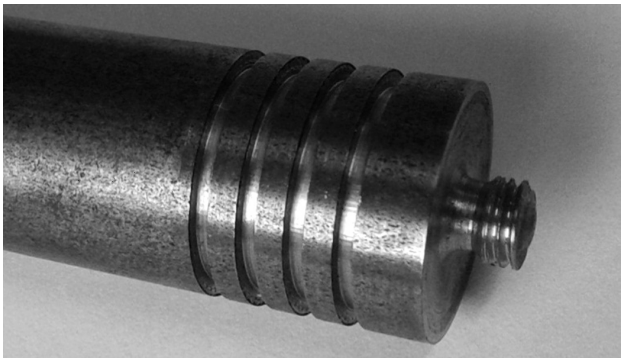

Figure 3: Tool used in the experiment
Slika 3: Orodje, uporabljeno za eksperiment

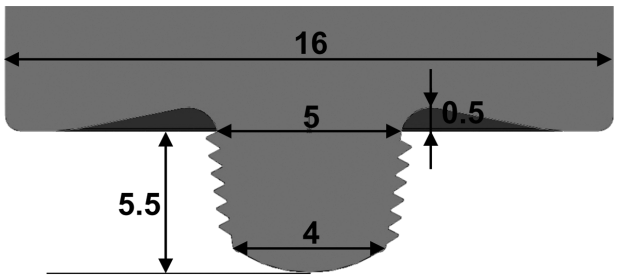

Figure 4: Tool dimensions
Slika 4: Dimenzije orodja

enables a calculation of the steady-state temperature field based on the custom FSW joining parameters for joining the parts of the same alloy[10]. For this experiment the model was upgraded so that the temperature field was calculated on the basis of joining two different alloys. The investigated model had 19277 nodes and the CPU time was two hours.

3 RESULTS AND DISCUSSION

The joint plate is shown in **Figure 5**. Some of the material was extruded during the joining because the plates were not in perfect alignment. The alignment of the plates had a big influence on the joint quality during the testing of the FSW joining parameters; in addition, the slot on the contact surface between the plates must be minimum.

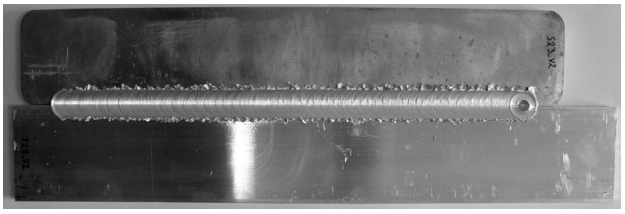

Figure 5: Plates joint with FSW (upper plate of AA413.0 alloy, lower plate of AA1050 alloy)
Slika 5: Plošči, spojeni s FSW-spojem (zgoraj zlitina AA413.0, spodaj zlitina AA1050)

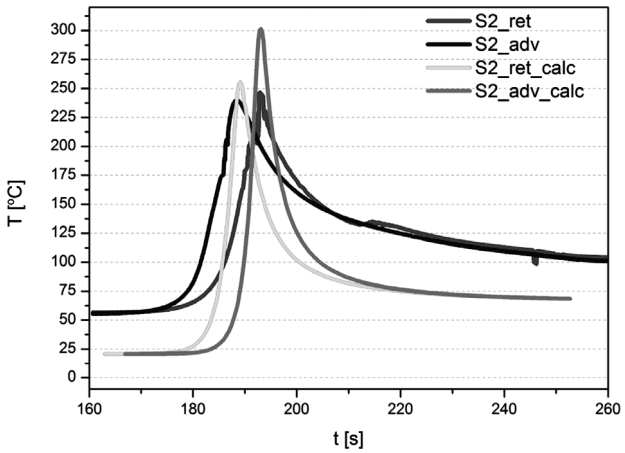

Figure 6: Measured and calculated temperatures in the joint
Slika 6: Izmerjene in izračunane temperature v spoju

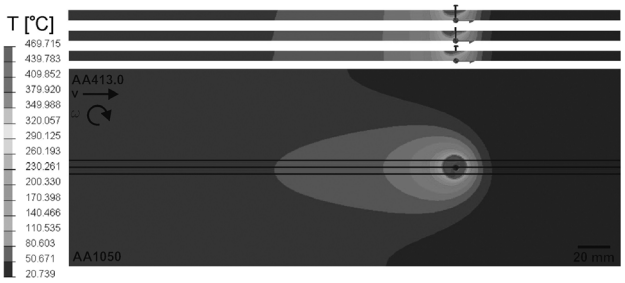

Figure 7: Temperature distribution calculated with the FSW module
Slika 7: Razporeditev temperature, izračunane s FSW-modulom

The temperatures measured with the thermocouples and numerically calculated are presented in **Figure 6**. The maximum temperature measured on the advancing side was 250 °C and on the retreading side of the joint it was 240 °C. Similar temperatures at the thermocouple places were calculated with the FEM software. The maximum calculated temperature in the joint was 470 °C. This temperature and calculated stationary temperature field are presented in **Figure 7**. In the upper part of

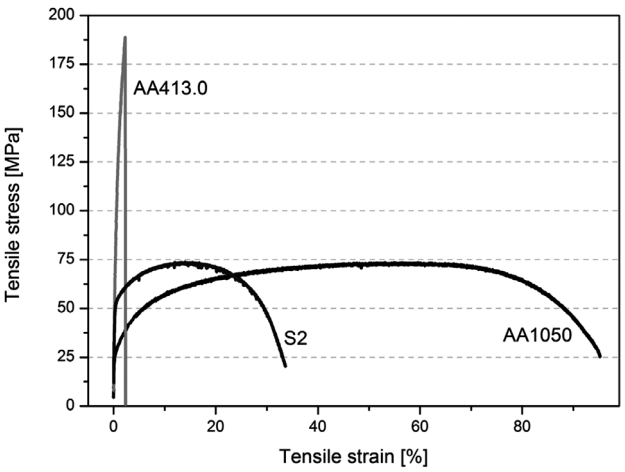

Figure 8: Tensile tests of the alloys and the FSW joint
Slika 8: Natezni preizkusi zlitin in FSW-spoja

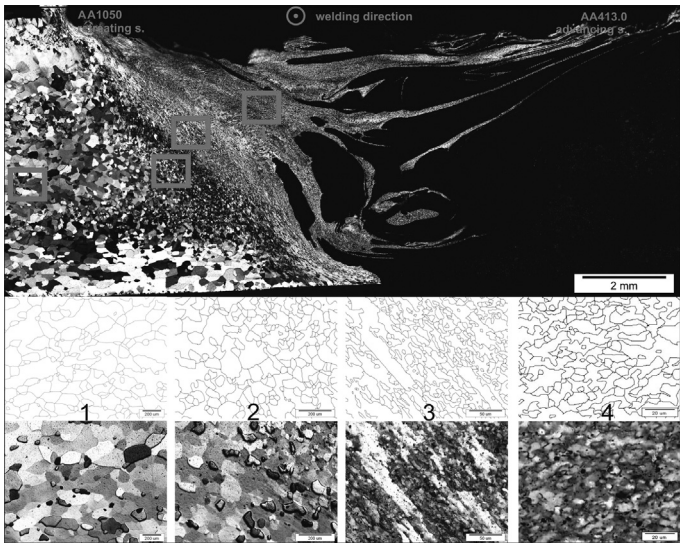

Figure 9: FSW cross-section in the polarolized light and grain size
Slika 9: Prerez FSW-spoja v polarizirani svetlobi in velikost zrn

Figure 7 the temperature field of the joint cross-section can be seen. These measurements show that FSW is a process joining different parts without melting the material. It can be seen that the heat input into the joint is very low. Due to a proper support and good clamping of the plates during FSW, no deformation was found after unclamping.

For a mechanical investigation of the joint, tensile tests were done. The results of the tensile tests of the joined alloys and the FSW joint can be seen in **Figure 8**. A contraction and defect of the joint appeared on the AA1050 alloy. The ultimate tensile stress of the joint was 74 MPa and it was the same as the ultimate tensile stress of the AA1050 alloy. Through the cross-section of the joint the Vickers hardness was measured. The hardness in the AA1050 alloy was 35 HV, 80 HV in the joint and 100 HV in the AA413.0 alloy. Good mechanical properties of the joint can also be seen from the microstructure investigation of the joint presented in **Figure 9**. According to standard ASTM E112 the mean intercept distance in the area marked with 1 was 92.37 μm, in area 2 the mean intercept distance was 44.86 μm, in area 3 the distance was 8.15 μm and in area 4 the distance was 5.56 μm. From the microstructure of the cross-section a good mixing of the used alloys can be seen. The stirring of the pin causes the grain size in the joint to be more than ten times smaller than the grain size in the base AA1050 alloy.

4 CONCLUSION

FSW has a big potential in joining a casting with other castings and/or extruded or rolled parts. In this article it was shown that the heat input for joining two different alloys with FSW is lower than for the joints made with other conventional welding processes. With the experiment we exactly determined the temperature in the stirring zone and calculated the established temperature field during the FSW process. A lower heat input leads to a small deformation of the workpiece and good mechanical properties of the joint.

The mechanical properties of the joint are better than those of the weaker alloy (AA1050) that was friction-stir welded. The good mechanical properties of the joint can be confirmed with the mean intercept distance between the grains in the joint. In these experiments the optimum FSW parameters for joining the AA413.0 and AA1050 alloys were used. Alloy AA413.0 must be on the advancing side, the tool rotational speed should be 475 min^{-1}, the joining speed should be 235 mm/min and the tool angle is 3°.

5 REFERENCES

[1] M. Ericsson, R. Sandstrom, International Journal of Fatigue, 25 (**2003**), 1379–1387
[2] Y. G. Kim, H. Fujii, T. Tsumura, T. Komazaki, K. Nakata, Materials Letters, 60 (**2006**), 3830–3837
[3] W. M. Thomas, Friction Stir Butt Welding International Patent Application, No. PCT/GB92 Patent Application No. 9125978.8, 1991
[4] R. S. Mishra, Z. Y. Ma, Materials Science and Engineering R, 50 (**2005**), 1–78
[5] S. R. Mishra, M. W. Mahoney, Friction Stir Welding and Processing, ASM International, 2007, 7–35
[6] S. Hirasawa, H. Badarinarayan, K. Okamoto, T. Tomimura, T. Kawanami, Journal of Materials Processing Technology, 210 (**2010**), 1455–1463
[7] M. K. Kulekci, U. Esme, O. Er, Mater. Tehnol., 45 (**2011**) 5, 395–399
[8] Y. G. Kim, H. Fujii, T. Tsumura, T. Komazaki, K. Nakata, Materials Letters, 60 (**2006**), 3830–3837
[9] ASM International: Volume 2, Properties and selection: Nonferous alloys and special-purpose materials, Metals Park, Ohio, 1990
[10] E. Feulvarch, Y. Gooroochurn, F. Boitout, 3D Modelling of Thermo-fluid Flow in Friction Stir Welding. In: Proceedings of the 7th international conference on trends in welding research, Callaway Gardens resort, Pine Mountain, Georgia, USA, 2005

UDK 621.941:004.896
Original scientific article/Izvirni znanstveni članek

ISSN 1580-2949
MTAEC9, 47(2)199(2013)

INCREASING TOOL LIFE DURING TURNING WITH A VARIABLE DEPTH OF CUT

POVEČANJE ZDRŽLJIVOSTI ORODJA PRI STRUŽENJU Z VARIABILNO GLOBINO REZA

Marek Sadílek, Robert Čep, Zuzana Sadílková, Jan Valíček, Lenka Petřkovská

VŠB-Technical University of Ostrava, Faculty of Mechanical Engineering, 17. listopadu 15/2172, 708 33 Ostrava, Czech Republic
marek.sadilek@vsb.cz

Prejem rokopisa – received: 2012-09-05; sprejem za objavo – accepted for publication: 2012-09-27

The article deals with the improvement of cutting-tool durability by using CAD/CAM systems. It proposes new roughing turning cycles where a variable depth of cut is applied. The experimental part verifies theoretical prerequisites when a flange is being machined with a sintered-carbide cutting tool. It compares the turning where the standard roughing cycle is used and the turning where the proposed roughing cycle with a variable depth of cut is applied.

Keywords: variable depth of cut, durability, CAD-CAM systems, turning

Članek obravnava izboljšanje zdržljivosti orodij za odrezavanje z uporabo sistema CAD/CAM. Predlagani so novi cikli grobega struženja, kjer se uporablja spremenljivo globino rezanja. V eksperimentalnem delu so potrjeni teoretični prvi pogoji pri struženju prirobnice z rezilnim orodjem iz sintranih karbidov. Primerjano je struženje, kjer je uporabljen standarden cikel odrezavanja, s tistim struženjem, kjer je uporabljen predlagan cikel odrezavanja s spremenljivo globino rezanja.

Ključne besede: spremenljiva globina rezanja, zdržljivost, sistem CAD-CAM, struženje

1 SUPPOSED PROCESS OF TOOL WEAR

Tool wear depends on numerous factors, for example: workpiece material, tool material and geometry, cutting parameters (cutting speed, feed, cutting depth), used process liquid, cutting machine and many others[1].

It is proved that cutting the depth does not have the greatest influence. Since it has its share in the intensity of tool wear (a growing cutting depth increases the tool wear as well) it makes sense to deal with cutting depth and we can consider it as a significant factor of tool wear.

1.1 Tool wear of a selected type of cutting tools

The most used cutting materials in the area of CNC machining are sintered carbide and cutting ceramics[2,3]. As seen in **Figure 1**, the tool-wear method depends on the applied tool materials. The tool wear of the cutting ceramics is rather linear without any marked stepped increases. The tool wear will therefore grow with an increasing depth of cut. It is, thus, not advisable to apply a variable depth of cut to the ceramics with such behavior. The types of cutting ceramics, such as the nitride ceramics, in which a more pronounced notch on the back is formed during the machining may be used exceptionally[4,5].

Sintered carbide tends to form a pronounced notch on the face and main back. This notch could be very advantageously used in the roughing cycles with a variable depth of cut. Efforts will be made to distribute this pronounced notch over the maximum possible length of the tool's cutting edge.

Figure 2 below describes the used marking of the tool wear according to ISO 3685.[6]

In applying a variable depth of cut (in the sintered carbide) the durability-improvement effect is expected to occur in the cutting edge provided the wear shaped as a notch on the back is distributed over the longer part of the cutting edge. These prerequisites were verified with the experiments during the practical machining of the concerned part – the flange.

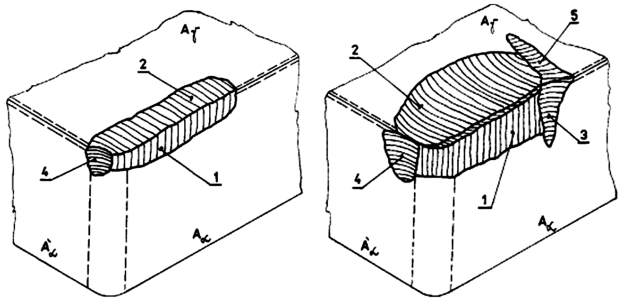

1 – surface of wear on the back
2 – crater wear
3 – notch wear on the main back
4 – notch wear on the minor back
5 – notch on the face

$A\alpha$ – main back
$A\alpha'$ – minor back
$A\gamma$ – face

Figure 1: Cutting-ceramics wear process and the tool-wear process of sintered carbides[4,5]

Slika 1: Proces obrabe rezilne keramike in obrabe orodja iz sintranih karbidov[4,5]

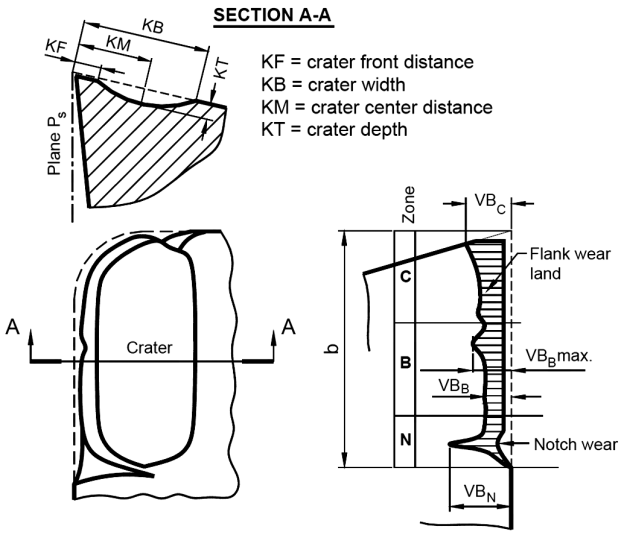

Figure 2: Tool wear according to ISO 3685:1993 [6]
Slika 2: Obraba orodja skladno z ISO 3685:1993 [6]

Both types of the cutting material were tested in practice by experimental machining of the selected turning parts. The theoretical assumption that the cutting ceramic does not tend to form a notch on the back was proven and it is essential for this tool-life improvement method. That is why only the experimental works where sintered carbide is used are stated below.

2 POSSIBILITIES OF A ROUGHING TOOL PATH IN CAM SYSTEMS

The basic types of the used machining cycles and operating stages for the 2-axis turning are as follows:

- straight (rectangle) turning,
- face turning,
- rough turning,
- finish turning,
- profile turning,
- groove turning,
- pocket turning,
- thread turning,
- hole machining,
- parting off (cutting off),
- rest cycle (residual turning),
- hand setting of tool motion.

The conventional roughing cycles in turning, where a cutting tool performs a constant depth of cut can be adapted and extended with the cycles when the tool cuts with a variable depth of cut. The proposed roughing cycles are as follows:

- rough cycle "decreasing of engagement" (**Figure 3**),
- roughing by creating a conical surface,
- roughing with the use of nonlinear methods, etc.

Figure 4 depicts a commonly used roughing cycle. A constant depth of cut is used in this roughing cycle. The machining process results in the wear that prevails in one point of the cutting edge only.

During the roughing strategy – the cut decrement – each chip removal is performed with a different depth of cut so a different cutting part of the tool is under stress during each cutting operation. This method of machining can be time-consuming due to several passes. This is compensated for by an increased tool life, a lower loading of the machine spindle and a reduced machine noise. The depth of cut is reduced when the final diameter is being approached. The maximum wear point is therefore moved outwards from the cut, prolonging the cutting-tool durability. This type of roughing cycle is already contained in the advanced CAM systems (EdgeCAM,

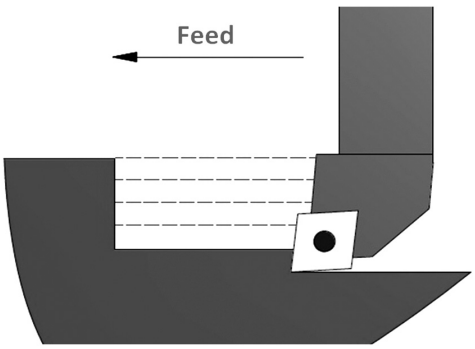

Figure 4: Roughing cycle with a constant depth of cut
Slika 4: Cikel odvzemanja s konstantno globino reza

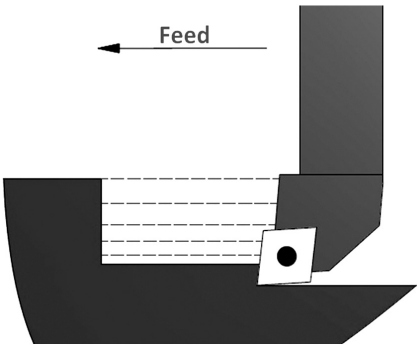

Figure 3: Roughing cycle – a decreased cut
Slika 3: Cikel odvzemanja – zmanjševanje odvzema

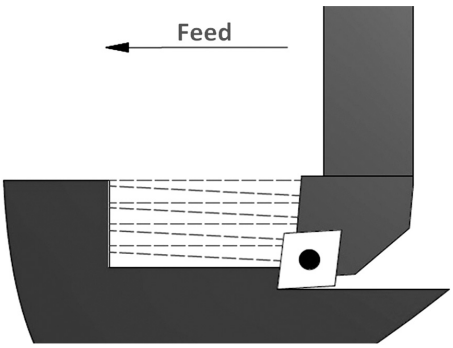

Figure 5: Roughing cycle creating a conical surface
Slika 5: Cikel odvzemanja, pri katerem nastaja konična površina

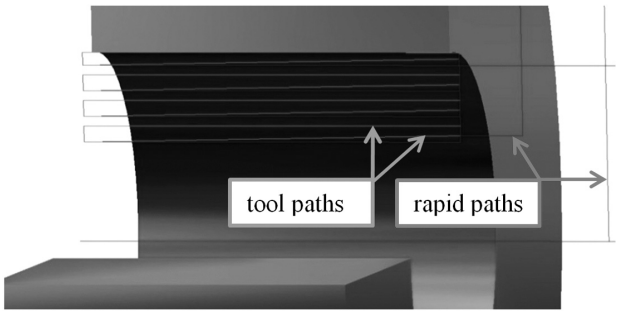

Figure 6: Roughing-cycle simulation when a conical surface is made during an internal turning
Slika 6: Simulacija cikla odvzemanja, pri katerem nastaja konična površina pri notranjem struženju

turning to profile). An application of this feature, when longer parts are turned, is advantageous for the elimination of the ever-decreasing workpiece stiffness.

The cutting, with which a conical surface is formed, starts with the deepest depth of cut which decreases in the feeding direction, as shown in **Figure 5**. The second cut is programmed to be parallel with the workpiece axis. This provides for an efficient removal of the conical surface formed in the previous cut. Thanks to this strategy, the tool wear moves along the cutting edge from the maximum to the minimum depth of cut (a_{pmax} to a_{pmin}). **Figure 6** shows a simulation of the machining (a programmed tool path) when turning the flanges, for which the experimental part was done.

The non-linear roughing-cycle method also ensures a variable depth of cut. For example, a tool path's wavy profile (**Figure 7**) will achieve the same effect as the previous methods. During both the first and the second cut, the machined material is on a gradual increase and decrease and a variable depth of cut is thereby achieved. It is also possible to shift the machined surface and, in doing so, change the depth of cut. However, this requires an advanced CAD/CAM system joined with the CNC cutting machines.

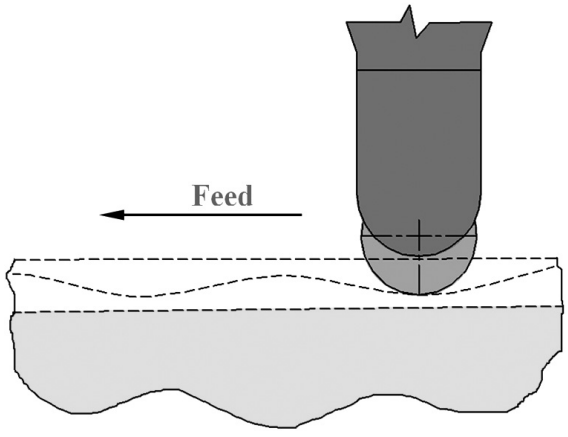

Figure 7: Roughing cycle – the nonlinear method
Slika 7: Cikel odvzemanja – nelinearna metoda

3 EXPERIMENTAL WORK

Two strategies were used during turning: the conventional method with a constant depth of cut and the cone-forming machining.

3.1 Experimental characterization

The verification of theoretical presumptions was carried out in practice. For this purpose we used the following cutting machine: Mori Seiki SL – 65 B with the drive system Fanuc and the spindle power of P = 71 kW. The worpiece material was the austenitic stainless steel 1.4401 that corresponds to DIN X5CrNiMo17-2-2 with a hardness of 180 HB. This material is mainly used in chemical industry, apparatus engineering, pulp industry and food industry. The dimensions of the worpiece (the flange) were as follows: its external diameter D = 350 mm, internal diameter d_1 = 56 mm, length L = 73 mm and the internal diameter of the semi-product before finishing d_2 = 157 mm. The cutting tool was an internal radius turning tool (the Sandvik company) with the cutting inserts: CNMG 12 04 12 – MR 2025 with the CVD coating. This tool is suitable for longitudinal medium roughing and roughing. During the cutting the cutting fluid was used. The cutting conditions differed only in the cut size and depth shape, as shown in **Table1**.

The different depths of cut (stock removals) in the internal roughing cycle are shown in **Figure 8**.

Here a gradual removal of the material from the first tool path to the last one (n^{th}) is shown. The total number of tool paths (n) depends on the size of the workpiece and the technological possibilities of the insert as well.

A representative sample of the tool wear has been selected from all of the performed experiments focusing

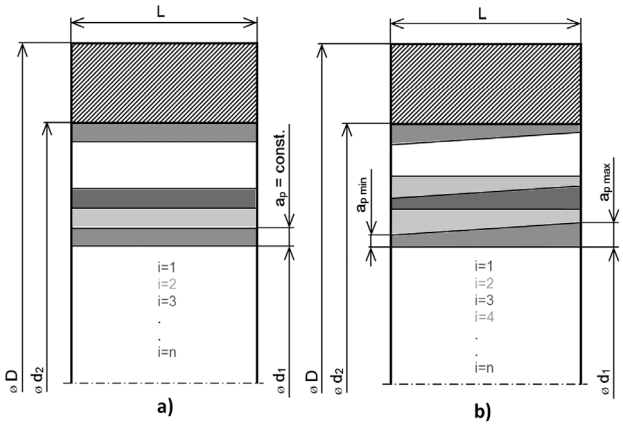

Figure 8: Tool paths: a) a constant depth of cut, b) a variable depth of cut (i <1,n> = number of tool paths; n = total number of tool paths; L, D, d_1 = dimensions of the workpiece; L, D, d_2 = dimensions of the semi-product before finishing)
Slika 8: Poti orodja: a) konstantna globina reza, b) spremenljiva globina reza (i <1,n> = število poti orodja, n = celotno število poti orodja, L, D, d_1 = dimenzije obdelovanca, L, D, d_2 = dimenzije nedokončanega polproizvoda)

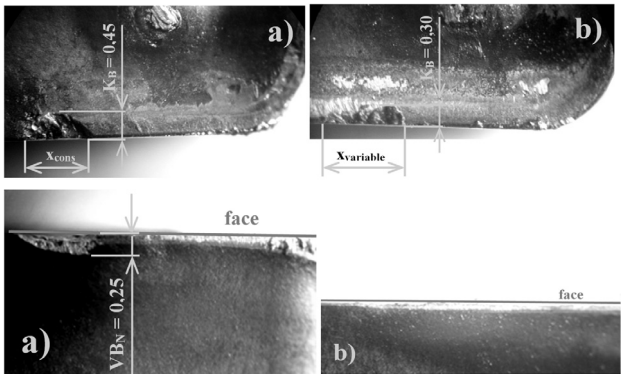

Figure 9: Comparison of the tool-face and back wear: a) a constant depth of cut, b) a variable depth of cut
Slika 9: Primerjava obrabe čela in začelja orodja: a) konstantna globina reza, b) spremenljiva globina reza

Table 1: Cutting conditions: the constant-depth-of-cut strategy and the conical-surface strategy
Tabela 1: Pogoji rezanja: strategija s konstantno globino rezanja in strategija s konično površino

Cutting conditions			rough turning	
			constant depth of cut	variable depth of cut
cutting speed	v_c	m min^{-1}	180	180
feed	f	mm r^{-1}	0.3	0.3
depth of cut	a_p	mm	4	a_{pmin} = 3 a_{pmin} = 5

on the wear in the form of a notch on the face and on the back.

With regard to the measurement during the production, the tool wear was measured with a microscope with an installed digital camera. To read the wear values the Micrometrics SE Premium software, version 7.2, was used.

The upper part of **Figure 9** shows the tool wear on the face. The lower part of the same figure shows the tool wear on the back. The strategy with a constant depth of cut reports, for the same period of time (machining time t = 18.6 min), a greater tool wear than the strategy with a variable depth of cut.

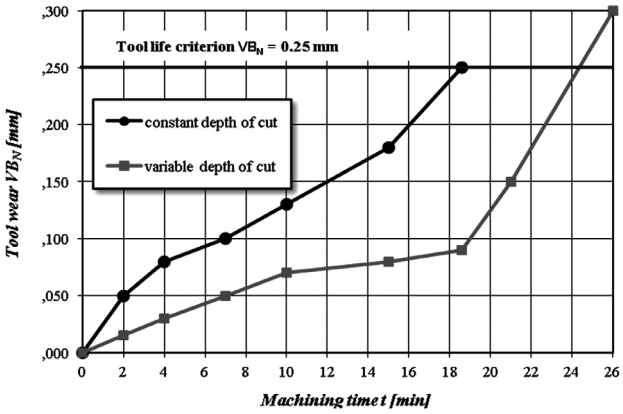

Figure 10: Dependence of the VB_N tool wear on time under the roughing strategy – a constant depth of cut and a variable depth of cut
Slika 10: Odvisnost obrabe VB_N orodja od časa odrezavanja – konstantna globina reza in spremenljiva globina reza

Figure 9 reveals a visible notch on the face (with the length x_{cons} of 1.03 mm) and on the back formed while using the constant depth of cut. The notch wear on the face is greater than in the case of the strategy with a variable a_p. There is also a visible notch on the back, VB_N = 0.25 mm. The strategy using a variable depth of cut causes no notch on the back, as shown in **Figure 9**, the bottom b part).

With the variable depth of cut, the notches are distributed over the tool's longer cutting edge corresponding to the variable depth of cut. The notches shift in relation to the changing depth of cut (from 3 mm to 5 mm depth of cut), $x_{variable}$ = 1.49 mm.

The dependence of the tool wear on time was recorded and entered into the "Dependence of VB_N tool wear on time" chart, as shown in **Figure 10.** The cutting process was interrupted in order to measure the tool wear after the tool path (between the cuts) so as not to disturb the cutting process by starting a cut and getting out of a cut and the measuring interval was kept to last for about 2 min.

This chart clearly implies that the roughing method with a variable depth of cut causes a lower wear VB_N in the same time and under the same cutting conditions. The wear has a slighter inclination in the second area of the chart (in this area the tool wear increases uniformly). The tool wear criterion was set to be VB_N = 0.25 mm.

The durability of the cutting edge in the roughing cycle with a constant depth of cut was, on average, 18 min. In the newly designed cycle with a variable depth of cut, the durability of the cutting edge was 26 min, i.e., the durability increased by 44 %.

4 DISCUSSION AND CONCLUSIONS

The proposed manufacturing technology of the flange and shaft components ensures a reduced tool wear, i.e., an increased turning-tool durability and life. There is a more favorable distribution of wear on the replaceable tool insert when employing the proposed turning technology.

An application of the new roughing cycle resulted in a decrease in the spindle load by 10 %. This reduction was monitored directly on the cutting machine – it was displayed on the indicator of the spindle load.

This change caused a reduction in the energy demand of the machine tool. The roughing cycle with a variable depth of cut was applied in the company of JohnCrane a.s. It gave excellent results in the form of an increased durability of the cutting edge by 44 % in the maintained machining time.

The increased durability of the tool significantly reduces the total costs for the cutting tools. These costs are also reduced by less frequent downtimes when a worn tool is replaced. However, the disadvantage of this

technology is a more complicated tool-path programming for the roughing cycle with a variable depth of cut.

The suggested roughing cycles may not have a positive influence on the machining process. It is necessary to carefully consider all the aspects associated with the proposed cycles. These can include a reduced rigidity of the machine tool caused by both the tool's simultaneous movement in the directions of the two axes and the requirements of the software (CAM system) and the CNC programmer.

Acknowledgement

We would like to thank the company of JohnCrane a.s. for allowing us to perform our experiments. This paper was supported by the Czech Science Foundation, Student Grant Competition (SP2011/23), VSB-Technical University of Ostrava.

5 REFERENCES

[1] A. Antic, B. P. Petrovic, M. Zeljkovic, B. Kosec, J. Hodolic, The influence of tool wear on the chip forming mechanism and tool vibrations, Mater. Tehnol., 46 (**2012**) 3, 279–285

[2] M. Sadílek, R. Čep, I. Budak, M. Sokovic, Aspects of Using Tool Axis Inclination Angle, Strojniški vestnik/Journal of Mechanical Engineering, 57 (**2011**) 9, 681–688

[3] M. Neslušan, I. Mrkvica, R. Čep, D. Kozak, R. Konderla, Deformation After Heat Treatment and Their Influence on Cutting Process, Tehnički vjesnik/Technical Gazette, 18 (**2011**) 4, 601–608

[4] R. Čep, A. Janásek, B. Martinický, M. Sadílek, Cutting tool life tests of ceramic inserts for car engine sleeves, Tehnički vjesnik/Technical Gazette, 18 (**2011**) 2, 203–209

[5] M. Forejt, A. Humár, M. Píška, L. Janíček, Experimental methods – syllabus, University of Technology, Faculty of Mechanical Engineering, Brno, 2003, 83

[6] ISO 3685:1993, Tool-life testing with single-point turning tools, International Organization for Standardization, Geneva, 1993, 48

UDK 543.424.2:621.793:620.3
Original scientific article/Izvirni znanstveni članek

ISSN 1580-2949
MTAEC9, 47(2)205(2013)

RAMAN INVESTIGATION OF SOL-GEL ANTICORROSION COATINGS ON ELECTRONIC BOARDS

RAMANSKE RAZISKAVE SOL-GEL PROTIKOROZIJSKIH PREVLEK NA ELEKTRONSKIH VEZJIH

Aleksander Rauter[1], Matjaž Koželj[1], Lidija Slemenik Perše[1], Angela Šurca Vuk[1], Boris Orel[1], Başak Bengű[2], Onder Sunetci[2]

[1]National Institute of Chemistry, Hajdrihova 19, 1000 Ljubljana, Slovenia
[2]Arcelik R&D, 34950 Cayirova Campus – Tuzla/Istanbul, Turkey
angela.surca.vuk@ki.si

Prejem rokopisa – received: 2012-09-10; sprejem za objavo – accepted for publication: 2012-10-12

Due to its non-destructive character and high spatial resolution, confocal Raman spectroscopy was found to be a good technique for detecting spray-deposited sol-gel coatings on electronic boards (EBs). EBs are demanding substrates to cover because of their non-flat surfaces, containing various metals, alloys, pins and other elements. Nanocomposite coatings were made on the basis of bis end-capped organic-inorganic hybrid precursors, *bis*-(3-(3-(3-triethoxysilyl)propyl)thioureido)propyl terminated polydimethylsiloxane (PDMSTU) and *bis*-[3-(triethoxysilyl)propyl]tetrasulphide (BTESPT), imparting a hydrophobic character to the produced anticorrosion coatings. Reactions of hydrolysis and condensation were initiated with an addition of the 0.1 M HCl catalyst. Nanoparticles were introduced in the sols as trisilanol-heptaisooctyl-polyhedral oligomeric silsesquioxanes (up to 5 nm). The obtained sols were spray deposited on the test substrate, i.e., the aluminium alloy AA 2024, and also on EB. The coatings on AA 2024 were used for potentiodynamic electrochemical and surface (SEM, AFM) characterisation of the prepared coatings. Extensive Raman spectroscopy measurements of the uncovered and covered EBs revealed that the sol-gel coatings on various elements and pins of EBs are clearly visible in the Raman spectra and that this is an appropriate technique for detecting the coatings on such demanding substrates.

Keywords: Raman spectroscopy, sol-gel, electronic boards, anticorrosion coatings, nanoparticles

Glede na nedestruktivni značaj in veliko prostorsko ločljivost ramanske spektroskopije smo to tehniko študirali s stališča možnosti detekcije napršenih sol-gel prevlek na elektronska vezja. Elektronska vezja so zahtevne podlage, kar zadeva njihovo prekrivanje, saj njihova površina ni ravna, na njej se nahajajo različne kovine, zlitine, konice in drugi elementi. Nanokompozitne prevleke smo pripravili na osnovi dvostransko funkcionaliziranih organsko-anorganskih prekurzorjev *bis*-(3-(3-(3-trietoksisilil)propil)tioureido)propil zaključenega poli(dimetilsiloksana) (PDMSTU) in *bis*-[3-(trietoksisilil)propil]tetrasulfida (BTESPT), ki v pripravljene protikorozijske prevleke vneseta hidrofoben značaj. Reakcije hidrolize in kondenzacije smo začeli z dodatkom katalizatorja 0,1 M HCl. Nanodelce smo v sole vključili kot trisilanol-heptaizooktil-poliedrične oligomerne silseskvioksane (do 5 nm). Tako pripravljene sole smo nanesli na preizkusne podlage, in sicer na aluminijevo zlitino AA 2024 in tudi elektronska vezja. Prevleke na AA 2024 smo uporabili za potenciodinamične elektrokemijske meritve in površinsko (SEM, AFM) karakterizacijo. Obširne ramanske meritve nezaščitenih in zaščitenih elektronskih vezij pa so pokazale, da lahko sol-gel prevleke na različnih elementih in konicah elektronskih vezij jasno ugotovimo v ramanskih spektrih in da je zato ta tehnika primerna za detekcijo prevlek na zahtevnih podlagah.

Ključne besede: ramanska spektroskopija, sol-gel, elektronska vezja, protikorozijske prevleke, nanodelci

1 INTRODUCTION

Raman spectroscopy has been recognised as a very useful tool for the investigation of organic and inorganic materials in various fields, for example in art and archaeology[1], for the investigation of electrode materials for lithium electrodes[2] as well as the materials produced from organic-inorganic hybrids[3,4]. Raman spectra show the energy shift of the excitation light (laser) as a product of an inelastic scattering of the molecules in a sample, resulting in obtaining the information about their chemical structure, i.e., Raman spectra represent the fingerprints of the molecules. Moreover, this vibrational technique can be useful for proving the correctness of technological processes[3], for instance, the efficiency of a deposition process for the coatings on various substrates, since it does not require background measurements and is a non-destructive technique. Such complex substrates include, for example, electronic boards (EBs) composed of various materials (metals, alloys, soldering alloys, plastic materials, etc.). Raman spectroscopy can clearly detect sprayed protective coatings on various individual elements of EBs.

Numerous enterprises have realised that the enormous amounts of electronic waste can be reduced with the application of anticorrosion coatings on various electronic components. However, the anticorrosion coatings for EBs must respond to a unique set of corrosion-related problems, since different elements (materials) are positioned in close proximity. This gives rise to a great possibility of galvanic corrosion, the corrosion of contact surfaces and joints or a growth of dendritic silver. In addition, the surfaces of EBs are not flat, so it is difficult to cover them homogeneously with a coating. Nowadays,

conformal paint coatings (parylene, urethane, acrylic, epoxy, etc.) are mostly used for the protection of EBs, but such coatings are expensive and do not usually offer satisfactory adhesion and protection (<10 years)[5]. Many conformal coatings, in particular the widely used acrylic coatings, often delaminate from the corners of the leads and EBs, and develop cracks, in which water may be entrapped, dissolving contaminants. This can result in dendritic growth between the components of the leads, leading to shorts, excessive power consumption and, therefore, EB malfunctions[5].

Nanocomposite barrier coatings prepared from organic-inorganic hybrid precursors, consisting of nanoparticles (SiO_2, Al_2O_3, ZrO_2, ...) or polyhedral oligomeric silsesquioxanes (POSS) are believed to be promising materials for successfully replacing conformal coatings. The preparation of good sol-gel nanocomposite coatings starts with an appropriate selection of precursors, nanoparticles, inhibitors and additives[6]. By introducing the appropriate groups to the composition we can achieve, in addition to the resistance to corrosion, that the sol-gel coatings also provide high oxidation, abrasion and water-resistant properties. In this work, bis end-capped ethoxysilyl-functionalised precursor *bis*-(3-(3-(3-triethoxysilyl)propyl)thioureido)propyl terminated poly(dimethylsiloxane) (PDMSTU in **Figure 1**) was synthesised as the organic-inorganic precursor for sol-gel nanocomposite coatings[7]. This organic-inorganic hybrid precursor also comprises a poly(dimethylsiloxane) chain, which imparts its hydrophobic character to the deposited anticorrosion coatings. The nanoparticles were included as polyhedral oligomeric silsesquioxane trisilanol-heptaisooctyl-POSS (TS-IOc_7-POSS in **Figure 1**), which, due to the open-cage structure, can bind in the sol-gel matrix via a formation of siloxane bonds. Another bis end-capped precursor, i.e., bis-[3-(triethoxysilyl)propyl]tetrasulphide (BTESPT in **Figure 1**), was included in the composition of the sol to increase the siloxane bonding in the coatings. The efficiency of the BTESPT

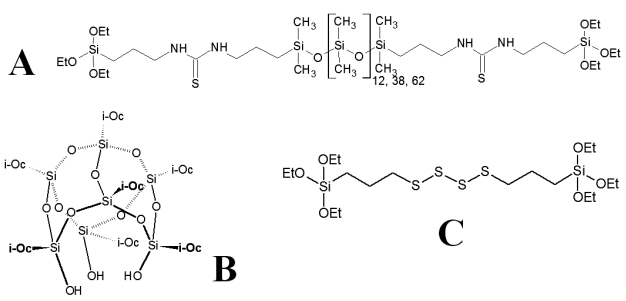

Figure 1: Structures of the precursors for the preparation of sol-gel nanocomposite anticorrosion coatings for EBs: A) *bis*-(3-(3-(3-triethoxysilyl)propyl)thioureido)propyl terminated poly(dimethylsiloxane) (PDMSTU), B) trisilanol-heptaisooctyl-POSS (TS-IOc_7-POSS) and C) *bis*-[3-(triethoxysilyl)propyl]tetrasulphide (BTESPT)

Slika 1: Strukture prekurzorjev za pripravo sol-gel nanokompozitnih protikorozijskih prevlek za elektronska vezja: A) *bis*-(3-(3-(3-trietoksisilil)propil)tioureido)propil zaključen poli(dimetilsiloksan) (PDMSTU), B) trisilanol-heptaizooktil-POSS (TS-IOc_7-POSS) in C) *bis*-[3-(trietoksisilil)propil]tetrasulfid (BTESPT)

coatings for the preparation of anticorrosion coatings for various alloys (AA 2024-T3 [8], AZ31 Mg [9]) has already been demonstrated. In the present paper, we would first like to show that the PDMSTU-based nanocomposite coatings can be applied on EBs with the spray-deposition technique. In addition, the suitability of Raman spectroscopy for detecting deposited coatings on all the different elements of an EB substrate is shown.

2 EXPERIMENTAL WORK

The organic-inorganic hybrid precursor *bis*-(3-(3-(3-triethoxysilyl)propyl)thioureido)propyl terminated polydimethylsiloxane (PDMSTU) was synthesised from aminopropyl terminated poly(dimethylsiloxane) 1000 (PDMS 1000)[7]. 23 g of PDMS 1000 was dissolved in 40 ml of tetrahydrofurane and 12.5 g of (3-isotiocianatopropyl)triethoxysilane was then added dropwise. The solution was refluxed for 2 days and the progress of the reaction was followed using FT-IR spectroscopy. After the conclusion of the reaction, tetrahydrofurane was removed *in vacuo* and a highly viscous yellow PDMSTU product was obtained.

The sol for the spray deposition on the EB substrate was prepared in ethanol by mixing PDMSTU : BTESPT : TS-IOc_7-POSS in a molar ratio of 1 : 2 : 0.5. As a catalyst of the sol-gel reactions, 0.1 M hydrochloric acid was applied in a molar ratio of PDMSTU : 0.1 M HCl = 1 : 18, based on the number of ethoxy groups in the PDMSTU and BTESPT precursor molecules. The sol was stirred for 4 days before spraying on the EB substrate. The time of the application was determined by following the hydrolysis and condensation reactions using FT-IR measurements (not shown). The sol gelled in ten days. For a comparison between morphological properties (SEM, AFM) and electrochemical measurements, the PDMSTU-based coating was deposited on the aluminium alloy AA 2024, also using the spray-deposition technique. Prior to spraying the sol on AA 2024, the substrate was polished and cleaned in hexane, acetone, methanol and distilled water. The deposited coating was thermally treated at 150 °C for half an hour prior to the treatment.

SEM micrographs were recorded on a FE-SEM Supra 35 VP electron scanning microscope.

An electrochemical potentiodynamic measurement of the PDMSTU-based coating deposited on the AA 2024 substrate was recorded on a PGSTAT 302N potentiostat-galvanostat. The coating was mounted as the working electrode in a K0235 flat cell (Princeton Applied Research) filled with 0.5 M NaCl. The reference electrode was a saturated Ag/AgCl electrode and the counter electrode was the Pt grid. The samples were held at an open circuit potential for 1800 s prior to scanning the potential with a scan rate of 0.5 mV/s from –0.9 V to –0.2 V.

Raman spectra of the uncovered and covered EB were collected using a confocal Raman spectrometer WITec alpha 300, combined with the AFM and SNOM (Scanning Near-Field Optical Microscopy) techniques. The excitation line used was 532 nm.

3 RESULTS AND DISCUSSION

The SEM micrograph revealed a homogeneous surface of the PDMSTU-based coating, but some defects on the surface can also be observed (**Figure 2**). AFM, on the other hand, confirmed the nanocomposite character of the coating, with a roughness factor of 110 nm (**Figure 3**).

A potentiodynamic measurement of the spray-deposited PDMSTU-based coating on AA 2024 revealed a cathodic current density that is lower, by about two decades of magnitude, than that of the pure AA 2024 substrate (**Figure 4**). Moreover, the anodic current density was lower by about one to two orders of magnitude (**Figure 4**). These values are comparable to those of the anticorrosion coatings prepared by dip-coating on the AA 2024 substrates from 1 % sols of bis-(3-(3-(3-triethoxysilyl)propyl)ureido)propyl terminated polydimethylsiloxane (PDMSU)[10], i.e., a similar precursor with the urea instead of thiourea groups between the poly(dimethylsiloxane) and ethoxysilylpropyl parts of the molecule (**Figure 1**). The PDMSU coatings, on the other hand, showed a better performance when prepared from more concentrated, 4 %, sols, i.e., the sols with an increasing thickness confirming their physical barrier character. Moreover, our PDMSTU-based coatings revealed superior properties compared to the pure BTESPT coatings made from water/ethanol solutions[8]. Specifically, the hydrophobic BTESPT coatings revealed a decrease of about one order of magnitude in the cathodic current density and of about 1–2 orders of magnitude in the anodic current density. A decrease in the cathodic current density of one order of magnitude in relation to the response of the pure AA 2024 substrate was also observed for the ethoxysilyl-functionalised POSS compounds, enabling a formation of compact tri-dimensional networks of regular POSS cubes via sol-gel reactions[11]. However, the addition of perfluoropropyl groups to the structure of these POSS compounds increased the reduction in the cathodic current density, even to above two orders of magnitude[12], which is superior to that of our PDMSTU-based coatings. The contact-angle measurements showed that poly(dimethylsiloxane) chains introduced some of the hydrophobic character to the PDMSTU-based coatings; the contact angle for water was 97° for the coatings on AA 2024 in the initial state and the surface-energy value was 32.1 mJ/m^2. The value was higher than the surface-energy values for the coatings prepared from PDMSU (29.7 mJ/m^2) [10], ethoxysilyl-functionalised POSS (28.7 mJ/m^2) [11] and perfluoropropyl ethoxysilyl-func-

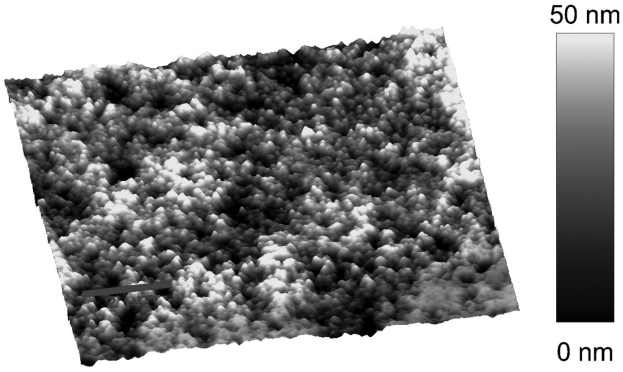

Figure 3: AFM image of the spray-deposited PDMSTU-based coating on AA 2024

Slika 3: AFM-posnetek prevleke, pripravljene na osnovi PDMSTU in napršene na podlago AA 2024

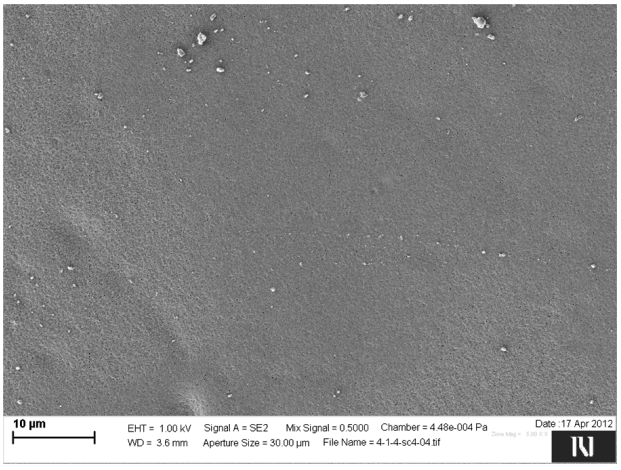

Figure 2: SEM micrograph of the spray-deposited PDMSTU-based coating on AA 2024

Slika 2: SEM-posnetek prevleke, pripravljene na osnovi PDMSTU in napršene na podlago AA 2024

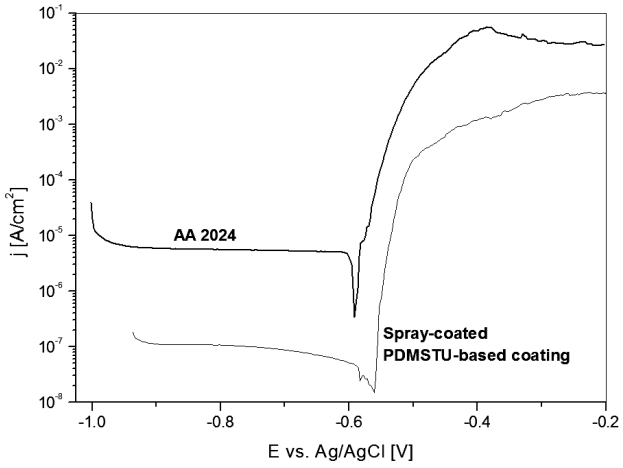

Figure 4: Potentiodynamic measurement of the spray-deposited PDMSTU-based coating on AA 2024

Slika 4: Potenciodinamične meritve prevleke, pripravljene na osnovi PDMSTU in napršene na podlago AA 2024

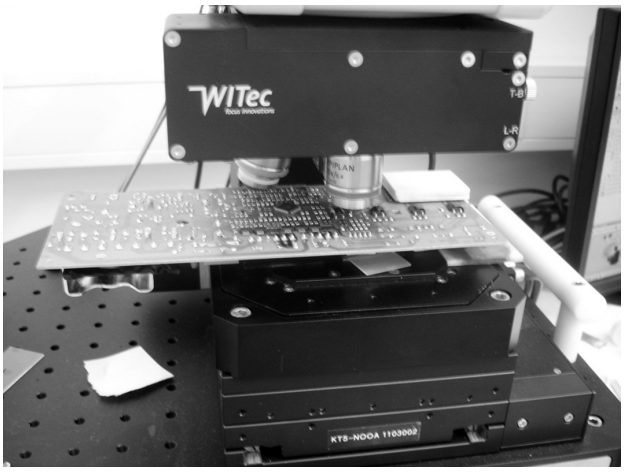

Figure 5: Measurement of the Raman spectra on the uncoated and coated EB substrate
Slika 5: Merjenje ramanskih spektrov nezaščitenega in zaščitenega elektronskega vezja

tionalised POSS (12.4 mJ/m^2) [12]. Since a good corrosion inhibition can be partly ascribed to the low surface value of the anticorrosion coatings, the coatings with the perfluoropropyl groups have been found to be the best in this respect. For comparison, the contact angle for water of the AA 2024 substrate was 86° and the surface-energy value was 37.1 mJ/m^2, respectively.

The most critical issue in the preparation of the anticorrosion coatings for EBs, apart from the development of the coatings' composition, is the coverage of all the elements (except the specific connectors that are masked during the spray deposition of a coating) on the non-flat EB surfaces. The coverage of pins often remains questionable, since the coating solutions may tend to flow down the slopes. When the sols exhibit proper rheological properties, this effect of sagging is prevented and all the elements are efficiently covered by the coating. Such defects in coverage can certainly be recognised during various end industrial application tests, but these are time consuming and costly. The proposed Raman spectroscopy is a more straightforward

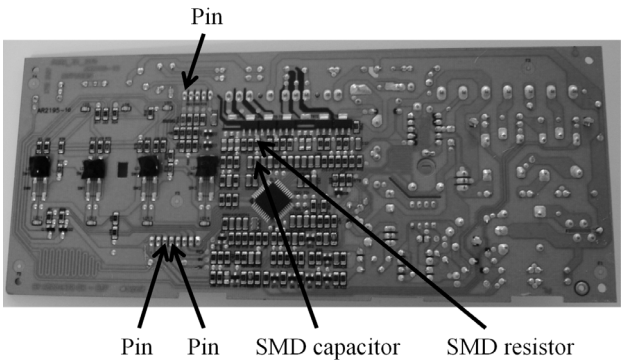

Figure 6: Positions of the pins and other elements that were measured on the uncoated and coated EB using Raman spectroscopy
Slika 6: Pozicije konic in drugih elementov, na katerih smo izmerili ramanske spektre na nezaščitenem in zaščitenem elektronskem vezju

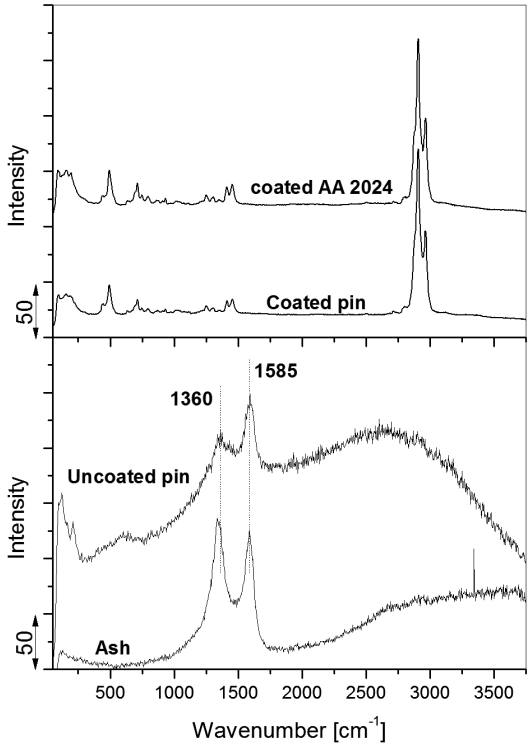

Figure 7: Raman spectra of the uncoated and coated pins on the EB substrate. The PDMSTU-based coating on the AA 2024 substrate is given for comparison, as well the characteristic Raman spectrum of an independent ash sample.
Slika 7: Ramanski spektri nezaščitenih in zaščitenih konic na elektronskem vezju. Za primerjavo podajamo ramanski spekter prevleke na osnovi PDMSTU, ki je napršena na podlago AA 2024. Podajamo tudi značilen ramanski spekter vzorca saj.

and quicker way of determining a possible non-coverage in the coatings. The PDMSTU-based coating sprayed on EB was therefore placed under the laser beam of the Raman spectrometer (**Figure 5**) and investigated at different points and elements (**Figure 6**). In **Figure 6**, only the elements that are described in this text (pins, SMD resistor and SMD capacitor) are shown, but other positions on EB were also studied.

Figure 7 shows the Raman spectra recorded on the pins of the uncoated and coated EBs. The spectra of the uncoated pins revealed two peaks, at 1.385 cm^{-1} and 1.360 cm^{-1}, which can be assigned to the presence of carbon. Namely, the spectrum of the ash sample revealed similar bands that are marked in the literature as G- and D-lines[2]. The so-called G-band corresponds to the strong C-C stretching E_{2g2} mode of the hexagonal graphite structure. The D-line (A_{1g}) that appeared from 1.350 cm^{-1} to 1.360 cm^{-1}, on the other hand, is the consequence of a turbostratic disorder, i.e., a disorder along the c axis due to a weak interlayer bonding[2]. When the EB substrate was covered with the PDMSTU-based coating, the characteristic bands of the coating appeared in the Raman spectrum (**Figure 7**). For comparison, the same bands also appeared in the Raman spectrum of the spray-deposited PDMSTU-based coating on the AA

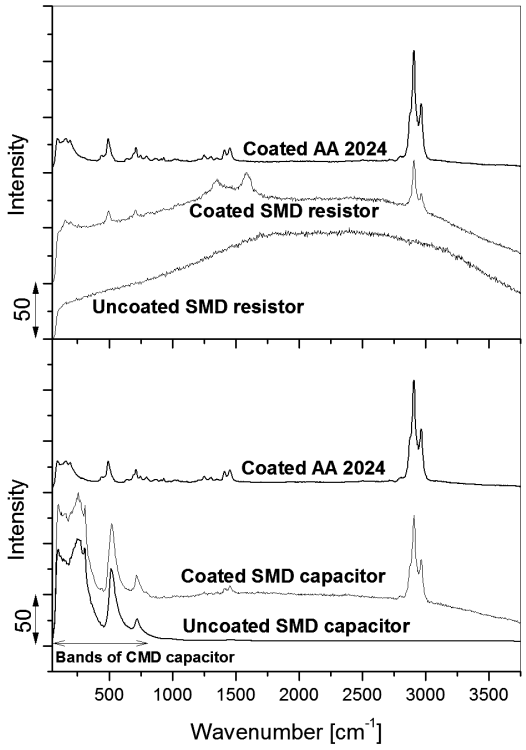

Figure 8: Raman spectra of the uncoated and coated SMD-resistor and SMD-capacitor elements on the EB substrate. The PDMSTU-based coating on the AA 2024 substrate is given for comparison.

Slika 8: Ramanski spektri nezaščitenega in zaščitenega SMD-upora in SMD-kondenzatorja na elektronskem vezju. Za primerjavo podajamo ramanski spekter prevleke na osnovi PDMSTU, ki je napršena na podlago AA 2024.

2024 substrate. Similarly, in the case of the SMD resistor and SMD capacitor, it was also found that the bands of the PDMSTU-based coating appeared in the Raman spectrum (**Figure 8**). In addition to the modes of the coating, carbon bands were also observed on the SMD resistor. On the other hand, the uncoated SMD capacitor revealed some bands by itself and they remained in the Raman spectrum of the covered SMD capacitor, in addition to the modes of the PDMSTU-based coating (**Figure 8**). The depicted spectra measured on the covered EB clearly revealed that the coating was successfully deposited covering all the different elements and parts of the investigated substrate. Other elements and pins were also investigated, but the results have not been shown due to a lack of space.

The Raman spectra measured on the coated EB substrate (**Figures 7** and **8**) clearly revealed that Raman spectroscopy is extremely well suited to the investigation of complex objects that do not allow a sample preparation. This is also due to the improvements in instrument configurations, for example, the use of confocal micro-Raman spectrometers that allow effective spatial resolution and Raman imaging as well as achieving a better contrast[1,2]. When non-typical samples, such as EBs are in question, Raman spectroscopy is important due to its non-destructive character, certainly when carefully set excitation conditions are used. In addition, the detection of coatings on the metallic parts of EBs is easy, since almost all the metals show no Raman bands. However, Raman spectroscopy is not a useful quantitative technique and it would be difficult to determine the amount of coating on various elements of EBs, since the sensitivity of the Raman response depends on the polarizability of the molecules and the characteristics of the measured spot. Another important drawback of Raman spectroscopy is the fluorescence caused by certain organic or other materials, i.e., in the case of the EB substrate, it was found on plastic areas. Nevertheless, all the aforementioned facts clearly show that Raman spectroscopy is a suitable technique for detecting the protective sol-gel coatings on EBs, not only after a deposition of the coatings, but also after their exposure to accelerated corrosion tests. The excellent spatial resolution of the confocal Raman spectrometers allows a detection of the corroded parts of the coatings on EBs and thus a determination of the most vulnerable parts of EB substrates.

4 CONCLUSIONS

Potentiodynamic electrochemical characterisation of the coatings prepared from organic-inorganic precursors bis-(3-(3-(3-triethoxysilyl)propyl)thioureido)propyl terminated poly(dimethylsiloxane) (PDMSTU) and bis-[3-(triethoxysilyl)propyl]tetrasulphide (BTESPT) revealed that the coatings possess the properties similar to the other coatings made of poly(dimethylsiloxane) or tetrasulphide-based precursors. Specifically, the cathodic current density of spray-deposited coatings was lower, by up to two orders of magnitude, than the cathodic current density of the pure AA 2024 substrate. The prepared coatings were also spray deposited on an electronic board (EB) and Raman spectroscopy was shown to be an appropriate technique for detecting the sol-gel protective coating on this substrate due to its non-destructive character and a high spatial resolution. On the basis of the present results, Raman spectroscopy will be used in future to determine the sites, at which corrosion has started after an exposure of the coated EB substrates to accelerated corrosion tests, including Raman imaging of larger surfaces. In order to assure a complete coverage of the elements, the sols will be studied using a detailed rheological characterisation. The sol with the optimal rheological properties will be chosen for further application.

Acknowledgement

This research was funded by the Slovenian Research Agency (Programme P1-0030) and the Ministry of Education, Science, Culture and Sport (MNT-ERA.NET project Bonaco, http://www.bonaco-project.com). A.

Rauter thanks the Slovenian Research Agency for the Ph. D. grant.

5 REFERENCES

[1] P. Vandenabeele, H. G. M. Edwards, L. Moens, Chem. Rev., 107 (**2006**), 675–686
[2] R. Baddour-Hadjean, J. Pierre Pereira-Ramos, Chem. Rev., 110 (**2010**), 1278–1319
[3] M. Gnyba, M. Keränen, M. Kozanecki, R. Bogdanowicz, B. B. Kosmowski, P. Wroczyński, Opto-Elecronics Rev., 10 (**2002**), 137–143
[4] I. Jerman, A. Šurca Vuk, M. Koželj, F. Švegl, B. Orel, Prog. Org. Coat., 72 (**2011**), 334–342
[5] McCullough, J. L. Wayt, J. N. Butch, US patent 6,127,038, 2000
[6] D. Wang, G. P. Bierwagen, Prog. Org. Coat., 64 (**2009**), 327–338
[7] M. Koželj, Synthesis of substituted trialkoxysilanes and their application for the preparation of materials via sol-gel procedures, Dissertation, University of Ljubljana, Ljubljana
[8] D. Zhu, W. J. van Ooij, Electrochim. Acta, 49 (**2004**), 1113–1125
[9] M. F. Montemor, M. G. S. Ferreira, Electrochim. Acta, 52 (**2007**), 7486–7495
[10] M. Fir, B. Orel, A. Šurca Vuk, A. Vilčnik, R. Ješe, V. Francetič, Langmuir, 23 (**2007**), 5505–5514
[11] I. Jerman, A. Šurca Vuk, M. Koželj, B. Orel, J. Kovač, Langmuir, 24 (**2008**), 5029–5037
[12] I. Jerman, B. Orel, A. Šurca Vuk, M. Koželj, J. Kovač, Thin Solid Films, 518 (**2010**), 2710–2721

UDK 519.61/.64:620.3:536.2
Original scientific article/Izvirni znanstveni članek

ISSN 1580-2949
MTAEC9, 47(2)211(2013)

NUMERICAL STUDY OF RAYLEIGH-BÉNARD NATURAL-CONVECTION HEAT-TRANSFER CHARACTERISTICS OF WATER-BASED Au NANOFLUIDS

NUMERIČNA ANALIZA PRENOSA TOPLOTE NANOTEKOČIN VODA-Au V RAZMERAH REYLEIGH-BÉNARDOVE NARAVNE KONVEKCIJE

Primož Ternik[1], Rebeka Rudolf[2,3], Zoran Žunič[4]

[1]Private Researcher, Bresterniška ulica 163, 2354 Bresternica, Slovenia
[2]University of Maribor, Faculty of Mechanical Engineering, Smetanova 17, 2000 Maribor, Slovenia
[3]Zlatarna Celje, d. d., Kersnikova ul. 19, 3000 Celje, Slovenia
[4]AVL-AST, Trg Leona Štuklja 5, 2000 Maribor, Slovenia
pternik@pt-rtd.eu

Prejem rokopisa – received: 2012-10-01; sprejem za objavo – accepted for publication: 2012-10-15

The present work deals with the natural convection in a square cavity filled with a water-based Au nanofluid. The cavity is heated from the lower and cooled from the adjacent wall, while the other two walls are adiabatic. The governing differential equations have been solved with the standard finite volume method and the hydrodynamic and thermal fields have been coupled using the Boussinesq approximation. The main objective of this study is to investigate the influence of the nanoparticles' volume fraction on the heat-transfer characteristics of Au nanofluids at a given base-fluid (i.e., water) Rayleigh number Ra_{bf}.
Accurate results are presented over a wide range of the base-fluid Rayleigh numbers ($10^2 \leq Ra_{bf} \leq 10^5$) and the volume fraction of Au nanoparticles ($0\ \% \leq \varphi \leq 10\ \%$). It is shown that adding nanoparticles to the base fluid delays the onset of convection. Contrary to what is argued by many authors, we show, with numerical simulations, that the use of nanofluids can reduce the heat transfer instead of increasing it.

Keywords: Rayleigh-Bénard natural convection, water-Au nanofluid, heat transfer, numerical modelling

V prispeveku obravnavamo naravno konvekcijo v kvadratni kotanji, napolnjeni z nanotekočino voda-Au. Kotanja je bila greta s spodnje in hlajena s prileže zgornje stene, preostali dve steni sta bili adiabatni. Vodilne diferencialne enačbe smo reševali s standardno metodo končnih prostornin. Hidrodinamično in temperaturno polje sta bila sklopljena z uporabo Boussinesqove aproksimacije. Glavni cilj prispevka je raziskati vpliv prostorninskega deleža nanodelcev na značilnosti prenosa toplote Au-nanotekočine pri podani vrednosti Rayleighjevega števila nosilne tekočine (vode) Ra_{bf}.
Natančni rezultati so predstavljeni za široko območje vrednosti Rayleighjevega števila nosilne tekočine ($10^2 \leq Ra_{bf} \leq 10^5$) in prostorninskega deleža Au-nanodelcev ($0\ \% \leq \varphi \leq 10\ \%$). Pokazali smo, da dodajanje nanodelcev v nosilno tekočino zakasni začetek naravne konvekcije. V nasprotju s trditvami mnogih avtorjev smo z numeričnimi simulacijami pokazali, da lahko uporaba nanodelcev prenos toplote zmanjša in ne poveča.

Ključne besede: Rayleigh-Bénardova naravna konvekcija, nanotekočina voda-Au, prenos toplote, numerično modeliranje

1 INTRODUCTION

Buoyancy-induced flow together with the associated heat transfer is an important phenomenon found in many engineering applications (e.g., selective laser melting process[1], cooling of electronic devices[2]). An enhancement of heat transfer in such systems is crucial from the energy-saving point of view. In recent years, nanosized particles dispersed in a base fluid, known as nanofluid, has been used and researched extensively to enhance the heat transfer. The presence of nanoparticles shows an unquestionable heat-transfer enhancement in forced convection applications[3]. However, with respect to the buoyancy-driven flow, there is still a dispute on the effect of nanoparticles on the heat-transfer enhancement.

Several researchers have been focused on the numerical modelling of buoyancy-induced flows. Recent numerical studies by Ternik et al.[4], Ternik and Rudolf[5], Oztop et al.[6] and Abu-Nada and Oztop[7] illustrated that the suspended nanoparticles substantially increase the heat-transfer rate for any given Rayleigh number. In addition, they showed that the heat-transfer rate in water-based nanofluids increases with an increasing volume fraction of Al_2O_3, Cu, TiO_2 and Au nanoparticles.

On the other hand, an apparently paradoxical behaviour of the heat-transfer deterioration was observed in many experimental studies[8-10]. For example, Putra et al.[8] reported that a presence of Al_2O_3 nanoparticles in a base fluid reduces the natural convective heat transfer. However, they did not clearly explain why the natural convective heat transfer is decreased with an increase in the volume fraction of nanoparticles.

The above review of the existing literature shows that the problem of natural convection in a bottom-heated horizontal cavity filled with a nanofluid is an issue still

far from being completely solved. Framed in this general background, the purpose of the present study is to examine the effect of adding Au nanoparticles to the base fluid at the conduction and convection heat-transfer rates in a square cavity heated from below (Rayleigh–Bénard configuration) over a range of base-fluid Rayleigh numbers $10^2 \leq Ra_{bf} \leq 10^5$ and volume fractions $0\ \% \leq \varphi \leq 10\ \%$.

2 NUMERICAL MODELLING

The standard finite-volume method, successfully used in many recent studies,[11–13] is used to solve the coupled conservation equations of mass, momentum and energy. In this framework, a second-order central differencing scheme is used for the diffusive terms and a second-order upwind scheme for the convective terms. Coupling of the pressure and velocity is achieved using the SIMPLE algorithm. The convergence criteria were set to 10^{-9} for all the relative (scaled) residuals.

2.1 Governing equations

For the present study, a steady-state flow of an incompressible water-based Au nanofluid is considered. It is assumed that both the fluid phase and nanoparticles are in thermal equilibrium. Except for the density, the properties of the nanoparticles and fluid (presented in **Table 1**) are taken to be constant. The Boussinesq approximation is invoked for the nanofluid properties to relate density changes to temperature changes, and to couple the temperature field with the velocity field.

The governing equations (mass, momentum and energy conservation) of such a flow are:[4,5]

$$\frac{\partial v_i}{\partial x_i} = 0 \tag{1}$$

$$\rho_{nf} v_j \frac{\partial v_i}{\partial x_j} - \frac{\partial}{\partial x_j}\left(\eta_{nf} \frac{\partial v_i}{\partial x_j}\right) = -\frac{\partial p}{\partial x_i} + (\rho\beta)_{nf}\, g(T - T_C) + \frac{\partial}{\partial x_j}\left(\eta_{nf} \frac{\partial v_j}{\partial x_i}\right) \tag{2}$$

$$(\rho c_p)_{nf} v_j \frac{\partial T}{\partial x_j} = \frac{\partial}{\partial x_j}\left(c_{nf} \frac{\partial T}{\partial x_j}\right) \tag{3}$$

where the cold-wall temperature T_C is taken to be the reference temperature for evaluating the buoyancy term $(\rho\beta)_{nf} g(T - T_C)$ in the momentum conservation equation.

Relationships between the properties of the nanofluid (*nf*) and those of the base fluid (*bf*) and pure solid (*s*) are given with the following empirical models[4,5]:

- Dynamic viscosity:

$$\eta_{nf} = \frac{\eta_{bf}}{(1-\varphi)^{2.5}}$$

- Density:

$$\rho_{nf} = (1-\varphi)\rho_{bf} + \varphi\rho_s$$

- Thermal expansion:

$$(\rho\beta)_{nf} = (1-\varphi)(\rho\beta)_{bf} + \varphi(\rho\beta)_s$$

- Heat capacitance:

$$(\rho c_p)_{nf} = (1-\varphi)(\rho c_p)_{bf} + \varphi(\rho\beta)_s$$

- Thermal conductivity:

$$k_{nf} = k_{bf} \frac{k_s + 2k_{bf} - 2\varphi(k_{bf} - k_s)}{k_s + 2k_{bf} + \varphi(k_{bf} - k_s)}$$

2.2 Geometry and boundary conditions

The simulation domain is shown schematically in **Figure 1**. The two horizontal walls of a square enclosure are kept at different constant temperatures ($T_H > T_C$), whereas the other boundaries are considered to be adiabatic. Both velocity components (i.e., v_x and v_y) are identically zero on each boundary because of the no-slip condition and the impenetrability of the rigid boundaries.

In the present study, the heat-transfer characteristics are presented in terms of the mean Nusselt number:

$$\overline{Nu} = \frac{1}{L}\int_0^L Nu(x)\,\mathrm{d}x \tag{4}$$

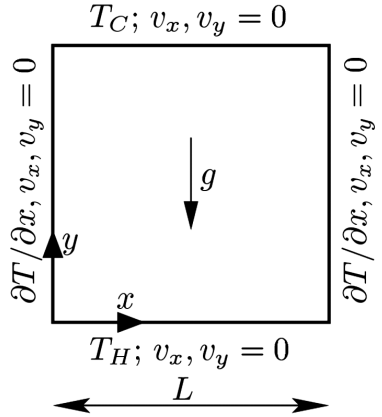

Figure 1: Schematic diagrams of the simulation domain
Slika 1: Shematski prikaz območja simulacije

Table 1: Thermo-physical properties of the Au nanofluid[4,5]
Tabela 1: Toplotno-fizikalne lastnosti Au-nanotekočine[4,5]

	η (Pa s)	ρ (kg/m^3)	c_p (J/kg K)	k (W/m K)	β (1/K)
Pure water	1.003×10^{-3}	997.1	4179	0.613	2.1×10^{-4}
Au	/	19320	128.8	314.4	1.416×10^{-7}

and the ratio of the nanofluid heat-transfer rate to the base-fluid one:

$$\frac{Q_{nf}}{Q_{bf}} = \frac{k_{nf}\,\overline{Nu}_{nf}}{k_{bf}\,\overline{Nu}_{bf}} = \frac{h_{nf}}{k_{bf}} \tag{5}$$

where h_{nf} and h_{bf} are the convection heat-transfer coefficients of the nanofluid and the base fluid.

In order to investigate the influence of volume fraction φ on the heat-transfer characteristics, the Rayleigh (Ra_{nf}) and the Prandtl numbers (Pr_{nf}) for the nanofluids are expressed as follows:

$$Ra_{nf} = \frac{(\rho\beta)_{nf}\,k_{bf}\,(\rho c_p)_{nf}\,\eta_{bf}}{(\rho\beta)_{bf}\,k_{nf}\,(\rho c_p)_{bf}\,\eta_{nf}}\,Ra_{bf}$$
$$Pr_{nf} = \frac{\eta_{nf}\,c_{p_{nf}}\,k_{bf}}{\eta_{bf}\,c_{p_{bf}}\,k_{nf}}\,Pr_{bf} \tag{6}$$

Using equation (6) we show that $Ra_{nf} < Ra_{bf}$ (**Figure 2a**) and $Pr_{nf} < Pr_{bf}$ (**Figure 2b**) for all the values of φ.The ratio of the water-Au-nanofluid Rayleigh and Prandtl numbers to the base-fluid Rayleigh and Prandtl numbers decreases with the increasing volume fraction of Au nanoparticles.

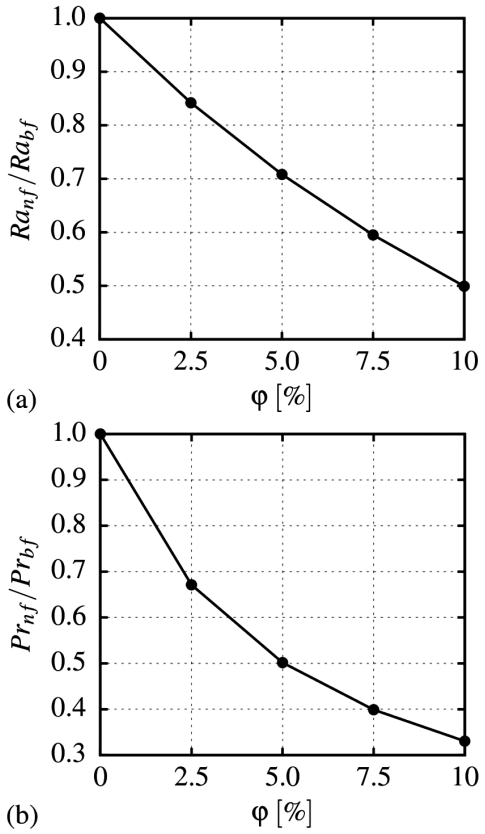

Figure 2: Variation of the dimensionless numbers of the water-Au nanofluid with the volume fraction of Au nanoparticles: a) Rayleigh number and b) Prandtl number

Slika 2: Spreminjanje brezdimenzijskih števil nanotekočine voda-Au s prostorninskim deležem Au-nanodelcev: a) Rayleighjevo število in b) Prandtlovo število

2.3 Grid-dependency study

The grid independence of the results has been established on the basis of a detailed analysis of three different uniform meshes: *M*1(50 × 50), *M*2(100 × 100) and *M*3(200 × 200. For the general primitive variable ϕ the grid-converged (i.e., extrapolated to the zero element size) value according to Richardson extrapolation is given as[11,12], $\phi_{ext} = \phi_{M3} - (\phi_{M2} - \phi_{M3})/(r^p - 1)$ where ϕ_{M3} is obtained on the basis of the finest grid and ϕ_{M2} is the solution based on the next level of the coarse grid, $r = 2$ is the ratio between the coarse- and the fine-grid spacing and $p = 2$ is the order of accuracy.

The numerical error $e = |(\phi_{M2} - \Phi_{ext})/\Phi_{ext}|$ for the mean Nusselt number $\overline{Nu}$ is presented in **Table 2**. It can be seen that the differences in the grid refinements are exceedingly small and the agreement between mesh *M*2 and the extrapolated value is extremely good (the discretisation error is well below 0.2 %). Based on this, the simulations in the remainder of the paper were conducted on mesh *M*2 that provided a reasonable compromise between high accuracy and computational efficiency.

Table 2: Effect of a mesh refinement upon the mean Nusselt number ($\varphi = 0.10$, $Ra_{bf} = 10^5$)

Tabela 2: Vpliv zgoščevanja mreže na srednjo vrednost Nusseltovega števila ($\varphi = 0{,}10$, $Ra_{bf} = 10^5$)

Mesh *M*1	Mesh *M*2	Mesh *M*3	$\overline{Nu}_{ext}$	*e*
3.325	3.304	3.299	3.298	0.184 %

2.4 Benchmark comparison

In addition to the aforementioned grid-dependency study, the simulation results have also been compared with the recent results of Turan et al.[14] for the Rayleigh-Bénard natural convection in a square cavity. The comparisons between the present-simulation results and the corresponding benchmark values (summarised in **Table 3**) are very good and entirely consistent with our grid-dependency studies.

Table 3: Comparison of the present results for $\overline{Nu}$ with the benchmark results

Tabela 3: Primerjava pričujočih rezultatov za $\overline{Nu}$ z referenčnimi rezultati

	$Ra = 10^3$		$Ra = 10^4$		$Ra = 10^5$	
	$Pr = 1$	$Pr = 10$	$Pr = 1$	$Pr = 10$	$Pr = 1$	$Pr = 10$
Present study	1.000	1.000	2.164	2.190	3.941	3.875
Turan et al.[14]	1.000	1.000	2.162	2.188	3.934	3.868

3 RESULTS AND DISCUSSION

Figure 3 presents the variation of the mean Nusselt number (equation 4) along the hot wall for different values of Ra_{bf} and Ra_{nf}. For $Ra_{bf} < 2586$, there is no convection in the nanofluid or the base fluid, and the heat transfer occurs due to pure conduction, so the mean Nusselt number equals 1 and is independent of the base-

fluid Rayleigh number (**Figure 3a**). As the base-fluid Rayleigh number increases, the nanofluid remains in the conductive regime, while convection appears in the base fluid. The point of transition (i.e., the value of Ra_{bf}) from conduction to convection depends on the volume fraction of Au nanoparticles. The higher is the value of φ, the more delayed is the onset of convection (**Figure 3a**). When the nanofluid is in the convective heat-transfer regime, the mean Nusselt number is a monotonic increasing function of Ra_{bf}.

On the other hand, it is interesting to notice that the transition from conduction to convection occurs at the same value of the nanofluid Rayleigh number, i.e., $Ra_{nf} \approx 2586$ (**Figure 3b**). Furthermore, the value of the mean Nusselt number at a given Ra_{nf} is practically independent of the nanoparticles' volume fraction. This finding is a reflection of the nanofluid Prandtl number values considered in the present study. Its value varies (decreases with the increasing) from Pr_{nf} (φ = 0 %) = 6.84 to Pr_{nf} (φ = 10 %) = 2.26 and for this range of the Prandtl-number values ($Pr > 1$) the relative balance between viscous and buoyancy forces is modified, so that the heat transport in the thermal boundary layer gets only marginally affected[14]. This marginal modification is reflected in a weak Prandtl-number (and therefore nanoparticles' volume fraction) dependence of the mean Nusselt number.

Figure 4 shows the effect of the base-fluid Rayleigh number on the ratio of the heat-transfer rate for the water-based Au nanofluid for different values of the volume fraction. In the range $Ra_{bf} < 2586$ the heat transfer occurs by pure conduction, so the ratio of heat transfer is equal to the ratio of thermal conductivities and is constant and independent of Ra_{bf}. For $Ra_{nf} < 2586$ and $Ra_{bf} > 2586$ the nanofluid remains in the conductive regime, while convection appears in the base fluid. The heat transfer is more important in the base fluid than in the nanofluid and the ratio Q_{nf}/Q_{bf} is on a decrease until $Ra_{nf} \geq 2586$. From this point onwards (i.e., the transition from conduction to convection) the ratio Q_{nf}/Q_{bf} is on an increase and its value becomes higher than 1, but remains lower than the ratio that is obtained when both the nanofluid and the base fluid are in the conductive regime. When the ratio $Q_{nf}/Q_{bf} > 1$, the heat-transfer rate in the nanofluid becomes higher than that in the base fluid.

Finally, in **Figure 4**, we observe that the heat transfer can decrease or increase depending on the value of the base-fluid Rayleigh number. For example, for a water-based Au nanofluid and for φ = 10 %, the ratio of the heat-transfer rate becomes higher than 1 when the base-fluid Rayleigh number reaches the value of around 9500, so we obtain an enhancement of the heat transfer only after this value ($Ra_{bf} > 9500$). Therefore, adding nanoparticles increases the heat transfer only for a given value of the temperature difference.

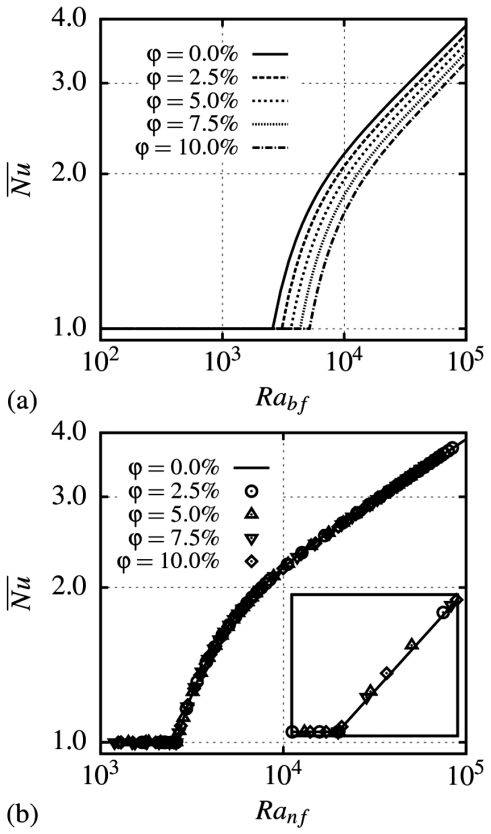

Figure 3: Variation of the mean Nusselt number along the hot wall with the: a) base-fluid Rayleigh number and b) nanofluid Rayleigh number

Slika 3: Spreminjanje srednjega Nusseltovega števila vzdolž tople stene z: a) Rayleighjevim številom nosilne tekočine in b) Rayleighjevim številom nanotekočine

4 CONCLUSIONS

In the present study, the steady laminar natural convection of water-based Au nanofluids in a square enclo-

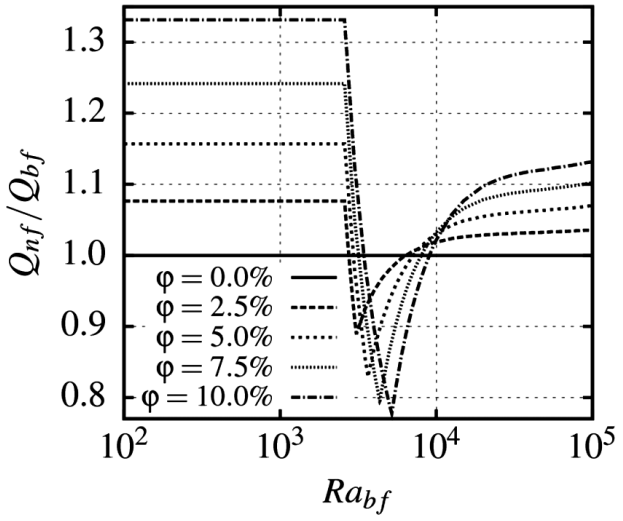

Figure 4: Effect of the base-fluid Rayleigh number on the ratio of heat transfer

Slika 4: Vpliv Rayleighjevega števila nosilne tekočine na razmerje prenosa toplote

sure with differentially heated horizontal walls and with the bottom wall at a higher temperature has been numerically analysed. The effects of the base-fluid Rayleigh number ($10^2 \leq Ra_{bf} \leq 10^5$) and the solid volume fraction ($0\ \% \leq \varphi \leq 10\ \%$) on heat-transfer characteristics have been systematically investigated in detail.

The influence of a computational grid refinement on the present numerical predictions was studied throughout the examination of the grid convergence at $Ra_{bf} = 10^5$ and $\varphi = 10\ \%$. By utilizing extremely fine meshes the resulting discretisation error for $\overline{Nu}$ is well below 0.2 %.

The numerical method was validated for the case of Rayleigh-Bénard natural convection in a square cavity, for which the results are available in the open literature. A remarkable agreement of the present results with the benchmark results of Turan et al.[14] yields sufficient confidence in the present numerical procedure and its results.

Highly accurate numerical results pointed out some important points such as:

- In the classical Rayleigh–Bénard configuration, just after the onset of convection, there is more heat transfer in the base fluid than in the nanofluid. For a fixed value of the base-fluid Rayleigh number Ra_{bf}, the nanofluid Rayleigh number Ra_{nf} decreases with the volume fraction of nanoparticles. Thus, the nanoparticles delay the onset of convection.
- In the convective heat-transfer regime the mean Nusselt number $\overline{Nu}$ is found to increase with the increasing values of the base-fluid Rayleigh number Ra_{bf}, but the $\overline{Nu}$ values obtained for the higher values of the nanoparticles' volume fraction φ are smaller than those obtained in the case of the base fluid ($\varphi = 10\ \%$) with the same numerical values of Ra_{bf}.
- The transition from the conductive to convective heat-transfer regime occurs at the same value of the nanofluid Rayleigh number, i.e., $Ra_{nf} \geq 2586$.
- The values of the mean Nusselt number at a given Ra_{nf} are practically independent of the nanoparticles' volume fraction.
- The heat transfer can decrease or increase depending on the value of the Rayleigh number. So, an addition of nanoparticles increases the heat transfer only for the given values of the temperature difference.

Acknowledgements

The research leading to these results was carried out within the framework of a research project "Production technology of Au nano-particles" (L2-4212) and has received the funding from the Slovenian Research Agency (ARRS).

5 REFERENCES

[1] N. Contuzzi, S. L. Campanelli, A. D. Ludovico, 3D finite element analysis in the selective laser melting process, International Journal of Simulation Modelling, 10 (**2011**), 113–121

[2] A. Ijam, R. Saidur, Nanofluid as a coolant for electronic devices (cooling of electronic devices), Applied Thermal Engineering, 32 (**2012**), 76–82

[3] W. Daungthongsuk, S. Wongwises, A critical review of convective heat transfer in nanofluids, Renewable & Sustainable Energy Reviews, 11 (**2009**), 797–817

[4] P. Ternik, R. Rudolf, Z. Žunič, Numerical study of heat transfer enhancement of homogeneous water-Au nanofluid under natural convection, Mater. Tehnol., 46 (**2012**) 3, 257–261

[5] P. Ternik, R. Rudolf, Heat transfer enhancement for natural convection flow of water-based nanofluids in a square enclosure, International Journal of Simulation Modelling, 11 (**2012**), 29–39

[6] H. F. Oztop, E. Abu-Nada, Y. Varol, K. Al-Salem, Computational analysis of non-isothermal temperature distribution on natural convection in nanofluid filled enclosures, Superlattices and Microstructures, 49 (**2011**), 453–467

[7] E. Abu-Nada, H. F. Oztop, Effects of inclination angle on natural convection in enclosures filled with Cu–water nanofluid, International Journal of Heat and Fluid Flow, 30 (**2009**), 669–678

[8] N. Putra, W. Roetzel, S. K. Das, Natural convection of nano-fluids, Heat and Mass Transfer, 39 (**2002**), 775–784

[9] B. H. Chang, A. F. Mills, E. Hernandez, Natural convection of microparticles suspension in thin enclosures, International Journal of Heat and Mass Transfer, 51 (**2008**), 1332–1341

[10] C. J. Ho, W. K. Liu, Y. S. Chang, C. C. Lin, Natural convection heat transfer of alumina-water nanofluid in vertical square enclosures: an experimental study, International Journal of Thermal Sciences, 49 (**2010**), 1345–1353

[11] I. Biluš, P. Ternik, Z. Žunič, Further contributions on the flow past a stationary and confined cylinder: Creeping and slowly moving flow of Power law fluids, Journal of Fluids and Structures, 27 (**2011**), 1278–1295

[12] P. Ternik, New contributions on laminar flow of inelastic non-Newtonian fluid in the two-dimensional symmetric expansion: Creeping and slowly moving conditions, Journal of Non-Newtonian Fluid Mechanics, 165 (**2010**), 1400–1411

[13] K. T. Raić, R. Rudolf, P. Ternik, Z. Žunič, V. Lazić, D. Stamenković, T. Tanasković, I. Anžel, CFD analysis of exothermic reactions in Al-Au multi-layered foils, Mater. Tehnol., 45 (**2011**) 4, 335–338

[14] O. Turan, N Chakraborty, R. J. Poole, Laminar Rayleigh-Bénard convection of yield stress fluids in a square enclosure, Journal of Non-Newtonian Fluid Mechanics, 171–172 (**2012**), 83–96

UDK 669.094.23:66.046.51:549.641.23
Original scientific article/Izvirni znanstveni članek

ISSN 1580-2949
MTAEC9, 47(2)217(2013)

ALUMOTHERMIC REDUCTION OF ILMENITE IN A STEEL MELT

ALUMOTERMIČNA REDUKCIJA ILMENITA V JEKLENI TALINI

Jaka Burja[1], Franc Tehovnik[1], Jakob Lamut[2], Matjaž Knap[2]

[1] Institute of Metals and Technology, Lepi pot 11, 1000 Ljubljana, Slovenia
[2] University of Ljubljana, Faculty of Natural Sciences and Engineering, Department of Materials and Metallurgy, Aškerčeva 12, 1000 Ljubljana, Slovenia
jaka.burja@imt.si

Prejem rokopisa – received: 2012-10-15; sprejem za objavo – accepted for publication: 2013-01-04

Experiments regarding the alumothermic reduction of ilmenite ($FeO{\cdot}TiO_2$), a mineral that contains iron and titanium oxides, were carried out. The results of the experiments showed that the alumothermic reduction takes place in steel, but the products obtained with the reduction suggest that the reaction mechanism is more complicated and includes different metallic phases other than a simple reduction of pure elemental titanium. Two kinds of experiments were carried out, the alumothermic reduction of ilmenite in a steel melt and the alloying of the alumothermic mixture into the steel melt. The experiments were carried out in order to get a view of the phase boundary between the steel and reduced titanium and the metallic phases that occur during the reduction, before the dissolution of titanium in the steel melt. Metallic phases that contained aluminium, iron and titanium were gained during the alumothermic reduction of ilmenite. Titanium was successfully alloyed into the steel melt by introducing the alumothermic mixture into the melt, while the presence of titanium nitrides confirms that the titanium was reduced in the melt and reacted with the dissolved nitrogen.

Keywords: alloying of titanium, ilmenite, alumothermic reduction, titanium in steel

Izvedeni so bili poskusi alumotermične redukcije ilmenita. Ilmenit je mineral, ki vsebuje titanove in železove okside ($FeO{\cdot}TiO_2$). Rezultati so potrdili, da v jeklu poteče alumotermična redukcija. Produkti redukcije pa kažejo na to, da je reakcijski mehanizem bolj zapleten, kot pa zgolj nastajanje elementarnega titana, saj nastajajo različne kovinske faze. Izvedeni sta bili dve vrsti poskusov: alumotermična redukcija ilmenita in legiranje alumotermične mešanice v jekleno talino. Dobljen je bil vpogled v procese na fazni meji med jekleno talino, titanom in nastalimi kovinskimi fazami, preden se titan raztopi v jeklu. Ugotovljeno je bilo, da se titan raztaplja v jeklu prek nastanka intermetalnih faz. Produkti redukcije so bile kovinske faze, ki so vsebovale aluminij, titan in železo. Prisotnost titanovih nitridov v jeklu, ki smo ga legirali z mešanico, pa je dokaz, da je bil titan legiran v kovinski obliki, kjer je reagiral z raztopljenim dušikom.

Ključne besede: legiranje titana, ilmenit, alumotermična redukcija, titan v jeklu

1 INTRODUCTION

Titanium is an important alloying element in steel making, among other things, it is used to stabilise stainless steel by forming titanium carbides and preventing the formation of chromium carbides. It has also been observed that additions of titanium significantly reduce the austenite grain size in the as-cast microstructure of continually cast steels.[1] Titanium's high chemical affinity to nitrogen and carbon is what makes it such a valuable alloying element, but unfortunately it also makes it difficult to alloy (low yields) and produce.[2] The production of titanium is complex and therefore expensive.[3] In steelmaking titanium is used in the form of ferrotitanium that contains iron and between 20 to 75 % of titanium, while its eutectic composition is at the mole fraction 71.1 % of Ti.[4,5] Ferrotitanium is mostly produced by remelting titanium scrap and iron; the high prices of titanium consequently mean that the price of ferrotitanium is also relatively high. Experiments that concern direct alloying of titanium from the oxide form may show an alternative way of producing ferrotitanium, as the minerals like ilmenite that contain titanium oxides are inexpensive. Alumothermic reduction was chosen because aluminium is often added to ferrotitanium in order to increase the yield by reducing the oxidised titanium in a steel melt.[6]

The Ellingham diagram (**Figure 1**) clearly shows that the Gibbs free energy for the alumothermic reduction of titanium is negative. The alumothermic reduction of titanium in the oxide form is as follows:

$$3TiO_2 + 4Al = 3Ti + 2Al_2O_3$$

The alumothermic reduction of ilmenite has an even lower Gibbs free energy because ilmenite contains iron oxides and its equation is as follows:

$$FeO{\cdot}TiO_2 + 2Al = Fe + Ti + Al_2O_3$$

As we can see from reaction (2) iron is another metal product besides titanium. The graph for the value of the Gibbs free energy for equations 1 and 2 is given in **Figure 2**[7].

Titanium forms TiO_2 if oxygen is present in the steel melt, while titanium oxide forms high temperature phases with other oxide components in the slag. If CaO is present perovskite $CaO{\cdot}TiO_2$ forms with its melting point at around 2000 °C. Titanium oxide particles can also get trapped in spinel $Al_2O_3{\cdot}MgO$, which can also

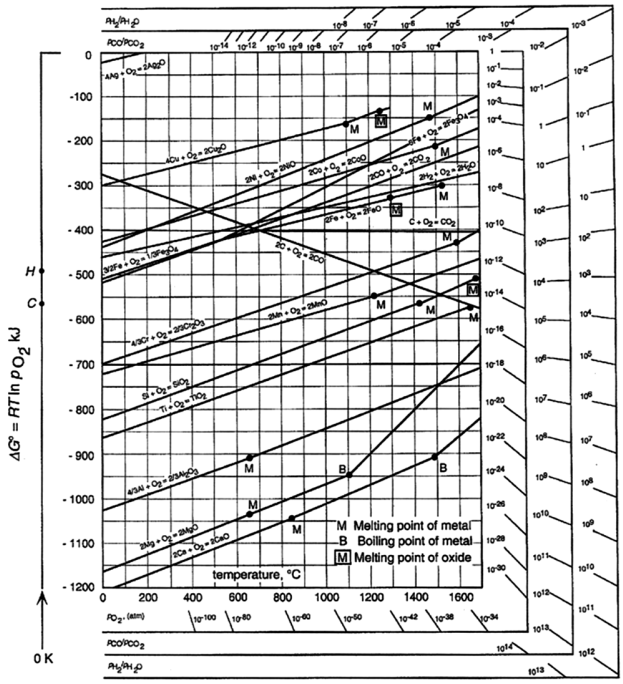

Figure 1: Ellingham-Richardson diagram
Slika 1: Ellingham-Richardsonov diagram

present a problem, because a spinel melts at the temperatures higher than 1600 °C and the titanium oxide particles have a melting point at around 1800 °C.[8] The formation of non-metallic inclusions that have a high melting point is problematic with respect to the cleanliness of steel and is therefore undesirable. The control of oxide non-metallic inclusions can be achieved by lowering the aluminium content and, therefore, the Al_2O_3 content and by decreasing the MgO content in the rafination slag.[8] The $CaO{\cdot}TiO_2$ content is lowered by lowering the basicity of the slag (CaO/SiO_2).[8]

In the production of stainless steel, a strong nitride-forming element, such as titanium, is often added to stabilise nitrogen and improve the mechanical properties of steel via the grain refinement during hot rolling. On the other hand, titanium nitride formed in liquid steel can agglomerate and cause a nozzle-clogging problem during continuous casting, and surface defects in the final products.[9] In practice the deposit material that is clogging the nozzle is titanium oxide and spinel, but research work has shown that the agglomerates form because titanium nitride particles get caught in the spinel; these are in turn oxidised and become titanium oxides. The particles remain rectangular like nitrides and not globular like oxides formed in the melt. The presence of oxygen is probably the result of porosity of the refractory material, from which the nozzles are made. The flow of the metal trough the nozzle creates a low pressure, which, in turn, promotes the diffusion of oxygen trough the pores into the melt.[10]

The experiments were carried out taking into account the specific nature of titanium and its behaviour as an alloying element.

2 EXPERIMENTS

The experiments were carried out using steel pipes filled with an alumothermic mixture of aluminium and ilmenite. These pipes were then introduced into the steel melt where the mixture was heated up to approximately the temperature of the steel melt. The mixture reacted at such high temperatures. In one set of the experiments the pipes were retrieved before they fully dissolved and still contained the mixture, which had been sintered by the high temperatures. The other set of experiments had been designed to alloy titanium into the steel and in this case the pipes were fully dissolved, together with the mixture. This procedure was carried out in order to recreate the conditions of alloying with the use of a cored wire.

The alumothermic mixture consisted of the ilmenite dust and aluminium dust. The molar ratio was 1 : 4 for ilmenite to aluminium, and the surplus of aluminium was

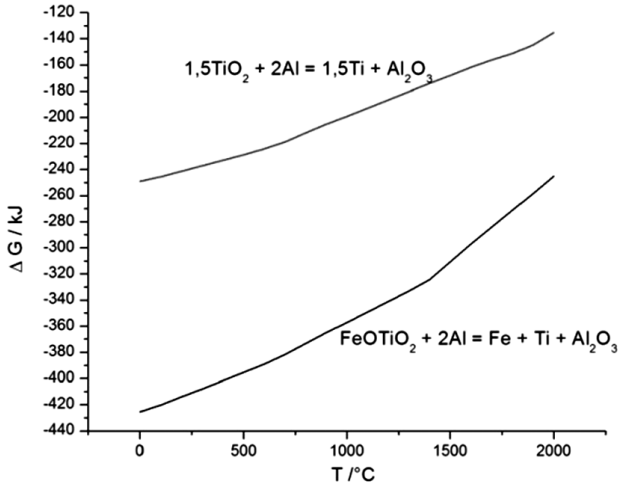

Figure 2: Gibbs free energy for equation 2[7]
Slika 2: Gibbsova prosta energija za reakcijo 2[7]

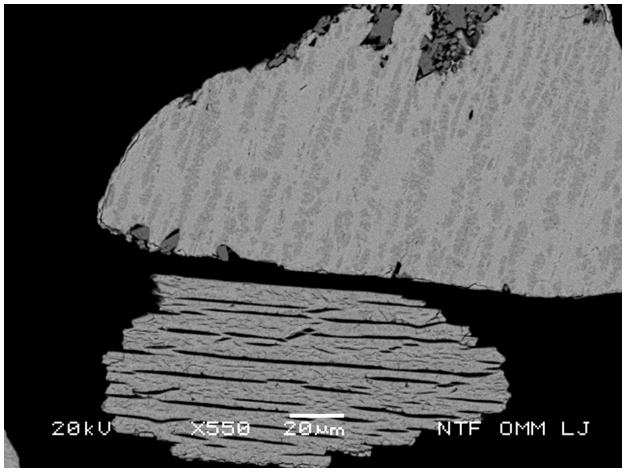

Figure 3: Ilmenite grains
Slika 3: Ilmenitna zrna

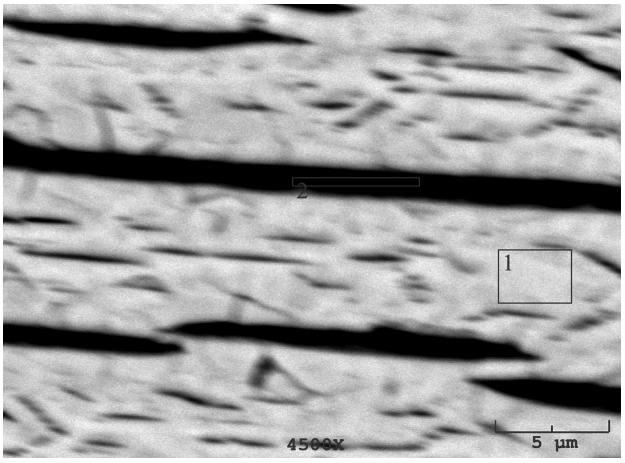

Figure 4: Phase analysis of ilmenite
Slika 4: Fazna analiza ilmenita

used so that the reduction took place. Theoretically, a molar ratio of 1 : 2 is needed to reduce ilmenite, as can be seen from equation 2.

Ilmenite is a mineral that mainly consists of iron and titanium oxides in the form of $FeO{\cdot}TiO_2$, but it also contains impurities such as magnesium oxides and manganese oxides. SEM analyses show that grains of ilmenite are far from being homogenous but have a "striped" appearance that can be seen in **Figure 3**.

The phase analysis in **Figure 4** clearly shows that the darker stripes are richer in titanium, while the lighter ones are richer in iron.

An electric induction furnace with a capacity to melt 18 kg of steel was used to melt the steel for the experiments.

A steel melt was prepared for the experiments that were developed to model the alumothermic reduction of ilmenite. The steel melt was heated to the temperature of 1500 °C, measured with an optical pyrometer. The chemical composition of the steel melt is not important for the experiment because the steel melt is only used as a medium to transfer heat to the alumothermic mixture, not to interact with it chemically. Then the pipe with the alumothermic mixture was submerged into the melt for approximately 40 s. The pipe was 25.4 mm in diameter and had a wall thickness of 2 mm. This method was chosen because it was essential that the mixture was quickly heated up to the temperature of the steel melt in order to prevent the aluminium dust from oxidising and thus losing its ability to reduce ilmenite.

Another experiment was made in order to determine whether titanium can be alloyed into the steel melt with the alumothermic ilmenite reduction. The aim was to alloy the mass fraction 0.3 % of titanium into 18 kg of steel. The required amount of ilmenite was 171 g and the amount of aluminium was 121 g.

First the steel was melted; it had a small quantity of alloying elements and a deep drawing quality. When the steel was melted a sample was taken for a chemical analysis. It was found that it did not contain detectable levels of titanium (the method of determining the titanium content was the classical chemical analysis). Then the melt was deoxidised with aluminium, after that the steel pipes were filled with the alumothermic mixture and submerged into the melt until they dissolved, thus, alloying the steel with titanium when the pyrometer gave a temperature reading of 1600 °C.

A sample of the alloyed steel was taken after the alloying was complete; the rest of the steel was cast into an ingot. Samples of slag were taken as well.

3 RESULTS

The steel pipes that were used for the reduction of ilmenite were partially melted, but there was a sintered mass in the pipe. Metallographic samples were made and a further SEM analysis showed that metallic phases containing aluminium, iron and titanium were present. **Figure 5** shows the products of the alumothermic reaction; metallic phases contain aluminium, iron and, most importantly, titanium.

Figure 6 shows a part of the sintered mass in the steel pipe after the reduction; individual intermetallic phases can be seen. The metallic phases are surrounded by the oxide products of the reduction.

The chemical compositions of the phases from **Figure 6** are given in **Table 1**.

In the experiment that investigated the option of alloying titanium, the mixture had reacted and the

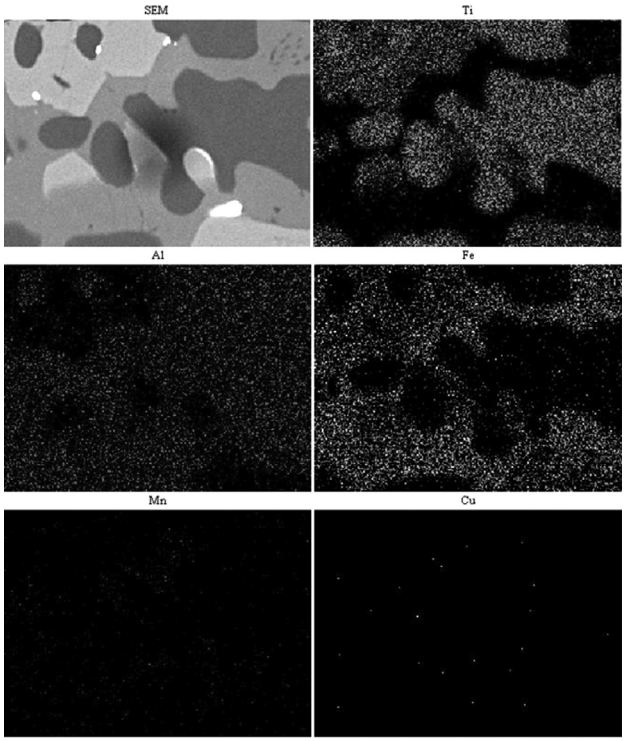

Figure 5: Mapping of alumothermic products
Slika 5: Ploskovna porazdelitev elementov redukcijskih produktov

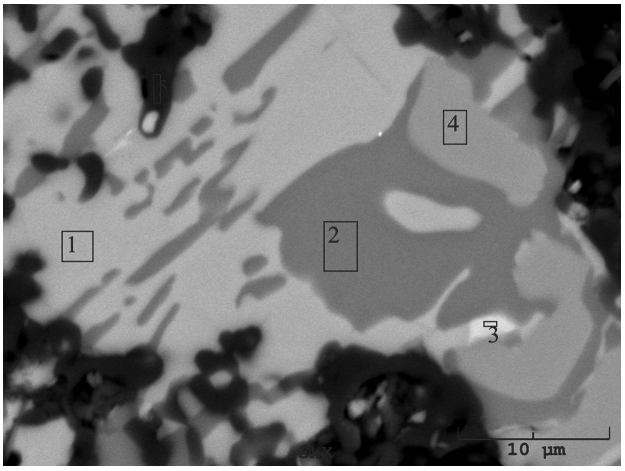

Figure 6: SEM image of the products of the alumothermic reduction
Slika 6: SEM-posnetek produktov alumotermične redukcije ilmenita

Table 1: Chemical compositions of the phases (in mass fractions *w*/%) from **Figure 6**
Tabela 1: Sestava faz (v masnih deležih *w*/%) s **slike 6**

1	48.4 % Al	6.0 % Ti	43.4 % Fe	1.3 % Cu		0.9 % Mn
2	52.2 % Al	45.5 % Ti	1.6 % Fe		0.7 % Si	
3	33.5 % Al	30.0 % Ti	28.7 % Fe	1.6 % Cu	5.4 % Si	0.8 % Mn
4	44.5 % Al	42.7 % Ti	12.8 % Fe			

product or the alumothermic reduction began to dissolve into the steel melt. The presence of titanium nitrides in the microstructure, as seen in **Figure 7**, confirms that titanium had indeed been alloyed into the steel and had reacted with the nitrogen in the steel melt. The chemical analysis showed that the content of titanium had been raised up to $w = 0.064$ %. The yield of titanium can be calculated with equation 2 and is therefore 21 %.

$$Yield = 0.064/0.3 \times 100\ \% = 21\ \% \tag{2}$$

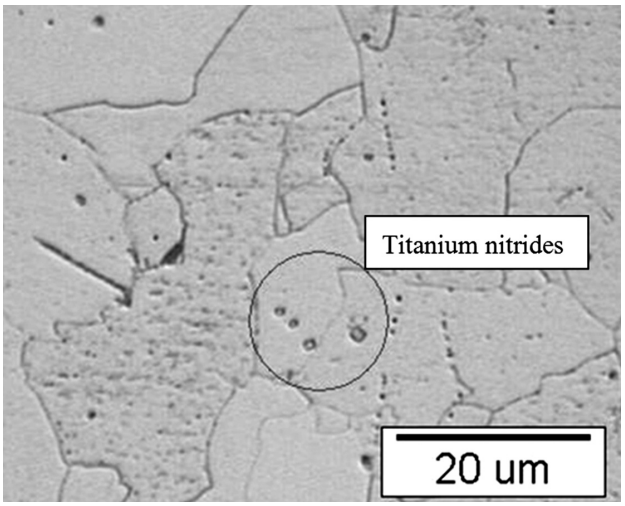

Figure 7: Titanium nitrides in the steel microstructure
Slika 7: Titanovi nitridi v mikrostrukturi jekla

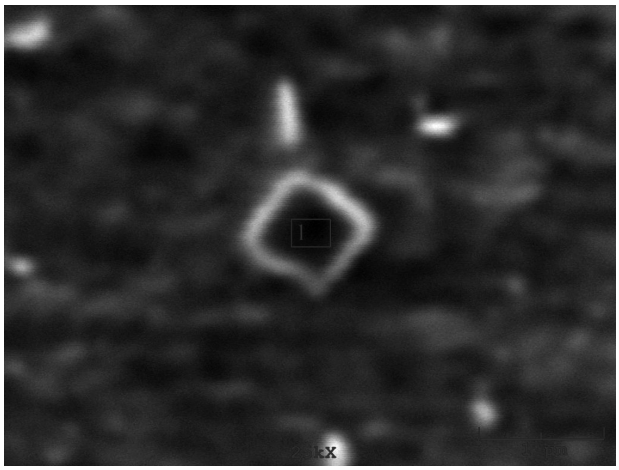

Figure 8: SEM image of a titanium nitride
Slika 8: SEM-posnetek titanovega nitrida

Figure 8 shows the SEM analysis of the nitrides confirming that the inclusions in **Figure 7** were indeed titanium nitrides.

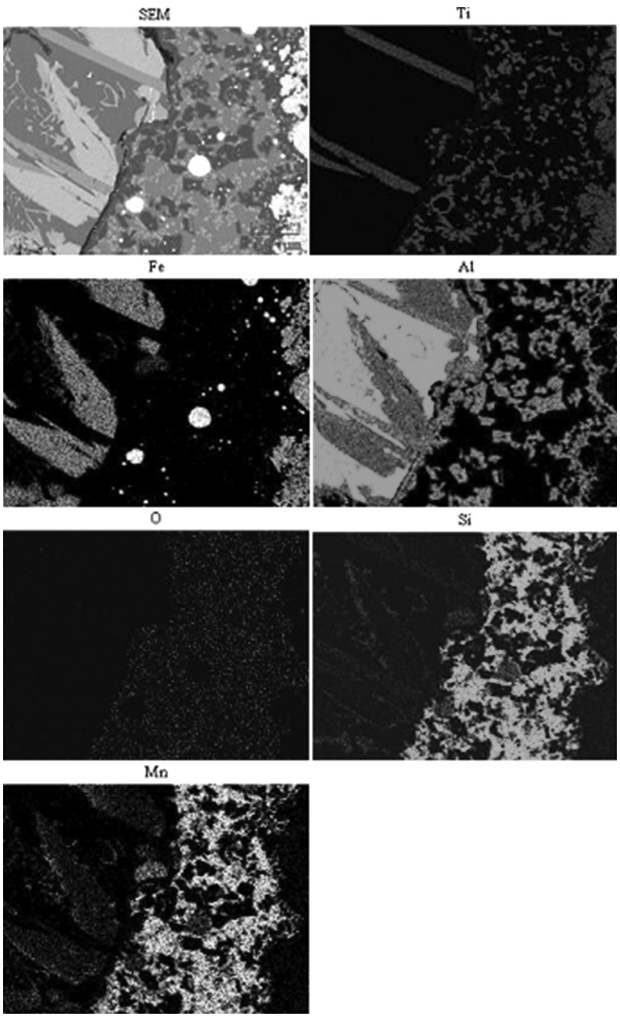

Figure 9: Mapping of the slag
Slika 9: Ploskovna porazdelitev elementov v žlindri

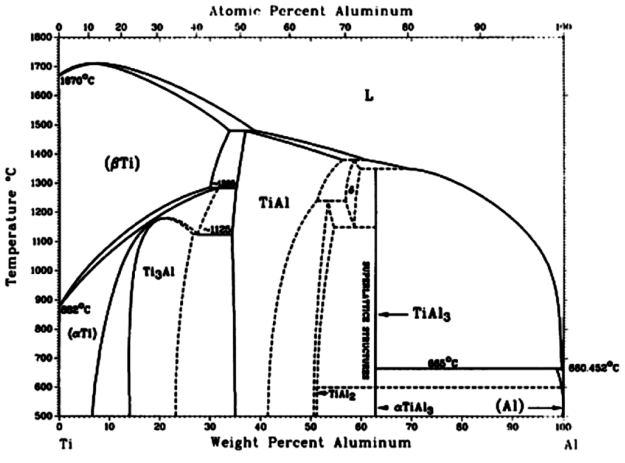

Figure 10: Ti-Al binary phase diagram[12]
Slika 10: Binarni fazni diagram Ti – Al[12]

Next the slag was analysed in order to further widen the understanding of the processes that took place during alloying. An interesting discovery was made during the analysis of the slag: a relatively large content of metallic phases.

The content of the elements is clearly shown in **Figure 9**, where the metallic parts in the slag are mostly aluminium, but the most important factor is that the metallic parts contain reduced titanium and that can be directly linked to a lower yield. There is also a significant amount of titanium in the oxide part of the slag as shown in **Figure 9**. A part of the alloying mixture had clearly floated onto the surface and got entrapped in the slag.

4 DISCUSSION

Alloying titanium into the steel melt by alumothermicaly reducing ilmenite can be divided into several stages: heating up the alumothermic mixture, the alumothermic reaction, the formation of alloys and intermetallic phases of iron, titanium and aluminium, the dissolution of the intermetallic phases and, therefore, titanium into the steel melt, and the reaction between titanium and nitrogen in the steel melt. The first part of the experiments showed us that elemental titanium does not form, instead intermetallic phases are formed and they consist mostly of aluminium. These results can be compared with those of N.J. Welham and associates, considering that the surplus of aluminium they used was significantly higher.[11] Possible future work should consider that aluminium is not needed just for the reduction, but for forming the alloys with titanium. The phase that contained the highest amount of titanium, 45.5 %, the phase number 2 from **Table 1**, was based on aluminium. It is clear that the tendency of titanium to form intermetallic phases with aluminium is higher than that to form them with iron. It can be speculated, from the phase diagram Ti–Al (**Figure 10**), that Al_3Ti with 63 % Al and 27 % Ti forms during the alumothermic reduction.[12] But in the cases that have a lower surplus of aluminium, AlTi should form, as can be seen from the Ti–Al phase diagram.

The experiments that dealt with the alloying of titanium into the steel melt show us quite a different problem than that of getting the right molar ratio of the ingredients for the reduction: the problem of a lower density and, therefore, buoyancy. A large part of the titanium that was reduced in the melt ended up in the slag due to its floating onto the surface of the melt and into the slag. The products of the alumothermic reduction were found in the slag together with aluminium. The metallic phases, especially aluminium, in the slag indicate that not only did some products of the reduction get entrapped in the slag, but aluminium and unreduced ilmenite did as well and the reduction also took place in the slag. The other part of the titanium was alloyed into the melt and formed nitride inclusions in the steel melt. A part of the alumothermic products clearly had time to dissolve in the melt.

A study of the thermodynamic stability of the intermetallic phases of aluminium and titanium and their effect on the thermodynamics and kinetics of the reduction should be made and their ability to dissolve in liquid steel should be observed. Further experiments with cored-wire injections should be studied. The effect of such alloying on the number and size of non-metallic inclusions should be studied as well.

5 CONCLUSIONS

Titanium can be alloyed into the steel melt by alumothermicaly reducing ilmenite.

Intermetallic phases of titanium and aluminium, not elemental titanium, form during the reduction.

The forming of intermetallic phases of titanium and aluminium requires an even higher surplus of aluminium.

The low density of the ingredients for the alumothermic reduction and the products further decreases the yield.

6 REFERENCES

[1] M. Ohno, C. Murakami, K. Matsuura, K. Isobe, Effects of Ti Addition on Austenite Grain Growth during Reheating of As-Cast 0.2 mass% Carbon Steel, ISIJ International, 52 (**2012**) 10, 1832–1840

[2] J. Jong-Oh, K. Wan-Yi, K. Dong-Sik, P. Jong-Jin, Thermodynamics of Titanium, Nitrogen, and Oxygen in Liquid Alloy Steels, Metals and Materials International, 14 (**2008**) 4, 531–537

[3] Extraction of Titanium – the Kroll process, available from: http://wwwchem.uwimona.edu.jm/courses/titanium.html

[4] G. Volkert, K. D. Frank, Metallurgie der ferrolegierungen, Berlin Heidelberg New York, 1972

[5] H. Okamoto, Fe-Ti (iron-titanium), Journal of Phase Equilibria, 17 (**1996**) 4, 369

[6] B. Koroušič, J. Triplat, B. Arh, Improvements To The Production Process For Stainless Steel Alloyed With Titanium, Mater. Tehnol., 37 (**2003**) 6, 347–352
[7] HTC Chemistry 5, (software)
[8] J. Wan Kim, S. Koo Kim, D. Sik Kim, Y. Deuk Lee, P. Keun Yang, Formation Mechanism of Ca-Si-Al-Mg-Ti-O Inclusions in Type 304 Stainless Steel, ISIJ International, 36 (**1996**), S140–S143
[9] P. Jong-Jin, J. Yong-Soo, H. In-Kook, C. Woo-Yeol, K. Dong-Sik, L. Yun-Yong, Thermodynamics of TiN Formation in Fe-Cr Melts, ISIJ, 45 (**2005**) 8, 1106–1111
[10] G. Yang, K. Kenichi Sorimachi, Formation of Clogging Materials in an Immersed Nozzle during Continuous Casting of Titanium Stabilized Stainless Steel, ISIJ International 33 (**1993**) 2, 291–297
[11] N. J. Welham, Mechanochemical reaction between ilmenite (FeTiO) and aluminium, Journal of Alloys and Compounds, 270 (**1998**) 1, 228–236
[12] ASM handbook, Vol. 3 – Introduction to Alloy Phase Diagrams, ASM International, 1992

UDK 621.78.019.84:621.318.1:537.622
Original scientific article/Izvirni znanstveni članek

ISSN 1580-2949
MTAEC9, 47(2)223(2013)

ANALYSIS OF CORROSION PROPERTIES OF MELT SPUN Nd-Fe-B RIBBONS COATED BY ALUMINA COATINGS

ANALIZA KOROZIJSKIH LASTNOSTI HITRO STRJENIH Nd-Fe-B-TRAKOV, OPLAŠČENIH Z ALUMINIJEVIM OKSIDOM

David Sojer[1], Irena Škulj[2], Spomenka Kobe[1], Janez Kovač[1], Paul John McGuiness[1]

[1]Institut "Jožef Stefan", Jamova cesta 39, 1000 Ljubljana, Slovenia
[2]Magneti Ljubljana, d. d., Stegne 37, 1000 Ljubljana, Slovenia
davidsojer@yahoo.com

Prejem rokopisa – received: 2012-12-04; sprejem za objavo – accepted for publication: 2013-02-05

We have coated Nd-Fe-B melt spun powders, used for the production of bonded magnets via the sol-gel route by Al_2O_3. Topography and chemical composition of as-spun and protected ribbons was compared by Auger electron spectroscopy, X-ray photoelectron spectroscopy, secondary electron spectroscopy and electron diffraction spectroscopy. To determine the corrosion properties, we have conducted a Highly accelerated stress test, at 110 °C and 90 % humidity, followed by measuring the weight change. To confirm the effectiveness of the coated layer, magnetic properties were compared with a vibrating sample magnetometer. Al_2O_3 coatings resulted in superior corrosion resistance and magnetic properties and thus expanding the applicability of bonded magnets to severe atmospheric conditions.

Keywords: Nd-Fe-B, bonded magnets, HAST, Al_2O_3 coatings

S sol-gel metodo smo oplaščili hitro strjene Nd-Fe-B-trakove za uporabo pri izdelavi plastomagnetov. Za analizo topografije in kemične sestave hitro strjenih in oplaščenih trakov smo uporabili Augerjevo elektronsko spektroskopijo, rentgensko fotoelektronsko spektroskopijo, spektroskopijo sekundarnih elektronov in elektronsko difrakcijsko spektroskopijo. Za določitev protikorozijske učinkovitosti oplaščenja smo izvedli pospešeni stresni preizkus pri temperaturi 110 °C in 90-odstotni vlažnosti, čemur je sledila analiza masnih izgub. Z vibracijskim magnetometrom smo primerjali magnetne lastnosti prahov pred oplaščenjem in po njem. Oplaščenje z Al_2O_3 se je izkazalo kot izvrstna protikorozijska zaščita materiala, ki je odlično zaščitila tudi magnetne lastnosti. Aplikacije plastomagnetov se s tem lahko razširijo tudi na področja, ki zahtevajo zahtevnejše atmosferske razmere, tj. pri višjih temperaturah in visoki vlažnosti.

Ključne besede: Nd-Fe-B, plastomagneti, HAST, oplaščenje z Al_2O_3

1 INTRODUCTION

Nd-Fe-B magnets market continues to grow[1]. They possess a high magnetic energy product, a combination of a high remanence (B_r) and sufficient coercivity (H_{cI}), a much desired property allowing miniaturization and diversification of application. Automotive industry, hard drives, or wind turbines are just am exemple of application where their use can be found[2].

Nd-Fe-B magnets can be produced by sintering or by bonding. Sintered magnets possess magnetic properties as high as with a B_r up to 1.4 T and an H_{cI} up to 2500 kA/m [3]. Machining is used to give the magnets their final shape. In contrast to sintered magnets, bonded Nd-Fe-B magnets are produced by blending various polymer binders, such as epoxy or nylon, where melt-spun ribbons play the role of raw material[4]. The blend is cast moulded or injection moulded into final shape. Therefore, bonded magnets are chosen when complex shapes are demanded, with the advantage of being less expensive than sintered magnets. The magnetic properties of bonded magnets are, however, inferior to those of sintered magnets. Commercial bonded magnets have a B_r up to 0.7 T and an H_{cI} up to 1400 kA/m.

Nd-Fe-B magnets are very susceptible to corrosion, mainly due to the high rare-earth content in the grain-boundary phase[5]. Susceptibility to corrosion is naturally increased at elevated temperatures and especially in humid environments, affected by rare-earth elements. This restricts not only their range of applications, but can also damage the magnetic material during the moulding process[6–8].

Adjusting the composition, by adding Co, Ga or TiC to the melt-spun ribbons[9,10] improves the corrosion resistance, but it also affects the magnetic properties, by reducing either the H_{cI} or B_r – or both of them. However, even with an optimized composition, additional corrosion protection is necessary. Attempts to protect the surface of ribbons have ben reported, such as direct surface oxidation during rapid solidification, electroplating, chemical vapour deposition and applying thin films of SiO_2, TiO_2 and MgO via the sol-gel route[11,12]. But, difficulties from the perspective of process control and mass production appear. Applying a thin film of SiO_2 or TiO_2 through a sol-gel route offered very good corrosion resistance, especially for TiO_2. The MgO thin film was investigated in strongly acidic media, and good corrosion resistance was reported, but with no corrosion

test in a humid environment. MgO has the same disadvantage as rare-earth elements, since both react rapidly in the presence of humidity.

The sol-gel approach was to some extent put to one side in the past, since the chemical reagents (precursors) used to be extremely expensive. But now, sol-gel precursors are increasingly widely used and more commercially available, while the price of Nd-Fe-B raw material has become extremely expensive and Nd-Fe-B magnets are in greater demand for use at high temperatures. As a result, the sol-gel approach is becoming very interesting from the commercial perspective.

In this paper we present an investigation of sol-gel-applied coatings of Al_2O_3, which were applied directly to the melt-spun ribbons. This method has several advantages over the coating of final products or other coatings, reported by other authors. Firstly, the ribbons are protected from oxidation during transport; secondly, such a coating offers better protection to the final magnets because each piece of melt-spun ribbon is coated; and thirdly, it tends not to reduce the overall Br of the final magnet, which is a problem associated with coating the outside of an already-bonded magnet. Such a coating can provide a much better corrosion-resistant protection than the standard protective film, usually applied around the final-shaped bonded magnet. A protective layer can be scratched off the magnet by force during transport or while installing the magnet into the final application. The same surface scratching does not damage the bonded magnets where the coating has been applied to each individual powder particle, since all the powder particles are coated.

We have investigated the influence of applied coatings on the corrosion resistance of powders in high humidity, using the Highly accelerated stress test (HAST) [13]. The presence of the coating layers was determined by electron diffraction spectrometry (EDS), and X-ray photoelectron spectroscopy (XPS). The appearance of the surface of the samples was analysed by scanning electron microscopy (SEM) before and after the HAST using secondary electron imaging (SEI) as well as backscattered-electron imaging (BEI). The magnetic properties of the samples before and after exposure to the HAST were analyzed with a vibrating-sample magnetometer (VSM).

2 EXPERIMENTAL

MQB commercial melt-spun ribbons, put through a sieving analysis, in the mesh between 100 μm and 250 μm were selected for the experimental work. We chose this size range because this is the standard size for the production of bonded Nd-Fe-B magnets. We analysed the powders using a SEM JEOL 7200. The samples for the SEM analysis were prepared by mixing the powder of selected size with acrylic resin, which was followed by the standard metallographic procedure of grinding and polishing. The result was a metallographic sample that contained a large number of powder particles, where we could observe the cross-section of the particles.

This was followed by the sol-gel process; the details of the sol-gel process are presented in **Figure 1**. The powders were first degreased and cleaned in isopropanol (IPA) and acetone, then dried at 60 °C, 1 h. 0.5 g of Al_2O_3 precursor, aluminium isopropoxide was added to 100 mL of IPA, respectively. 10 g of MQB powder in were added to 100 mL of IPA and stirred. The mixture of precursor and IPA was then slowly added to a mixture of MQB powders and IPA, while stirring to ensure an even distribution of precursor, powder and IPA. No water was added to promote the chemical reaction. The mixture of powder, aluminium isopropoxide and IPA was stirred for 10 min, and then the IPA was removed from the powders. The powders were then dried at 60 °C for 15 min,

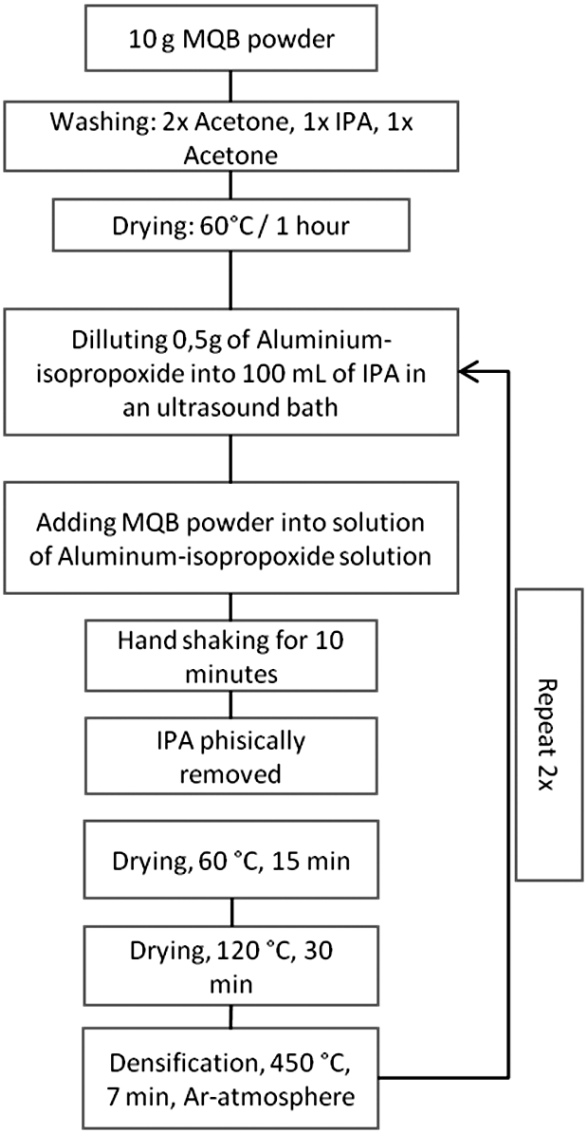

Figure 1: Scheme of the sol-gel process
Slika 1: Shema sol-gel procesa

followed by additional drying at 120 °C for 30 min. The coated powders were then put in a glass tube under an argon atmosphere and heated to 450 °C for 7 min to densify the Al_2O_3 coating. Three coatings were applied by repeating the above-described process two more times. This treatment was applied because we wanted to thicken the Al_2O_3 coating and to ensure that all the particles were covered with Al_2O_3, leading to full coverage of the surface.

The presence of the coating layer was confirmed by XPS spectrometer produced by Physical Electronics Inc., model TFA XPS. The Al monochromatized source of X-ray light with the power of 200 W was used. The energy of the X-ray beam was 1486.6 eV. The analysis area was 0.4 mm in diameter. The energy scale was aligned to the carbon C 1s spectrum at 284.8 eV. Main peaks in this spectrum are O 1s, C 1s, Al 2p, Al 3s and Fe 2p. Unfortunately the Nd 3d peak at binding energy of 980 eV was not possible to identify in this spectrum due to strong overlap with oxygen KLL peak at this energy. Also the boron peak B 1s at energy of 190 eV is not visible due to low sensitivity of B in XPS spectroscopy.

We also took advantage of the XPS and used it to perform a profile analysis on the Al_2O_3 coated particles in order to determine the thickness of the Al_2O_3 coating layer. The sputtering rate was estimated to be about 2 nm/min on the Ni layer of known thickness. Relative sensitivity factors provided by instrument producer were used to calculate elemental concentrations. The analysis depth of the XPS method is about 3–5 nm.

HAST followed the XPS analysis to determine the corrosion behaviour of the uncoated and coated particles. The HAST experiment was performed in an industry-standard HAST chamber, type Kambič. The conditions of the corrosion test were 110 °C, 90 % humidity, and the duration of the corrosion test was set to 192 h (8 d). The powders were carefully weighed to (2 ± 0.01) g before the HAST test, with an accuracy of ±0.1 mg, and placed in separate Al_2O_3 vessels. During the corrosion test, the powders were removed from the HAST chamber every 48 h, with the purpose of following the corrosion rate. After each removal the vessels containing the powders were dried at 120 °C, for exactly 30 min, then weighed. This step was repeated until the final 192 h. Weight change was calculated as a weight increase expressed in a mass fraction (w/%)using the equation:

$$(\text{mass}\ (x\ h) - \text{mass}(0\ h)) / \text{mass}\ (0\ h)$$

with x being the number of hours inside the HAST chamber.

We also used the SEM to observe the surface topology of the MQB powders to compare the effect of temperature and humidity on coated and uncoated particles.

VSM measurements were conducted on a Lakeshore 7307 VSM, which was used to compare the magnetic properties of the as-spun and the sol-gel-coated ribbons with the ribbons subjected to the HAST test.

3 RESULTS AND DISCUSSION

The SEM analysis of the selected powders showed that the actual size distribution is larger. The reason for that can be seen in **Figure 2**. The powder particles are far from being spherical; rather they are thin, elongated particles of irregular shape.

Following the SEM analysis the particles were cleaned. In this way we were hoping to remove all the dust, grease, and at least partially also the Nd-oxide layer from the surface. Cleaning the surface was also necessary as part of the preparation for coating via the sol-gel route.

EDS analysis of the sol-gel-processed powders showed the presence of aluminium. The results are given in **Table 1**. **Figure 3** presents a SEI image of the coated powders, with spots indicating the points of EDS analyses. The oxygen content cannot be determined using EDS, for the reasons already mentioned. Also, it is

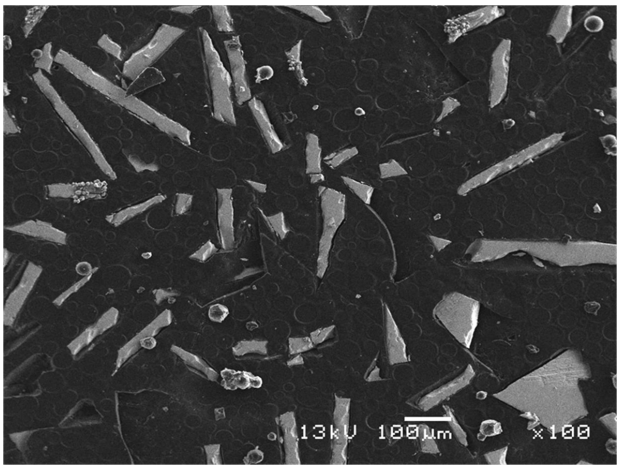

Figure 2: SEI image of MQB as-spun ribbons
Slika 2: SEI-posnetek MQB hitro strjenih trakov

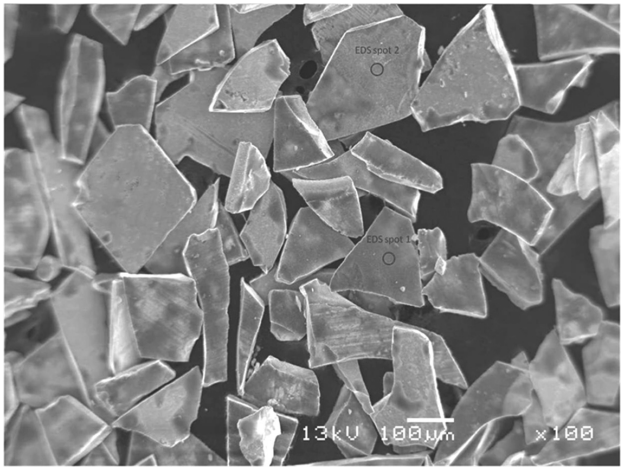

Figure 3: SEI image of Al_2O_3 sol-gel-processed powder, with marked spots for EDS analysis
Slika 3: SEI-posnetek prahu, oplaščenega z Al_2O_3 po sol-gel metodi, z označenimi točkami, kjer so bile izvedene EDS-analize

clear that the aluminium concentration varies a lot, probably for the same reasons as mentioned in the previous section for SiO_2 coated particles. Nevertheless, aluminium was present at all the measured points, from which we concluded that the particles were fully covered.

Table1: Results from the EDS analysis of Al_2O_3 sol-gel-processed powder
Tabela 1: Rezultati EDS-analize prahu, oplaščenega z Al_2O_3 po sol-gel metodi

Element	spot 1 (*x*/%)	spot 2 (*x*/%)
Al	14.8	3.53
Fe	73.77	82.43
Nd	11.43	14.04

To prove the presence of an Al-oxide structure on the particle surfaces we used XPS. Since XPS can be used for depth-profile analyses we tried to determine not only the composition of the top layer, but also to determine how thick the oxide layer is. The results of the depth profile by XPS are presented in **Figure 4**. It is clear that Al and oxygen are present in high concentrations throughout the measured depth profile. There is also some Nd present in the top layer. In contrast, iron is not present in the top layer; its concentration rises slowly towards the end of the measured profile.

From this we could draw two conclusions. First, Al-oxide of some sort is present throughout the measured profile. The most probable composition of this oxide is Al_2O_3, since it is the product of the sol-gel reaction. Second, the measured compositions are rather stable throughout the measured profile. This is attributed to the diameter of the sputtering beam, which was estimated to be 0.4 mm and the possible tilt angle of the measured particle to the sputtering beam. First is beyond the size range of the measured powder (0.1–0.25 mm), meaning that the sputtering might have been conducted on neighbouring powder particles, resulting in a very stable, and misleading, concentration depth profile. The tilt angle is difficult to control, since we are dealing with rather small particles, which align randomly. So, we could have been sputtering a particle, which was not exactly perpendicular to the sputtering beam, causing a seemingly thicker layer of elements than they actually are. On the other hand, it could mean this is the actual depth profile, meaning the oxide layer is thicker than the measured profile.

3.1 HAST

Uncoated, and Al_2O_3-coated particles were put through the HAST, as described previously. The mass change in the mass fractions (%) is given in **Figure 5**. All the particles gained weight rapidly during the first 48 hours. However, the mass increase of the uncoated particles was much higher than that of all the coated particles. The Al_2O_3 coated only once provided good corrosion protection, but Al_2O_3 was clearly more effective. After the first 48 h the rate of oxidation of the Al_2O_3 coated particles was still approximately three times slower than that of the uncoated particles.

It is unknown to us, why the weight increase rate in the first 48 h is much higher than in the following time. It could be possible that moist oxidized the Nd-Fe-B flakes in case of uncoated particles, while in the case of sol-gel coated particles some moist diffuses into the gelated coating, due to H_2O deprivation inside the coated layer. Second option is that some water diffused through the coating layers under the effect of high pressure and temperature. It would be impossible to evaporate this water during drying. But it is difficult to provide information, whether this water formed to create oxides. If it did, we should observe some spalling behaviour of the coating layer on the SEI images on **Figure 5**. But no spalling was found.

The SEM images shown in **Figure 6** reveal the difference between the uncoated and coated particles. The uncoated particles are clearly corroded, while the Al_2O_3

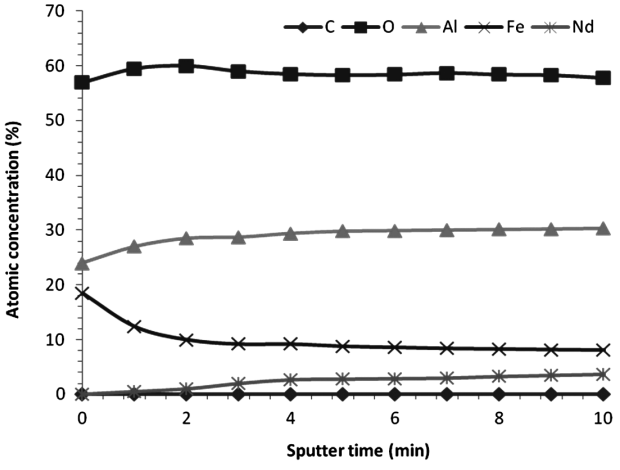

Figure 4: XPS depth profile on Al_2O_3 coated powder
Slika 4: Profilna XPS-analiza prahu, oplaščenega z Al_2O_3

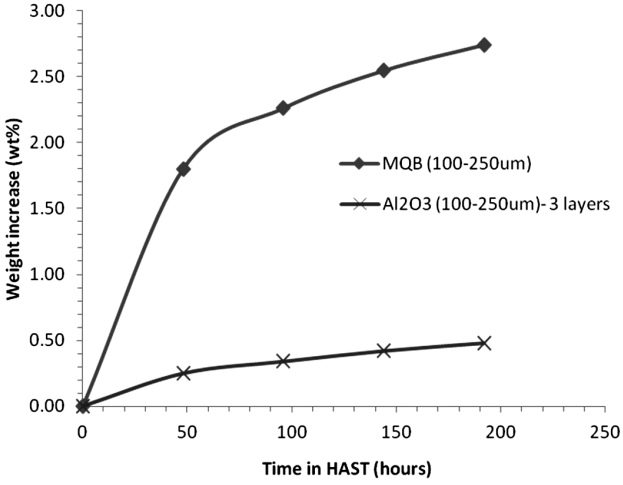

Figure 5: Effectiveness of the Al_2O_3 coating during the HAST
Slika 5: Učinkovitost Al_2O_3 oplaščenja po HAST-u

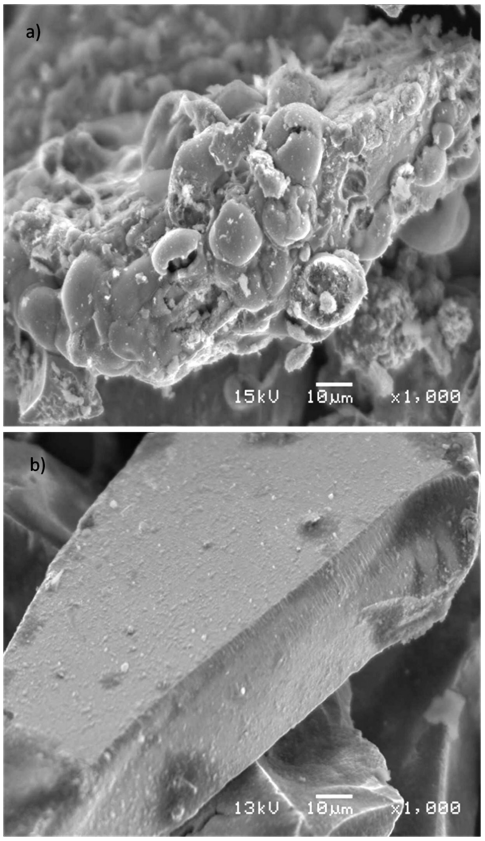

Figure 6: SEI images of particles after HAST: a) uncoated, b) Al_2O_3 – three times coated

Slika 6: SEI-posnetki prašnih delčkov po HAST-u: a) neoplaščeni, b) oplaščeni z Al_2O_3 (3-krat)

coated particles look unaffected by the conditions of the test. The Al_2O_3 particles that were coated three times, in particular, do not look any different than prior to the HAST experiment. Also, we could not spot any spalling behaviour.

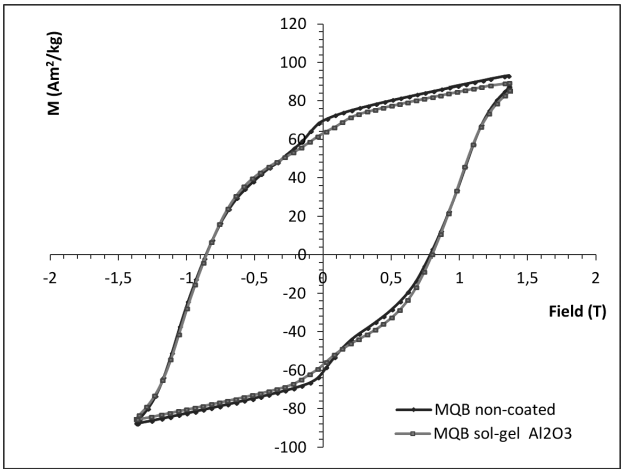

Figure 7: VSM comparison of magnetic properties between powders prior to the HAST

Slika 7: Primerjava magnetnih lastnosti neoplaščenih in oplaščenih prahov pred HAST-om

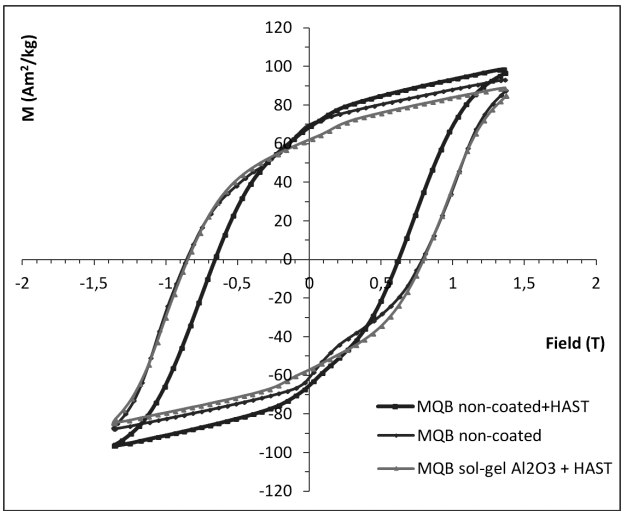

Figure 8: VSM measurements of the uncoated powder and coated powders after the HAST

Slika 8: Primerjava magnetnih lastnosti neoplaščenih in oplaščenih prahov po HAST-u

3.2 VSM measurements

We measured uncoated and Al_2O_3 coated MQB powders before and after the HAST. The results presented as a $B - H$ curve, normalized to sample mass can be seen in **Figures 7** and **8**. For a clearer view, **Figure 7** contains only the results of the powders prior to the HAST, while **Figure 8** represents powders after the HAST test, and the MQB powder prior to HAST test, as a comparison. The H_{cI} is plotted on the x-axis, while the B_r is plotted on the y-axis.

As can be seen in **Figure 8**, the MQB uncoated and Al_2O_3 coated samples' magnetic properties are practically identical.

As for the H_{cI} of the uncoated powder, it dropped by 20 % after the HAST. This drop in H_{cI} can be attributed to corrosion, which changes the microstructure of the affected particle. Al_2O_3-coated powder lost magnetic none of the magnetic properties after the HAST, showing the coating layer to be extremely effective.

4 CONCLUSIONS

1. We have successfully coated Nd-Fe-B powders with Al_2O_3 using the sol-gel process.
2. VSM measurements proved the effectiveness of Al_2O_3 coating, since magnetic properties remained as prior to the HAST test.
3. The sol-gel coating technique of Al_2O_3 proved to be a reliable and non-complicated process for enhancing the corrosion properties of the Nd-Fe-B powders, suitable for mass production.
4. This method is unique compared to other techniques, since it protects all the individual magnetic powder particles, making the corrosion protection much more reliable. Thus, the magnetic raw material is protected

from atmospheric conditions throughout the production process, starting with the transport of the powder, the moulding, installing into the final application, and use during the final application.

5. With the price of used metal alkoxide precursor falling rapidly, this process offers a commercially affordable corrosion-protection route for Nd-Fe-B melt spun ribbons used in bonded magnets.
6. We have demonstrated that the application of bonded magnets can be expanded to high-temperature and high-humidity environments, ranging up to 110 °C and 90 % humidity.

Acknowledgments

This research was partially financed by the European Union.

5 REFERENCES

[1] L. Yang, Development of NdFeB Magnet Industry in New Century, Journal of Iron and Steel Research, 13 (**2006**), 1–11

[2] L. Yang, The inexorable rise of China's NdFeB magnet industry, Metal Powder Report, 63 (**2009**), 8–10

[3] B. M. Ma, J. W. Herchenroeder, B. Smith, M. Suda, D. N. Brown, Z. Chen, Recent development in bonded NdFeB magnets, Journal of Magnetism and Magnetic Materials, 239 (**2002**), 418–423

[4] H. Masaaki, Overview and outlook of bonded magnets in Japan, Journal of Alloys and Compounds, 222 (**1995**), 8–12

[5] G. Yan, P. J. McGuiness, J. P. G. Farr, I. R. Harris, Environmental degradation of NdFeB magnets, Journal of Alloys and Compounds, 478 (**2009**), 188–192

[6] J. Xiao, J. Otaigbe, Polymer-bonded magnets III. Effect of surface modification and particle size on the improved oxidation and corrosion resistance of magnetic rare earth fillers, Journal of Alloys and Compounds, 309 (**2000**), 100–106

[7] Q. Chen, J. Asuncion, J. Landi, B. M. Ma, The effect of the coupling agent on the packing density and corrosion behavior of NdFeB and SmCo bonded magnets, Journal of Applied Physics, 85 (**1999**), 5684–5686

[8] D. N. Brown, Z. Chen, P. Guschl, P. Campbell, Developments with melt spun RE–Fe–B powder for bonded magnets, Journal of Magnetism and Magnetic Materials, 303 (**2006**), 371–374

[9] A. Gebert, M. Rada, A. Kirchner, J. Lyubina, O. Gutfleisch, L. Schultz, Corrosion Behavior of NdFeB-Based Nanocrystalline Permanent Magnets, Journal of Metastable and Nanocrystalline Materials, 631 (**2005**), 631–634

[10] A. A. El-Moneim, A. Geberta, M. Uhlemann, O. Gutfleisch, L. Schultz, The influence of Co and Ga additions on the corrosion behavior of nanocrystalline NdFeB magnets, Corrosion Science, 44 (**2002**), 1857–1874

[11] S. N. B. Hodgsoa, C. G. Hoggarth, H. A. Davies, R. A. Buckley, Protection of NdFeB magnets by ultra-thin sol gel derived films, Journal of Materials Processing Technology, 92–93 (**1999**), 518–524

[12] Q. Li, S. Y. Zhang, J. P. Wang, H. Gao, Process analysis of MgO film on NdFeB magnet by sol–gel method, Surface Engineering, 25 (**2009**), 589–593

[13] N. Sinnadurai, The correct model for and use of HAST, International symposium on microelectronics, Boston MA, 4339 (**2000**), 733–736

UDK 669.131.6
Professional article/Strokovni članek

ISSN 1580-2949
MTAEC9, 47(2)229(2013)

INFLUENCE OF THE MICROSTRUCTURE ON MACHINING A CENTRAL HOUSING MADE OF PEARLITE GREY CAST IRON

VPLIV MIKROSTRUKTURE NA OBDELOVALNOST CENTRALNEGA OHIŠJA IZ PERLITNE SIVE LITINE

Neva Štrekelj, Milanka Nunić, Iztok Naglič, Boštjan Markoli

Faculty of Natural Sciences and Engineering, University of Ljubljana, Aškerčeva 12, 1000 Ljubljana, Slovenia
neva.strekelj@omm.ntf.uni-lj.si

Prejem rokopisa – received: 2012-07-31; sprejem za objavo – accepted for publication: 2012-10-03

This article presents the cause(s) of a relatively increased wear and failure of cutting tools during the final treatment of a central housing made of pearlitic (grey) cast iron with lamellar graphite. Castings with a proper (designated as 'good') and an inadequate (designated as 'bad') microstructures were investigated. Chemical analyses showed a higher concentration of carbide-forming elements in the bad casting, particularly at the edges. Vickers hardness was also measured and the results indicated a higher hardness of bad castings. A microstructural analysis showed that the good casting had the targeted microstructure of the pearlitic matrix and the type A graphite with the size of 4–6. In addition to the narrow, initially austenitic zone that extended only by about 200 μm into the bad casting, steadite was observed, which adversely affected the properties. Moreover, the shape of the graphite and its distribution were uneven, which was also reflected in a low machinability of the bad casting. The inner regions of the castings included graphite of a suitable shape and size, while the edges showed that the solidification of the alloy started by following a stable system with a solidification of the primary austenite and continued according to a metastable one. In the bad casting this area occurred just below the surface, while in the good casting it stretched into the interior. In the bad casting the type B graphite was mainly developed. The influence of the quality of the cutting tools was not investigated.

Keywords: microstructure, grey cast iron, machining

Namen članka je bil ugotoviti vzrok relativno povečane obrabe in lomljenja nožev pri obdelavi centralnega ohišja iz perlitne sive litine z lamelnim grafitom. Analiza je bila opravljena na ulitku s primerno (označen kot 'dober' ulitek) in neprimerno (označen kot 'slab' ulitek) mikrostrukturo. Preverjena je bila kemijska analiza. Rezultati so pokazali višjo koncentracijo karbidotvornih elementov v slabem ulitku, zlasti na robovih. Izmerjena je bila mikrotrdota po Vickersu, pri čemer so nastopile težave zajemanja grafita v posamezen vtisek, vendar pa se je izkazalo, da je slabši ulitek trši od dobrega. Analiza mikrostrukture je pokazala, da ima dober ulitek predpisano mikrostrukturo iz perlitne osnove in grafita tipa A, velikosti 4–6. V slabem ulitku je poleg ozke izhodne avstenitne cone, ki se razteza v notranjost le približno 200 μm, opažena še prisotnost steadita, ki neugodno vpliva na lastnosti sive litine. Poleg tega je oblika grafita in njegova porazdelitev neenakomerna, kar se tudi izraža kot slabša obdelovalnost ulitka. V notranjosti ulitkov sta bili velikost in oblika grafita primerni, medtem ko je bilo na robovih opaziti, da se je strjevanje zlitine začelo po stabilnem sistemu z izločanjem primarnega avstenita, nadaljevalo pa po metastabilnem. Pri slabem ulitku je to območje segalo tik pod površino, pri dobrem pa bolj v notranjost. V slabem ulitku se je grafit razvijal večinoma z obliko B. V okviru raziskav vpliv kvalitete rezilnega orodja ni bil obravnavan.

Ključne besede: mikrostruktura, siva litina, končna strojna obdelava

1 INTRODUCTION

A central housing is a casting made of grey cast iron with lamellar graphite in the pearlitic matrix. It is the essential supporting component for a turbocharger, which is under heavy loads so the accuracy and quality of the final machining are essential. The final mechanical machining was carried out using common practice in casting from two different foundries.

The grey cast iron with lamellar graphite is an iron-based alloy with certain amounts of carbon and silicon.[1] It can also contain manganese, phosphorus and sulphur. The toughness and tensile strength of such a material are usually lower because of the graphite lamellae intersecting the metallic matrix, which may also cause a notch effect. Mechanical properties depend heavily on the quantity, size, shape and distribution of the graphite particles.[2–4] The notch effect is more pronounced if these are larger and vice versa.

Moreover, alloying elements can affect the machinability of grey cast iron with lamellar graphite, as grey cast iron with fine lamellae (which is due to the additions of modifying alloying elements) is very hard and has high strength[3]. In practice it is found that the greatest difficulty in the final machining of grey cast iron is the presence of the so-called hard spots.

Therefore, a comparison of the two castings of the central housing from two different foundries was performed in order to establish the effect of the microstructure on machinability. The reasons for the poor machinability of the castings can also be the cutting tools themselves, but this was not studied in this investigation.

The castings supplied by the first foundry were made with the Croning cast procedure, while in the second case the castings were cast into a bentonite-clay-mixture mould.

For a reliable identification of the constitution of grey cast-iron castings and revealing the cause(s) for the poor machinability, it is important to calculate the values of certain indicators of microstructural features. In our case we calculated the following ones: the graphitization factor (k), the amount of eutectic graphite (*AEG*), the degree of saturation (S_C) and the carbon equivalent (*CE*). For calculation purposes the data on chemical compositions were used as supplied by the foundries.

1.1 Calculation of the graphitization factor k (degree of graphitization)

In addition to the slow cooling rates, the cast iron should have a chemical composition ensuring a sufficiently high tendency to form graphite or a tendency towards graphitization. This criterion is met if the graphitization factor k is properly adjusted in relation to the cooling rate or wall thickness of the castings as expressed in the equation (1)[5,6]:

$$k = \frac{4}{3}\,\mathrm{Si}\left(1 - \frac{5}{3\mathrm{C} + \mathrm{Si}}\right) \tag{1}$$

1.2 Calculation of the amount of eutectic graphite (AEG)

$$\mathrm{AEG} = \mathrm{C}_{\mathrm{total}} - 2{,}0 + 0{,}1(\mathrm{Si} + \mathrm{P}) \tag{2}$$

The amount of eutectic graphite (equation (2)[6]) greatly influences the properties of grey cast iron (in addition to the state of the matrix – ferrite and pearlite or pearlite only[7]). Because of its physicochemical properties graphite has a strong, favourable influence in terms of tribology, namely, it reduces the friction and acts as a lubricant for the cutting tools.

1.3 Calculation of the degree of saturation (S_C)

The influence of individual elements on a eutectic composition is expressed with the degree of saturation, which is given as follows (Pfannenschmidt[8]):

$$S_C = \frac{\mathrm{C}}{4{,}23 - 0{,}312\mathrm{Si} - 0{,}330\mathrm{P} + 0{,}066\mathrm{Mn}} \tag{3}$$

1.4 Calculation of the carbon equivalent (CE)

Since grey cast iron contains the chemical elements that promote a formation of graphite instead of cementite, influencing the amount of carbon developed in the form of graphite, it is essential to use an equivalent amount of carbon in a Fe-C system according to the equation (4)[5]:

$$CE = \%\ \mathrm{C} + 0{,}30\ \%\ \mathrm{Si} + 0{,}33\ \%\ \mathrm{P} \tag{4}$$

2 EXPERIMENTAL WORK

In order to identify the cause(s) for the problems arising during the final machining of the castings (the good and the bad one), the following methods were used:

- Light optical microscopy (LOM);
- Chemical analyses via a mass spectroscopy – the results obtained from the foundries were verified;
- Microhardness measurements via Vickers hardness and
- Size, type and distribution of the graphite determination.

According to the given geometry and the final machining process, critical points on the castings were selected and samples were cut out using a water-cooled circular saw (**Figure 1**). The specimens were metallographically prepared and were suitable for determining the shape, size, type and distribution of the graphite without etching. Furthermore, the samples were etched (2 % nital), so that the constitution of the matrix was revealed along with the presence of the other microstructural constituents. The samples prepared in this way were suitable for the microhardness measurements and an investigation using LOM.

The microhardness measurements using the Vickers method were carried out on one good and two bad castings, using a Shimadzu microhardness tester. The used loads were of 100 g with the loading times of 10 s.

The method of LOM using a ZEISS Axio Imager. A1m microscope gave an insight into the size, shape and distribution of the microstructural components.

The procedure for determining the shape, size and type of graphite followed the EN ISO 945: 1994 instructions.[9]

Figure 1: Samples of the: a) good casting and b) bad casting
Slika 1: Vzorci: a) dobrega ulitka in b) slabega ulitka

3 RESULTS AND DISCUSSION

3.1 Calculations

For a reliable identification of the constitution of grey cast-iron castings and determination of the cause(s) for a difficult machining of a product, the values of certain indicators of microstructural features had to be assessed.

In both cases the graphitization factor was greater than 1, i.e., 1.713 and 1.528, which confirmed that the cast iron in our case was grey cast iron. In the good casting the graphitization factor was slightly higher than in the bad one. The values suggested that lamellar graphite should be one of the constituents of a microstructure. It was obvious that the bad casting had a smaller amount of eutectic graphite (1.566) than the good one (1.712), which, of course, caused poorer machinability of the bad casting. The values of the degree of saturation for both castings clearly indicated that microstructural differences in both castings were to be expected. In both castings the alloy was hypoeutectic, since the S_c was less than one in both cases (0.970 and 0.920). When the undercooling of the melt is taken into account (common in the foundry operations) the solidification starts with primary crystallization of both graphite and austenite. With a lower value of the S_C the amount of austenite in the microstructure was higher, thus, when the cooling was fast a higher quantity of pearlite was obtained, which increased the wear of the cutting tools. The values of the carbon equivalent were 4.165 in the good casting and 3.980 in the bad casting indicating that the bad casting is more hypoeutectic than the good one. These calculations alone do not provide sufficient grounds for predicting the casting behaviour during the final machining. Therefore, the measurements of microhardness, chemical analyses and a microstructural characterization of the castings were necessary.

3.2 Microhardness

Microhardness measurements for one good and two bad castings were performed. **Figure 2** shows the points of the microhardness measurements on individual castings. Points 1–6 (**Figure 2a**) on the good casting represent the edges where the process of the machining was carried out. Points 7 and 8 were in the inner region of the good casting. It should be noted that the imprints of the microhardness measurements very often included graphite. This is not in accordance with the principles of reliable hardness measurements, therefore the results are somewhat compromised. But for the evaluation of the casting machinability the hardness of the whole casting is important and, thus, the results clearly indicated why the machining of a bad casting was more difficult and the cutting-tool wear greater.

The microhardness on the edges of the good casting (points 1–5, **Figure 2a**) was 160–260 HV, while for the bad casting (bad 1) it was higher, as high as 350 HV (point 7, **Figure 2b**). Similar values were obtained with the microhardness measurements for the other bad casting (not in **Figure 2**), where the microhardness of the matrix was ≈335 HV. The results of the hardness measurements are graphically presented in **Figure 3**.

Apparently the highest microhardness was on the edges of all the castings, but for the bad castings the values were significantly higher. The difference between the maximum hardness of the bad and the good casting was almost 100 HV, which clearly indicated a higher probability of an increased wear of the cutting tools.

For the clarification of the reasons for the increased tool wear the microhardness measurements were not sufficient. Therefore, the data on the chemical compositions of the castings from the foundries were reviewed.

3.3 Chemical composition of the castings

The results of the microchemical analyses of the good and bad castings were compared considering the foundry data and are summarized in **Table 1**. Chemical analyses revealed small differences between the bad and the good castings in the contents of carbon, silicon and

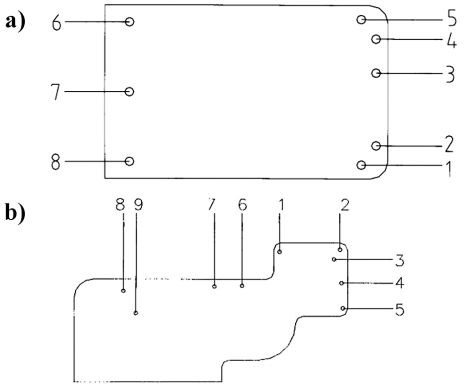

Figure 2: Areas of microhardness measurements: a) good casting, b) bad casting

Slika 2: Področja meritev mikrotrdote: a) dobrega ulitka, b) slabega ulitka

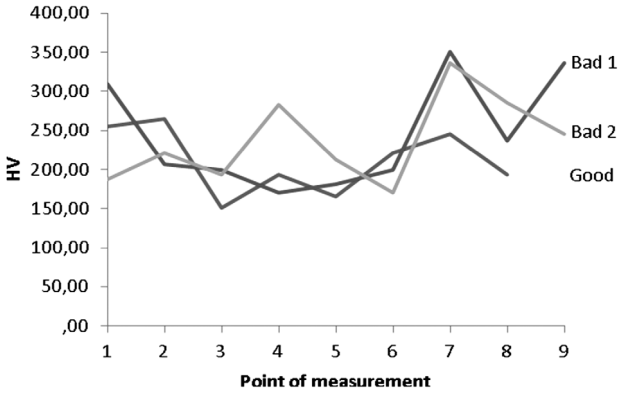

Figure 3: Microhardness measurements where the points of measurements correspond to the numbers in **Figure 2** for the two bad and one good casting

Slika 3: Mesta meritev mikrotrdote, ki odgovarjajo številkam na **sliki 2** v dveh slabih in enem dobrem ulitku

manganese (**Table 1**). The good casting had higher amounts of carbon and silicon, while the content of manganese (as well as chrome, sulphur and phosphorus) was lower. This explained, to a great extent, the difference in the machining between the good and the bad castings.

Table 1: Results of the microchemical analyses carried out in the foundries in mass fractions (*w*/%)
Tabela 1: Rezultati mikrokemijskih analiz iz livarn v masnih deležih (*w*/%)

Element	Good casting (*w*/%)	Bad casting (*w*/%)
C	3.49	3.36
Si	2.13	1.96
Mn	0.51	0.79
Cr	0.06	0.07
P	0.45	0.11
S	0.05	0.06

Lower contents of silicon and carbon with increased levels of manganese meant a higher propensity to white solidification (in the bad casting) and, thus, a higher amount of pearlite. Chromium can also contribute to this by stabilizing and forming carbides, thus increasing the casting hardness. Furthermore, phosphorus formed hard microstructural constituents, for example Fe_3P, which appeared within the ternary eutectic (α_{Fe}+Fe_3C+Fe_3P) called steadite. Ultimately, the casting parameters and casting geometry can influence the homogeneity of a microstructure.

3.4 Metallographic analysis

In this part of the investigation the form and the distribution of the graphite was analysed first.

Based on the images of the good casting (**Figures 4a, b**) graphite was mainly of form A and size 4–6 and its skeleton showed a better contiguity than the one in the bad casting (**Figures 5a, b**). In the bad casting the graphite skeleton was frequently interrupted by austenitic areas, which were also more extensive. This caused a larger dynamic load for the cutting tools because of a great number of the transitions from the areas with a better machinability into the areas with a poorer machinability.

The constitution of the castings after the etching was determined also by using LOM. An image of the edge of the good casting (**Figure 6a**) showed a ferrite-graphite area, which had extended into the casting interior, where the matrix was slowly becoming pearlitic. It was obvious that the solidification of the casting was conducted separately with the primary solidification of the austenite on the edge of the casting and eutectic crystallization of the graphitic eutectic. Then the consecutive evolution of the microstructure followed the constitution of the Fe-Fe_3C system and the microstructure of the casting

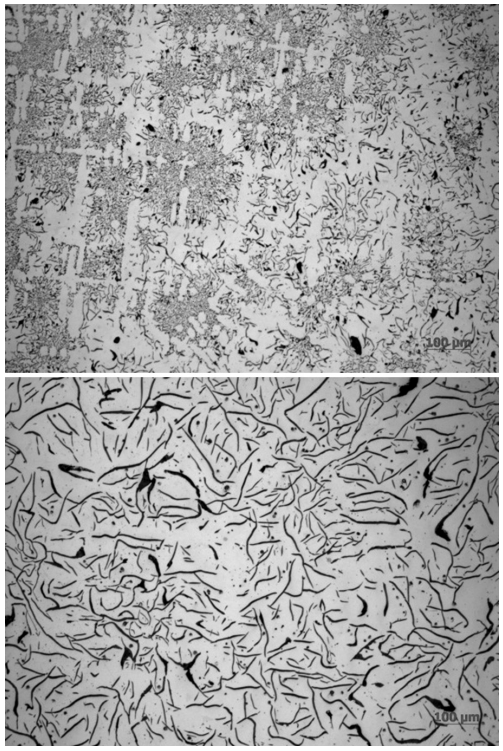

Figure 4: LOM images of the distribution and shape of graphite A, 4–6 in size, in the good casting
Slika 4: Posnetka porazdelitve in oblike grafita A, velikosti 4–6 v dobrem ulitku

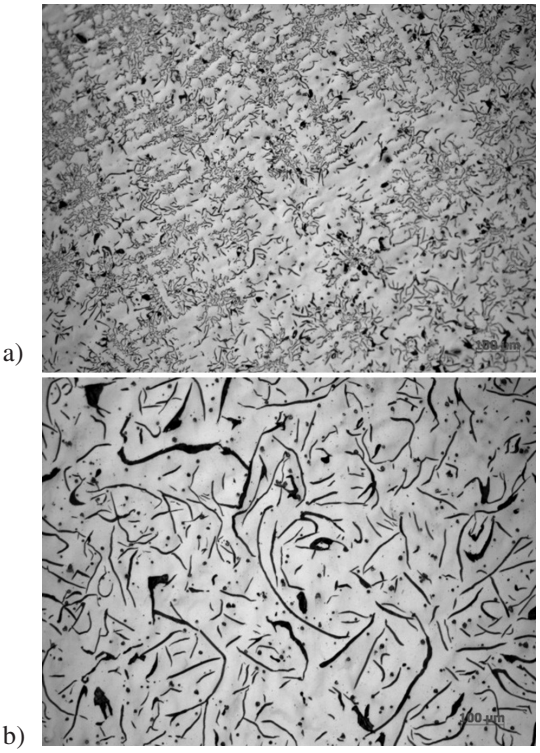

Figure 5: LOM images of the distribution and shape of graphite, showing larger graphite lamellae and a poorer contiguity of the graphite skeleton in the bad casting
Slika 5: Posnetka porazdelitve in oblike grafita, ki kažeta večje grafitne lamele in slabšo kontiguiteto grafitnega skeleta v slabem ulitku

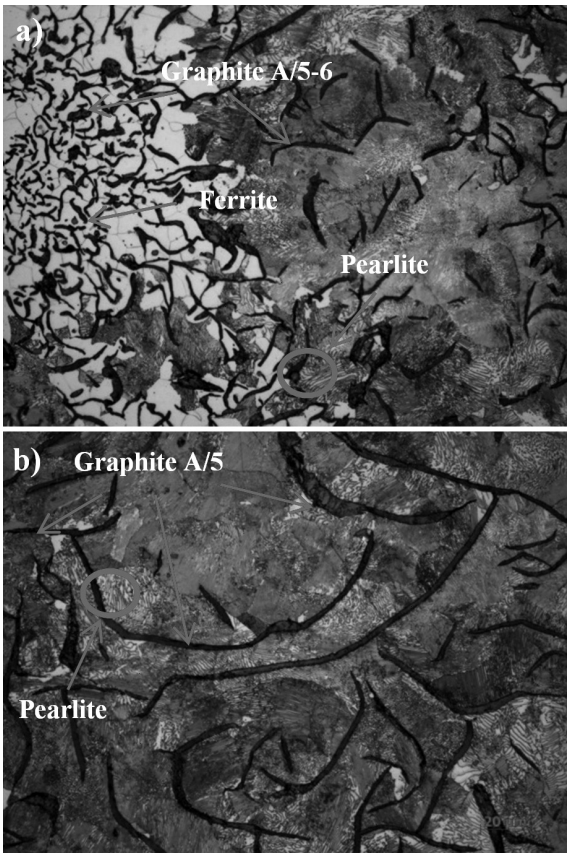

Figure 6: LOM images of the good casting: a) on the edge, showing a ferrite-graphite area and b) in the centre, showing fine lamellar pearlite and graphite lamellae

Slika 6: Posnetka mikrostrukture dobrega ulitka: a) na robu, ki kaže feritno-grafitno območje, in b) v sredini, ki kaže lamelarni perlit in lamele grafita

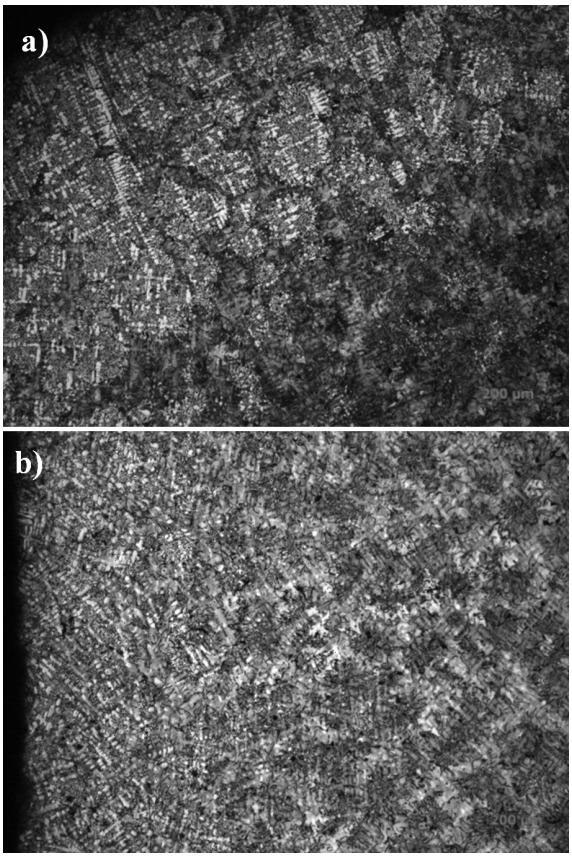

Figure 8: LOM images of: a) the good-casting edge, where the ferrite zone was ≈1200–1500 μm thick and b) the bad-casting edge, where the ferrite zone was only ≈200 μm thick

Slika 8: Posnetka mikrostrukture: a) roba dobrega ulitka, feritno območje sega ≈1200–1500 μm globoko v vzorec in b) roba slabega ulitka, feritno območje sega le ≈200 μm globoko v vzorec

interior consisted of fine lamellar pearlite, interrupted by graphite lamellae (A5) (**Figure 6b**).

Furthermore, the ferrite-graphite zone situated mostly on the edge of the casting extended into the casting interior to a depth of ≈1200–1500 μm. This was exactly the depth to which the cutting tools reached during the final machining. According to the hardness measurements of the matrix on the edge of the casting and the presence of the graphite skeleton, it is clear that the good casting exhibited a better machinability and caused a lower wear of the cutting tools.

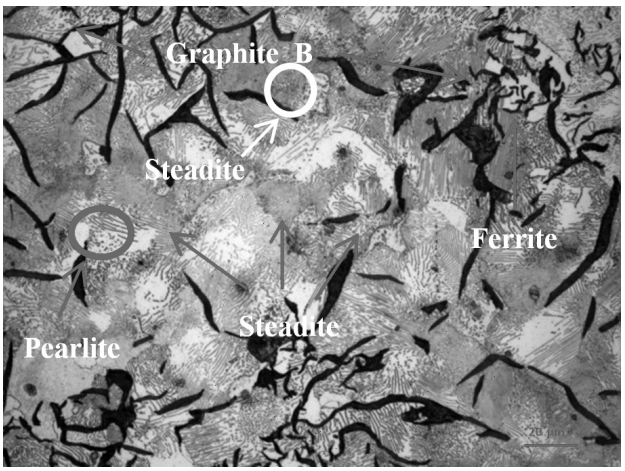

Figure 7: LOM image of the bad-casting edge, showing the pearlite matrix, graphite A-B, 4-5 in size, and steadite

Slika 7: Posnetek mikrostrukture roba slabega ulitka, ki kaže perlitno osnovo, grafit A-B, velikosti 4–5, in steadit

Metallographic analyses of the bad casting showed a pearlite matrix and graphite (A–B and 4–5), but also the presence of steadite (**Figure 7**). In addition to steadite, the form of the graphite was less favourable in terms of the final machinability. The graphite skeleton also has a lower contiguity.

When comparing the depths of the ferrite zones in the good (**Figure 8a**) and bad castings (**Figure 8b**), it was obvious that the latter had a less profound ferrite zone. The depth of this area was only ≈200 μm in the case of the bad casting, while in the good one it was ≈1200–1500 μm. Thus, during the final machining of the bad casting, the cutting tool quickly reached the hard pearlite matrix, which also contained extremely hard and brittle particles of steadite. Because of the coarser and more unevenly distributed graphite in the casting, the wear of the cutting tools was even higher.

4 CONCLUSIONS

In this article the possible causes for a poorer final machinability of grey cast-iron castings with lamellar graphite are discussed and the potential reasons for the increased wear and failures of the cutting tools were presented. The conclusions can be summarized as follows:

- Established calculations confirmed that the investigated material was hypoeutectic grey cast iron with lamellar graphite. The calculations were not absolutely accurate and provided only the information about which type of grey cast iron was most likely to be formed.
- The hardness of grey cast iron with lamellar graphite was measured via Vickers microhardness, because it enables the measurements of the hardness of individual microconstituents and the matrix. The hardness of bad castings was higher than that of the good casting.
- Chemical analyses showed higher contents of manganese and phosphorus in the bad casting and higher silicon levels in the good casting.
- The casting edges of the polished samples showed a dendritic morphology, which was a result of the solidification sequence with primary austenite. Then it transformed into ferrite and graphite and/or into pearlite. In the casting interior we identified the size and shape A of graphite. In the bad casting a larger quantity of type-B graphite with fine lamellar graphite and uneven distribution of graphite was observed.
- The depths of the transformed primary austenite in the bad and good castings were compared and clearly the depth in the good casting was greater.
- Microstructural analyses showed a presence of graphite, pearlite and, on the edges of the casting, also the undercooled D graphite and ferrite. The bad casting also contained a significant amount of steadite, which was one of the main reasons for the difficult final machining of the central housing.
- The main reason for a poor machinability and greater wear of the cutting tools lies in the constitution of the microstructure. The nucleation of austenitic primary crystals and of the graphite from the eutectic is not optimal or it is even harmful. It is obvious that the transformed primary austenitic particles are relatively large. Undercooled forms of graphite were also observed.
- The influence of the cutting-tool quality should be taken into account when the final and definitive reason for the breakage and wear of cutting knives is determined.

5 REFERENCES

[1] Y. Boran, International Iron & Steel Symposium, Karabük, Turkey, 2012

[2] T. Alp, A. A. Wazzan, F. Yilmaz, Arabian Journal for Science and Engineering, 30 (**2005**), 163–175

[3] H. Nakae, H. Shin, Materials Transactions, 42 (**2001**), 1428–1434

[4] D. J. Celentano, M. A. Cruchaga, B. J. Schulz, International Journal of Cast Metals Research, 18 (**2005**), 237–247

[5] D. M. Stefanescu, ASM Handbook, volume 15, Casting, ASM International, 1998

[6] M. Nunić, Influence of microstructure on machining of central housing made of pearlite CI, Diploma work, Ljubljana, 2011 (in Slovenian)

[7] P. Mrvar, M. Petrič, J. Medved, Key Engineering Materials, 457 (**2010**), 163–168

[8] Društvo livarjev LR Slovenije, Žepni livarski priročnik, Ljubljana, Založba Litostroj, 1960 (in Slovenian)

[9] Available from World Wide Web: http://www.atilim.edu.tr/~ktur/mate401/Dosyalar/26-ELKEM_poster-graphite%20structures%20in%20cast%20irons.pdf

UDK 620.3
Professional article/Strokovni članek

ISSN 1580-2949
MTAEC9, 47(2)235(2013)

THE WET-CHEMICAL SYNTHESIS OF FUNCTIONALIZED $Zn_{1-x}OMn_x$ QUANTUM DOTS UTILIZABLE IN OPTICAL BIOSENSORS

MOKRA KEMIJSKA SINTEZA FUNKCIONALIZIRANIH KVANTNIH DELCEV $Zn_{1-x}OMn_x$, UPORABNIH V OPTIČNIH BIOSENZORJIH

Mohamad Alizadeh[1], Reza Salimi[1,2], Hassan Sameie[1,2], Ali Asghar Sarabi[1], Ali Asghar Sabbagh Alvani[2], Mohammad Reza Tahriri[3]

[1]Amirkabir University of Technology, Faculty of Polymer Engineering & Color Tech., 424 Hafez Ave., 15875-4413 Tehran, Iran
[2]Amirkabir University of Technology, Color and Polymer Research Center (CPRC), 424 Hafez Ave., 15875-4413 Tehran, Iran
[3]Amirkabir University of Technology, Biomaterials Group, Faculty of Biomedical Engineering, P.O. Box, 15875-4413 Tehran, Iran
sabbagh_alvani@aut.ac.ir

Prejem rokopisa – received: 2012-08-09; sprejem za objavo – accepted for publication: 2012-10-03

ZnO quantum dots (QDs) were successfully synthesized via the precipitation technique, and the effect of the Mn^{2+} ion concentration as dopant on the optical properties was studied. In order to control the particle size by limiting the growth of the particles after the nucleation and to provide a side group on the surface, which can be further conjugated to bio-cells, polyethylene glycol (PEG) was used as a bio-compatible capping agent. XRD analyses revealed a single-phase ZnO wurtzite crystal structure. A TEM micrograph illustrates that the final QDs were about 15 nm in diameter and had a spherical shape. Also, the organic groups on the surface of nano-particles (NPs) were characterized with Fourier transform infrared spectroscopy (FTIR). It is clear from the photo-luminescence spectra that doping Mn^{2+} ions in the host lattice led to an appearance of a new visible emission band in the range of 410–450 nm because of the $^4T_1 \rightarrow {}^6A_1$ transition. The results show that the final QDs have a potential for biochemical optical sensing.

Keywords: quantum dots, surface modification, biosensor, photoluminescence

Kvantni delci (QD) ZnO so bili uspešno sintetizirani s tehniko izločanja in preučevan je bil učinek koncentracije ionov Mn^{2+} kot dopantov na optične lastnosti. Polietilen glikol (PEG) kot omejitveno sredstvo je bil uporabljen za kontrolo velikosti delcev z omejevanjem rasti delcev po nukleaciji in za zagotovitev posebne skupine na površini, ki jo je mogoče naprej združevati z biocelicami. XRD-analize so odkrile enofazni ZnO s kristalno strukturo wurtzita. Posnetek s TEM pokaže, da so končni QDs okrogle oblike s premerom okrog 15 nm. Organske skupine na površini nanodelcev (NPs) so bile določene s FTIR-spektroskopijo. Iz fotoluminiscenčnega spektra izhaja, da dopiranje ionov Mn^{2+} v gostujočo mrežo povzroči prehod $^4T_1 \rightarrow {}^6A_1$ in zato pojav novega vidnega emisijskega pasu v območju 410–450 nm. Rezultati kažejo, da imajo končni QDs potencial biokemičnega optičnega zaznavanja.

Ključne besede: kvantni delci, modifikacija površine, biosensor, fotoluminiscenca

1 INTRODUCTION

The synthesis of semiconductor quantum dots (QDs) has received a great deal of interest because of their potential for biomedical applications in imaging, drug targeting and delivery. Compared with the conventional organic fluorophores, QDs have significant advantages, for example, a narrow and size-tunable emission spectrum, broadband excitation, a high resistance against photo-bleaching and a good chemical stability[1,2]. Due to their size-dependent properties and dimensional similarities to biomolecules, these bio-conjugate QDs are well suited as contrast agents for the in-vivo magnetic resonance imaging (MRI) as carriers for drug delivery, and as structural scaffolds for tissue engineering[3]. ZnO nano-particles are environment friendly and have a wide band-gap of 3.37 eV and a rather large exciton binding energy, which makes the exciton state stable even at room temperature. Therefore, wide band-gap semiconductor nanocrystals can be doped with transition metal ions[4,5]. An important section of synthesising NPs is surface modification. Most surface modifications of NPs for bio-imaging applications are based on chemisorption since it offers a stronger and more robust bond and a more stable surface ligand, compared with physisorption. A successful conjugation of biomolecules to NPs depends on a proper surface modification. Poly ethylene glycol (PEG) has been commonly conjugated to various drugs, liposomes, polymeric micelles and nanoparticles to prolong their blood-circulation time by reducing the nonspecific adsorption of proteins via a steric stabilization effect[6,7]. In this paper, we report on a wet chemical synthesis of $Zn_{1-x}OMn_x$ QDs and functionalizing them with PEG to achieve the appropriate particle size and good optical properties used in biological labelling. The main advantages of this process are the ability to control the ZnO purity and the use of biocompatible capping agents that provide triple functions: (1) to control the particle size by limiting the growth of the particles after the nucleation, (2) to provide a side group on a surface

that can be further conjugated to a bio-cell, (3) to eliminate surface defects that would affect the optical properties of ZnO nanocrystals.

2 EXPERIMENTAL WORK

Manganese acetate tetrahydrate ($Mn(Ac)_2{\cdot}4H_2O$), zinc acetate dihydrate ($Zn(Ac)_2{\cdot}2.5H_2O$), polyethylene glycol (M_w = 400 g/mol), extra pure water, ethanol and hydroxide sodium were used as the starting materials. We have developed a room-temperature technique for synthesising semiconductor nanocrystals that employs a capping agent to control both the size and the shape. The manganese precursor ($Mn(OAc)_2{\cdot}4H_2O$) dissolved in 1 ml of water and then 100 ml of ethanol was added to the solution. After stirring the solution for 2 h, $Zn(OAc)_2{\cdot}2.5H_2O$ was added; then the temperature raised to 50 °C and the solution was stirred again. After that the obtained solution was quenched in ice, and the required PEG was added as a capping agent. The mixture was again stirred for 3 h and then hydrolyzed by adding NaOH under ultrasound for 2 h. The solvents were then removed with the rotation vaporization. Eventually, the resulting mixture was washed with water leading to a precipitation of $Zn_{1-x}Mn_xO$ nanocrystals. The resulting powders were analyzed with X-ray diffraction (XRD; Bruker AXS: D8 Advance), transmission electron microscopy (TEM; a Hitachi H-800 electron microscope) and fluorescence spectrophotometer (Perkin-Elmer LS-55, the exciting source: a near-ultraviolet-Xenon lamp) and Fourier transform infrared spectroscopy (Equninox-55).

3 RESULTS AND DISCUSSION

ZnO colloids were prepared with the precipitation from the solution using $Zn(CH_3CO_2)_2$ and NaOH. The overall reaction of the synthesis of ZnO nanoparticles from Zn(II) acetate can be written as:

$$Zn(CH_3CO_2)_2 + 2NaOH \rightarrow \rightarrow ZnO + 2Na(CH_3CO_2)_2 + H_2O \quad (1)$$

The XRD pattern of the ZnO nanocrystals synthesized via precipitation is shown in **Figure 1**. The main phase can be indexed to the pure phase of zinc oxide according to JCPDS 80-0075. Also, the wurtzite structure of the ZnO lattice of a nanocrystalline sample can be confirmed.

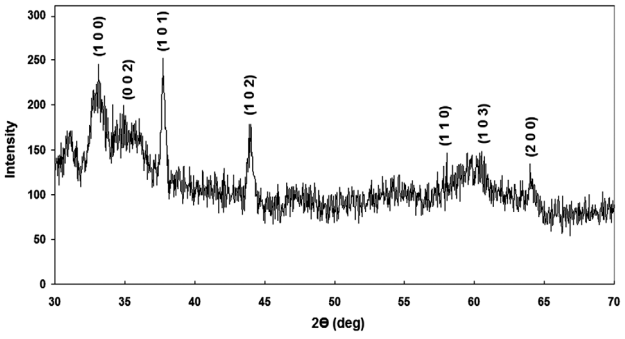

Figure 1: XRD pattern of ZnO prepared with precipitation
Slika 1: Rentgenski praškovni posnetek ZnO, pridobljen z izločanjem

From the FTIR spectrum presented in **Figure 2a**, it is obvious that PEG properly caps the surface of the QDs. The main peaks can be related to different groups as follows: 1) the peaks around 3670 cm^{-1} and 3407 cm^{-1} are due to the O-H stretching; 2) the peaks around (2974, 2916 and 1241) cm^{-1} are attributed to the C-H stretching from the $-CH_3$ alkanes, the C-H stretching from the $-CH_2-$ alkanes and the R-O-R stretching (the conjugate ether), respectively. In addition, the TEM image of the ZnO:Mn QDs caped with PEG is illustrated in **Figure 2b**. It is clearly observed that nanoparticles are spherical in shape and their average size is approximately 10 nm.

The PL spectrum of the Mn-doped ZnO d-dots with different doping concentrations (from mol fraction 0–7 %) are shown in **Figure 3**(**a–d**). It is worth mentioning that by varying the Mn doping concentration, the relative PL intensities of the dual-colour emissions can be well manipulated. The UV emission (356 nm) is characteristics of the ZnO host and usually influenced by the

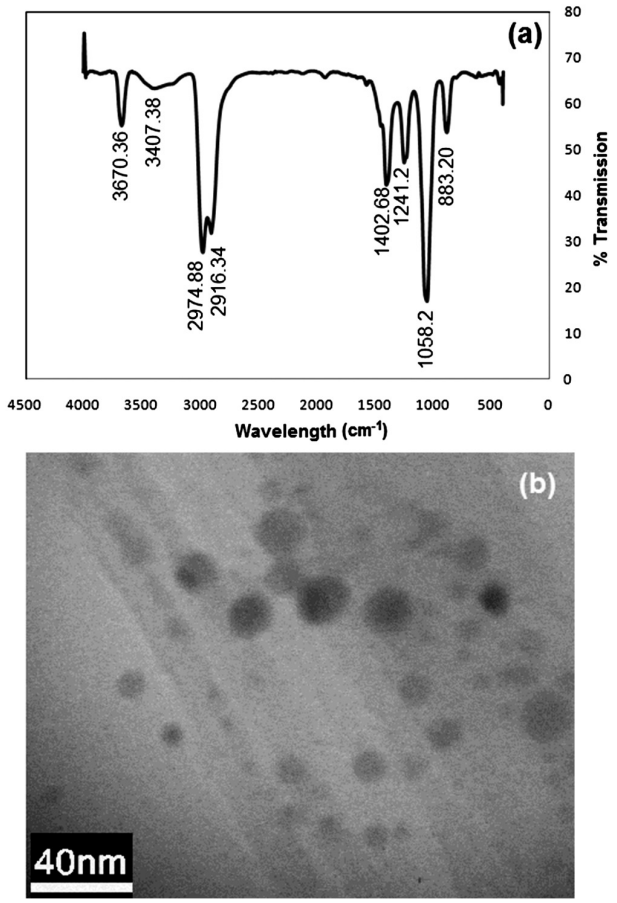

Figure 2: a) FTIR spectra of the PEG-capped ZnO nanoparticles and b) a TEM image of 5 % Mn-doped ZnO nano-particles
Slika 2: a) FTIR-spekter s PEG omejevanih ZnO-nanodelcev in b) TEM-posnetek s 5 % Mn dopiranih ZnO-nanodelcev

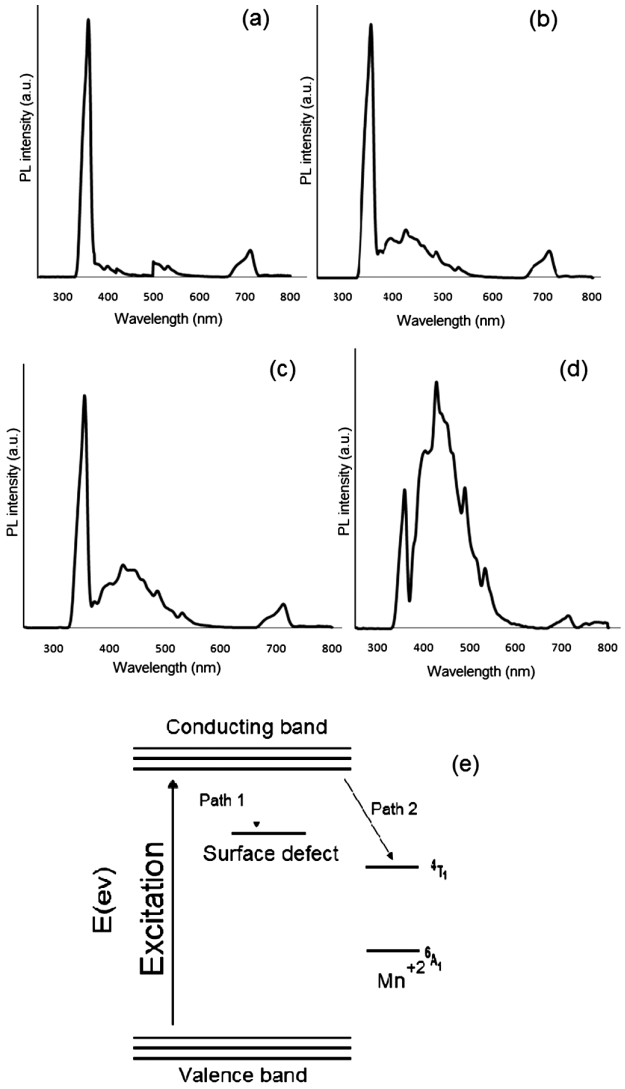

Figure 3: PL emission spectra of the $Zn_{1-x}OMn_x$ QDs with different doping concentrations: a) x = 0 %, b) x = 2 %, c) x = 5 %, d) x = 7 % excited at 325 nm and e) a schematic representation of the emission levels of the Mn-doped ZnO d-dots

Slika 3: Spekter PL-emisij $Zn_{1-x}OMn_x$ QD z različnimi koncentracijami dopiranja: a) x = 0 %, b) x = 2 %, c) x = 5 %, d) x = 7 % vzbujenih pri 325 nm in e) shematičen prikaz nivojev emisij z Mn dopiranega ZnO d-delcev

doping situation. Also, the blue emission band, centred at about 426 nm, is attributed to the transition between the $^4T_1 \rightarrow {}^6A_1$ energy levels of the Mn^{2+} 3d states. A schematic representation of the emission levels of the Mn-doped ZnO d-dots is briefly illustrated in **Figure 3e**. When an intrinsic q-dot is excited by the photons with the energy higher than its band gap, an exciton (an electron-hole pair) will be generated. A direct recombination of an electron-hole pair, typically being quantum-confined in the case of nanocrystals, gives the well-known band-edge emission, or exciton emission. However, the emission of a d-dot is fundamentally different. After the exciton is generated by the absorption of the host semiconductor nanocrystal, the energy of a photogenerated electron and a hole pair will be transferred into the electronic levels of the Mn^{2+} ions. The recombination in a Mn^{2+} ion center leads to the characteristic dopant emission from the Mn^{2+} ion, namely the $^4T_1$ to $^6A_1$ transition.

4 CONCLUSION

In this research, ZnO:Mn QDs have been successfully synthesized with a precipitation synthesis and then the surface of nanoparticles was covered with hydroxyl groups. In the meantime, the effect of the dopant concentration on the optical characteristics was investigated in detail. According to experimental results, the functionalized QDs can be used as a core of optical biosensors after conjugating with the desired anti-bodies.

Acknowledgment

The authors would like to acknowledge the Iranian Nano Technology Initiative Council for supporting the research.

5 REFERENCES

[1] X. Gao, W. Chan, S. Nie, Quantum-dot nanocrystals for ultrasensitive biological labelling and multi color optical encoding, J. Biomed. Opt., 7 (**2002**), 532–537

[2] T. Jamieson, R. Bakhshi, D. Petrova, R. Pocock, Biological applications of quantum dots, Biomater., 28 (**2007**), 4717–4732

[3] A. Smith, H. Duan, A. Mohs, S. Nie, Bioconjugated quantum dots for invivo molecular and cellular imaging, Adv. Drug Deliv. Rev., 60 (**2008**), 1226–1240

[4] Y. Yang, Y. Jin, H. He, Q. Wang, Y. Tu, H. Lu, Z. Ye, Dopant-Induced Shape Evolution of Colloidal Nanocrystals: The Case of Zinc Oxide, J. Am. Chem. Soc., 132 (**2010**), 13381–13394

[5] E. Badaeva, C. M. Isborn, Y. Feng, S. T. Ochsenbein, D. R. Gamelin, X. Li, Theoretical Characterization of Electronic Transitionsin Co^{2+} and Mn^{2+} Doped ZnO Nanocrystals, J. Phys. Chem. C, 113 (**2009**), 8710–8717

[6] H. Mok, K. H. Bae, C. H. Ahn, T. G. Park, PEGylated and MMP-2 Specifically DePEGylated Quantum Dots: Comparative Evaluation of Cellular Uptake, Langmuir, 25 (**2009**), 1645–1650

[7] R. Gref, Y. Minamitake, M. T. Peracchia, V. Trubetskoy, V. Torchilin, R. Langer, Science, 263 (**1994**), 1600–1603

UDK 669.715:620.18:620.17
Professional article/Strokovni članek

ISSN 1580-2949
MTAEC9, 47(2)239(2013)

INFLUENCE OF ALUMINIUM-ALLOY REMELTING ON THE STRUCTURE AND MECHANICAL PROPERTIES

VPLIV VEČKRATNEGA PRETALJEVANJA ALUMINIJEVIH ZLITIN NA STRUKTURO IN MEHANSKE LASTNOSTI

Michal Cagala, Marek Břuska, Petr Lichý, Jaroslav Beňo, Nikol Špirutová

VŠB-Technical University of Ostrava, Faculty of Metallurgy and Materials Engineering, Department of Metallurgy and Foundry, 17. Listopadu 15/2172, Ostrava – Poruba, Czech Republic
michal.cagala@vsb.cz

prejem rokopisa – received: 2012-08-31; sprejem za objavo – accepted for publication: 2012-10-02

The aim of this work was to assess the repeated-remelting influence upon the mechanical properties, thermomechanical properties, chemical composition and structure changes of the selected material. An Al-Cu-type aluminum alloy was chosen on the basis of the ever increasing experiments with non-ferrous metals in the industry. The technical nomenclature of the selected alloy is RR.350 according to the German standard ALUFOND 60. The RR.350 alloy is known for its poor foundry properties which deteriorate due to remelting and affect mechanical properties and the cast-material structure. This negative influence upon the structure and usable properties of a re-melted alloy is further confirmed in the submitted paper. The samples for tensile-strength determination were cast into a metal mould. The gating system and the riser, which served as a charge for the second melt, were removed from the casting. In this way we re-melted the material four times. The samples were machined and ruptured within the temperature range between 20 °C and 350 °C. A sample for metallography and hardness determination (HBS) was taken from the cast material. It can be seen in the tensile-strength diagram that the mechanical properties of the first melt are higher, by 11 % at the temperature of 20 °C, than the properties of the third melt. This difference is evident up to 100 °C. At the temperatures of above 100 °C the cast-material strength characteristics are the same. This tendency shows itself on all the materials tested so far. The hardness and microhardness evaluations show that the material reaches the highest values with the fourth melt. This phenomenon is attributed to the repeated reoxidation and exclusion of oxide membranes. Further, the material structure properties and chemical-composition change were evaluated. The results of this study confirmed a negative influence of alloy remelting upon the material properties and structure.

Keywords: aluminium alloys, metallographic analysis, microstructures, thermomechanical properties, remelting, mechanical properties

Namen tega dela je bil oceniti ponavljanje pretaljevanja na mehanske lastnosti, termomehanske lastnosti, kemijsko sestavo in spremembe mikrostrukture izbranega materiala. Izbrana je bila vrsta aluminijeve zlitine Al-Cu na podlagi naraščanja preizkusov na neželeznih kovinah v industriji. Tehnična oznaka izbrane zlitine, skladno z nemškim standardom ALUFOND 60, je RR.350. Zlitina RR.350 je poznana zaradi slabih livarskih lastnosti, ki se s pretaljevanjem poslabšujejo in vplivajo na spremembe mehanskih lastnosti in mikrostrukture v litem stanju. V predstavljenem članku je potrjen negativni vpliv pretaljevanja na uporabne lastnosti. Vzorci za natezne preizkuse so bili uliti v kovinsko kokilo. Ulivni in napajalni sistem, ki se je uporabljal za sekundarno napajanje, je bil odstranjen iz ulitka. Tako je bil material štirikrat pretaljen. Izdelani vzorci so bili porušeni v temperaturnem intervalu med 20 °C in 350 °C. Iz ulitega materiala so bili odrezani vzorci za metalografijo in za meritve trdote (HBS). Iz nateznih diagramov je razvidno, da ima prva talina za okrog 11 % višjo natezno trdnost pri 20 °C v primerjavi s tretjo talino. Ta razlika se opazi do temperature 100 °C. Pri temperaturah nad 100 °C so trdnostne lastnosti materiala v litem stanju enake. Ta tendenca se je pokazala pri vseh do sedaj preizkušenih materialih. Primerjava trdote in mikrotrdote kažeta, da je najvišjo vrednost dosegel material četrte taline. Ta pojav se pripisuje ponovljeni reoksidaciji in odsotnosti oksidnih kožic. Ocenjene so bile tudi značilnosti mikrostrukture in določene kemijske sestave. Rezultati teh preiskav so potrdili negativen vpliv večkratnega pretaljevanja na mikrostrukturo in lastnosti materiala.

Ključne besede: aluminijeve zlitine, metalografska analiza, mikrostrukture, termomehanske lastnosti, pretaljevanje, mehanske lastnosti

1 INTRODUCTION

At present the significance of non-ferrous metal alloys as structural materials is growing thanks to their good mechanical and thermomechanical properties, low specific weight and heat-treatment possibility enhancing usable properties of the alloy. By virtue of the aforementioned properties, non-ferrous metal alloys replace iron-based alloys in various industry branches. Non-ferrous metals utilization in various industry branches will have an increasing trend in the future. Considering the rising prices of the materials, the enterprises engaged in the processing of alloys and in the manufacture of castings seek for a production-cost reduction. This trend has been intensified due to the contemporary economic crisis. One saving way is the utilization of recycled material or remelting of foundry returns.

Some of the most widely used non-ferrous metal alloys are aluminum-based alloys. In this paper we have focused on the Al-Cu alloy RR.350. Due to its favourable properties, low weight, minimal dilatation and capability to resist high temperatures up to 350 °C, the RR.350 alloy is used for the thermally stressed castings and the castings subjected to higher pressures[1]. This alloy has an extensive usability not only in the automotive industry. The RR.350 alloy is used in heat-treatment conditions when its usable properties reach the highest values. This study is focused on an evaluation of the

Figure 1: Test bar
Slika 1: Preizkusna palica

mechanical and thermomechanical properties of the above-mentioned alloy after multiple remelting in casting conditions. After the melting and casting of the samples, a gating system, which then served as a new charge, was cut off. These steps were performed four times and then the material changes after remelting were assessed. The research team focused on the changes in following properties: tensile strength, hardness, micro-hardness, alloy chemical composition and alloy structure after remelting. The research took place in the VŠB – Technical University Ostrava laboratories.

2 MATERIALS AND METHODS

To observe the re-melting of non-ferrous metals, an Al-Cu alloy with the technical nomenclature of RR.350 was chosen. The chemical composition of the alloy used for the experiment is shown in **Table 1**.

Table 1: Chemical composition of the RR.350 alloy (in mass fractions, *w*/%)
Tabela 1: Kemijska sestava zlitine RR.350 (v masnih deležih, *w*/%)

Fe	Cu	Mn	Mg	Ni	Zn
0.368	4.731	0.310	0.034	1.937	0.126
Ti	**Pb**	**Sn**	**Co**	**Cr**	**Al**
0.117	0.011	0.042	0.203	0.007	92.115

The original alloy with the as-delivered chemical composition was melted in an electric resistance furnace in a graphite-fireclay crucible and marked as I. melt. For the casting of the test bars, a metal mould equipped with a silicon sprayed-on coat preventing the sticking of the casting to the mould was used. The mould consists of a gating system with a bottom gate (for the laminar filling of the mould), a test bar and a riser. The riser is over dimensioned to eliminate defects, for instance the shrinkage cavities. After having cast a batch of the test bars marked as I. melt, the gating system with the riser, which served as a charge for the next heat, was removed. In this way we re-melted the original material four times. The test bars (**Figure 1**) were machined and subjected to a tensile test in the temperature range of 20 °C to 350 °C. The measurement was performed on the INOVA PRAHA tensile-testing machine. The heating of the samples was performed in a resistance furnace with an inert atmosphere. At each temperature, three samples were ruptured and the numerical values of their diameters were entered into the diagram.

For the hardness measurement, nine samples were used and each of them was subjected to three incisions. The sample preparation for the hardness testing (HB) was performed in a metallographic laboratory. At first, we cut off a one-centimeter-long cylinder from the cast sample with the help of an emulsion-cooled saw. Then the surface polishing on a horizontal water-cooled grinder followed using the emery cloths with a granularity of 360 up to 1.200. As a test specimen, a hardened ball of 2.5 mm in diameter was used. The test sample was placed on a work plate and adjusted so that the indentor could be pointed to the centre. Now the indentor arm was moved to the vertical position and the arm movement onto the sample was switched on. The machine carried out the loading to the value of 306.5 N, with the holding time of 10 s, followed by a release of the indentor.

The metallographic analysis was done with the help of a GX 51 microscope, equipped with light polarization, with a magnification of 12.5–1000.

The chemical analysis was performed on a GDS-LECO spectrometer with the aid of the reference-material calibration with guaranteed element content.

3 EXPERIMENTAL RESULTS AND DISCUSSION

The obtained results confirm a negative influence upon the remelted alloy.

The measured results of the tensile tests (**Figure 2**) show that the maximum strength of the original material (I. melt) is reached at the temperatures of 20 °C and 100 °C. During the third remelting, the tensile strength values at the temperatures of 20 °C and 100 °C decreased by approximately 24 MPa, which was 11 %. At the temperatures of over 100 °C, the strength values

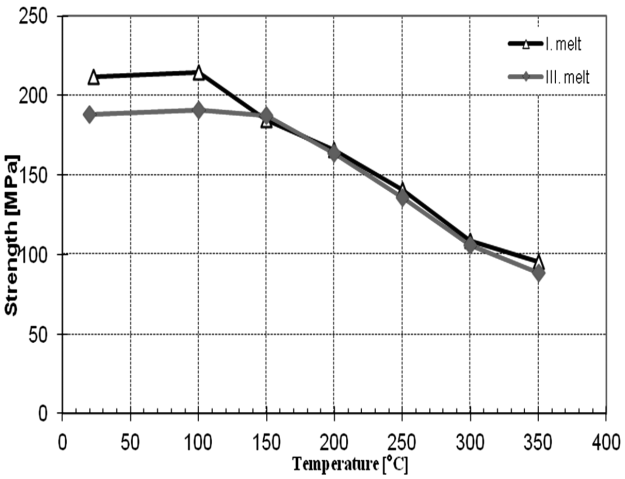

Figure 2: Dependence of tensile strength on temperature for different melts
Slika 2: Odvisnost natezne trdnosti od temperature pri različnih talinah

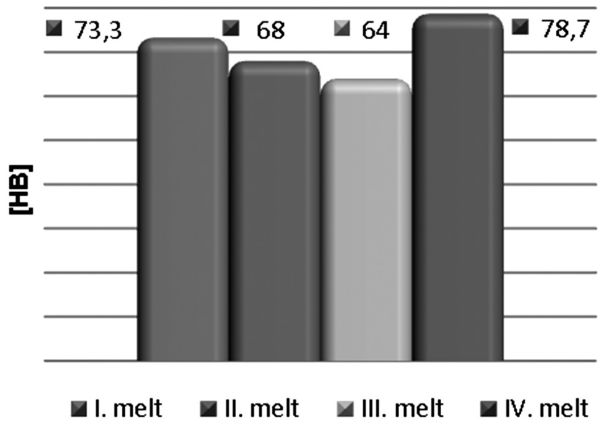

Figure 3: Values of Hardness of individual melts
Slika 3: Trdota materiala posameznih talin

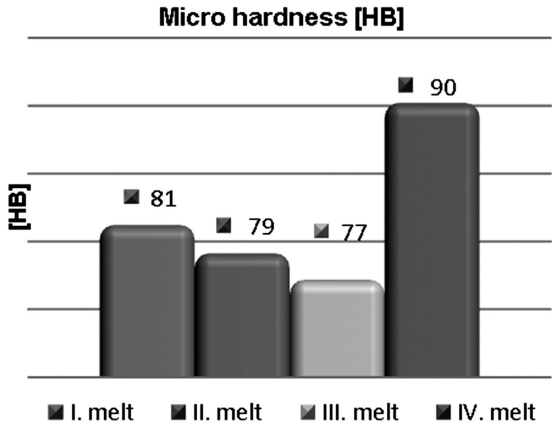

Figure 4: Values of Micro-Hardness of individual melts
Slika 4: Mikrotrdota materiala posameznih talin

of both melts were the same. This tendency was similar for the most of the tested materials[2]. The equation of the values of the tensile strength at elevated temperatures can be explained with the melting of low-melting components in the material which could occur by segregation in the material.

For this paper, the tensile-strength values of I. and III. melts were selected. II. and IV. melts will be finished and published in the next papers.

In both diagrams, the hardness values (**Figure 3**) and the microhardness values (**Figure 4**) are the highest for IV. melt. This tendency can be explained with the repeated melt oxidation and the formation of oxide membranes and intermetallic phases. The formation of oxides and intermetallic phases increases the alloy hardness and decreases the tensile strength owing to the unsuitably excluded shapes causing the notch effects in the material matrix[3]. Through their properties, aluminum oxides and intermetallics have a negative effect on the machining of the casting.

Multiple remelting does not affect only mechanical properties, but it changes chemical composition and structure morphology as well.

Comparing I. and II. melt (**Tables 1** and **2**) we can see that weakening of the alloy occurred at II. melt on account of decrease of some elements. The biggest decrease was observed for Cu (0.9129 %), Mn (0.06921 %), Ni (0.2191 %), Mg (0.0213 %). Compared to this, Al content was increased (1.318 %).

Table 2: Chemical analysis of II. melt (*w*/%)
Tabela 2: Kemijska sestava II. taline (*w*/%)

Fe	Cu	Mn	Mg	Ni	Zn
0.234	3.8181	0.24079	0.0127	1.7179	0.0828
Ti	**Pb**	**Sn**	**Co**	**Cr**	**Al**
0.172	0.00366	0.0141	0.271	0.000426	93.433

Table 3: Chemical analysis of III. melt (*w*/%)
Tabela 3: Kemijska sestava III. taline (*w*/%)

Fe	Cu	Mn	Mg	Ni	Zn
0.251	3.7737	0.25548	0.0112	1.6621	0.0758
Ti	**Pb**	**Sn**	**Co**	**Cr**	**Al**
0.159	0.00257	0.00947	0.529	0.000488	93.541

Comparing I. and III. melts (**Tables 1** and **3**) we can see that a weakening of the alloy also occurred with III.

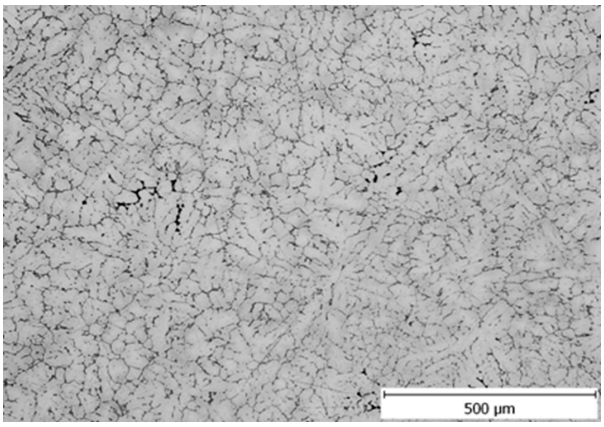

Figure 5: I. melt – magnified 100-times
Slika 5: I. talina – povečava 100-kratna

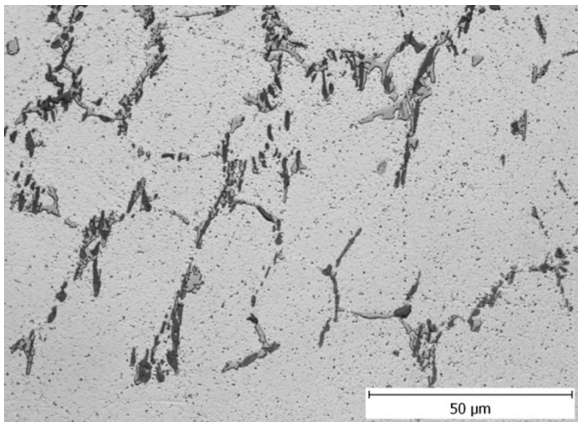

Figure 6: I. melt – magnified 1000-times
Slika 6: I. talina – povečava 1000-kratna

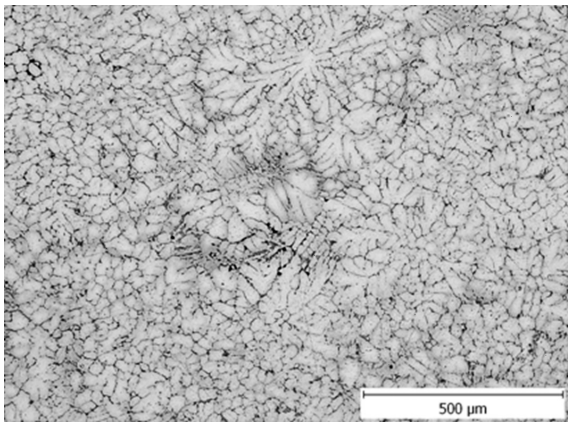

Figure 7: II. melt – magnified 100-times
Slika 7: II. talina – povečava 100-kratna

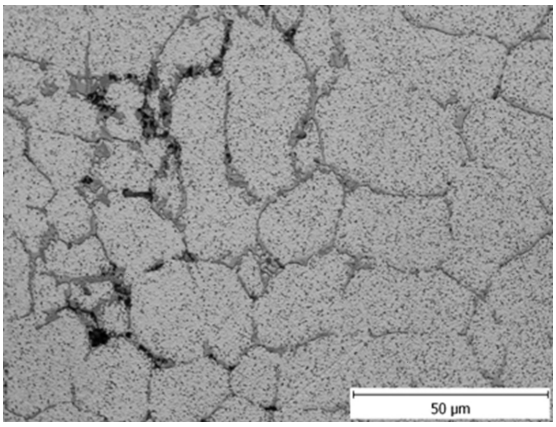

Figure 10: III. melt – magnified 1000-times
Slika 10: III. talina – povečava 1000-kratna

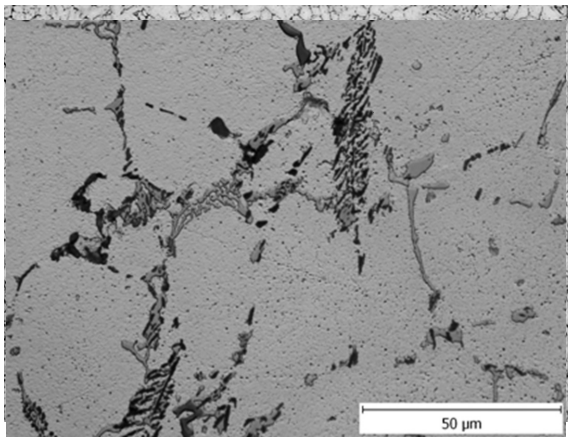

Figure 8: II. melt – magnified 1000-times
Slika 8: II. talina – povečava 1000-kratna

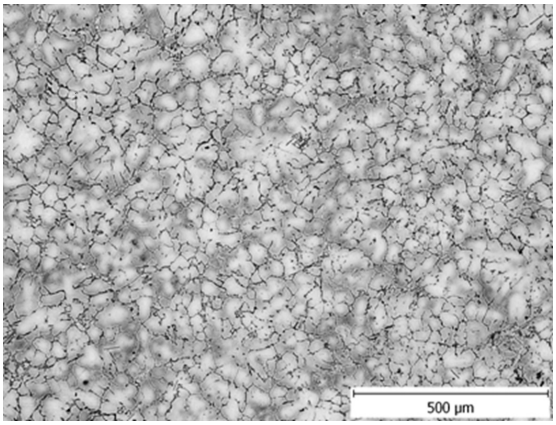

Figure 11: IV. melt – magnified 100-times
Slika 11: IV. talina – povečava 100-kratna

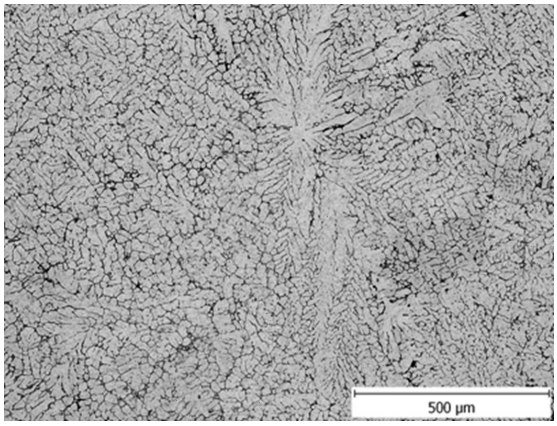

Figure 9: III. melt – magnified 100-times
Slika 9: III. talina – povečava 100-kratna

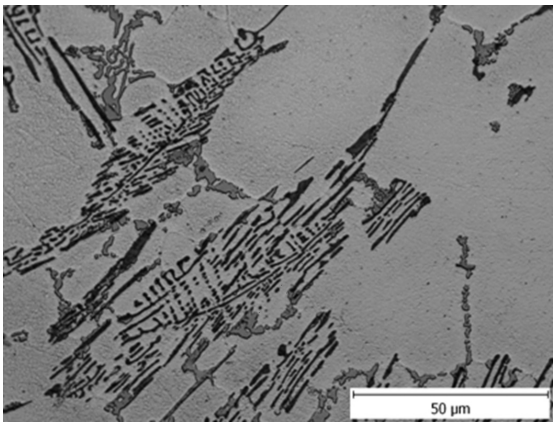

Figure 12: IV. melt – magnified 1000-times
Slika 12: IV. talina – povečava 1000-kratna

melt due to a decrease in some elements. The biggest decrease was again observed for Cu (0.9573 %), Mn (0.05452 %), Ni (0.2749 %) and Mg (0.0228 %). On the other hand, the Al content was increased (1.426 %).

Due to multiple remelting the material structure changes its morphology as well (**Figures 5** to **12**). The changes in the material structure are shown as grain coarsening, unevenness of dendritic cells and dendrites[4], higher content of cavities and coarsening of intermetallic phases.

4 CONCLUSIONS

Properties of the RR.350 alloy after repeated remelting were observed. For each remelting, the basic material properties were determined, i.e., tensile strength, hardness, structure and chemical composition. The cast-material tensile strength dropped by 11 % at the temperatures of up to 100 °C. The hardness reached the highest values in the case of IV. melt. The material structure change influenced most of the above-mentioned changes. By multiple remelting, a grain coarsening, unevenness of dendritic cells, a higher content of cavities and coarsening of the intermetallic phases occur. The reason for a decrease in the alloying elements is the re-melt loss in the resistance furnace. The RR.350-alloy testing offers other ways of mechanical-property enhancement. An advisable option is a substitution of the elements decreased due to multiple remelting and follow-up inoculations with an AlTi5B1 master alloy[5]. Further, the alloy can be very well hardened with the help of a heat treatment (the strength values reach up to 300 MPa). As mentioned above, the alloy is susceptible to various kinds of cavities, therefore degassing before casting would be advisable. For the manufacture of castings, we can also recommend filtration to remove the inclusions which decrease mechanical properties.

This paper was created within the project No. CZ.1.05/2.1.00/01.0040 "Regional Materials Science and Technology Centre", under the frame of the operation programme "Research and Development for Innovations" financed by the Structural Funds and by the state budget of the Czech Republic.

5 REFERENCES

[1] J. Roučka, Metalurgie neželezných slitin, VUT Brno, 2004

[2] R. Kořený, Možnosti zvýšení kvality vysokopevnostních a žáropevných slévárenských slitin hliníku, VŠB, Ostrava, 1991

[3] F. Píšek, L. Jeníček, P. Ryš, Nauka o materiálu I., Nauka o kovech 3. svazek: Neželezné kovy, Academia, Praha 1973

[4] L. Bäckerud, G. Chai, J. Taminen, Solidification Characteristic of Aluminium Alloys, Foundry Alloys, Volume 2, ASF Skanaluminium, Stockholm, 1990

[5] D. Bolibruchová, E. Tillová, Zlievarenské zliatiny Al-Si, ŽU v Žilině, 2005

UDK 621.778:620.172
Professional article/Strokovni članek

ISSN 1580-2949
MTAEC9, 47(2)245(2013)

TENSILE PROPERTIES OF COLD-DRAWN LOW-CARBON STEEL WIRES UNDER DIFFERENT PROCESS PARAMETERS

NATEZNE LASTNOSTI HLADNO VLEČENE MALOOGLJIČNE JEKLENE ŽICE PRI RAZLIČNIH PARAMETRIH PROCESA

Cem S. Çetinarslan[1], Ali Güzey[2]

[1]Department of Mechanical Engineering, Faculty of Engineering and Architecture, Trakya University, 22180 Edirne, Turkey
[2]Arsay Wire Production Company-Kirklareli, Turkey
cemc@trakya.edu.tr

Prejem rokopisa – received: 2012-10-01; sprejem za objavo – accepted for publication: 2012-10-23

This study demonstrates the influence of drawing-process parameters such as reduction (deformation) ratio and drawing velocity on the tensile properties of various low-carbon cold-malleable steel wires. Standard tensile tests were realized on four types of wires – SAE1006, SAE1008, SAE1015 (Cq15) and SAE10B22 (20MnB4) – at various process parameters. This experimental study shows how two of the main process parameters, the deformation ratio and drawing velocity, clearly influence the tensile properties (yield stress, ultimate tensile strength, and elongation at rupture) of steel-wire materials.

Keywords: wire drawing, tensile properties, deformation (reduction) ratio, drawing velocity

Ta študija prikazuje vpliv procesnih parametrov pri vlečenju, kot sta odvzem (deformacija) in hitrost vlečenja, na natezne lastnosti različnih maloogljičnih mehkih jeklenih žic. Izvršen je bil standardni natezni preizkus na štirih vrstah žice SAE1006, SAE1008, SAE1015 (Cq15) in SAE10B22 (20MnB4) po različnih procesnih parametrih. Ta eksperimentalna študija je pokazala, kako dva glavna procesna parametra, stopnja deformacije in hitrost vlečenja, vplivata na natezne lastnosti (napetost tečenja, natezna trdnost in raztezek pri pretrgu) jeklene žice.

Ključne besede: vlečenje žice, natezne lastnosti, stopnja deformacije (odvzem), hitrost vlečenja

1 INTRODUCTION

Wire drawing is a metal-reducing process, in which a wire rod is pulled or drawn through a single die or a continuous series of dies, thereby reducing its diameter.

Wire drawing is one of the most common plastic-deformation processes. A wire rod is pulled or drawn through a die or a series of dies, causing a reduction of its diameter. In general, drawing is known as a process performed at room temperature. Drawing of low-carbon-content steel wires is generally conducted at room temperature employing a number of passes or reductions through several dies. Sometimes it may be performed at elevated temperatures for large wires to reduce drawing forces.

Generally, steel wire is made of plain-carbon steel grades. The steel-wire materials are semi-products suitable for cold-drawing processes. Although a steel wire can be produced from stainless steel and other alloyed steels, in industry it is mostly produced using plain-carbon steels. The steel containing up to 1 % C is usually used for steel-wire production; however, the largest part of steel-wire production constitutes low-carbon steels with less than 0.1 % C.[1]

Ferrous wires are used as semi products for electrical wiring, ropes (rope wires are usually made of pearlitic steel and have very high tensile properties), cables, structural components, springs, nails, spokes, musical instruments, electrodes, paper clips, etc.[2]

Several studies on wire-drawing processes and some process parameters that affect the wire-drawing process have been performed. Toribio and Ovejero have investigated the effect of cumulative cold drawing on the pearlite interlamellar spacing in eutectoid steel. Interlamellar spacing in fully pearlitic steels decreases progressively during the cold-drawing process and the diminishing rate is not constant throughout the manufacturing route.[3] The effect of degree of deformations, ranging from 5 % to 30 % reductions, on the mechanical properties of cold-drawn, mild-steel rods was experimentally investigated by Alawode and Adeyemi.[4] Languillaume et al. have presented the results of a study concerning the influence of heavy cold drawing and post-deformation annealings on the microstructure of such pearlitic steel wires.[5] On the other hand, Vega et al. have studied the effect of the process variables such as the semi-die angle, the reduction in area and the friction coefficient on the drawing-force value. The results of this study indicate clearly that friction has a significant effect on the drawing force, which becomes lower due to a decrease in the area reduction.[6] The influence of the main process parameters (the wire yield stress – S, the cross-sectional area reduction – Re and the die half angle – α) on the shape quality and area fraction of the round-to-hexagonal

composite wire drawing were investigated by Norasethasopon.[7] This study shows that *Re* and *S* strongly influence the shape quality, and *S* slightly influences the change in the area fraction of the core. The change in the area fraction of the core, which equals zero, was obtained with the value of α that increased with the increasing *S*. *Re* and *S* strongly influence the drawing stress. Within this order, *Re* and *S* directly, strongly and inversely influenced the optimal die half angle. The pass schedule of a wire-drawing process designed to prevent a delamination of a high-strength-steel cord wire was studied by Lee et al.[8] From their findings it is clear that the applied drawing process reduced the diameter of the wire from 3.5 mm to 0.95 mm, and that it consisted of nine passes. On the other hand, another model for predicting the fatigue strength of two different eutectoid-steel wires, one of them being zinc coated, used in ropeway applications, has been presented by Beretta and Boniardi.[2] Within this method the fatigue process of wires has been described in terms of propagation of the surface defects caused by cold drawing.

The aim of our research was to investigate the tensile properties of various low-carbon cold-malleable steel wires with respect to drawing velocity and deformation ratio. These parameters also have an influence on the final wire quality, the drawing force, the lubrication in the process, the mechanical properties and the die wear.

2 EXPERIMENTAL PROCEDURE

2.1 Preparation process

Wire-rod (raw) materials were of four different types of low-carbon steel: SAE1006, SAE1008, SAE1015 (Cq15) and SAE10B22 (20MnB4). The steel chemical compositions are given in **Table 1**.[9]

First, the chemical compositions of the steels were measured using a SPECTROLAB M7 spectrometric test device. Then the surface-cleaning process including two stages, the mechanical and chemical cleaning, was performed. The first step, the mechanical surface cleaning, was applied to remove the scale layer from the wires and then the chemical purification was realized. The chemical cleaning consisted of causticization (for 25 min in a $KMnO_5$ + NaOH solution at 70 °C), dipping into an acid bath (for 1 h in a HCl concentrated solution at room temperature), washing and rinsing, passivation with lime and, finally, drying (for 1h at 100 °C).

2.2 Wire-drawing process

After these treatments the drawing process was performed. **Figure 1** shows the outlet of a drawing die with a coil (end product) and a drawing die (matrix) with a soap box. A wire first passes through the soap box and then through the die (matrix). The reduction of the diameter of a metal wire is realized by pulling it through the die (**Figure 2**). The working region of a die is typically and made of W carbide. The die is cooled with a cooling hose (water) as shown in **Figure 1**. A series of dies is used to obtain the required diameter reduction of the wire. **Table 2** shows a series of dies with the reductions of 5.5 to 2.2, to 1.8 and to 2.1 made in 8 or 9 passes, used to obtain the wire diameters of (4.80, 4.00 and 3.01) mm. The reduction ratio (*R*/%) was determined for each diameter decrease as to the equation:

$$R/\% = \frac{D_{\text{inlet}}^2 - D_{\text{outlet}}^2}{D_{\text{inlet}}^2} \times 100 \quad (1)$$

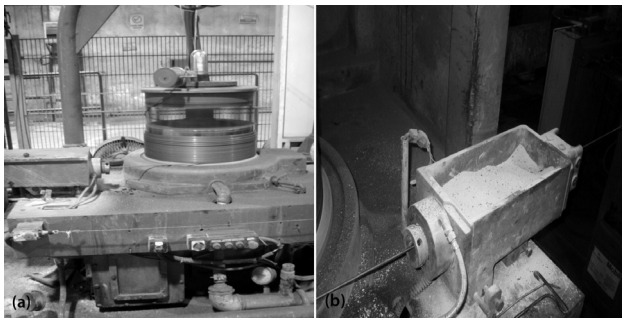

Figure 1: a) Outlets of a drawing die with a wire coil and b) a drawing die (matrix) with a soap box

Slika 1: a) Sestav vlečne matrice z navijalcem žice, b) matrica za vlečenje s posodo za milo

Table 1: Chemical compositions of wire-rod (raw) steels
Tabela 1: Kemijska sestava jekla v palicah

Steel Type	%C	%Si	% Mn	%P	%S	%Cu	%Cr	%Ni	%Mo	%Al	% B
SAE1006	0.06	0.2	0.35	0.04	0.05	0.30	0.15	0.3	0.03	–	–
SAE1008	0.08	0.30	0.55	0.03	0.05	0.35	0.3	0.25	0.03	0,02	–
SAE1015	0.14	0.15	0.40	0.02	0.015	0.1	0.08	0.1	0.05	0.03	
SAE10B22	0.21	0.15	1.00	0.015	0.015	0.1	0.08	0.1	0.05	0.02	0.002

Table 2: Series of dies for each steel type for the drawing process (reduction of 5.5 to 4.8, to 4.00 and to 3.01)
Tabela 2: Serija orodij za vsako vrsto jekla pri vlečenju (odvzem 5,5 do 4,8, do 4,00 in do 3,01)

Inlet dia.	Outlet dia.	Pass number	1	2	3	4	5	6	7	8	9
5.50	2.20	8	4.80	4.21	3.72	3.31	2.96	2.67	2.41	2.20	–
5.50	1.80	8	4.67	4.00	3.44	2.98	2.60	2.29	2.02	1.80	–
5.50	2.10	9	4.82	4.25	3.77	3.37	3.02	2.73	2.49	2.28	2.10

Figure 2: Drawing die (matrix) with a tip (pressure type)
Slika 2: Orodje za vlečenje (matrica) s konico (tlačne vrste)

In a multipass drawing process, the temperature rise during each pass can affect the mechanical properties of the final product (such as its bending and torsion properties, and its tensile strength).[8]

A wire-drawing process was carried out with different drawing velocities and different total-reduction ratios of the deformation to determine how the tensile properties of various low-carbon wires were affected.

The effect of drawing velocity and deformation ratio was investigated in some references. One of those focused on the influence of drawing speed on the properties of multiphase TRIP (transformation induced plasticity) steel wires[10] and the other on the study of the effect of total-reduction ratio on wire breaks by Cu fine-wire drawing.[11]

In general, each pass ratio is between 1.68 and 1.09.

$$D_{\text{final-1}} = k \cdot D_{\text{final}} \qquad (k = 1.68\text{–}1.09) \qquad (2)$$

2.3 Tensile test

Experiments were carried out on a tensile-test machine at room temperature (**Figures 3** and **4**) and

Figure 3: Tensile-test machine
Slika 3: Stroj za natezne preizkuse

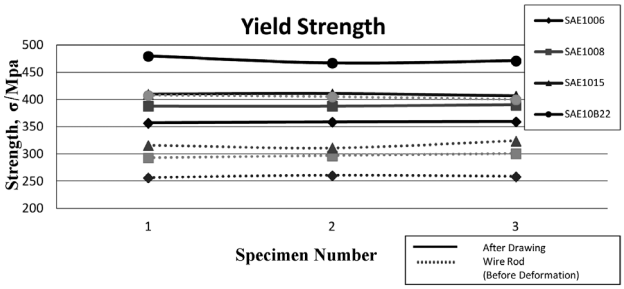

Figure 4: Variation in the yield-strength values for a rod and coil steel wire at a constant velocity and reduction ratio (from ϕ5.50 to ϕ4.81)
Slika 4: Spreminjanje meje plastičnosti palice in žice v kolobarju pri konstantni hitrosti in odvzemu (od ϕ5,50 do ϕ4,81)

SAE1006, SAE1008, SAE1015 (Cq15) and SAE10B22 (20MnB4) coil wires (end products) were used as test steels. The wires were submitted to tensile tests to determine the yield stress, the ultimate tensile strength and the elongation at rupture. Wire cuts of 250 mm in length were used as the test specimens. The tensile strength was determined on a 3 t tensile tester with a ram (lower jaw) speed of 10 mm/min using various test parameters and three experiments were carried out and then averaged for each point in the diagrams.

3 RESULTS AND DISCUSSIONS

3.1 Test results at a constant drawing velocity (3.6 m/s) and a constant reduction ratio (from ϕ5.50 to ϕ4.81)

Firstly, the wire-rod specimens were tested and then the coil (drawn) wires were tested at a constant drawing velocity and a constant reduction ratio from ϕ5.50 to ϕ4.81. Experimental findings on the yield strength, tensile strength and elongation at rupture were determined for wire rods (before drawing) and coil (drawn) wires and are given in **Table 3**.

The yield-strength values of rod wires and coil wires were found as expected and, as shown in **Figure 4**, they increase in accordance with the increasing C content. The increase in the C content causes brittleness, making

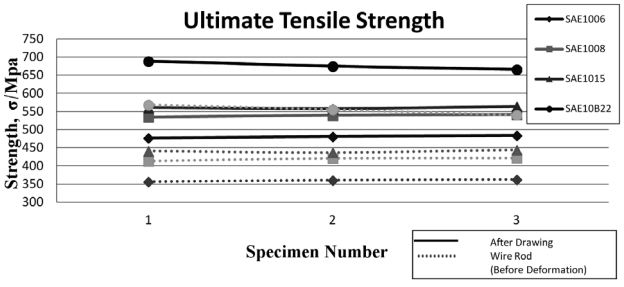

Figure 5: Variation in the ultimate tensile-strength values for a rod and coil steel wire at a constant velocity and reduction ratio (from ϕ5.50 to ϕ4.81)
Slika 5: Spreminjanje vrednosti natezne trdnosti palice in žice v kolobarju pri konstantni hitrosti in odvzemu (od ϕ5,50 do ϕ4,81)

Table 3: Tensile properties of a rod and coil steel wire at a constant drawing velocity and a constant reduction ratio (from ϕ5.50 to ϕ4.81)
Tabela 3: Natezne lastnosti palice in žice v kolobarju pri konstantni hitrosti vlečenja in konstantnem odvzemu (od ϕ5,50 do ϕ4,81)

	Dia., ϕ/mm		Material type	V m/s	Yield Strength $Rp_{0,2}$/MPa		Ultimate Tensile Strength R_m/MPa		Elongation at Rupture %	
Specimen No	Wire rod (before drawing)	Coil (after drawing)			Wire rod (before drawing)	Coil (after drawing)	Wire rod (before drawing)	Coil (after drawing)	Wire rod (before drawing)	Coil (after drawing)
1	ϕ5.50	ϕ4.81	SAE1006	3.6	257	357	357	477	41	29
2	ϕ5.50	ϕ4.81	SAE1006	3.6	261	359	361	481	44	30
3	ϕ5.50	ϕ4.81	SAE1006	3.6	259	360	363	484	43	31
1	ϕ5.50	ϕ4.81	SAE1008	3.6	293	388	413	535	39	32
2	ϕ5.50	ϕ4.81	SAE1008	3.6	297	388	421	540	38	28
3	ϕ5.50	ϕ4.81	SAE1008	3.6	301	390	422	542	40	29
1	ϕ5.50	ϕ4.81	SAE1015	3.6	316	410	441	561	41	28
2	ϕ5.50	ϕ4.81	SAE1015	3.6	311	411	437	558	40	28
3	ϕ5.50	ϕ4.81	SAE1015	3.6	324	407	444	564	41	32
1	ϕ5.50	ϕ4.81	SAE10B22	3.6	408	480	568	689	36	25
2	ϕ5.50	ϕ4.81	SAE10B22	3.6	405	467	555	675	37	26
3	ϕ5.50	ϕ4.81	SAE10B22	3.6	400	471	540	666	39	29

plastic deformation more difficult. The ultimate tensile-strength values of the rod materials and coils of the tested steels are also in line with the increasing C content (**Figure 5**). The variation in the elongation at rupture is shown in **Figure 6**. The values of the elongation at rupture for drawn wires decreased with the increasing plastic deformation for all the tested steels. The (20MnB4) steel shows a slight decrease in the elongation due to a higher C content.

The wire specimens used for the tensile tests are shown in **Figures 7** and **8**.

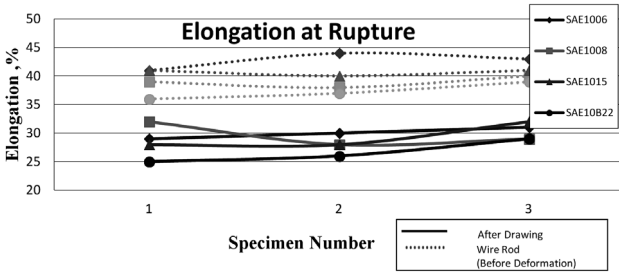

Figure 6: Variation in the elongation-at-rupture (%) values for a rod and coil steel wire at a constant velocity and reduction ratio (from ϕ5.50 to ϕ4.81)
Slika 6: Spreminjanje raztezka pri pretrgu (%) za palico in žice v kolobarju pri konstrantni hitrosti in odvzemu (od ϕ5,50 do ϕ4,81)

3.2 Test results at a constant drawing velocity (3.6 m/s) and different reduction ratios (from ϕ5.50 to ϕ4.81, to ϕ4.00 and to ϕ3.01)

The coil materials were tested at a constant drawing velocity (3.6 m/s) and different reduction ratios (from ϕ5.50 to ϕ4.81, ϕ4.00 and ϕ3.01). The reduction ratio was determined as depending on the constant inlet diameter (ϕ5.50) and different outlet diameters (ϕ4.81, ϕ4.00 and ϕ3.01). Experimental findings are given in **Table 4**. The yield strength, tensile strength and elongation at rupture were determined for the wire rods (before drawing) and for drawn wires after various reduction ratios.

Figure 7: SAE1008 specimen
Slika 7: Vzorec SAE1008

Figure 8: SAE10B22 (20MnB4) specimen
Slika 8: Vzorec SAE10B22 (20MnB4)

Table 4: Tensile properties of a rod and coil steel wire at a constant drawing velocity (3.6 m/s) and different reduction ratios (from ϕ5.50 to ϕ4.81, to ϕ4.00 and to ϕ3.01)

Tabela 4: Natezne lastnosti palice in žice v kolobarju pri konstantni hitrosti vlečenja (3,6 m/s) in različnih odvzemih (od ϕ5,50 do ϕ4,81, do ϕ4,00 in do ϕ3,01)

	Dia., ϕ/mm		Material type	V m/s	Yield Strength $Rp_{0,2}$/MPa		Tensile Strength R_m/MPa		Elongation at Rupture %	
Specimen No	Wire rod (before drawing)	Coil (after drawing)			Wire rod (before drawing)	Coil (after drawing)	Wire rod (before drawing)	Coil (after drawing)	Wire rod (before drawing)	Coil (after drawing
1	ϕ5.50	ϕ4.81	SAE1006	3.6	258	357	359	477	43	36
2	ϕ5.50	ϕ4.00	SAE1006	3.6		505		605		24
3	ϕ5.50	ϕ3.01	SAE1006	3,6		623		725		12
1	ϕ5.50	ϕ4.81	SAE1008	3.6	294	388	407	535	42	34
2	ϕ5.50	ϕ4.00	SAE1008	3.6		536		643		22
3	ϕ5.50	ϕ3.01	SAE1008	3.6		664		774		11
1	ϕ5.50	ϕ4.81	SAE1015	3.6	316	410	438	561	40	33
2	ϕ5.50	ϕ4.00	SAE1015	3.6		558		676		18
3	ϕ5.50	ϕ3.01	SAE1015	3.6		684		808		8
1	ϕ5.50	ϕ4.81	SAE10B22	3.6	406	480	571	689	38	31
2	ϕ5.50	ϕ4.00	SAE10B22	3.6		649		811		15
3	ϕ5.50	ϕ3.01	SAE10B22	3.6		772		944		5

The yield-strength values for all the specimens increase with the increasing reduction ratio (**Figure 9**); and the ultimate tensile strength for all the specimens shows similar tendencies (**Figure 10**). Variations in the elongation at rupture are shown in **Figure 11**. In general, the values of the elongation at rupture for coil wires decrease as the reduction ratio increases. The decrement is a bit larger for the relatively high C-content steel specimens, SAE1015 (Cq15) and SAE10B22 (20MnB4), as the increase in the reduction ratio is more effective for the steels containing a higher C content with respect to the strain hardening. In addition, the Mn content is also a strength-increasing alloying element for the steel SAE10B22.[12]

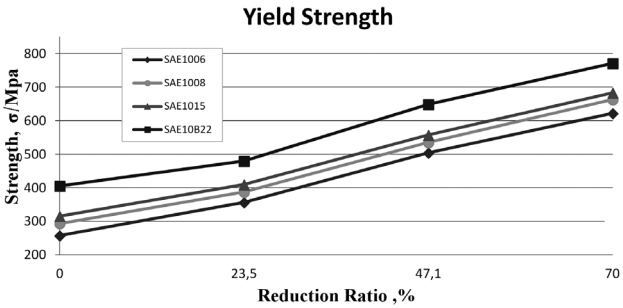

Figure 9: Variation in the yield-strength values for a rod and coil steel wire at a constant velocity and different reduction ratios (from ϕ5.50 to ϕ4.81, to ϕ4.00 and to ϕ3.01)

Slika 9: Spreminjanje meje plastičnosti za palico in žico v kolobarju pri konstantni hitrosti in različnih odvzemih (od ϕ5,50 do ϕ4,81, do ϕ4,00 in do ϕ3,01)

3.3 Tensile-test results at a constant drawing velocity (3.6 m/s) and different reduction ratios – different inlet diameters and constant outlet diameters

Firstly, the wire rods were tested. The tests for coil wires were realized at the constant drawing velocity (3.6 m/s) and different reduction ratios (from ϕ5.50 to ϕ4.81

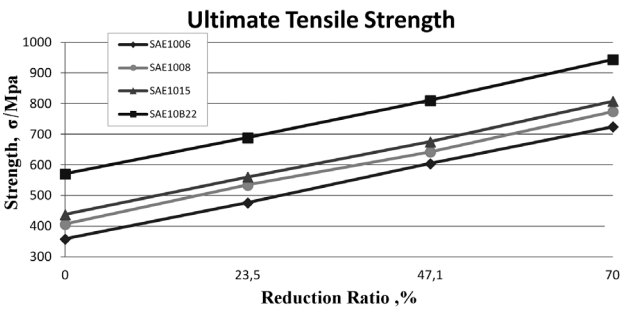

Figure 10: Variation in the ultimate-tensile-strength values for a rod and coil steel wire at a constant velocity and different reduction ratios (from ϕ5.50 to ϕ4.81, to ϕ4.00 and to ϕ3.01)

Slika 10: Spreminjanje naztezne trdnosti palice in žice v kolobarju pri konstantni hitrosti in različnih odvzemih (od ϕ5,50 do ϕ4,81, do ϕ4,00 in do ϕ3,01)

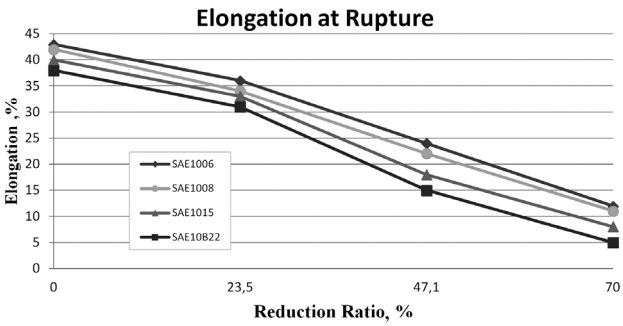

Figure 11: Variation in the elongation-at-rupture (%) values for a rod and coil steel wire at a constant velocity and different reduction ratios (from ϕ5.50 to ϕ4.81, ϕ4.00 and to ϕ3.01)

Slika 11: Spreminjanje raztezka pri pretrgu (%) palice in žice v kolobarju pri konstantni hitrosti in različnih odvzemih (od ϕ5,50 do ϕ4,81, do ϕ4,00 in do ϕ3,01)

Table 5: Tensile properties of a rod and coil steel wire at a constant velocity (3.6 m/s) and different reduction ratios – different inlet diameters and a constant outlet diameter – (from ϕ5.50 to ϕ4.81 and from ϕ6.50 to ϕ4.81)
Tabela 5: Natezne lastnosti palic in žice v kolobarju pri konstantni hitrosti (3,6 m/s) in različnih odvzemih – različen vstopni premer in enak izhodni premer – (od ϕ5,50 do ϕ4,81 in od ϕ6,50 to ϕ4,81)

	Dia., ϕ/mm		Material type	V m/s	Yield Strength $Rp_{0,2}$/MPa		Tensile Strength R_m/MPa		Elongation at Rupture %	
Specimen No	Wire rod (before drawing)	Coil (after drawing)			Wire rod (before drawing)	Coil (after drawing)	Wire rod (before drawing)	Coil (after drawing)	Wire rod (before drawing)	Coil (after drawing)
1	ϕ5.50	ϕ4.81	SAE1006	3.6	258	357	358	477	43	36
2	ϕ6.50	ϕ4.81	SAE1006	3.6		500		605		24
1	ϕ5.50	ϕ4.81	SAE1008	3.6	292	388	405	535	42	34
2	ϕ6.50	ϕ4.81	SAE1008	3.6		531		643		22
1	ϕ5.50	ϕ4.81	SAE1015	3.6	314	410	436	562	40	33
2	ϕ6.50	ϕ4.81	SAE1015	3.6		553		676		18
1	ϕ5.50	ϕ4.81	SAE10B22	3.6	406	480	567	689	38	31
2	ϕ6.50	ϕ4.81	SAE10B22	3.6		645		811		15

and from ϕ6.50 to ϕ4.81). These ratios were determined according to different inlet diameters and constant outlet diameters. The results are shown in **Table 5** and **Figures 12**, **13** and **14**. The yield strength, tensile strength and elongation at rupture were determined for the wire rods

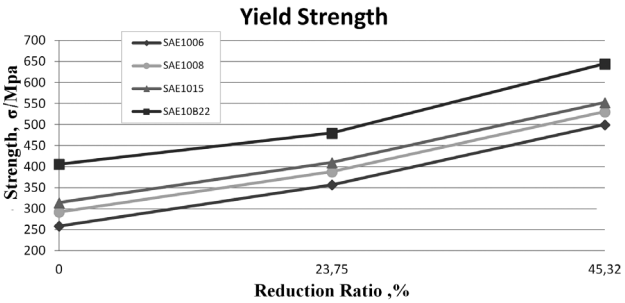

Figure 12: Variation in the yield-strength values for a rod and coil steel wire at a constant velocity (3.6 m/s) and different reduction ratios – different inlet diameters and constant outlet diameters (from ϕ5.50 to ϕ4.81 and from ϕ6.50 to ϕ4.81)
Slika 12: Spreminjanje meje plastičnosti palice in žice v kolobarju pri konstantni hitrosti (3,6 m/s) in različnih odvzemih – različen vstopni premer in enak izstopni premer (od ϕ5,50 do ϕ4,81 in od ϕ6,50 do ϕ4,81)

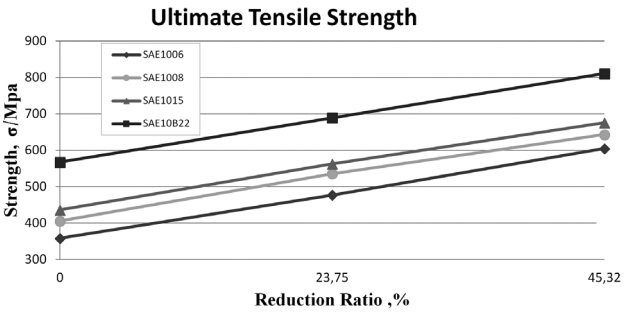

Figure 13: Variation in the ultimate-strength values for a rod and coil steel wire at a constant velocity (3.6 m/s) and different reduction ratios – different inlet diameters and constant outlet diameters (from ϕ5.50 to ϕ4.81 and from ϕ6.50 to ϕ4.81)
Slika 13: Spreminjanje natezne trdnosti palice in žice v kolobarju pri konstantni hitrosti (3,6 m/s) in različnih odvzemih – različen vstopni premer in konstanten izstopni premer (od ϕ5,50 do ϕ4,81 in od ϕ6,50 do ϕ4,81)

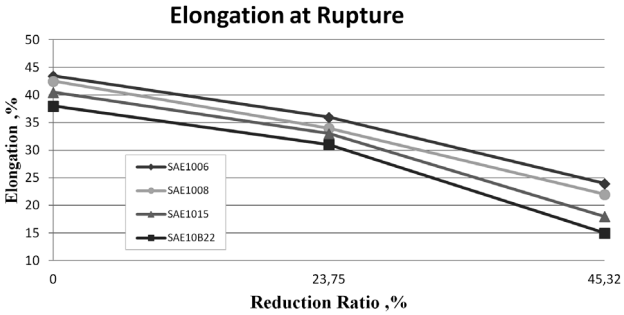

Figure 14: Variation in the elongation-at-rupture (%) values for a rod and coil steel wire at a constant velocity (3,6 m/s) and different reduction ratios – different inlet diameters and constant outlet diameters (from ϕ5.50 to ϕ4.81 and from ϕ6.50 to ϕ4.81)
Slika 14: Spreminjanje raztezka pri pretrgu (%) palice in žice v kolobarju pri konstantni hitrosti (3,6 m/s) in različnih odvzemih (od ϕ5,50 do ϕ4,81 in od ϕ6,50 do ϕ4,81)

(before drawing) and coil (drawn) wires with different ratios.

The yield strength, ultimate tensile strength and elongation at rupture were affected by the reduction ratio for each material as shown in Section 3.2. As the approximate reduction ratios (45.7 % for the reduction of ϕ6.5 to ϕ4.81 and 47.1 % for the reduction of ϕ5.50 to ϕ4.00) were considered, it was understood that the variation in the inlet diameters was not significant.

3.4 Tensile-test results at a constant reduction ratio (from ϕ5.50 to ϕ4.81) and with different drawing velocities (3.6 m/s and 2.4 m/s)

The coil-wire tests were realized at a constant reduction ratio from ϕ5.50 to ϕ4.81 and different drawing velocities (3.6 m/s and 2.4 m/s). The results are shown in **Table 6** and **Figures 15**, **16** and **17**. It is observed that the yield stress and the ultimate tensile strength of the specimens increase with the increasing drawing velocity for each type of the materials. A higher C content leads to a higher yield and ultimate tensile

Table 6: Tensile properties of a coil steel wire at a constant reduction ratio and different drawing velocities (3.6 m/s and 2.4 m/s)
Tabela 6: Natezne lastnosti žice iz kolobarja pri konstantnem odvzemu in različnih hitrostih vlečenja (3,6 m/s in 2,4 m/s)

	Dia., ϕ/mm		Material type	V m/s	Yield Strength $Rp_{0,2}$/MPa	Tensile Strength R_m/MPa	Elongation at Rupture, %
Specimen No	Wire rod (before drawing)	Coil (after drawing)			Coil (after drawing)	Coil (after drawing)	Coil (after drawing)
1	ϕ5.50	ϕ4.81	SAE1006	3.6	357	477	36
2	ϕ5.50	ϕ4.81	SAE1006	2.4	310	455	38
1	ϕ5.50	ϕ4.81	SAE1008	3.6	388	535	34
2	ϕ5.50	ϕ4.81	SAE1008	2.4	350	510	36
1	ϕ5.50	ϕ4.81	SAE1015	3.6	410	561	33
2	ϕ5.50	ϕ4.81	SAE1015	2.4	370	536	35
1	ϕ5.50	ϕ4.81	SAE10B22	3.6	480	689	31
2	ϕ5.50	ϕ4.81	SAE10B22	2.4	444	650	33

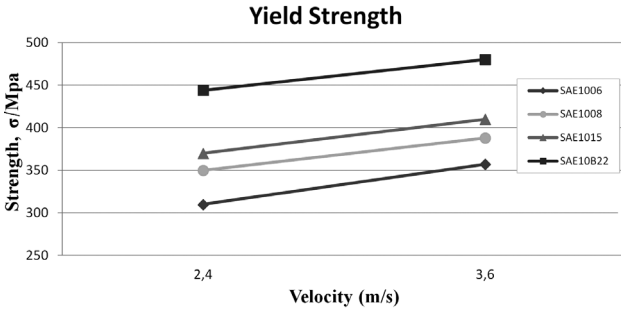

Figure 15: Variation in the yield-strength values for a coil steel wire at a constant reduction ratio (from ϕ5.50 to ϕ4.81) and with different drawing velocities (3.6 m/s and 2.4 m/s)
Slika 15: Spreminjanje meje plastičnosti žice v kolobarju pri konstantnem odvzemu (od ϕ5,50 do ϕ4,81) in različnih hitrostih vlečenja (3,6 m/s in 2,4 m/s)

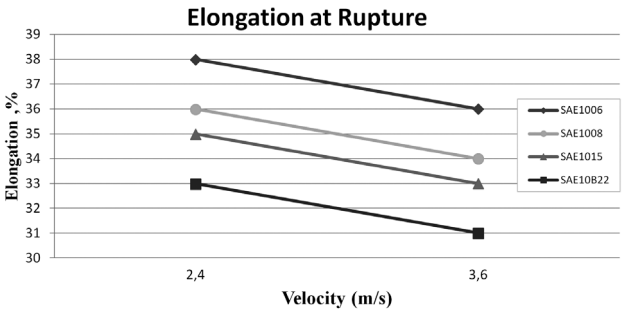

Figure 17: Variation in the elongation-at-rupture (%) values for a coil steel wire at a constant reduction ratio (from ϕ5.50 to ϕ4.81) and with different drawing velocities (3.6 m/s and 2.4 m/s)
Slika 17: Spreminjanje raztezka pri pretrgu (%) žice iz kolobarja pri konstantnem odvzemu (od ϕ5,50 do ϕ4,81) in različnih hitrostih vlečenja (3,6 m/s in 2,4 m/s)

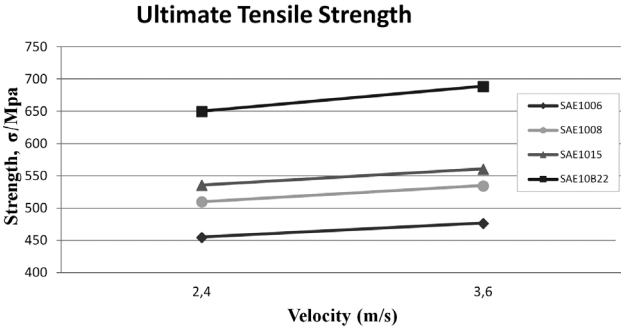

Figure 16: Variation in the ultimate-tensile-strength values for a coil steel wire at a constant reduction ratio (from ϕ5.50 to ϕ4.81) and with different drawing velocities (3.6 m/s and 2.4 m/s)
Slika 16: Spreminjanje natezne trdnosti žice iz kolobarja pri konstantnem odvzemu (od ϕ5,50 do ϕ4,81) in različnih hitrostih vlečenja (3,6 m/s in 2,4 m/s)

strength and a higher drawing velocity. Drawing velocity slightly affects the elongation, which decreases as the drawing velocity increases. These values are quite similar for all the steels.

4 CONCLUSIONS

The wire drawing of SAE1006, SAE1008, SAE1015 (Cq15) and SAE10B22 (20MnB4) low-carbon, malleable-steel wires was investigated and their tensile properties were determined experimentally. This study contributes to the knowledge of tensile properties and the behaviour of drawn low-carbon steel wires during the cold-drawing process. The effect of the process parameters (reduction ratio, drawing velocity) were studied and it was found that the processing parameters have a major influence on the tensile properties in all four types of the low-carbon drawn steel wire.

The obtained results can be summarized as follows:

- The experiments have shown that the yield strength and ultimate tensile strength increase, while the elongation at rupture decreases for all the steels when the reduction (deformation) ratio is increased.
- The drawing velocity has a significant effect on the tensile properties (the yield and the ultimate tensile strength) of low-carbon steel wires. A high drawing velocity causes high strength properties. The values of elongation at rupture also decrease as the drawing velocity increases.

- It was determined that the reduction ratio has a larger influence on the tensile properties of low-carbon steel wires than the drawing velocity.
- Due to a high C content, the tensile-strength properties of the wires increased for all the reduction ratios. In addition, Mn was also one of the strongly influential elements and its effect was amplified by increasing the strain rate for the SAE10B22 steel.[12,13] The increase in the C content enhances the work-hardening rate.[14] The work-hardening ability of steel increases with an increase in the C content. Thus, the C content causes a significant variation in the tensile strength of drawn steel wires. Moreover, it is known that B enhances the tensile properties of low-carbon steels.[15,16]
- The strength of rod wires can be improved using the wire-drawing process according to the experimental findings in this investigation. Furthermore, the wire-drawing-process parameters, like the reduction ratio and drawing velocity, also have a significant effect on the tensile properties of steel wires.

Acknowledgements

The authors would like to thank Mr. Uğur UZ for his help with the experimental work and to the ARSAY WIRE PRODUCTION COMPANY, Kirklareli/Turkey and the YILMAR STEEL WIRE AND SPRING COMPANY, Bursa/Turkey for their technical support in the experimental processes.

5 REFERENCES

[1] T. Altan, S. Oh, H. L. Gegel, Metal forming, ASM, New York, 1983

[2] S. Beretta, M. Boniardi, Fatigue strength and surface quality of eutectoid steel wires, Int. J. Fatigue, 21 (**1999**), 329–335

[3] J. Toribio, E. Ovejero, Effect of cumulative cold drawing on the pearlite interlamellar spacing in eutectoid, Scripta Mater, 39 (**1998**) 3, 323–328

[4] A. J. Alawode, M. B. Adeyemi, Effects of degrees of deformation and stress-relief temperatures on the mechanical properties and residual stresses of cold drawn mild steel rods, J. Mater. Process. Tech., 160 (**2005**) 2, 112–118

[5] J. Languillaume, G. Kapelski, B. Baudelet, Evolution of the tensile strength in heavily cold drawn and annealed pearlitic steel wires, Mater. Lett., 33 (**1997**), 241–245

[6] G. Vega, A. Haddi, A. Imad, An investigation of process parameters effect on the copper-wire drawing, Mater. Design, 30 (**2009**), 3308–3312

[7] S. Norasethasopon, Influence of process parameters on shape quality and area fraction in round-to-hexagonal composite wire drawing, J. Mater. Process. Tech., 203 (**2008**), 137–146

[8] S. K. Lee, D. C. Ko, B. M. Kim, Pass schedule of wire drawing process to prevent delamination for high strength steel cord wire, Mater. Design, 30 (**2009**), 2919–2927

[9] A. Güzey, The Investigation of manufacturing process of ferrous wires, MSc Thesis, Trakya University, Natural and Applied Science Institute, Edirne 2009

[10] M. Suliga, Z. Muskalski, S. Wiewiórowska, The influence of drawing speed on properties of TRIP steel wires, J. Achieve. Mater. Manuf. Eng., 26 (**2008**) 2, 151–154

[11] H. Cho, H. H. Jo, S. G. Lee, B. M. Kim, Y. J. Kim, Effect of reduction ratio, inclusion size and distance between inclusions on wire breaks in Cu fine wiredrawing, J. Mater. Process Tech., 130–131 (**2002**), 416–420

[12] A. A. Gol'denberg, N. P. Sukhikh, T. M. Mineeva, Effect of manganese and nickel on the strength of steel under rigid loading conditions, Met. Sci. Heat Treat., 13 (**1971**) 6, 487–489

[13] M. Itabashi, K. Kawata, Carbon content effect on high-strain-rate tensile properties for carbon steels, Int. J. Impact Eng., 24 (**2000**), 117–131

[14] R. Song, D. Ponge, D. Raabe, Improvement of the work hardening rate of ultrafine grained steels through second phase particles, Scripta Mater., 52 (**2005**), 1075–1080

[15] M. I. Haq, N. Ikram, The effect of boron addition on the tensile properties of control-rolled and normalized C-Mn steels, J. Mater. Sci., 28 (**1993**) 22, 5981-5985

[16] P. Haušild, J. Siegl, P. Málek, V. Šíma, Effect of C, Ti, Zr and B alloying on fracture mechanisms in hot-rolled Fe–40 (at.%)Al, Intermetallics, 17 (**2009**), 680–687

UDK 620.179.1:620.179.11:691.714.018.8
Professional article/Strokovni članek

ISSN 1580-2949
MTAEC9, 47(2)253(2013)

IMPELLER-BLADE FAILURE ANALYSIS

PREISKAVA POŠKODBE LOPATICE ROTORJA

Roman Celin, Franc Tehovnik, Franc Vodopivec, Borut Žužek

Institute of Metals and Technology, Lepi pot 11, 1000 Ljubljana, Slovenia
roman.celin@imt.si

Prejem rokopisa – received: 2013-01-10; sprejem za objavo – accepted for publication: 2013-01-31

The axial pumps are used in a wide variety of applications, such as drainage control, power plants and process cooling. A fresh-water, vertical, axial-pump, stainless-steel impeller failed. The impeller was a single cast from stainless steel. A visual examination indicated that the fracture originated near the blade-to-hub attachment. During the investigation standard nondestructive and destructive methods were used. Specimens from the failed blades were taken for a material characterization. The goal of the examination was to determine a possible cause for the impeller-blade failure. After the examination it was determined that the most probable cause for the impeller-blade failure was the fatigue stress.

Keywords: blade, impeller, cast stainless steel, crack

Aksialne črpalke se uporabljajo za različne namene, kot so namakanje, hlajenje procesne opreme in komponent termoelektrarn. Lopatica rotorja vertikalno postavljene aksialne črpalke se je nepričakovano poškodovala. Lopatica in rotor sta bila ulita iz nerjavnega jekla kot celota. Vizualna preiskava rotorja je odkrila razpoko na vstopnem robu lopatice v bližini pesta. Med preiskavo vzroka nastanka poškodbe so bile uporabljene standardizirane porušitvene in neporušitvene metode. Iz lopatice rotorja so bili izdelani preizkušanci za karakterizacijo materiala. Namen preiskave je bil odkriti verjeten vzrok za poškodbo lopatice. Po končani preiskavi je bilo ugotovljeno, da je najbolj verjeten vzrok za nastanek razpoke utrujanje materiala zaradi vibracij lopatic rotorja.

Ključne besede: lopatica, rotor, lito nerjavno jeklo, razpoka

1 INTRODUCTION

Centrifugal pumps are turbomachines used for transporting liquids by raising a specified volume of the flow to a specified pressure level. The basic centrifugal-pump components are: the casing, the bearing housing, the pump shaft and the impeller.[1] A pump configuration of the components may vary depending on the fluid-flow direction that can be radial, semi-axial or axial. Axial-flow pumps achieve larger flow rates than radial pumps and are used in drainage control, power plants and process cooling. **Figure 1** shows a generic design of a vertical, axial, centrifugal pump with the main components.

Any pump operation is determined by the flow rate Q (m^3/s), the head H (m) and impeller revolutions n (min^{-1}). The head is the measurement of the height (m) of the liquid column the pump creates from the kinetic energy that the pump gives to the liquid. The design and operation of a pump also depends on the operation efficiency, the stability of the head-capacity characteristic, vibration and noise. An important issue is also a possible pump failure due to fatigue, cavitation, hydro-abrasive wear or erosion corrosion. Most vertical pumps are out of sight during the operation and, for this reason,

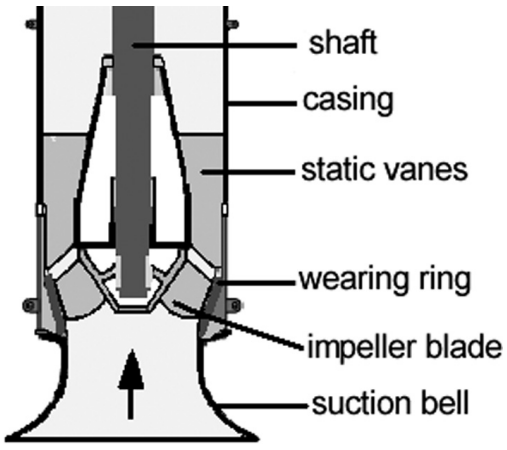

Figure 1: Vertical, axial, centrifugal pump
Slika 1: Vertikalna aksialna centrifugalna črpalka

Figure 2: Damaged impeller blade
Slika 2: Poškodovana lopatica rotorja

it is important to monitor the shaft vibrations and other operational parameters.

Twelve months after a plant outage a vertical, axial-flow, fresh-water pump, stainless-steel impeller failed. The hub and impeller blades were a single cast made of the ASTM A743 stainless steel (grade 316). This stainless-steel grade was a material of choice because of its good erosion-resistant properties. The axial-pump flow rate was $Q = 8.453$ m^3/s, the head was $H = 13.72$ m and the number of revolutions was $n = 370$ min^{-1}. A complete pump assembly was dismantled and the maintenance crew immediately discovered a very distinct crack on an impeller blade (**Figure 2**). The pump owner decided to carry out a failure analysis.

A failure analysis is a broad discipline that includes materials and mechanical engineering. The purpose of this paper is to present a failure-analysis procedure applied in the case of an impeller-blade failure investigation at the Institute of Metals and Technology (IMT, Ljubljana, Slovenia).

2 EXAMINATION PROCESS

The failure analysis is explained in books[2–6] and papers.[7–11] The examination process starts when a component under observation has lost its designated function in a system. In general, the examination process or analysis of a damaged component is performed in several steps, which are described below. The first step is usually the on-site visit and the gathering of all the available information on the failed component and the in-service conditions of the component.

The next step includes nondestructive examinations. There is a variety of nondestructive techniques available[12]. The search for material imperfections is performed with X-ray, magnetic particle, ultrasonic, liquid penetrant, eddy current, and other nondestructive testing procedures. The most common is the visual examination aiming to determine the general mechanical and structural conditions of the components. The result of a visual examination is a record in the form of a sketch, dimension-measurement data or a photography, identifying discontinuities or imperfections on the surface of the components such as cracks, wear, tear, corrosion, erosion, etc.

Based on the results of a visual examination and the on-site information further decisions on the course of the examination are made. Usually that means establishing a plan for a destructive testing that involves the cutting off a sample material from the failed component, and an investigation of the samples in a laboratory for a chemical analysis, metallography, a mechanical testing and others depending on the testing plan.

A chemical analysis is performed on the original material to verify if the material sample meets the appropriate specification or standard, and whether a deviation from the specifications could have contributed to the failure. A wet chemical analysis, atomic absorption, X-ray photoelectron, Auger electron and inductively coupled plasma-mass spectrometry (ICP MS) are some of the suitable methods of a chemical analysis.

The tensile test is one of the most frequently used tests for evaluating the mechanical properties of materials.[13] A tensile force is applied with a machine and a gradual elongation and the final fracture of the test samples are obtained. The tensile test provides the force-extension data that can quantify the quasi-static mechanical properties of a material: yield strength, ultimate tensile strength, elongation and reduction of area at fracture.

Charpy (CVN) toughness tests are widely used to determine the impact toughness of a material and the effect of temperature on the sensitivity of structural steels to brittle fracture. Notched specimens are submitted to the impact of a hammer with the kinetic energy of 300 J. The fracturing occurs in a ductile, mixed or brittle mode and, accordingly, very different quantities of energies are consumed.

A careful investigation of the macrostructure and microstructure of a failed material can provide the most important information. A macroscopic examination of a component sample evaluates the surface of the component sample at a low magnification (usually up to 10 times). The type of a fracture such as ductile, brittle or torsion can be identified.

Metallographic examinations are performed with an appropriate magnification of optical and scanning electron microscopes (SEM). During an optical microscopic examination the grain size, microcracks, the general microstructure and inclusion content are determined. Scanning electron microscopy is used to determine small details of a microstructure, fracture, precipitate size and distribution and characteristics of crack initiation and propagation. Furthermore, with the use of an energy dispersive analysis (SEM/EDS) corrosion products on a fracture surface can be identified. It is useful to compare the microstructure of the samples removed from a failed component with the samples removed from the sound sections of a component.

A collection of visual, metallographic and SEM results along with a chemistry analysis, mechanical data and on-site information provides a solid ground for an examiner to put together conclusions on the causes and mechanism of a component failure. This is no easy task, because, in many cases, the failure reasons are not obvious even if a lot of information is available. Sufficient experience in a failure analysis is necessary to identify the cause of a failure.

3 RESULTS AND DISCUSSION

3.1 Visual examination

Only a visual examination[14] was performed on the failure site. The stainless-steel impeller (**Figure 3**) was a cone-shaped hub with an approximate thickness of 35 mm with six blades attached. The blades vary in thick-

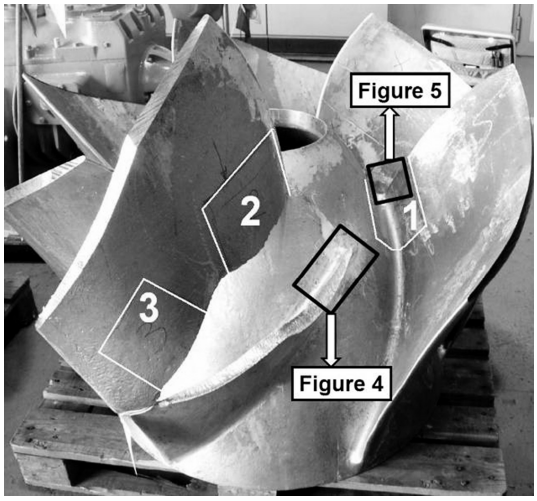

Figure 3: Positions of **Figures 4** and **5** with samples 1, 2 and 3 before the removal
Slika 3: Položaj **slik 4** in **5** ter oznake vzorcev 1, 2 in 3 pred odvzemom

ness from approximately 25 mm near the hub to an average of 10 mm at the top of the blade. **Figures 2** and **3** show that the cast surface of the blades and the hub was not ground. Several areas were detected on the blades and at the attachment zone of the blades and the hub (**Figures 4** and **5**) where weld-repair work on the cast was performed by the supplier.

Figure 4: Crack surface with a repair-weld build up at the blade leading-edge attachment to the hub
Slika 4: Površina razpoke z reparaturnim zvarom na stiku čela lopatice in pesta

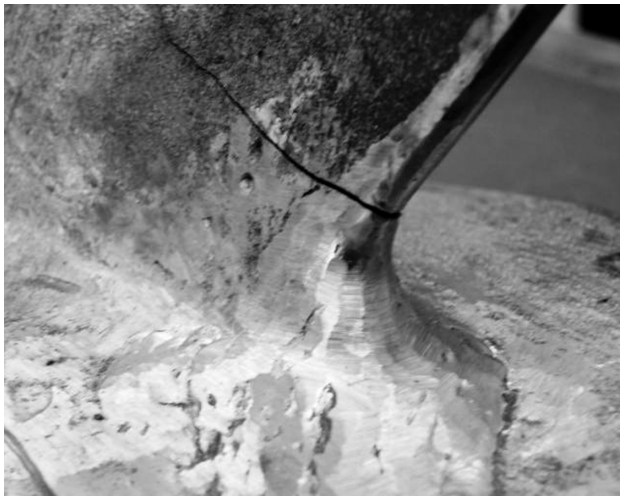

Figure 5: Crack at the leading edge of the blade
Slika 5: Razpoka na vodilnem robu lopatice

The top of the blade started to rub against the inner ring surface and possibly the impeller operated in a damaged condition for some time. The material loss at the top of the blade, caused by friction wearing, is noticed on **Figure 3**.

The most obvious feature on **Figures 2** and **3** is the blade splitting over the entire hub. The crack propagated at an angle of approximately 30°–35° from the blade leading edge toward the outer edge. The visual examination of the other blades revealed a through-thickness crack at the leading edge of the blade marked as sample 1 and it is shown, in detail, on **Figure 5.**

The crack initial point on both blades (**Figures 3, 4** and **5**) was above the weld-heat-affected zone. It was not possible to determine the exact initial point of the crack on the blade leading edge. The crack surface was smooth and mostly plastically deformed due to the surface grinding during the pump operation.

Tree samples (**Figure 3)** were chosen for further analysis. **Figure 5** shows sample 1 which was used for a fracture analysis, while samples 2 and 3 were used for manufacturing the tensile and Charpy V-notch specimens.

3.2 Chemical analysis

A quantitative chemical analysis was performed on the impeller-blade sample material. It was made with an ICP mass spectrometer. The results of the composition analysis are shown in **Table 1**.

Table 1: Chemical-composition comparison in mass fractions (*w*/%)
Tabela 1: Kemijske sestave materiala rotorja v masnih deležih (*w*/%)

	Cr	Ni	Mo	Mn	Si	P	C	S	N
sample 1	17.5	9.73	2.05	1.07	1.03	0.022	0.03	0.003	0.044
material test report	19.2	9.6	2.3	1.08	1.28	0.03	0.01	0.01	–
ASTM A 743 CF3M	17-21	9-13	2-3	1.5	1.5	0.04	0.03	0.04	–

The sample-1 chemical-composition-analysis results and impeller-manufacturer material-test report were in accordance with the ASTM grade A743 (316L) cast stainless-steel specification requirements presented in **Table 1**.

3.3 Mechanical testing

A series of standard tensile tests[15] and impact tests[16] were performed with the specimens machined from the samples shown in **Figure 1**. The goal of the standard mechanical tests was to find out if the sample material was in accordance with the manufacturer's material-test report and the ASTM specification. The tensile-test results are presented in **Table 2**.

Table 2: Tensile-test results
Tabela 2: Rezultati nateznega preizkusa

	Yield strength $R_{p0,2}$ /MPa	Tensile strength R_m/MPa	Elongation A/%
sample 2			
1	262	524	57
2	284	527	59
3	301	562	64
material test report			
US units	48 PSI	91 PSI	30
ASTM A 743 specification			
SI units	min. 205	min. 485	30
US units	min. 30 PSI	min. 70 PSI	30

The yield-strength and tensile-strength results for the three machined specimens are in accordance with the manufacturer's material-test results and ASTM specification requirements.

The Charpy impact tests were performed at room temperature, according to the SIST EN standard, on a testing machine with an impact pendulum of a 300 J capacity. The Charpy-test results on the three V-notch samples were 250 J, 203 J and 261 J of the absorbed pendulum energy, which is above the minimum required value of 100 J from the owner's specification.

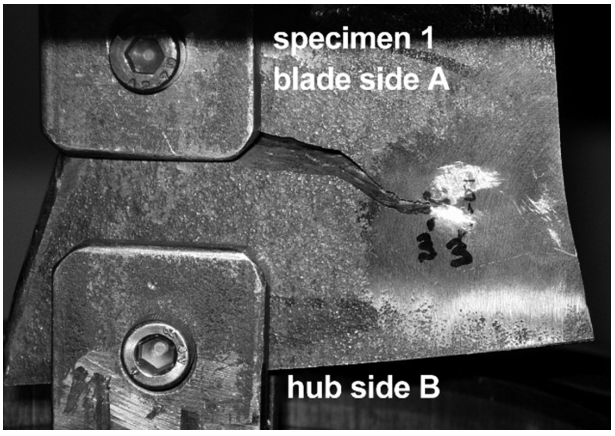

Figure 6: Sample-1 crack opening on a tensile-testing machine
Slika 6: Razpiranje vzorca 1 na trgalnem stroju

Figure 6 shows sample 1, cut from the hub, clamped on the tensile-testing machine with the purpose to obtain the fracture surface without any grinding or other damage.

3.4 Metallographic examination

Figure 7 shows the cast A743-steel microstructure of the hub at the blade side B of specimen 1 and **Figure 8** shows the microstructure of the blade leading edge (side A).

It consists of dendritic austenite grains with the inserts of δ ferrite at some grain boundaries. The content of the δ ferrite was of about 5 %. The microstructure shown on both pictures is without any peculiarity and it is typical for the cast stainless steel.

3.5 Scanning electron microscopy (SEM)

Figure 9 shows the side-A fracture-surface view. The bright area (marked as 1.2) on the right is the fracture

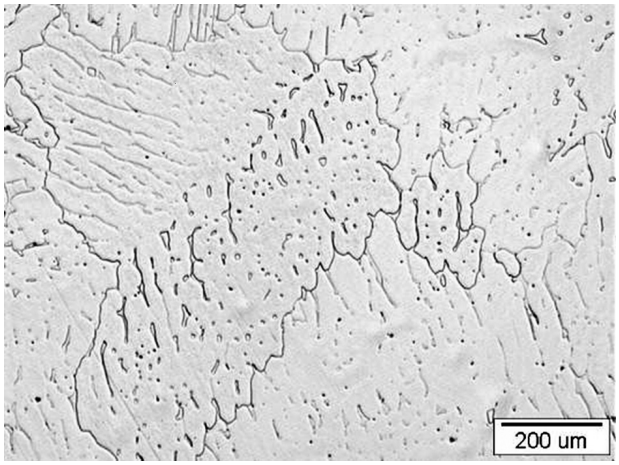

Figure 7: As-cast microstructure of the hub-to-blade attachment
Slika 7: Mikrostruktura ulitka na stiku pesta in lopatice

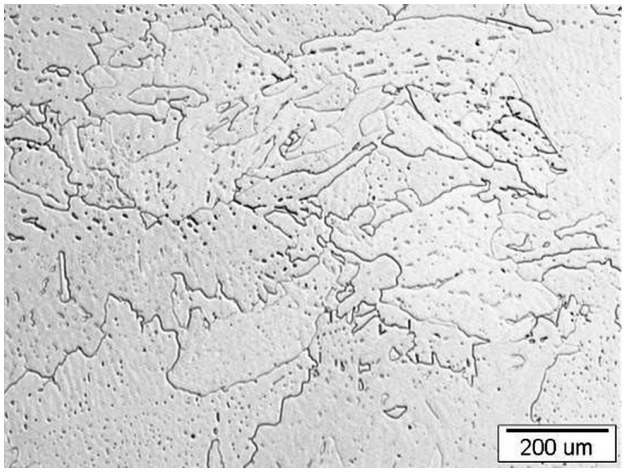

Figure 8: Microstructure of the blade leading edge (sample 1 – side A)
Slika 8: Mikrostruktura roba lopatice (vzorec 1 – stran A)

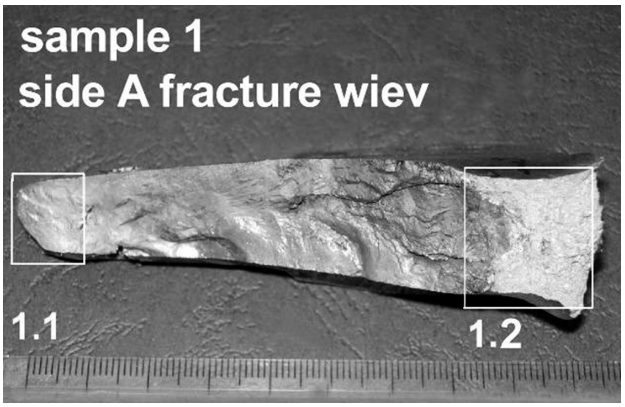

Figure 9: Side-A fracture surface of sample 1
Slika 9: Površina preloma na strani A vzorca 1

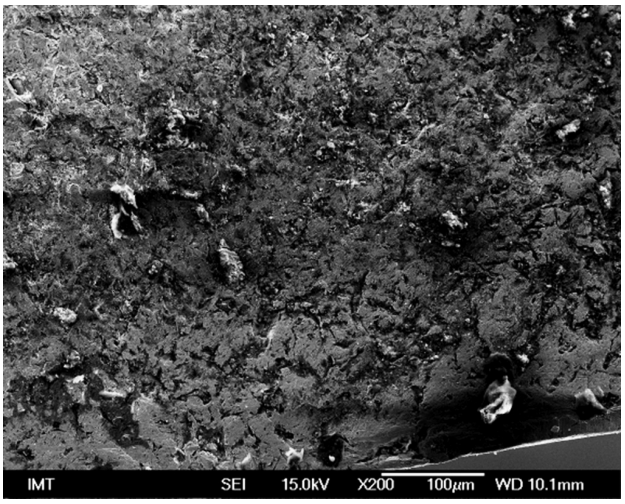

Figure 10: SEM image of plastically deformed surface area 1.1
Slika 10: SEM-posnetek deformirane površine, označene z 1.1

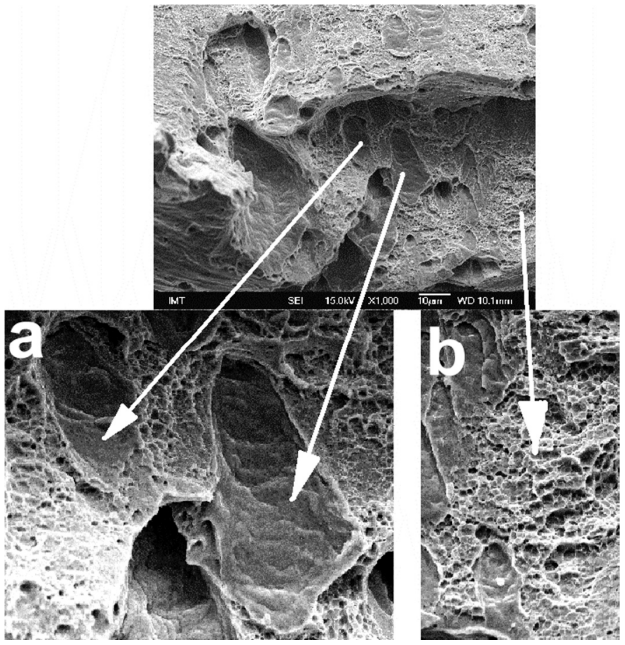

Figure 11: a) Interphase fracture and b) ductile fracture
Slika 11: a) Medfazni in b) žilav prelom

surface obtained by tensile-machine crack opening (**Figure 6**).

The sample-1 side-A fracture surface has the same features as the fracture surface shown on **Figure 4.** The surface is smooth and the mostly plastically deformed area marked as 1.1 **(Figure 9)** was carefully examined with an optical microscope. Because of the plastically deformed surface, the exact crack point of origin was impossible to ascertain. Also, the crack propagation mode could not be distinguished on the damaged surface **(Figure 10)** and the fatigue striations were not detected either.

The area (marked as 1.2 on **Figure 6**) enabled a SEM investigation of the fracture surface, and **Figure 11** shows two fracture modes. One **(Figure 11 a)** presents an interphase crack propagation on the interface of austenite and the inserts of δ ferrite, while the other **(Figure 11 b)** looks like a ductile fracture with small dimples.

4 CONCLUSIONS

The examination procedure described was performed to determine the mechanism of a failure of stainless-steel impeller blades. According to the owner's data the impeller operated within the design parameters. For the given application, the impellers appear to have been fabricated within the tolerances and specifications required by the owner. The surface of the hub and blades was as cast. In general, an as-cast condition of a surface as well as the weld-repair places are sensitive regions prone to a crack formation because of dynamic loading.

The metallographic examination did not reveal a deteriorative influence of a weld on the microstructure around the crack-initiation area. The crack-initiation point could not be determined because of the deformed surface.

After the examination it was concluded that the most probable cause for the impeller-blade failure was the fatigue caused by the flow-induced vibrations due to a turbulent flow over the blades and the internal stresses caused by the welding repair of the casting defects.

The crack-initiation point on the blade leading edge was probably a weak spot between the columnar dendritic grains of the cast.

5 REFERENCES

[1] J. F. Gülch, Centrifugal pumps, Springer-Verlag, Berlin 2008, 61 or 368
[2] K. A. Esakul, Handbook of case histories in failure analysis, Vol. 1, ASM International, 1992, 251
[3] H. M. Tawancy, A. Ul-Hamid, N. M. Abbas, Practical engineering failure analysis, Marcel Dekker, New York 2004, 14
[4] W. T. Becker, R. J. Shipley, ASM Handbook, Vol. 11, Failure analysis and prevention, Materials Park: ASM International, 2002, 316
[5] A. K. Das, Metallurgy of failure analysis, Mc Graw-Hill, New York 1997, 55

[6] C. Brooks, A. Choudhury, Failure analysis of engineering materials, Mc Graw-Hill, New York 2002, 8
[7] M. Torkar, F. Tehovnik, M. Godec, Mater. Tehnol., 46 (**2012**) 4, 423–427
[8] A. van Bennekom, F. Berndt, M. N. Rassol, Eng. Failure Analysis, 8 (**2001**) 2, 145–156
[9] M. Muhič, J. Tušek, F. Kosel, D. Klobčar, M. Pleterski, Thermal fatigue cracking of die-casting dies, Metallurgy, 49 (**2010**) 1, 9–12
[10] G. Kosec, A. Nagode, I. Budak, A. Antić, B. Kosec, Failure of the pinion from the drive of a cement mill, Eng. Failure Analysis, 18 (**2011**) 1, 450–454
[11] R. B. Setterlund, V. K. Malhotra, L. K. Friesen, Failure of 13 % Chromium Stainless Steel Impeller From Hydrogen Recycle Compressor, Proc. of the Corrosion 2000, Orlando, USA, 2000
[12] ASM Handbook, Volume 17, Nondestructive Evaluation and Quality Control
[13] ASM Handbook, Volume 8, Mechanical Testing and Evaluation
[14] SIST EN 13018, Non-destructive testing – Visual testing – General principles
[15] SIST EN ISO 6892-1, Tensile testing, Method of test at ambient temperature
[16] ISO 148-1, Charpy pendulum impact test